ELECTRON ACCELERATION IN AURORAL FIELD-ALIGNED CURRENTS

Alexandra P. Cran-McGreehin

A Thesis Submitted for the Degree of PhD
at the
University of St Andrews

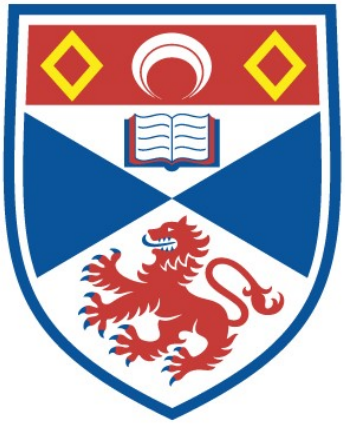

2006

Electron acceleration in auroral field-aligned currents

Alexandra P. Cran-McGreehin

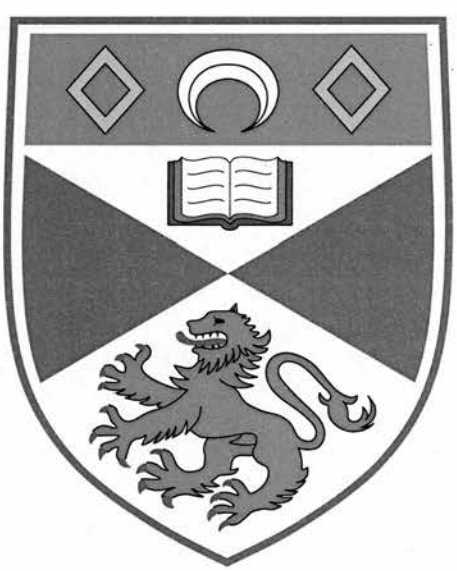

Thesis submitted for the degree of Doctor of Philosophy
of the University of St Andrews

July 12, 2006

Abstract

Field-aligned currents at Earth's high latitudes are principally carried by accelerated electrons. Current densities, typically $\sim\mu\text{Am}^{-2}$ at ionospheric altitudes, are sustained by parallel potential drops of $\sim$100 - 1000 V. This Thesis presents Vlasov models of upward and downward current regions, where electrons are described via distribution functions. The ion density profile is fixed, and quasi-neutrality is invoked to solve numerically for the potential variation.

In both cases, an ambipolar electric field traps ionospheric electrons. For downward currents, an energetic ionospheric electron beam emerges into the magnetosphere where it is accelerated around the B/n peak at altitudes of 500 - 6000 km to carry the current. The electric field maximises just Earthward of the B/n peak. The magnitude and altitude of the potential is found to depend solely on the equilibrium properties immediately above the B/n peak. An analytic non-linear current-voltage relation, analagous to the linear Knight relation for upward currents, is derived.

Energetic magnetospheric electrons precipitate into the ionosphere to carry upward currents. The continuous potential variation is solved for current densities $\sim$1 μAm^{-2}. Acceleration extends above the B/n peak for $\sim$1 R_E, and is increasingly concentrated at the peak for higher current densities. The presence of mirroring electrons is vital to the system, as they play a major role in satisfying quasi-neutrality, and support the majority of the parallel electric field.

Ion outflow is a feature of both current regions, but is stronger and extends to lower altitudes for downward currents: this is presented as a possible explanation for observed lower-altitude acceleration in downward currents compared to upward currents.

The effect of downward currents on E region number density is studied using an Alfvén wave model of magnetosphere-ionosphere interaction, employing a height-integrated Pedersen conductivity. It is found that significant E region depletion and current broadening are more common on the nightside than on the dayside, and occur in $\sim$10 - 100 s.

Declaration

I, Alexandra Cran-McGreehin, hereby certify that this thesis, which is approximately 50,000 words in length, has been written by me, that it is the record of work carried out by me and that it has not been submitted in any previous application for a higher degree.

Signature of candidate .. .... **Date** ....13/11/2006.....

I was admitted as a research student in October, 2002 and as a candidate for the degree of Doctor of Philosophy in October, 2003; the higher study for which this is a record was carried out in the University of St Andrews between 2002 and 2006.

Signature of candidate ... ... **Date** ....13/11/2006.....

I hereby certify that the candidate has fulfilled the conditions of the Resolution and Regulations appropriate for the degree of Doctor of Philosophy in the University of St Andrews and that the candidate is qualified to submit this thesis in application for that degree.

Signature of supervisor . .... **Date** ....13/11/2006.....

In submitting this thesis to the University of St Andrews I understand that I am giving permission for it to be made available for use in accordance with the regulations of the University Library for the time being in force, subject to any copyright vested in the work not being affected thereby. I also understand that the title and abstract will be published, and that a copy of the work may be made and supplied to any *bona fide* library or research worker.

Signature of candidate .. ... **Date** ....13/11/2006.....

Acknowledgements

There are many people who deserve my gratitude for their support during my Ph.D.: firstly, my supervisor Andy Wright, without whom this thesis would simply not exist. He was always willing to provide help when it was necessary, but also encouraged me to solve problems independently, which gave me much satisfaction. He has also been extremely supportive and considerate during some difficult times.

Alan Hood provided much expertise and enthusiasm for Chapter 5, including his infamous method of characteristics. I would also like to thank Thomas Neukirch for many useful discussions, including, most recently, reassurance concerning my instabilities (electron instabilities, of course!).

I am endebted to the Carnegie Trust for the Universities of Scotland, who sponsored my doctoral studies, and enabled me to travel to several summer schools and conferences.

Thanks are also due to all those with whom I have shared this journey: my officemates Paul, Lorna, Mike, Michelle, Dee and Gavin have all provided help, amusement and welcome distraction!

I am extremely grateful to my parents: they have supported me throughout my education and have always encouraged me to excel and fulfil my potential. My mum has always been there for me, ready with a consoling hug or an encouraging chat. My dad was definitely the first mathematical influence in my life, teaching me Pythagoras' theorem at the age of six!

Finally, I wish to thank my handsome husband, Simon, for being my constant companion. He has stood by me through some difficult times, and we have shared much happiness. He is kind, loving and devoted to me, and I am truly blessed to be married to him!

Contents

List of Figures

Chapter 1

Introduction

1.1 The aurora borealis

During the night luminous clouds were seen, gold and white, with long streamers, which lit up the hills. Some think it is Heaven's Sword, but others think that it is a deep hole, with a large blazing fire in the sky.
Earliest written record of the northern lights, China 208 BC *(Jago (2002))*

The dazzling, mystical *aurora borealis*, pictured below, have captured the imagination of the human race for centuries. These seemingly inexplicable and powerful displays have invoked both fear and wonder into generations of people, and it is not surprising that they are the subject of much folklore. The breadth of these myths is astounding. Whilst Eskimos in Greenland thought that the dead were trying to contact living relatives, the Scots believed that supernatural Merry Dancers were endeavouring to catch the attention of a beautiful lady! In the Nordic countries, some imagined that huge polar volcanoes were responsible, whilst others thought that the lights were the reflections of herring swimming close to the water's surface: the lights were thus a useful fishing guide. The Danish story is beautiful: swans flying too far north were caught in the ice, and the furious flapping of their wings as they tried to escape produced the haunting auroral displays *(Brekke and Egeland (1983))*.

The aurora are normally seen in extreme northerly and southerly regions, but every fifty or a hundred years, a huge blood-red display will extend far further towards the equator to London, Paris, Vienna and Rome. The ferocity of these displays led many to believe that they were a portent of war or disease. This belief was reinforced by one such aurora on 9th September 1898, which was followed by the assassination of the beautiful Empress Elisabeth of Austria and Hungary, pictured below, in Geneva the very next day.

Kristian Olaf Birkeland, a Norwegian scientist born in 1867, was not stirred by this occurrence, assured that it was simply a tragic coincidence. Much of the following historical account is taken from his biography by *Jago (2002)*. He was convinced that the northern lights had a more scientific, yet no less awe-inspiring, cause. Indeed, he was not the first to think this: in 450 BC, the Greek Anaxagoras postulated that the Sun was not indeed a god, but a ball of fire, and that the aurora, comets and lightning were caused by fiery

gases descending from the sky and bursting into flame. He was imprisoned for his heretical ideas, and a hundred years later, Aristotle firmly deposed his theory by stating categorically that there was no connection between the heavens and the Earth. This belief lingered for centuries, but Birkeland did not subscribe to it.

Birkeland realised that scientific observation would be needed to dispel some of the myths about the aurora and discover more about their actual origin. So, although he hated strenuous physical activity, he organised a mission to study the northern lights towards the end of the nineteenth century. He arranged for a small purpose-built observatory to be erected at the top of Haldde mountain in northern Norway, a thousand metres above sea level. Not only would this provide a wonderful vantage point from which to see and study the sky, but the view would be unsullied by electric lighting from cities. Another smaller observatory was built four kilometres away on a neighbouring mountain, to allow for contemporaneous observation of the lights, and thus the determination of their height above the ground. There was even telegraphic communication between the two observatories. Birkeland recruited four eager young helpers for this expedition: Bjørn Helland-Hansen, a surgical student at Christiania University in Oslo, Elisar Boye, a Latin scholar, Kristoffer Knudsen, a telegraphic engineer, and Sem Sæland, a multidisciplinary science student.

Led by a local postman, this team set out on 14th October 1899 carrying their heavy equipment up to the summit of Haldde mountain. The weather was atrocious, and the frostbite suffered by Helland-Hansen during this journey ended not only his contribution to the mission, but also his career as a surgeon, as many of his fingertips subsequently had to be amputated. The team eventually arrived at the small building, which had four rooms: a kitchen complete with stove, a bedroom, a workroom, and the instrument room. Birkeland had sought to secure the best equipment from abroad to collect his data. He had an anemometer to measure wind speeds, an electrometer to measure atmospheric electric data, an alcohol thermometer which could withstand incredibly cold conditions, a barometer to measure air pressure, a hygrometer to measure

Figure 1.1: A dazzling auroral display in Alaska, courtesy of alaska.com

air humidity, photographic equipment, wind kites to measure wind speeds thousands of metres above the ground, and lastly, but most importantly, a finely-tuned magnetometer. It had long been recognised that the aurora constituted a navigational threat by interfering with compass readings, but no-one knew why. With all this equipment, Birkeland hoped to answer some of the age-old questions about the lights: Did they create a crackling noise? Did they cause one's hair to stand on end, or burn flesh, or cause headaches? Did they touch the ground? Were they brighter during colder conditions? Did they occur during the daytime?

The small company of men lived on the top of the mountain for the entire winter, coming down only once to celebrate Christmas. A good proportion of this time was spent in perpetual darkness, when the sun never rose. Although perfect for auroral observation, this was a mental drain on the team. The cold and sometimes severe weather conditions were also a trial, described vividly by Birkeland in his notebook:

"The wind sometimes roars so against the house that you would have thought you were sitting at the foot of a waterfall; and the floors tremble and everything shakes. We are able to gauge the storm outside by the noise within. Often we cannot get out of the house ourselves for several days and it takes three strong men to shut our little door. One strong anemometer was blown apart in the course of a few days and we found pieces of it 50 to 100 metres from the place it had been put up...Even indoors the situation is not always comfortable. Water freezes a couple of feet from the stove and the lamp is often blown out on the table in the middle of the room, although in a general sense the house is well-enough built."

Serious observational work began at the beginning of November: data was taken all day, especially frequently between 6 pm and 1 am, when the lights were at their most active. The data was painstakingly logged in ledgers, and photographs were developed in the hut. Several questions were immediately answered during the mission: the aurora was observed to occur about 100 km above the ground, produced no audible crackling noises, and had no adverse physical effects on any of the team during their stay. The results which emanated from this expedition would change planetary science forever, but they were not

Figure 1.2: Empress Elisabeth of Austria and Hungary, who was tragically assassinated in Geneva the day after a huge auroral display over Europe in September 1898[1].

without their cost; not only did Helland-Hansen lose his fingers, but two of Birkeland's friends died in an avalanche on their way up to the mountain at the end of the mission.

Birkeland published his initial findings very soon afterwards in *The Norwegian Expedition of 1899-1900 for the study of the Aurora Borealis*. His main breakthrough can be found in the following paragraph:

"It emerges from our results, that the magnetic perturbations and the aurora borealis are secondary and local phenomena attaching to the same cosmic phenomenon. This primary phenomenon consists, there is no doubt, of electric currents in the upper levels of the atmosphere; in the polar regions, where they seem to have their point of departure, these currents are fairly well defined and concentrated. The currents pass, on average, at a height of approximately 100 km above the terrestrial surface and can cause strong magnetic perturbations of a total intensity above 400,000 amperes."

Birkeland wished to test this theory by building a miniature Earth and demonstrating the process described above, but he had no funds available to him after his ambitious and expensive Norwegian expedition. So, he turned his attention to a more lucrative project: an electromagnetic cannon. As tensions were brewing throughout Europe, he knew that there would be widespread interest in his invention; this proved to be so, but unfortunately, in a public demonstration on 6th March 1903, his cannon short-circuited and produced a terrifyingly huge arc of electricity! Nothing was injured except Birkeland's pride, but this incident led to an even more profitable venture with engineer Sam Eyde. The world was facing a severe lack of natural fertiliser, and whilst it was known that atmospheric nitrogen and oxygen could be harnessed to produce nitric acid under extreme conditions equivalent to lightning, no-one had been able to set up an efficient, financially-viable mechanism to achieve this. Birkeland's electrical arc was just what was needed, and he managed to perfect his technique in conjunction with Eyde's hydroelectric plant. They set up a company called Electrochemical Industry (ELKEM), which would provide Birkeland with the financial means to

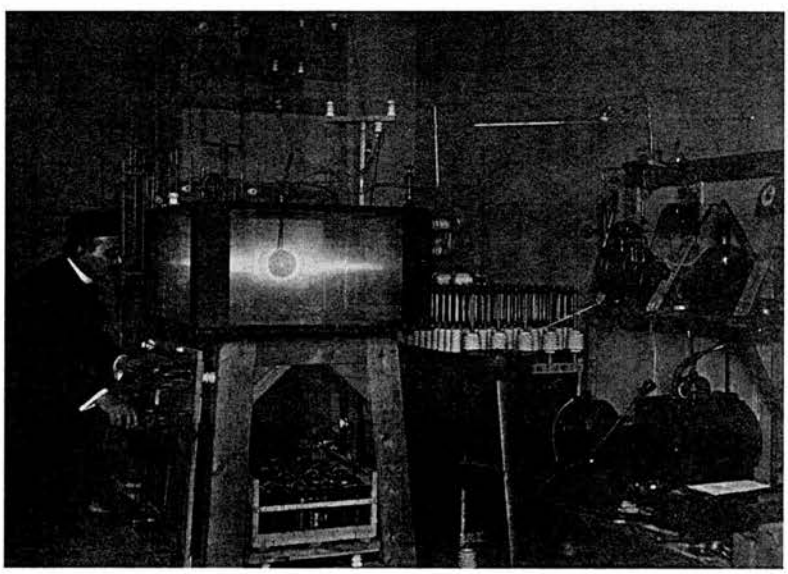

Figure 1.3: A photograph of Birkeland examining his terrella[2], in which he managed to recreate the northern lights and other phenomena in space.

carry out his desired research for the rest of his life, whilst also solving a major world problem.

With the aid of this wealth, Birkeland took over half of the lecture theatre in Christiania University in order to recreate the aurora in a laboratory. He created an electromagnet by wrapping copper wire around an iron core and insulating it with silk. He then placed this in a hollow brass globe, which had a phosphorescent coating of barium platinocide which would glow when impacted by sufficiently energetic electrons. A cathode ray tube bombarded this miniature magnetised Earth with high-velocity electrons in an evacuated chamber, and this mechanism did indeed recreate the northern lights, as shown in the photograph in Figure 1.3. Later, Birkeland was also able to use this "terrella" to recreate many other cosmic features, such as comets and Saturn's rings, which stunned audiences in Oslo. Birkeland's understanding of interplanetary and planetary science was unparalleled, and formed the basis of our understanding of the aurora and the Sun-Earth connection. In Birkeland's own words at the beginning of one public lecture:

"To understand the distances that I have captured in this vessel, imagine that our sun is a grain of sand a millimetre in diameter. In that case, the Earth would be an invisible speck of dust ten centimetres away. And the next nearest star, Alpha Centauri, would be twenty kilometres away. It is in this vast, infinite space that the genesis of all celestial bodies is to be found. All matter that we see, be it our own bodies, our Earth, other planets, the sun, our solar system and other solar systems, all matter is composed of flying atoms which are continuously ejected from our sun and other suns by electrical forces and which condense to form particles. And these in turn condense to form large spheres, ultimately planets and all there upon. It follows from this that everything that is matter, all living beings in the universe, are linked, one to the other."

1.2 The magnetosphere

The magnetosphere is the area of space surrounding the Earth which is under the influence of its magnetic field. An excellent account of the magnetosphere is given in *Cowley (1996)*, from which much of the following discussion is drawn. This magnetic field is created by a dynamo process, where thermal convection in the centre of the Earth drives currents that flow through the molten, electrically-conducting iron core. To first order, this magnetic field is a dipole whose axis is tilted with respect to the spin axis of the Earth by 11°. This dipole axis wanders slowly with time, and is believed to flip every 100,000 years or so. The magnetic field strength at the Earth's surface is 25×10^3 nT at the equator, and 60×10^3 nT at the poles.

If the Earth were alone in space, then its magnetosphere would be symmetrical, with essentially dipolar magnetic field lines. However, there is a constant fully-ionised stream of particles flowing towards the Earth from the Sun, called the solar wind. This is mainly composed of hydrogen and helium ions from the Sun's upper atmosphere, which is so hot that the particles are energetic enough to escape the gravitational attraction of the Sun and form a steady outflowing stream of material. The solar wind has a number density of 6 cm^{-3} at Earth's orbit, and travels at supersonic speeds of 300 to 800 km s^{-1}, and its pressure distorts the magnetosphere into a teardrop shape shown in Figure 1.4, with a long tail which streams antisunward for several hundred Earth radii.

In most space environments, magnetic fields and plasma flows are "frozen together"; that is, magnetic fields are transported by flowing plasmas, and they bend and twist together. At large distances, the lines of the Sun's magnetic field (called the Interplanetary Magnetic Field, or IMF) would radiate out in straight lines if the Sun were not rotating; however, they are bent into an Archimedean spiral shape by this rotation, as shown in Figure 1.5. Thus, at the outer boundary of the magnetosphere called the magnetopause, there is a transition from the Earth's magnetic field to the IMF, resulting in sharp changes to the direction and strength of the ambient magnetic field. The magnetic field is weaker in the solar wind ($\sim$ 5 nT) than it is in the magnetosphere, but the number density inside the magnetosphere is significantly smaller than in the solar wind; thus, the magnetosphere is a cavity.

The magnetosphere is compressed to around 70,000 km (10-12 Earth radii) on the sunward side. This distance can vary, as the magnetospheric boundary occurs where there is pressure balance between the Earth's magnetic field and the solar wind ram pressure. So, a faster solar wind flow forces the magnetospheric boundary closer to the Earth. A shock wave called the bow shock forms in the solar wind ahead of the Earth, caused by the flow of supersonic material around the obstacle created by the magnetospheric cavity. This shock wave has the effect of decreasing the solar wind velocity, allowing for subsonic flow around the magnetosphere. It also compresses and heats the plasma, forming a turbulent region called the magnetosheath just upstream from the magnetopause.

1.2.1 The solar wind-magnetosphere interaction

If the frozen-in approximation is rigorously applied to the solar wind-magnetosphere system, then there can be no mixing of the two plasmas, and two totally separate regions are formed. This implies a closed

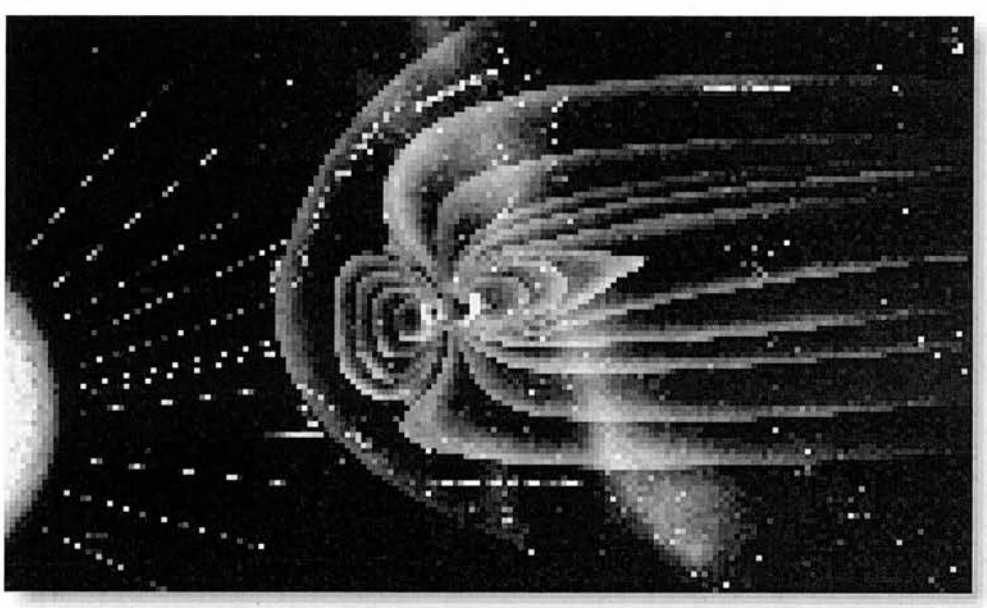

Figure 1.4: The Earth's magnetosphere is distorted by the supersonic solar wind which impinges on it from the Sun[3].

magnetospheric cavity whose size is determined by the solar wind pressure; this was first postulated by Chapman and Ferraro in the early 1930s. It also means that there can be no energy and momentum transfer between the solar wind and magnetospheric plasma. However, under certain conditions, the frozen-in approximation can break down *(Kivelson and Russell (1995))*. This can occur when the magnetic field gradient is very large (that is, the magnetic field varies over a very short distance and is associated with a large current density) and plasma is moving slowly towards the boundary. This is exactly what happens at the magnetopause, which is by nature a thin boundary between two completely different magnetic fields, with the solar wind flowing towards it. If, in addition, we have oppositely directed field lines on either side of the boundary, a process called diffusion becomes important, and field lines can break and reconnect, as shown in Figure 1.6. The reconnected field lines move away from the reconnection site, and solar wind and magnetospheric plasmas mix freely on them. It is via this process that plasma, energy and momentum can be transferred between the solar wind and the magnetosphere. Since the Earth's magnetic field points northward, reconnection can occur most easily when there is a southward-pointing IMF; the most obvious location for this would be at the sunward tip of the magnetopause.

This process leads to what is known as an open magnetosphere, first proposed by Dungey in 1961. When reconnection has taken place on the dayside of the magnetopause, the reconnected field lines move through the magnetosphere as shown in Figure 1.7, giving rise to a characteristic convection pattern. The solar wind field line labelled 2 heads towards the nose of the magnetopause, where the two field lines labelled 1 and 3 reconnect. The part of the field line in the solar wind is then dragged anti-sunward by the solar wind flow, which also pulls the magnetospheric part of the field line anti-sunward, due partially to the magnetic tension force, which acts to reduce field line curvature; this effect is particularly evident

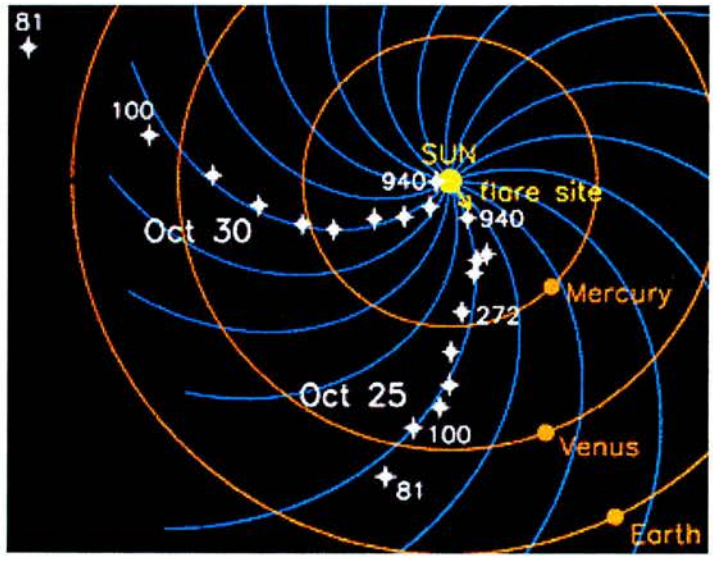

Figure 1.5: The Sun's magnetic field lines are bent into an Archimedean spiral by the Sun's rotation. This figure shows a snapshot of the Sun's magnetic field using a radio wave instrument on board the Ulysses spacecraft in October 1994. Electrons in the solar wind tend to follow the magnetic field lines, and as they do so, their collisions with other atomic particles give rise to radio waves. The white symbols show the locations of moving streams of electrons, illustrating the spiral pattern. This figure is included courtesy of NASA's Goddard Space Flight Center[4].

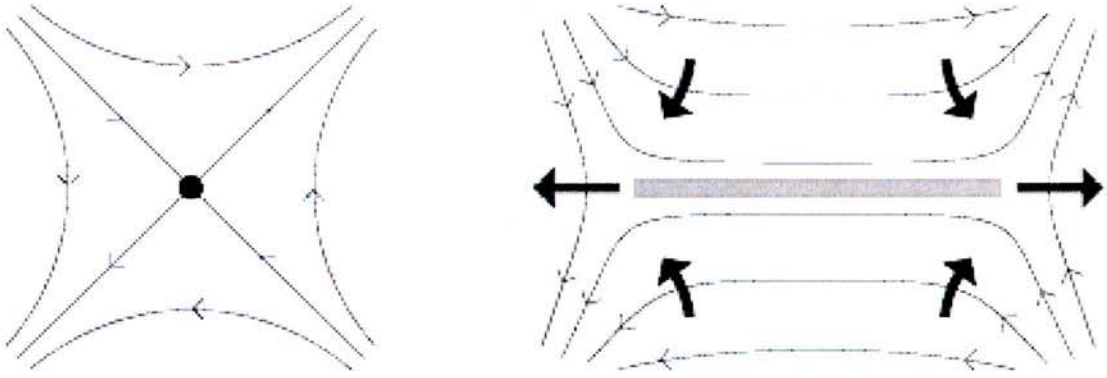

Figure 1.6: A schematic of 2D reconnection, showing oppositely-directed magnetic field lines moving towards each other, breaking and reconnecting at a point (left) or small region (right), and then moving away from the reconnection site. This mechanism is responsible for coupling the solar wind and magnetosphere.

in the progression from field line 3 to 4. So, the ionospheric footpoint of this field line is driven from the noon sector to the midnight sector, and this convection process naturally draws field lines out to form the magnetotail. In the magnetotail, field lines above and below the equator line (labelled 5) are oppositely directed; again, there is a thin boundary layer between these two regions called the neutral sheet (shown in Figure 1.8). The field lines convect towards one another, and reconnection occurs again (labelled 6). The reconnected field lines are accelerated away from the reconnection site, with half of them heading anti-sunward into the magnetotail, where they ultimately rejoin the solar wind flow. The other reconnected field lines are closed, and are accelerated towards the Earth to become the dipolar field lines on the nightside. Once they convect around to the dayside, the cycle is complete. The overall cycle generally takes about 12 hours.

The Dungey model was not immediately embraced by the scientific community, but two separate pieces of evidence subsequently supported the theory. Firstly, *Fairfield and Cahill (1966)* showed that geomag-

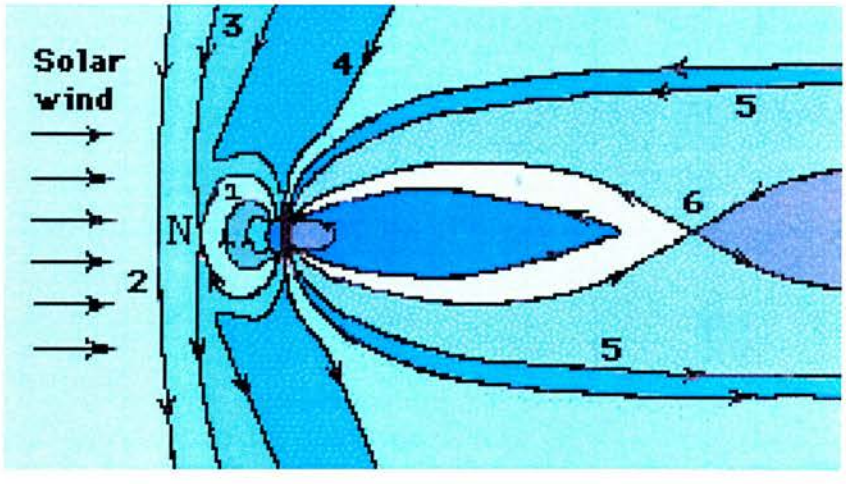

Figure 1.7: Schematic of the Dungey convection cycle[5], initiated by dayside magnetopause reconnection.

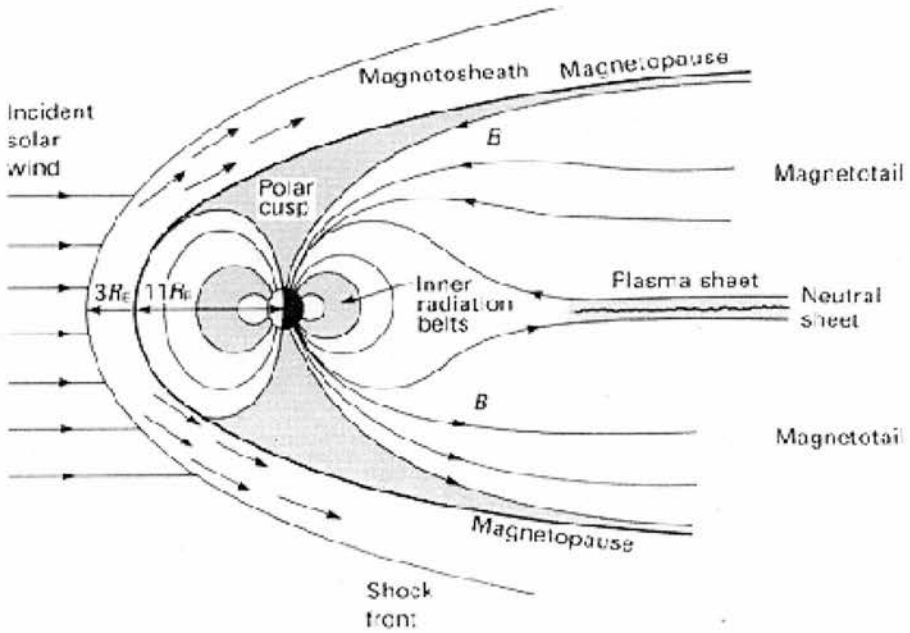

Figure 1.8: Picture showing the different regions of the Earth's magnetosphere[6].

netic activity is dependent on the north-south component of the IMF. Secondly, there is evidence that electrons which flow outwards from the Sun with a characteristic spectrum are also seen on polar cap field lines. This demonstrates that polar cap field lines are directly connected to the IMF.

If magnetopause reconnection carried on unchecked, the entire geomagnetic field would soon be connected with the IMF. The reality is more complicated, probably a compromise between the entirely closed and open magnetospheric pictures introduced above. The magnetopause reconnection rate is modulated by the direction and strength of the IMF. As explained above, reconnection occurs most easily with a southward-pointing IMF; during a northward-pointing IMF, reconnection can occur poleward of the cusps, but this is not as efficient a mechanism. Between these two extremes, reconnection can be possible at various different points on the dayside magnetopause where the geomagnetic field and IMF are oriented favourably.

Reconnection allows about 10-20% of the solar wind magnetic flux to be transported into the magnetosphere, but it is not the only mechanism which contributes to magnetospheric flow dynamics. The Earth rotates on its axis, and the neutral atmosphere rotates with it. This in turn causes the plasma on dipolar field lines within a few Earth radii to corotate, due to high neutral-charged particle collisions within the upper atmosphere. During northward IMF, weak Dungey cycle convection allows the corotation region to extend out further, and it shrinks as convection flows increase during a southward IMF.

1.2.2 Regions of the magnetosphere

There are different regions inside the magnetosphere which have radically different properties; these come about principally due to the convection patterns described in the previous section. These regions are shown in Figure 1.8, and Table 1.1 (taken from *Kivelson and Russell (1995)*) gives the important properties.

The dipolar corotating region at mid to equatorial latitudes is called the plasmasphere. It consists mostly of dense, cold plasma of predominantly ionospheric origin. Within the dipolar regions, there are two radiation belts, the most stable of which is the inner radiation belt, a compact region extending about 1 Earth radius above the equator. Charged particles tend to oscillate along magnetic field lines, and so will be trapped almost indefinitely along a closed dipolar field line. The inner radiation belt is typically composed of very energetic protons (~10-100 MeV), which are a by-product of collisions between cosmic rays and atmospheric atoms. These protons are not produced very quickly, but their number density accumulates over years due to the efficient trapping. These energetic protons can penetrate spacecraft, and prolonged exposure can damage scientific equipment and humans. Thus, spacecraft tend to avoid these regions!

The polar cusps are the transitional regions in the northern and southern hemispheres between sunward and tailward directed dipolar field lines. They consist of open reconnected field lines extending from the northern and southern polar regions out into the solar wind. These field lines allow energetic solar wind electrons (~500 eV) to flow directly down into the Earth's atmosphere in a thin "polar rain". There are not often enough of them to produce a visible aurora, but they are readily detected. This polar rain is far more intense in the northern polar cap when the IMF points away from the Sun, that is, when there is a direct connection between the Sun and the northern polar cap. Conversely, when the IMF points towards the Sun, the polar rain is stronger in the southern polar cap.

In the magnetotail, above and below the neutral sheet, there are two regions consisting of open magnetic field lines with one end embedded in the Earth, and the other end streaming into the tail to join the solar wind flow. Since the general flow is anti-Sunward, it is very easy for plasma to flow away into the tail and back into the solar wind, but it is very hard for plasma to flow the other way. Thus, the tail lobes are very rarefied regions, with a typical ion density of 0.01 cm^{-3}. Between the two lobes, there is a hotter and denser region called the plasma sheet; this is centred on the equator and surrounds the neutral sheet to a thickness of around 2-6 Earth radii. In this region, the typical electron number density is between 0.1 and 1 cm^{-3}, and typical electron and ion temperatures are 1 and 5 keV, respectively.

	Magnetosheath	Tail lobe	Plasma sheet boundary layer	Central plasma sheet
n (cm^{-3})	8	0.01	0.1	0.3
T_i (eV)	150	300	1000	4200
T_e (eV)	25	50	150	600
B (nT)	15	20	20	10
β	2.5	3×10^{-3}	0.1	6

Table 1.1: Properties of the different magnetospheric regions, where n is electron number density, T_i and T_e are the ion and electron temperatures respectively, and B corresponds to the ambient magnetic field strength. The symbol β represents the ratio of plasma pressure to magnetic pressure. If $\beta \ll 1$, the plasma is referred to as "cold", and if $\beta \geq 1$, then the plasma is "warm".

1.3 The ionosphere

The ionosphere is the partially-ionised, electrically-conducting upper layer of the Earth's atmosphere, which acts as an interface between the neutral atmosphere beneath it and the magnetospheric plasma above it *(Kelley (1989))*. The ionisation is caused by two main processes: photoionisation, as a result of solar radiation emanating from the Sun, and precipitation of energetic particles from the magnetosphere which impact on neutrals. The former process is generally dominant, and the maximum number density of the ionosphere is greater during the day ($\sim 10^{12}$ m^{-3}) than at night ($\sim 10^{11}$ m^{-3}), when recombination processes reduce the number of ions and electrons present, and photoionisation is not replenishing the supply.

The existence of the ionosphere was first postulated by Balfour Stewart in 1882, in an article called "Terrestrial Magnetism" which he wrote for inclusion in the *Encyclopaedia Britannica (Kivelson and Russell (1995))*. The intensity of Earth's surface magnetic field had been observed to fluctuate on a daily basis, and he concluded that this phenomenon was caused by "convective currents established by the sun's heating influence in the upper regions of the atmosphere". Stronger evidence for the existence of the ionosphere was provided by the invention of the radio transmitter and receiver at the beginning of the twentieth century. Guglielmo Marconi was the first to send radio signals, and in December 1901, he transmitted the first ever wireless signals across the Atlantic Ocean between Poldhu, Cornwall and St John's, Newfoundland, a distance of 2100 km. The observed reflection of radio waves in these transatlantic transmissions led both A. E. Kennelly and O. Heaviside to conclude independently in 1902 that this reflection occurred at a highly electrically-conducting layer of the Earth's atmosphere (at that time referred to as the Kennelly-Heaviside layer). This theory was confirmed by E. V. Appleton and M. A. F. Barnett in Britain, and by G. Breit and M. A. Tuve in the U.S.A., who sent short radio wave pulses vertically into the atmosphere and timed their return, to estimate the altitude of the ionosphere. Appleton used the letter E to denote the electric vector of the reflected wave. Vectors of waves reflected at higher altitudes were labelled F, whilst the occasional waves reflected at lower altitudes were represented by D. Nowadays, the ionosphere is still considered to have three regions, called the D, E and F layers. The F layer is sometimes subdivided into the F_1 and F_2 layers.

The Earth's gravitational field confines the neutral atmosphere close to the Earth's surface, since the individual molecules do not have sufficient speeds to escape. The gravitational force (F_g) acting on a particle of mass m at a radial distance r from the centre of the Earth is given by

$$F_g = \frac{GM_E m}{r^2} \tag{1.1}$$

where M_E is the Earth's mass and G is the gravitational constant, which can be used to define g, Earth's gravitational acceleration:

$$g = \frac{GM_E}{R_E^2} \tag{1.2}$$

near to the Earth's surface. In this equation, $R_E = 6370$ km is the Earth's radius. The work done (W_g)

to enable a particle to escape the Earth's gravitational field, that is, to move it from the Earth's surface to infinity along a radial path, is given by

$$\begin{aligned} W_g &= \int_{R_E}^{\infty} F_g \, \mathrm{d}r \\ &= \frac{GM_E m}{R_E} \\ &= gmR_E \end{aligned} \tag{1.3}$$

Thus, a particle in the Earth's atmosphere can escape if its kinetic energy is sufficient to provide this escape energy, that is if

$$\begin{aligned} \frac{mv^2}{2} &\geq gmR_E \\ \Rightarrow v &\geq \sqrt{2gR_E} = 1.12 \times 10^4 \text{ m/s} \end{aligned} \tag{1.4}$$

This is known as the escape velocity, which is independent of the particle's mass. Ionospheric plasma typically has a temperature of $\sim$1 eV, corresponding to electron and O^+ ion speeds of 5.93×10^5 m/s and 3.46×10^3 m/s, respectively. Comparing these speeds with the escape velocity in equation (1.4), we can see that O^+ ions are gravitationally bound, whilst electrons are not. However, as the electrons move away from the Earth to escape, the resultant charge separation between them and the gravitationally-bound ions sets up an ambipolar electric field which draws the electrons back into the ionosphere to preserve quasi-neutrality.

At equilibrium, ionospheric ions are in hydrostatic balance, that is

$$\rho_i \mathbf{g} = \nabla p_i \tag{1.5}$$

where ρ_i is the ion density and $p_i = n_i k T_i$ is the ion pressure; here, n_i is the ion number density, k is Boltzmann's constant, and T_i is ion temperature. Finally, $\rho_i = m_i n_i$, where m_i is ion mass. If we consider the z direction to be vertically upwards, then $\mathbf{g} = -g\hat{\mathbf{z}}$, and equation (1.5) becomes

$$\frac{\mathrm{d}}{\mathrm{d}z}\left(\frac{\rho_i k T_i}{m_i}\right) = -\rho_i g \tag{1.6}$$

If we further assume that T_i is independent of z, then

$$\frac{\mathrm{d}\rho_i}{\mathrm{d}z} = -\frac{m_i g \rho_i}{k T_i}$$

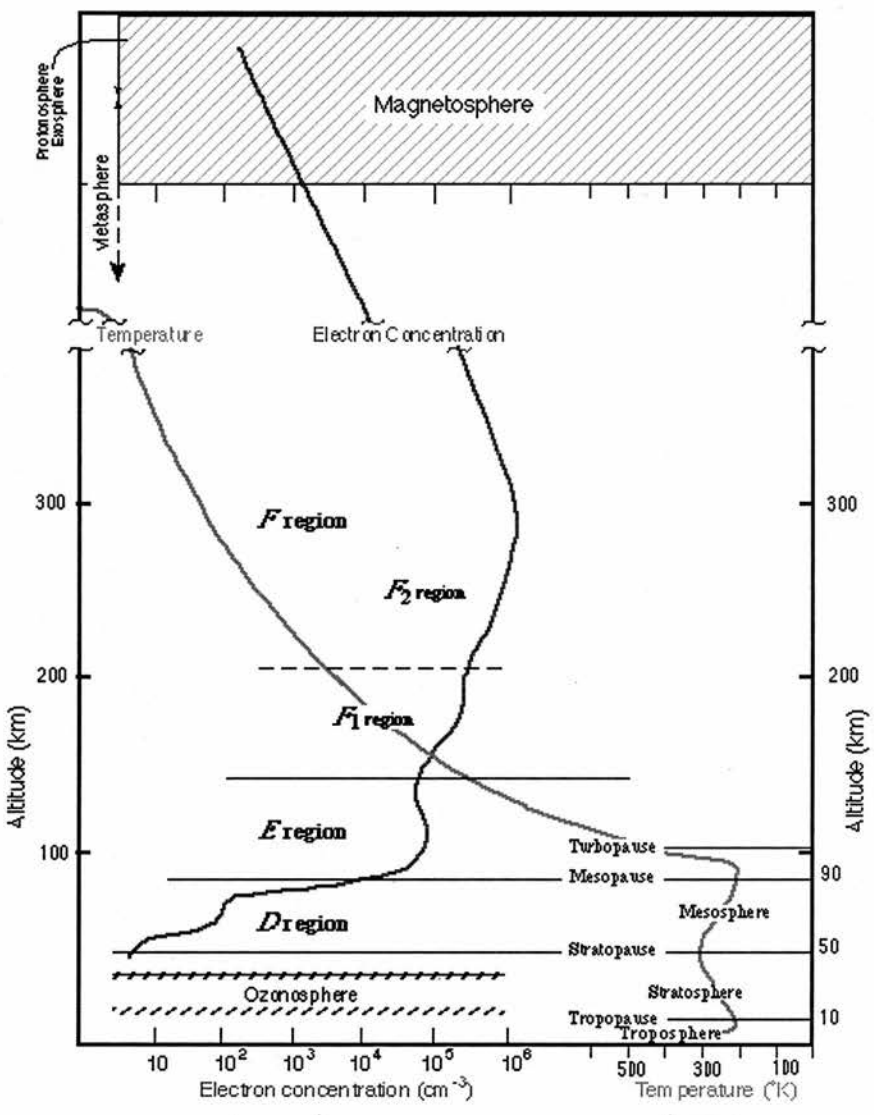

Figure 1.9: Diagram showing the D, E and F regions of the ionosphere[7], with a typical electron density and temperature altitude profile.

$$\begin{aligned} \Rightarrow \rho_i &= a \exp\left[-\int_0^z \frac{m_i g}{kT_i} \mathrm{d}z\right] \\ &= a \exp\left[-\frac{m_i g z}{kT_i}\right] \\ &= a \exp\left[-\frac{z}{h}\right], \end{aligned} \tag{1.7}$$

where the scale height h is defined as

$$h = \frac{kT_i}{m_i g} \tag{1.8}$$

The atomic mass of oxygen is taken to be 2.6762×10^{-26} kg, Boltzmann's constant $k = 1.3807 \times 10^{-23}$ J/K, and we take the ion temperature T_i to be 2000 K. Putting these values into equation (1.8), we find that $h = 105.3$ km.

The electron and ion density altitude profile of the ionosphere is dynamic, caused by the balance of two opposing processes: ionisation, which produces ions and electrons, and recombination, in which charged particles combine in various ways to form neutrals, sometimes with release of a photon. Examples of recombination are:

$$NO^+ + e^- \rightarrow N + O, \quad \text{(dissociative recombination)} \tag{1.9}$$

$$O^+ + e^- \rightarrow O + \text{photon}, \quad \text{(radiative recombination)} \tag{1.10}$$

The three layers of the ionosphere are independently produced by absorption of solar radiation of different energy ranges by certain constituent parts of the neutral atmosphere at each layer. Figure 1.9 shows typical density and temperature altitude profiles for the different regions of the ionosphere.

The F region, extending from 150 to 500 km and comprising mainly O^+ ions, contains a peak in density at around 250 km altitude. In simple terms, since the altitude profile of ionisation will depend both on the neutral number density, which decreases with altitude, and the intensity of the incident solar radiation, which increases with altitude, these two factors will lead to the formation of a density peak, at the altitude at which most photoionisation occurs. At altitudes above this peak, the ion and electron number density decays with the scale height in equation (1.8). The E region exists between 90 and 150 km. Ultraviolet solar radiation and less energetic solar x-rays produce mainly O_2^+ and NO^+ ions in this layer. Finally, the ionisation in the neutral-dominated D layer is produced by very energetic solar radiation (x-rays, Lyman-α radiation and cosmic rays) which can penetrate to this deep level of the Earth's atmosphere. Again, O_2^+ and NO^+ ions dominate in this layer. At night time, photoionisation is essentially non-existent, and the radiative recombination process for O^+ ions in equation (1.10) has a reaction rate which is 1000 times slower than that for the dissociative recombination process for heavier ions in equation (1.9); hence, the night time electron density of the D and E regions falls much more drastically than that of the F region.

Study of the ionosphere is complex, as it involves understanding and application of both classical fluid mechanics, due to the high neutral number density, and plasma physics, to describe the charged particle behaviour. In this Thesis, the ionosphere will simply be used as the cool, dense boundary in which the Earth's magnetic field lines are embedded.

1.4 Mathematical descriptions of plasmas

1.4.1 Particle orbit theory

Plasmas differ from other large collections of particles, such as fluids and gases, in that the particles of a plasma are charged; this means that their motions are directly affected by electric and magnetic fields around them. In an essentially collisionless plasma such as the magnetosphere, where the external magnetic field is strong, it is instructive to study single particle motion. This is known as particle orbit theory. The discussion presented here is adapted from *Boyd and Sanderson (1969)* and *Baumjohann and Treumann (1997)*.

A single particle of charge q and mass m in an electromagnetic field will feel an electrostatic Coulomb force, $q\mathbf{E}$, where $\mathbf{E}$ is the electrostatic field, and the Lorentz force, $q(\mathbf{v}\times\mathbf{B})$, where $\mathbf{v}$ is the particle velocity and $\mathbf{B}$ is the external magnetic field. Thus, the particle's equation of motion is given by

$$m\frac{\mathrm{d}\mathbf{v}}{\mathrm{d}t} = q(\mathbf{E}+\mathbf{v}\times\mathbf{B}) \tag{1.11}$$

The relationship between fields and particles is described by Maxwell's equations, stated below:

$$\nabla\times\mathbf{B} = \mu_0\mathbf{j} + \epsilon_0\mu_0\frac{\partial\mathbf{E}}{\partial t} \tag{1.12}$$

$$\nabla\times\mathbf{E} = -\frac{\partial\mathbf{B}}{\partial t} \tag{1.13}$$

$$\nabla\cdot\mathbf{E} = \frac{\rho}{\epsilon_0} \tag{1.14}$$

$$\nabla\cdot\mathbf{B} = 0 \tag{1.15}$$

where $\mathbf{j}$ is the electric current density in the plasma, ρ is the electric space charge density, and ϵ_0 and μ_0 are the permittivity and permeability of a vacuum, respectively. Equation (1.15) states that magnetic monopoles cannot exist, that is, magnetic field lines are always closed. Equation (1.14) tells us that the electric field is produced by the difference in ion and electron charge densities, that is, by normally small charge separations in the plasma. Equations (1.12) and (1.13) indicate that the electric and magnetic fields are coupled: a spatial variation in the electric field results in a temporal variation in the magnetic field (and vice versa), whilst a spatial variation in the magnetic field produces a current. In equation (1.12),

$$\epsilon_0\mu_0 = \frac{1}{c^2} \tag{1.16}$$

where c is the speed of light, so, unless there are fast electric field oscillations present (as in electromagnetic wave propagation), the second term in equation (1.12) may safely be neglected.

Basic particle gyration

If the plasma has no electric field, then the particle equation of motion in (1.11) reduces to

$$m\frac{\mathrm{d}\mathbf{v}}{\mathrm{d}t} = q(\mathbf{v} \times \mathbf{B}) \tag{1.17}$$

Taking the dot product of this with $\mathbf{v}$, and noting that $\mathbf{v} \cdot (\mathbf{v} \times \mathbf{B}) = 0$ (since $\mathbf{v} \times \mathbf{B}$ is perpendicular to $\mathbf{v}$), we see that

$$m\frac{\mathrm{d}\mathbf{v}}{\mathrm{d}t} \cdot \mathbf{v} = \frac{\mathrm{d}}{\mathrm{d}t}\left(\frac{mv^2}{2}\right) = 0 \tag{1.18}$$

This tells us that the particle kinetic energy is conserved in this regime. Working in Cartesian coordinates, and assuming a uniform magnetic field $\mathbf{B} = B_0\hat{\mathbf{z}}$, the components of equation (1.17) are

$$m\dot{v}_x = qB_0v_y \tag{1.19}$$

$$m\dot{v}_y = -qB_0v_x \tag{1.20}$$

$$m\dot{v}_z = 0 \tag{1.21}$$

Equation (1.21) reveals that v_z, the velocity parallel to the magnetic field, is constant. Taking the derivatives of equations (1.19) and (1.20), and substituting for $\dot{v}_x$ and $\dot{v}_y$ gives

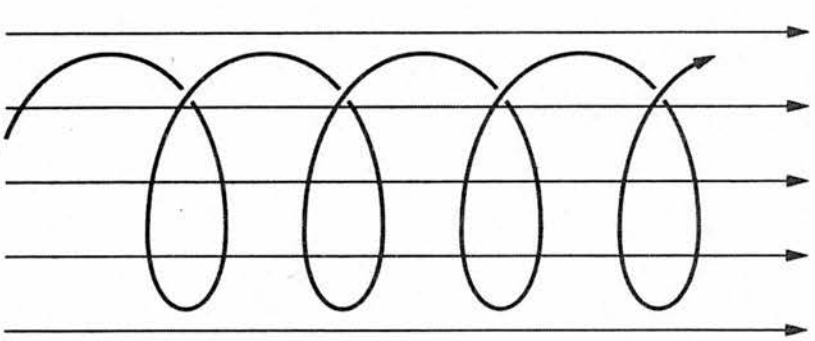

Figure 1.10: Basic particle gyration around magnetic field lines.

$$\begin{aligned} \ddot{v}_x &= -\left(\frac{qB_0}{m}\right)^2 v_x \\ \ddot{v}_y &= -\left(\frac{qB_0}{m}\right)^2 v_y \end{aligned} \tag{1.22}$$

where

$$\frac{qB_0}{m} = \omega_0 \tag{1.23}$$

is known as the particle gyrofrequency. Equations (1.22) have oscillatory solutions given by $v_x = A\cos\omega_0 t$ and $v_y = -A\sin\omega_0 t$. Now, $v_x^2 + v_y^2 = v_\perp^2 = A^2$, which is a constant, since both the kinetic energy and parallel velocity are conserved. So,

$$\begin{aligned} v_x &= v_\perp \cos\omega_0 t \\ v_y &= -v_\perp \sin\omega_0 t \end{aligned} \tag{1.24}$$

which can be integrated to give

$$\begin{aligned} x - x_0 &= \frac{v_\perp}{\omega_0}\sin\omega_0 t \\ y - y_0 &= \frac{v_\perp}{\omega_0}\cos\omega_0 t \end{aligned} \tag{1.25}$$

where (x_0, y_0) is the centre of the orbit. From this, the particle gyroradius is given by

$$r = \frac{v_\perp}{\omega_0} = \frac{mv_\perp}{\mid q \mid B_0} \tag{1.26}$$

So, a particle under the influence of an external constant magnetic field describes a circular path around a field line, which will be stretched out into a slinky spring shape when the particle has a velocity parallel to the magnetic field, $v_\parallel$. This motion is illustrated in Figure 1.10. In general, a particle always exhibits this relatively fast gyratory motion around a point called the guiding centre, whilst the guiding centre itself may drift more slowly under the influence of particular forces. It is often advantageous to simplify equations by ignoring the gyratory motion and concentrating on the motion of the guiding centre of the particle. In computer simulations, for example, a small time-step would be required to calculate the gyratory motion of particles, compared to a larger time-step which can be used to deduce the overall guiding centre motion. For the case in equation (1.25), the velocity of the guiding centre is given by $(0, 0, v_\parallel)$.

Electric drifts

We now extend the analysis above to include a uniform electrostatic field. This has the effect of causing the particle to drift in a certain direction as it gyrates. We consider a steady electric field with components $(E_x, 0, E_\parallel)$. The parallel component of the equation of motion in (1.11) is thus

$$m\dot{v}_\parallel = qE_\parallel \tag{1.27}$$

which can be integrated to give

$$v_\parallel = v_{\parallel 0} + \frac{qE_\parallel t}{m} \tag{1.28}$$

where $v_{\parallel 0}$ is the initial parallel velocity. Clearly, for long timescales, this would lead to relativistic particle speeds. Also, equation (1.28) shows that particles of opposite charge are accelerated in opposite directions, resulting in a current that increases with time. This will become unsustainable, and we must assume that $E_\parallel = 0$. Now, the perpendicular components of equation (1.11) are

$$\dot{v}_x = \omega_0 v_y + \frac{qE_x}{m} \tag{1.29}$$

$$\dot{v}_y = -\omega_0 v_x \tag{1.30}$$

Taking the derivative of equations (1.29) and (1.30) and substituting for $\dot{v}_x$ and $\dot{v}_y$ yields

$$\ddot{v}_x = -\omega_0^2 v_x$$

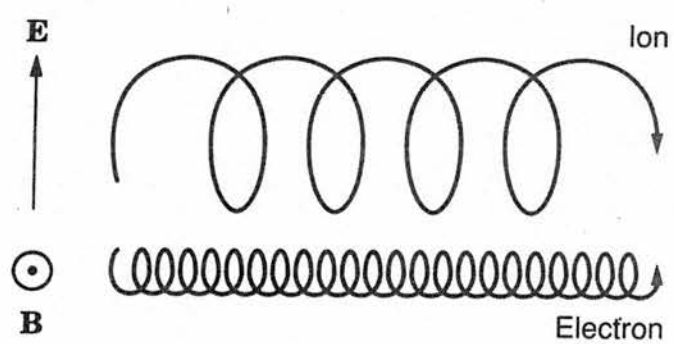

Figure 1.11: $\mathbf{E} \times \mathbf{B}$ drift in an electromagnetic field. Electrons and ions are accelerated in the same direction, which is perpendicular to both the electric and magnetic fields.

$$\ddot{v}_y = -\omega_0^2 \left(v_y + \frac{E_x}{B_0} \right) \tag{1.31}$$

Solving the first of these is trivial, whilst the solution to the second is given by the complementary function and a particular integral:

$$\begin{aligned} v_x &= v_\perp \cos \omega_0 t \\ v_y &= -v_\perp \sin \omega_0 t - \frac{E_x}{B_0} \end{aligned} \tag{1.32}$$

Thus, the particle still moves with the same gyratory motion, but also drifts in the y direction, perpendicular to both the electric and magnetic fields. This is known as the $\mathbf{E} \times \mathbf{B}$ drift, and has the general form

$$\mathbf{v}_E = \frac{\mathbf{E} \times \mathbf{B}}{B^2} \tag{1.33}$$

This drift is independent of the particle's charge, and so electrons and ions both drift in the same direction with the same speed. Thus, the $\mathbf{E} \times \mathbf{B}$ drift does not lead to charge separation, and hence currents. Figure 1.11 illustrates this drift. Physically, this motion can be understood qualitatively in terms of forces: at first, the ion is accelerated in the direction of the electric field, increasing $v_\perp$ and hence the gyroradius given in equation (1.26). When it turns around and starts moving in the opposite direction, it is decelerated by the electric field, thus decreasing $v_\perp$ and the gyroradius. This has the effect of shifting the guiding centre of the particle in the $\mathbf{E} \times \mathbf{B}$ direction. The same guiding centre motion is true for the electrons, since although they are accelerated and decelerated in the opposite way to ions, this effect is cancelled out since they gyrate in the opposite sense as well. In this case, the guiding centre velocity is given by $(0, -E/B, v_{\parallel 0})$.

Magnetic drifts

Up until now, we have assumed a homogeneous magnetic field. If, however, the magnetic field has gradients and curved field lines, these can also lead to different particle drifts. Firstly, we consider what happens when there is a magnetic field gradient, given by $\mathbf{B} = (0, 0, B(y))$, and no electric field. Taking the components of the equation of motion in (1.17), we obtain

$$\begin{aligned} \dot{v}_x &= \omega(y) v_y \\ \dot{v}_y &= -\omega(y) v_x \\ \dot{v}_z &= 0 \end{aligned} \tag{1.34}$$

where $\omega(y) = qB(y)/m$. Thus, differentiating and substituting for $\dot{v}_x$ and $\dot{v}_y$,

$$\begin{aligned} \ddot{v}_x &= -\omega^2(y)v_x + v_y^2\frac{\mathrm{d}\omega}{\mathrm{d}y} \\ \ddot{v}_y &= -\omega^2(y)v_y - v_x v_y\frac{\mathrm{d}\omega}{\mathrm{d}y} \end{aligned} \tag{1.35}$$

We are assuming that $\mathbf{B}$ is almost constant on one particle orbit, that is, the particle gyroradius $\sim y - y_0$, where y_0 is the guiding centre, is much smaller than $\omega(y)/(\mathrm{d}\omega/\mathrm{d}y)$, the scale length over which the magnetic field changes. Thus, $\omega(y)$ may be expanded about y_0 such that

$$\begin{aligned} \omega(y) &= \omega(y_0) + (y - y_0)\left[\frac{\mathrm{d}\omega}{\mathrm{d}y}\right]_{y_0} + \ldots \\ &\approx w_0 + (y - y_0)\omega_0{}' \end{aligned} \tag{1.36}$$

Substituting this Taylor expansion into the equations in (1.35) yields

$$\begin{aligned} \ddot{v}_x + \omega_0^2 v_x &= -2\omega_0\omega_0{}'(y - y_0)v_x + \omega_0{}' v_y^2 \\ \ddot{v}_y + \omega_0^2 v_y &= -2\omega_0\omega_0{}'(y - y_0)v_y - \omega_0{}' v_x v_y \end{aligned} \tag{1.37}$$

Now, the terms on the right-hand sides of these equations are small, so we can replace $y - y_0$, v_x and v_y by their equilibrium quantities given in equations (1.24) and (1.25). Substituting these in yields

$$\begin{aligned} \ddot{v}_x + \omega_0^2 v_x &= -\frac{\omega_0{}'}{2} v_\perp^2 \left(3\cos 2\omega_0 t + 1\right) \\ \ddot{v}_y + \omega_0^2 v_y &= \frac{3}{2}\omega_0{}' v_\perp^2 \sin 2\omega_0 t \end{aligned} \tag{1.38}$$

Solving these equations again requires us to find the complementary functions and particular integrals; the particular integrals are found by considering the forms $v_{x,p} = A_x \cos 2\omega_0 t + B_x \sin 2\omega_0 t - C_x\omega_0{}' v_\perp^2/2$ and $v_{y,p} = A_y \cos 2\omega_0 t + B_y \cos 2\omega_0 t$. The solutions are found to be

$$\begin{aligned} v_x &= v_\perp \cos\omega_0 t + \frac{v_\perp^2\omega_0{}'}{2\omega_0^2}\cos 2\omega_0 t - \frac{v_\perp^2\omega_0{}'}{2\omega_0^2} \\ v_y &= -v_\perp \sin\omega_0 t - \frac{v_\perp^2\omega_0{}'}{2\omega_0^2}\sin 2\omega_0 t \end{aligned} \tag{1.39}$$

We note that the solutions now contain oscillations at double the frequency of the basic gyromotion,

but we are primarily interested in the non-oscillatory drift in the equation for v_x. During one period, the average drift velocity is given by

$$\bar{\mathbf{v}}_G = \left(-\frac{v_\perp^2 \omega_0{}'}{2\omega_0^2}, 0, v_\parallel \right) \tag{1.40}$$

So, when a magnetic field in the z direction has a variation (gradient) in the y direction, a drift in the orthogonal x direction is produced. This gradient drift can generally be written as

$$\mathbf{v}_G = \frac{m v_\perp^2}{2qB^3} (\mathbf{B} \times \nabla B) \tag{1.41}$$

In general, a magnetic field gradient leads to a gradient drift in a direction perpendicular to both the magnetic field and its gradient. This drift is dependent on charge and perpendicular energy, so electrons and ions will drift in opposite directions, and more energetic particles will drift more quickly. This drift is illustrated in Figure 1.12. Here, $\mid B \mid$ increases in the upward direction. Hence, since the particle gyroradius $r \propto B^{-1}$, it will increase as the particle moves down, and decrease as the particle moves up, resulting in a shift of the guiding centre and a net motion to the side.

Curved field lines also lead to particle drifts. Let us consider slightly curved field lines given by $\mathbf{B} = (0, B_y(z), B_0)$, where B_y and its derivative are small. Taking the components of the equation of motion in (1.17) gives rise to

$$\begin{aligned} \dot{v}_x &= \omega_0 v_y - \omega(z) v_z \\ \dot{v}_y &= -\omega_0 v_x \\ \dot{v}_z &= \omega(z) v_x \end{aligned} \tag{1.42}$$

where $\omega(z) = qB_y(z)/m$. We then differentiate the first two of these equations, and substitute for $\dot{v}_x$ and $\dot{v}_y$, neglecting small quantities, and taking $v_z \approx v_\parallel$ to first order:

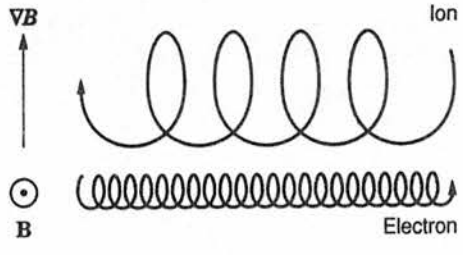

Figure 1.12: ∇B drift caused by inhomogeneous magnetic field. Electrons and ions drift in opposite directions.

$$\begin{aligned} \ddot{v}_x + \omega_0^2 v_x &= -\omega'(z) v_\parallel^2 \\ \ddot{v}_y + \omega_0^2 v_y &= \omega_0 \omega(z) v_\parallel \end{aligned} \tag{1.43}$$

These two differential equations can be solved by finding complementary functions and particular integrals, as before. We obtain

$$\begin{aligned} v_x &= v_\perp \cos \omega_0 t - \frac{\omega'(z)}{\omega_0^2} v_\parallel^2 \\ v_y &= -v_\perp \sin \omega_0 t + \frac{\omega(z)}{\omega_0} v_\parallel \end{aligned} \tag{1.44}$$

There are drifts in both directions. The drift of $\bar{v}_y = \omega(z) v_\parallel / \omega_0$ in the y direction actually simply maintains motion parallel to $\mathbf{B}$, since the ratio of $\bar{v}_y$ with $\bar{v}_z = v_\parallel$ is given by

$$\frac{\bar{v}_y}{\bar{v}_z} = \frac{\omega(z)}{\omega_0} = \frac{B_y}{B_0} \tag{1.45}$$

The drift in the x direction is known as the curvature drift, and occurs in a direction perpendicular to both the background magnetic field, $\mathbf{B}$, and its curvature, $(\mathbf{B} \cdot \nabla)\mathbf{B}$. It can be generally written as

$$\mathbf{v}_C = \frac{m v_\parallel^2}{q B^4} (\mathbf{B} \times (\mathbf{B} \cdot \nabla)\mathbf{B}) \tag{1.46}$$

Again, electrons and ions drift in opposite directions, and the speed of the drift is dependent on the particle parallel kinetic energy: the more energetic the particle, the faster it will drift. As the particle gyrates towards the centre of curvature of the field line, it is accelerated by the centripetal force, thus increasing $v_\perp$ and the gyroradius. Then, as the particle gyrates away from the centre, it is decelerated, which decreases $v_\perp$ and the gyroradius. This leads to the drifting motion in the x direction described above.

Magnetic moment

The magnetic moment, μ, given by

$$\mu = \frac{m v_\perp^2}{2B} \tag{1.47}$$

is an adiabatic invariant of a particle's gyratory motion, that is, it remains approximately constant on a particle trajectory, and does not change when a particle moves into regions of stronger or weaker magnetic

fields. This can be shown for a steady magnetic field, $\mathbf{B}$, by considering the energy conservation relation in the absence of an electric field,

$$W_{\parallel} + W_{\perp} = \text{constant} \tag{1.48}$$

where $W_{\parallel}$ and $W_{\perp}$ are the parallel and perpendicular particle kinetic energies, respectively. Differentiating this gives

$$\frac{\mathrm{d}W_{\parallel}}{\mathrm{d}t} + \frac{\mathrm{d}W_{\perp}}{\mathrm{d}t} = 0 \tag{1.49}$$

where $(\mathrm{d}/\mathrm{d}t) = (\partial/\partial t) + (\mathbf{v} \cdot \nabla)$ denotes the derivative along the guiding centre trajectory. We can use equation (1.47) to write

$$\frac{\mathrm{d}W_{\perp}}{\mathrm{d}t} = \mu \frac{\mathrm{d}B}{\mathrm{d}t} + B \frac{\mathrm{d}\mu}{\mathrm{d}t} \tag{1.50}$$

where

$$\frac{\mathrm{d}B}{\mathrm{d}t} = v_{\parallel} \frac{\partial B}{\partial z} \tag{1.51}$$

and z is the magnetic field-aligned coordinate. In order to find an expression for $\mathrm{d}W_{\parallel}/\mathrm{d}t$, we consider particle motion in an axially symmetric magnetic field which increases slowly with z. Equation (1.15) can be written in cylindrical co-ordinates as

$$\frac{1}{R} \frac{\partial (R B_R)}{\partial R} + \frac{\partial B_z}{\partial z} = 0 \tag{1.52}$$

which can easily be integrated under the assumption that the field is approximately constant over one particle orbit, and that $B = \sqrt{B_R^2 + B_z^2} \approx B_z$, since $B_R \ll B_z$:

$$\begin{aligned} R B_R &= -\int_0^r R \frac{\partial B_z}{\partial z} \, \mathrm{d}R \\ &\approx -\frac{\partial B}{\partial z} \int_0^r R \, \mathrm{d}R \\ \Rightarrow B_R &\approx -\frac{r}{2} \frac{\partial B}{\partial z} \end{aligned} \tag{1.53}$$

where r is the particle gyroradius. Now, taking a similar approximation (first order in small quantities) of the parallel component of the particle equation of motion in equation (1.11) and substituting in the result in equation (1.53), we see that

$$m\frac{\mathrm{d}v_{\parallel}}{\mathrm{d}t} = qv_{\perp}B_R = -\frac{qrv_{\perp}}{2}\frac{\partial B}{\partial z} \tag{1.54}$$

Using the definition of the particle gyroradius in equation (1.26), the equation can be rewritten as

$$m\frac{\mathrm{d}v_{\parallel}}{\mathrm{d}t} = -\mu\frac{\partial B}{\partial z} \tag{1.55}$$

Multiplying equation (1.55) by $v_{\parallel}$ and using equation (1.51) yields

$$\frac{\mathrm{d}W_{\parallel}}{\mathrm{d}t} = -\mu\frac{\mathrm{d}B}{\mathrm{d}t} \tag{1.56}$$

Finally, substituting equations (1.50) and (1.56) into equation (1.49) yields the desired result that

$$\frac{\mathrm{d}\mu}{\mathrm{d}t} = 0 \tag{1.57}$$

Thus, the magnetic moment is an invariant of particle motion in an inhomogeneous magnetic field, provided that the field varies over distances that are long compared to the particle gyroradius. We will use this adiabatic invariant in the modelling in this Thesis, since it leads to a phenomenon called magnetic mirroring of charged particles on the Earth's dipolar field lines.

Magnetic mirroring

As a particle enters a region of higher magnetic field strength, invariance of μ tells us that its perpendicular kinetic energy must also increase. By conservation of energy in equation (1.48), we see that the particle's parallel kinetic energy must decrease to compensate. If the magnetic field strength increases sufficiently, the particle will lose all of its parallel kinetic energy, stop, and then start to move in the opposite direction along the field line: this is called magnetic mirroring, and the point at which it happens is the mirror point. If a particle is on a closed dipolar magnetic field line of the Earth, then it will have two mirror points, and is thus trapped on that field line.

A particle's pitch angle, α, is given by

$$\alpha = \tan^{-1}\left(\frac{v_{\perp}}{v_{\parallel}}\right) \tag{1.58}$$

At its mirror point, $v_{\parallel} \rightarrow 0$, and the particle has a 90° pitch angle. Given that $v_{\perp} = v\sin\alpha$ at an arbitrary point, where v is the particle speed, and noting invariance of μ in equation (1.47), a particle's pitch angle at any point is given by

$$\sin\alpha = \sqrt{\frac{B}{B_M}} \tag{1.59}$$

where B_M is the magnetic field strength at its mirror point.

1.4.2 Other modelling methods

Whilst particle orbit theory is very useful for studying low density plasmas where collisions are negligible, it is less accurate when collective particle behaviour becomes an important factor. There are other approaches in this case. Kinetic theory is a statistical approach, where one uses distribution functions to describe each population of charged particles (electrons, protons, heavier ions etc) in phase space. A Maxwellian, for example, is a distribution of the form $f \propto f_0 \exp(-W_\perp/kT)\exp(-W_\parallel/kT)$, where T is the plasma temperature: thus, most particles have zero velocity, and the statistical chance of finding particles of higher velocities decreases exponentially. One can then study the evolution of this distribution function under different conditions. The multi-fluid approach is simpler, as one retains the different charged particle populations, but assigns an average velocity to each population rather than analysing the spread in velocities. Each population is treated as a fluid, and will have its own averaged density, velocity and temperature. The magnetohydrodynamic (MHD) approach takes the multi-fluid approach a step further, and treats the plasma as a single conducting fluid. Here, macroscopic variables are used, so the entire plasma has an average density, velocity, pressure and temperature. Each of these modelling techniques has its advantages and disadvantages, and one must consider these when choosing which one to use in a given scenario: kinetic theory retains a lot of information about separate charged particle populations, but this may be too time-consuming and complicated, for example, in a computer code. If MHD is suitable, this could provide a better approach.

1.5 The Earth's current circuit

There is a complex current circuit flowing around the Earth, in the ionosphere and magnetosphere, which arises from a number of different factors. A schematic of this circuit is shown in Figure 1.13. Firstly, there are two current sheets (thin layers of current) which flow near the Earth. The first of these occurs at the magnetopause, the thin boundary between the magnetospheric and solar wind plasma. Since the magnetic field changes both in direction and strength over this boundary, Ampère's law in equation (1.12) tells us that there must be a current sheet associated with it. In this case, the sheet has a thickness of about 100 km. The second current sheet occurs in the equatorial plane of the Earth's magnetotail, and is due to the fact that magnetic field lines are directed uptail above the equatorial plane and downtail below it, as shown in Figure 1.8. This sudden change in the magnetic field direction again leads to a current.

When reconnection occurs in the magnetotail, hot plasma is accelerated Earthward on field lines that become more dipolar. Particle orbit theory tells us that most charged particles in this plasma are trapped on field lines due to magnetic mirroring. Now, dipolar field lines have both a gradient and curvature associated with them, so the electrons and ions will exhibit both gradient and curvature drifts, as described in the previous section. This causes the ions to drift westward, and the electrons eastward, resulting in a net westward ring current flowing around the Earth. The plasma is usually hotter on the nightside, and gets progressively colder as the particles flow to the dayside, which leads to a partial ring current which flows

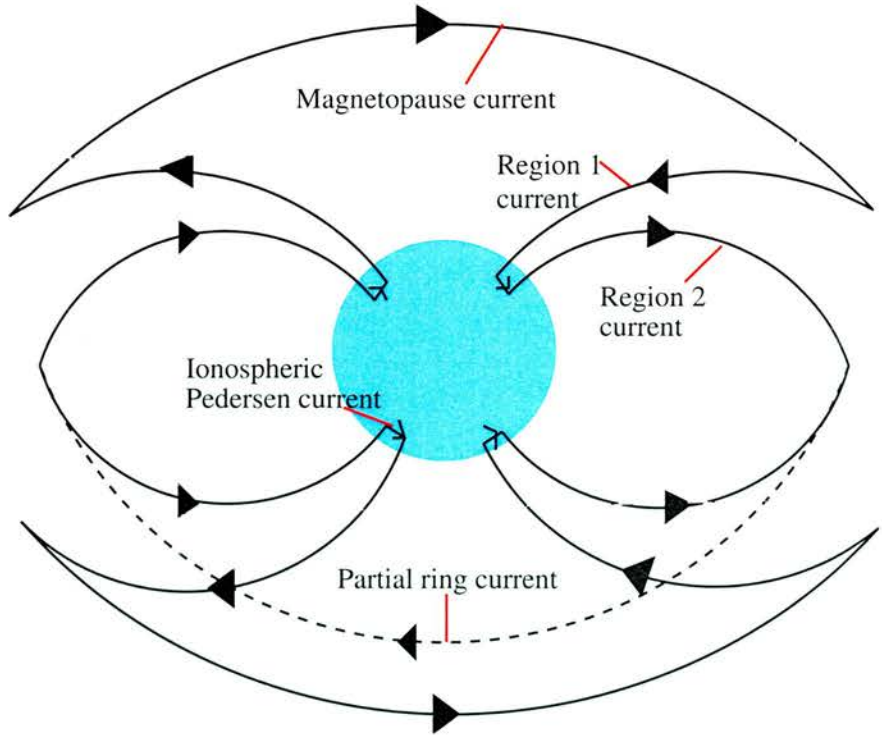

Figure 1.13: Schematic of the Earth's current circuit (viewed from the magnetotail), showing the magnetospheric and ionospheric currents, and the magnetic field-aligned currents which couple them. Adapted from *Cowley (2000)*.

from dawn to dusk. The ring current flows between 2 and 7 Earth radii. Due to the higher energy of ions, they are principally responsible for carrying the current; during quiet times, H^+ ions are the main carriers, whilst during more energetic times, O^+ ions also contribute significantly.

Currents also flow in the ionosphere, between around 90 and 200 km. They arise due to the interaction between magnetospheric plasma and the dense ionosphere. Collisions become important at these altitudes, acting as a drag on flow and causing charge separations which lead to electrical currents *(Cowley (2000))*. Electrons move so quickly that they are scarcely affected by these collisions, and continue to $\mathbf{E} \times \mathbf{B}$ drift as usual at these altitudes. Ions, however, are much heavier than electrons, gyrate much more slowly, and are hence affected far more by ion-neutral collisions. The closer one gets to the Earth, the higher the neutral number density, and hence the more frequent the ion-neutral collisions. Above about 125 km, both electrons and ions basically $\mathbf{E} \times \mathbf{B}$ drift, but the ions also drift in the direction of the magnetic field, $\mathbf{E}$, due to collisions, leading to a Pedersen current in this direction. At $\sim$ 125 km altitude, the ion-neutral collision frequency is approximately equal to the ion gyrofrequency, so below this, the ions are barely mobile, whilst the electrons still $\mathbf{E} \times \mathbf{B}$ drift, leading to a Hall current in the $-\mathbf{E} \times \mathbf{B}$ direction *(Cowley (2000))*.

These ionospheric and magnetospheric currents require to be closed, and this is achieved via upward and downward magnetic field-aligned currents (FACs), which link the ionospheric currents to the magnetopause and partial ring currents. Whilst the other currents described above occur naturally as a result of Ampère's Law and particle motion in a magnetic field, the field-aligned currents are primarily carried by electrons which have to be accelerated to close the circuit. The nature of this acceleration is the primary focus of the work in this Thesis.

Other currents also flow along Earth's field lines. Field-aligned cusp currents occur on newly reconnected field lines on the dayside of the Earth, such as that produced when field lines numbered 1 and 3 in Figure 1.7 reconnect. They are the means by which momentum and energy are directly transferred from the solar wind to the ionosphere. During substorms, the usual cross-tail current in the Earth's magnetotail is disrupted, and a system called the substorm current wedge is formed as the current is diverted via Earthward (downward) field-aligned currents to the east of the wedge, a westward current through the ionosphere, and a tailward (upward) field-aligned current to the west of the wedge.

1.6 Field-aligned currents and their observation

Field-aligned currents are a common feature of space plasmas, their main role being to couple two different regions of plasma by carrying current between them along magnetic field lines. As well as flowing along the Earth's auroral field lines, coupling the hot, tenuous magnetosphere with the cool, dense ionosphere, field-aligned currents also occur in the Jovian system, coupling Jupiter with Io and the Jovian magnetodisc. The field-aligned current region of the Earth consists of two current sheets (upward and downward) which are extended in longitude, but narrow in latitude ($\sim$100 km). Upward field-aligned currents are predominantly carried by accelerated downflowing electron beams, and it is these electrons which cause the visible aurora by exciting atoms and molecules in the Earth's neutral atmosphere to emit light. Although first postulated by Birkeland at the turn of the twentieth century, these currents were only first detected by *Iijima*

and Potemra (1976) using TRIAD satellite magnetometer data at 800 km altitude. The observable signatures of field-aligned currents are east-west deflections in the Earth's background magnetic field, which are closely mirrored by north-south variations in the electric field at ionospheric altitudes. Ions then travel through the ionosphere to carry the Pedersen current, and the auroral circuit is closed by ionospheric electrons being evacuated upwards along field lines to carry the downward field-aligned current. There was sporadic evidence for the existence of downward current regions: *Klumpar and Heikkila (1982)* observed a unidirectional upgoing electron beam at 1400 km, and *Boehm et al. (1995)* presented FREJA satellite data indicating the presence of energetic (~2 keV) upflowing electrons.

The Earth's magnetosphere is our closest example of a naturally occurring space plasma, and as such, provides much opportunity to gain insight into basic plasma properties such as particle energisation and instabilities. Previous missions had succeeded in identifying field-aligned current regions, but two recent missions, FAST and Cluster, have provided a wealth of detailed particle and electric field data which have helped to identify and explain much of the finer structure.

1.6.1 The FAST satellite

The Fast Auroral SnapshoT (FAST) explorer *(Carlson et al. (1998b))* is a NASA satellite that was launched on August 21, 1996 in California. Its primary aim has been to provide detailed particle and field data to allow study of the small-scale physics of space plasmas and accelerated particles in the Earth's auroral region. It is a small, light satellite weighing 191 kg, with a diameter of 1.02 m and a height of 0.93 m. It was sent into a highly elliptical orbit such that it crosses the auroral zones four times during each orbit of 133 minutes. It was built to achieve 1 to 3 orders of magnitude higher resolution data than any previous auroral mission, but only collects data at this resolution when passing through the auroral regions of primary interest.

A picture of the FAST satellite is given in Figure 1.14, showing the major scientific instruments on board. Electric fields are measured by special detectors; they are derived from the voltage difference between two spherical sensors. A DC fluxgate magnetometer and an AC search-coil magnetometer both measure magnetic fields. The satellite boasts sixteen electrostatic analysers, which are able to provide the first continuous observance of ion and electron distributions (including energetic particles) at all pitch angles. To provide more detailed ion information, an ion spectrometer gives the full three-dimensional distribution function of major ion species present in the plasma every 2.5 seconds, including H^+, He^+, He^{++}, O^+, O_2^+, and NO^+ ions. Finally, Langmuir probes extending from the spacecraft provide the thermal density and temperature of the ambient plasma.

1.6.2 The Cluster mission

The European Space Agency's Cluster mission is unique in its study of the magnetosphere. This is because it consists of four identical spacecraft called Rumba, Salsa, Samba and Tango, which carry identical instruments and fly in a tetrahedral configuration through different regions of the magnetosphere. This is hugely advantageous, as it allows for study of three-dimensional, time-varying phenomena, and it is possible to

distinguish for the first time between temporal and spatial variations. The separation distances vary from 600 to 20,000 km, depending on the region and processes being investigated.

An artist's impression of the four spacecraft is shown in Figure 1.15. The satellites, which each weigh 1200 kg and are 2.9 m in diameter and 1.3 m in height, were first launched in French Guyana in 1996. Unfortunately, their carrier rocket, Ariane-501, broke up 37 seconds after launch, and all of the satellites were lost. ESA decided to resurrect the mission, and built four new identical satellites which were successfully launched in two pairs on 16 July and 9 August 2000. They follow an elliptical polar orbit, with a perigee of

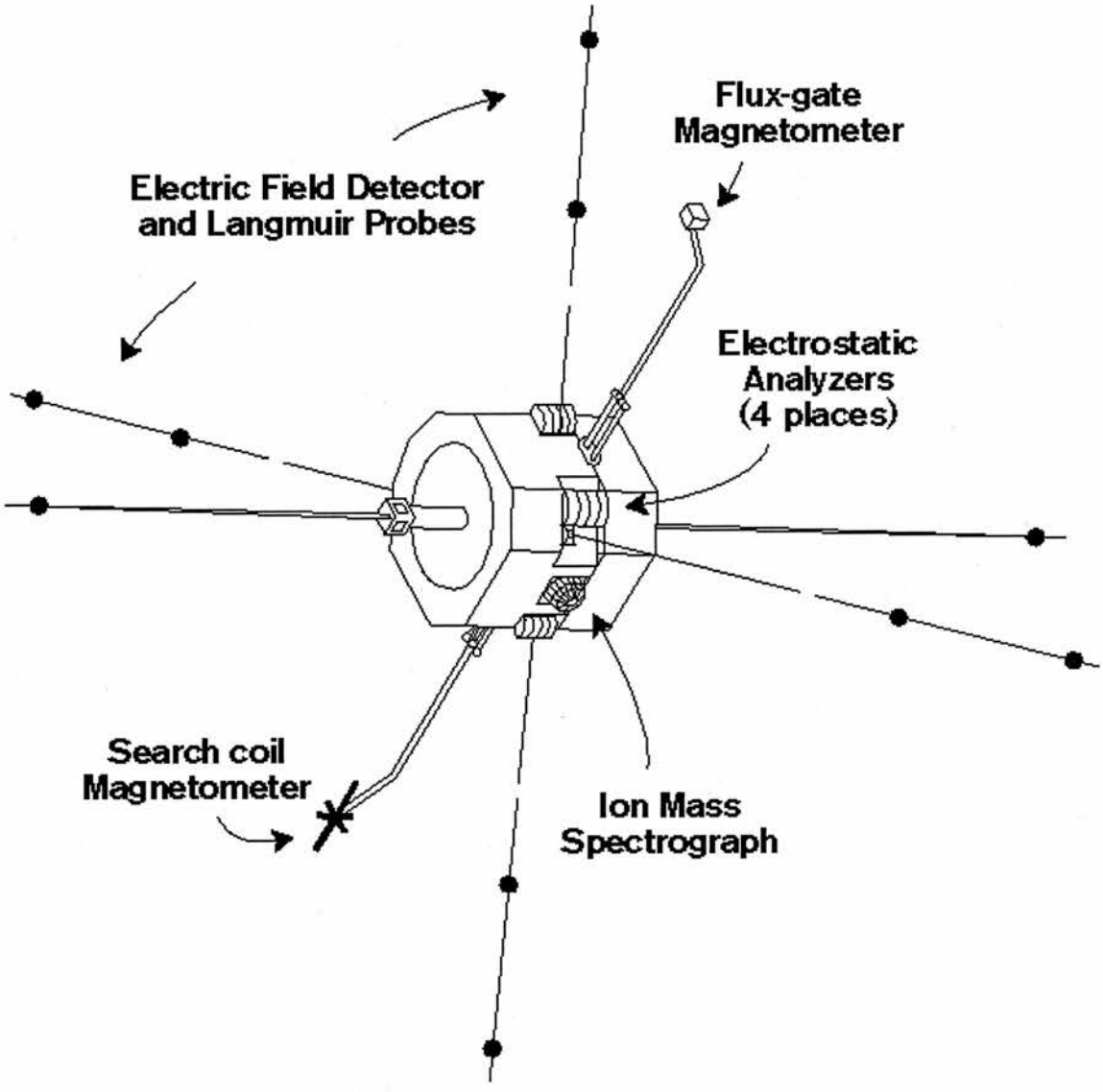

Figure 1.14: This picture shows the different instruments present on the FAST satellite[8]. The magnetometers and electric field detectors measure magnetic and electric fields respectively; the electrostatic analysers continuously measure 360° ion and electron pitch angle distributions; the ion mass spectrograph gives the full three-dimensional distribution function for major ion species; and the Langmuir probes measure thermal plasma density and temperature.

19,000 km and an apogee of 119,000 km, and their orbital period is 57 hours. The satellites carry scientific equipment similar to that on the FAST explorer, but the Cluster mission is far less focused, and aims to study many different regions of the magnetosphere.

The primary aim of the Cluster mission is to investigate the small-scale three-dimensional structure of the Earth's plasma environment. Areas of interest include the solar-wind magnetosphere interaction, especially the bow shock and magnetopause; aspects of magnetotail dynamics, such as the formation of the neutral line, and cross-tail currents; the polar cusps and the auroral zone. Cluster data has proved extremely useful in the auroral zone, yielding much data on the small-scale, elusive downward current regions.

1.7 Properties of the field-aligned current region

1.7.1 Electron acceleration and parallel electric fields

Once accelerated electron beams had been observed to carry field-aligned currents, the main aim of research was to discover the acceleration mechanism responsible. Initial observations of converging electric field structures using the S3-3 satellite by *Mozer et al. (1977)* led to the idea of quasi-static U-shaped potential contours shown in Figure 1.16, which give rise to parallel electric fields at low altitudes of 1-2 R_E. More recently, correlated observations of upward electron beams with diverging electric field signatures have indicated that similar U-shaped potentials generate an oppositely-directed quasi-static parallel electric field

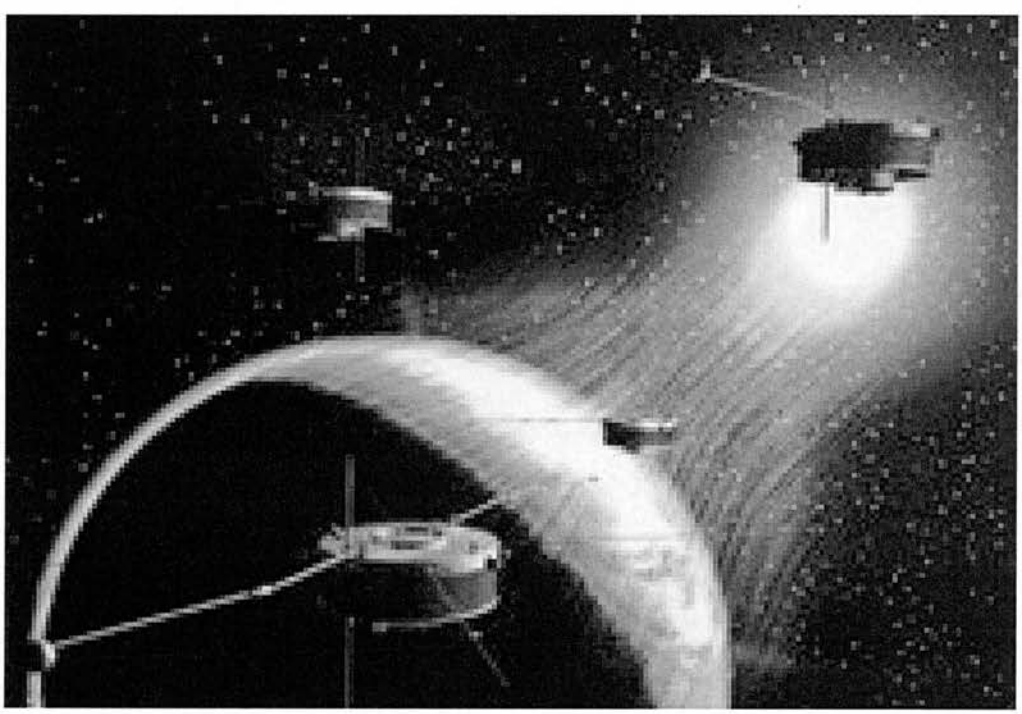

Figure 1.15: An artist's impression of the four Cluster spacecraft, courtesy of ESA[9].

in the downward current region (e.g. *McFadden et al. (1999)*).

There has been much observational evidence for the existence of such quasi-static electric fields. In the upward current region, the electric field will accelerate electrons downwards and ions upwards. Thus, *Mozer and Hull (2001)* used electron and ion data from the Polar satellite when it was flying through the middle of acceleration regions to plot the ratio of upgoing ion energy to the sum of upgoing ion energy and downgoing electron energy (equivalent to the total potential drop) as a function of altitude for several events. The ratio is small at lower altitudes, since the ions have only just entered the acceleration region and thus have only been slightly accelerated, whilst the electrons, entering the acceleration region from above, have experienced much of the acceleration already. The ratio increases with altitude, since the ions will have been accelerated more and more at greater heights, and the electrons less and less. In a different approach, *Tanaka et al. (2003)* reported correlated downgoing electron acceleration and ion deceleration, indicating the presence of a parallel potential structure above the satellite.

If one assumes *a priori* that a parallel potential exists on a field line, there are several ways to estimate it from satellite data. In the upward current region, for example, the magnetospheric electron population is accelerated downwards through the potential, and some of these electrons precipitate with a classic accelerated distribution, with a characteristic energy peak corresponding to the potential drop they have experienced: measuring this energy peak at low altitudes is one way to estimate the potential. The precipitating electrons do not return to the magnetosphere, and so an empty area of phase space corresponding to these lost electrons develops in the magnetospheric electron population: measuring the width of this loss cone at high altitudes gives a second estimate of the potential. Finally, the potential will accelerate ions upwards, so measuring the ion beam energy at high altitudes gives a third value for the potential. *Reiff et al. (1988)* used data from the Dynamics Explorer pair of spacecraft when they were in magnetic conjunction on auroral field lines, DE1 at high altitudes of 9,000-15,000 km and DE2 at low altitudes of 400-800 km, to estimate the total potential drop in these three different ways. The results were very similar, indicating that a quasi-static parallel electric field did indeed exist at altitudes between the two spacecraft.

Despite the wealth of direct and circumstantial evidence for quasi-static electric fields, there is opposition to the theory. *Bryant (1999)* states that a static, and hence conservative, electric field is incapable of net electron acceleration, since the U-shaped contours shown in Figure 1.16 must close into O-shaped contours at some distance. Thus, any energy gained by the electrons in the auroral regions must have been lost on entering the potential structure. *Bryant and Perry (1995)* demonstrate that stochastic acceleration via lower hybrid waves, which have been observed by the FAST satellite in the auroral region, produces many of the observed auroral electron features, including beams, conics and widened loss cones. Thus, as an alternative to the quasi-static electric field theory, *Bryant (2002)* proposes the existence of the lower hybrid wave acceleration mechanism at high altitudes, after which these accelerated electrons may then pass through O-shaped contours which would explain observations but would provide no net acceleration. *Janhunen et al. (1999)* agree with this hypothesis, since Polar data often did not find significant perpendicular electric fields (which are indicative of the high end of a U-shaped contour) above the acceleration region at 4 R_E. As a result of these observations, *Janhunen and Olsson (2000)* also propose O-shaped contours, which would look the same as U-shaped contours at low altitudes, but would explain the lack of perpendicular electric field signatures at higher altitudes. They then propose a plasma-wave energisation region similar to that of *Bryant (2002)* above the O-shaped contours, which would provide the observed electron acceleration. A

test-particle simulation of this scenario did reproduce expected electron spectra.

There are several comments to be made about this. Whilst it is true that a totally static electric field cannot provide a net energisation of electrons in a steady state, it is all a question of scale. Spatially, the U-shaped contours may well close at some point, but it is clear that magnetospheric electron populations above auroral field lines lie above the U-shaped contour, and thus will be accelerated by it. Secondly, timescale is important: a keV electron traverses 1 R_E in $\sim$1 s, so whilst an electric field which varies on longer timescales could not be called steady, it appears static to the electron *(Wright (2005))*. Thus, the fluctuating electric field appears static to the electron. *Block and Fälthammar (1990)* showed that electrons would experience an essentially static field for frequencies of up to several Hz. Ions, being heavier, move more slowly, and are thus more susceptible to the temporal fluctuations of the electric field: for them to experience a dc field, the frequency must be lower than $\sim$0.1 Hz. Thus, *Block and Fälthammar (1990)* concluded that there is a range of frequencies for which electrons experience a static field and are accelerated, but ions do not, giving selective acceleration. Whilst this may be true in some cases, observations of electrons and ions accelerated in opposite directions (e.g. *Mozer and Hull (2001))* suggest that ions can sometimes be affected by parallel electric fields as well as electrons.

Global Ultra-Low-Frequency (ULF) Alfvén waves $\sim$1-4 mHz oscillating on auroral field lines over a period of hundreds of seconds are commonly associated with field-aligned current systems, as observed by *Samson et al. (1996)*. The process is outlined by *Wright et al. (2003)*. During the upward current phase, the Alfvén wave gives energy to precipitating electrons which then cause optical emissions in the ionosphere: thus, the energy is lost from the Alfvén wave, and it is damped. After half an Alfvén wave cycle, a region of upward current will switch to a region of downward current, and vice-versa; a snapshot of this is shown in Figure 1.17. Observational evidence for Alfvén wave acceleration is provided by *Vaivads et al. (2003)*, who use a Cluster and DMSP satellite conjunction at high and low altitudes to study an inverted-V upward current event: they conclude that the acceleration is provided by an Alfvén wave with a period of at least several minutes, such that it can be regarded as a potential structure below Cluster.

Parallel electric fields can also be generated as Alfvén waves travel to lower altitudes, where they encounter a strongly inhomogeneous region where electron inertial effects become important. A two-fluid model of this, presented by *Wright et al. (2002)*, retained nonlinear electron inertial effects to produce a parallel electric field of $\sim$1 mV/m over $\sim$1 R_E which accelerated electrons to $\sim$1 keV, consistent with observational evidence of the overall current region. Alfvén waves on adjacent field lines can also phase-mix, resulting in small scales, large currents and the importance of electron inertial effects. These effects become important when the perpendicular scale decreases to about ten times the electron inertial length $\sim$5 km *(Liu et al. (1995))*. These have been observed by *Louarn et al. (1994)* using Freja data: they are associated with strong electric field perturbations of $\sim$100 mV/m and have perpendicular scales $\sim$1 km. At higher altitudes, kinetic effects become important, and *Wygant et al. (2002)* presented the first coordinated observations of kinetic Alfvén waves and electrons and ions accelerated from the associated parallel electric field at 4-7 R_E, using the Polar spacecraft. They point out that these waves can provide acceleration at higher altitudes than other mechanisms, which rely on mirroring via Earth's converging magnetic field. Acceleration such as this at higher altitudes allows more electrons to penetrate to lower altitudes to be accelerated further by low-altitude quasi-static electric fields. Polar observations of these high altitude kinetic Alfvén waves at $\sim$4 R_E have been correlated with ionospheric electron energy flux

(Keiling et al. (2002)), low-altitude Alfvén waves observed by the FAST satellite at ~4000 km *(Dombeck et al. (2005))*, and auroral activity *(Keiling et al. (2003))*, providing good evidence that Alfvén waves play an important role in magnetosphere-ionosphere coupling.

In another approach to explain auroral quasi-static electric fields, it has been suggested that, as magnetospheric ion and electron populations approach the Earth and mirror, the ions manage to penetrate to lower altitudes than the electrons on average, due to their higher mass and parallel kinetic energy, resulting in a charge imbalance which sets up a parallel electric field that accelerates electrons downwards. An electrostatic particle-in-cell simulation of a global auroral flux tube by *Schriver (1999)*, driven by this mechanism, gives rise to a parallel potential of up to 2.7 kV over ~3000 km, broadly consistent with observations.

Whilst many view quasi-static acceleration and acceleration via Alfvén waves as two separate mechanisms, they may just be two different ways to tell the same story. *Lysak (1998)* argues that quasi-static electric fields may simply be signatures of narrow-scale Alfvén waves; and a numerical model by *Rönnmark and Hamrin (2000)* showed that shear Alfvén waves set up parallel electric fields which became electrostatic when the magnetospheric driving force became stationary. Another example of unification was given by *Chaston et al. (2002)*, who managed to recreate particle and field data from an inverted-V upward current event (usually associated with "quasi-static" acceleration) observed by FAST at 3600 km using a 1D MHD model of Alfvén wave propagation. Thus, the Alfvén wave and quasi-static frameworks can coexist.

Acceleration is necessary in the upward current region as electrons must overcome a substantial magnetic mirror force in order to carry current down into the ionosphere. *Knight (1973)* modelled this situation

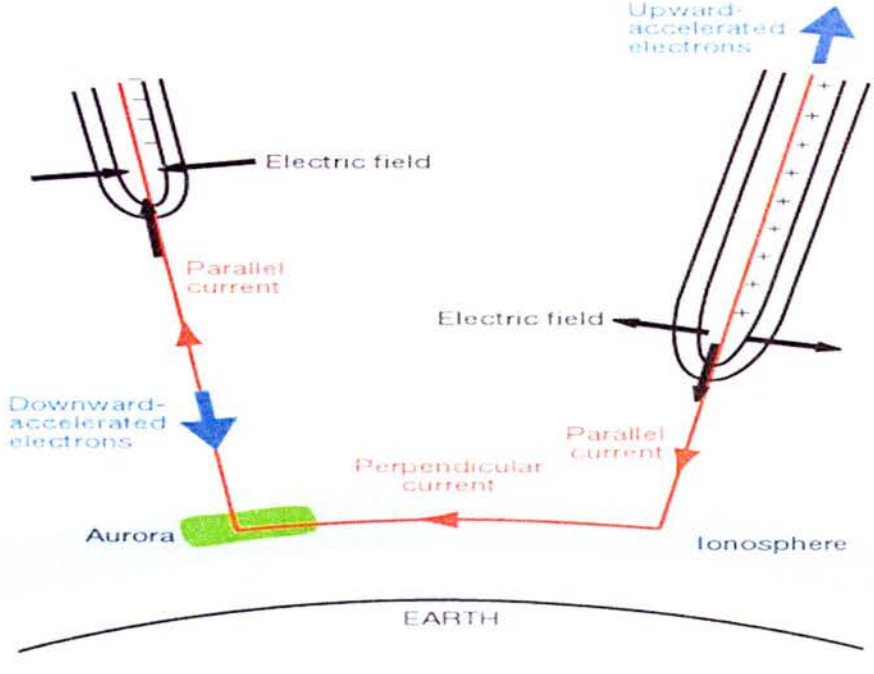

Figure 1.16: Schematic of the potential structures supporting the field-aligned current region, courtesy of *Marklund et al. (2001)*. The upward current region (left) is supported by a converging electric field, and the downward current region (right) is supported by a diverging electric field.

adiabatically for a Maxwellian magnetospheric electron source population, and obtained a linear current-voltage relation for the upward current region. Similar linear relationships can be derived for different magnetospheric source populations, including bi-Maxwellian and Kappa distributions *(Janhunen and Olsson (1998))*. Knight's linear relationship has been confirmed by several sets of observations, including those from the Dynamics Explorer 1 satellite in *Weimer et al. (1987)*. Some studies, however, including *Sakanoi et al. (1995)*, have found that a given potential will result in a larger current density than that predicted by Knight's theory; they interpret this as evidence that lower-energy electrons which should be excluded from precipitating on energy grounds must contribute to the current via temporal changes in the accelerating electric fields.

A linear current-voltage relationship may provide a good overall picture of the upward current region, but it does not yield any information as to how the accelerating potential is distributed along the field line, and hence the magnitude of the parallel electric field. Observations suggest that the acceleration may occur in localised potential steps, called double layers. The extent of a double layer is generally a few Debye lengths (λ_D), where

$$\lambda_D = \sqrt{\frac{\epsilon_0 k T_e}{e^2 n_e}} \tag{1.60}$$

and T_e and n_e are electron temperature and number density respectively. Double layers come in two forms: weak layers such that $e\phi < kT_e$, where ϕ is electrostatic potential, and strong layers such that $e\phi > kT_e$. *Temerin et al. (1982)* published the first observations of small-amplitude weak double layers in a naturally-occurring plasma; the S3-3 satellite measured electric fields of ~10 mV/m at altitudes of 6,000-8,000 km. Viking data by *Boström et al. (1988)* and *Koskinen et al. (1990)* showed that these weak double layers occurred on a very small scale ~100 m, and are associated with a potential drop of ~1 V; the frequency of occurrence of these weak double layers led the authors to postulate that much of the ~1 kV potential generally required over a distance of ~1000 km could be provided by multiple weak double layers along an auroral field line.

The downward current is principally carried by upgoing electrons of ionospheric origin *(Pellinen et al. (1995))*, and it was theoretically assumed that these electrons would require little or no acceleration, since the ionosphere is a plentiful source of electrons. However, *Marklund et al. (1994)* and *Marklund et al. (1997)* presented FREJA satellite data which showed intense electric fields (~1 Vm^{-1}) in the downward current region. Recent FAST observations (e.g. *Ergun et al. (1998a))* have also supported the idea of the existence of quasi-static potential structures in this region via correlated increases in potential and electron energy.

In the past, it was hard to measure the parallel electric field directly, since it is often much smaller than the perpendicular field. However, with the advent of satellites such as FAST and Cluster which have improved temporal and spatial resolution, it is possible to detect the parallel electric fields, even over very short distances. Thus, *Mozer and Kletzing (1998)* and *Hull et al. (2003a)* used Polar data to detect large-amplitude parallel electric fields ~25-300 mV/m in the upward current region over a distance of ~10 km; *Hull et al. (2003b)* interpreted these as strong double layers accelerating electrons at the interface between the dense ionospheric and tenuous magnetospheric plasmas. These observations agree with *Mozer and Hull*

(2001), who observe this narrow low-altitude potential sheath, with further acceleration required at mid- and high-altitudes to help electrons to overcome the magnetic mirror force. This higher-altitude acceleration is associated with weaker electric fields, and may also occur in several potential steps.

Similarly, *Ergun et al. (2001)* and *Ergun et al. (2004)* used the FAST satellite to obtain direct measurements of the parallel electric field in both current regions $\sim$100 mV/m, with an extent of $\sim$100 m. These were also interpreted as strong double layers, which accounted for about 10-15 % of the total field-aligned potential. Several of these double layers along an auroral flux tube could thus account for much of the observed electron acceleration. As such, strong double layers have superceded weak double layers as prime candidates for auroral acceleration.

1.7.2 Properties of field-aligned current regions

Upward current sheets are relatively broad, existing over $\sim$100 km, with smaller-scale downward current sheets $\sim$10 km at their edges *(Frey et al. (1998))*. The numerical model in *Rönnmark and Hamrin (2000)* predicts this difference in latitudinal width, which generally results in higher current densities in downward current regions *(Elphic et al. (1998))*. *Schriver et al. (2003)* used a conjunction of the FAST and Polar satellites to study the auroral region, and observed broad current sheets as outlined above, with smaller-scale "bursty" electron precipitation embedded in the larger regions, resulting in a finer structure of current reversal. *Scoffield et al. (2005)* used simultaneous observations of field-aligned currents using one of the SuperDARN radars and FAST at 2000 km altitude and compared these to a global ULF model by *Wright and Allan (1996)*: the overall structure was in agreement with the model, but much finer-scale structuring $\sim$50 km was seen, presumably associated with electron inertial Alfvén waves. *McFadden et al. (1998)* also used the improved temporal and spacial resolution on FAST to observe fine-scale field-aligned potentials $\sim$1-10 km in the upward current region, and *Karlsson and Marklund (1996)* found that the most intense downward current events observed by Freja had the smallest scale-sizes $\sim$1 km.

In upward current regions, the downflowing electron beam excites perpendicular ion-cyclotron waves *(Mozer et al. (1997))* and generates intense radio emissions called auroral kilometric radiation with frequencies of 100 to 500 kHz *(Ergun et al. (1998b))*. Accelerated particle distributions are often unstable, and require thermalisation via wave-particle interactions; *McFadden et al. (1990)* found evidence of such a process in the form of a plateau in the precipitated electron distribution at low altitudes. Also, the precipitating electrons and corresponding upflowing ion beams are classic ingredients for a two-stream instability, which is responsible for the generation of electron phase-space holes. These have been observed by *Pottelette and Treumann (2005)* and modelled by *Oppenheim et al. (1999)* and *Newman et al. (2001)*. *Singh et al. (2005)* present one-dimensional particle-in-cell simulations of an auroral flux tube which recreate strong double layers and much of the associated turbulence discussed above.

Detailed analysis of the downward current region, including that by *Andersson et al. (2002)* and *Ergun et al. (2003a)*, has also revealed complex characteristics: the potential increase in a double layer occurs along a narrowly confined region of $\sim$10 Debye lengths; the resulting unstable electron beam is seen along another similarly small region; and finally, the beam is stabilised by strong wave turbulence and electron phase-space holes. Ion cyclotron waves are also found in this region *(Cattell et al. (1998))*, as well as

quasi-electrostatic whistler emissions known as VLF saucers *(Ergun et al. (2003b))*. Solitary structures interpreted as positively-charged electron phase-space holes *(Ergun et al. (1998c))* are seen to move anti-Earthward at between 500 and 5000 km/s, and can be associated with potentials of ~100 V, which could contribute considerably to upward electron acceleration.

Whilst it would be expected that the electric field in the downward current region would result in ions accelerated downwards in the opposite direction to the electrons, this turns out not to be the case. As the potential structure develops, ions at lower altitudes are trapped between it and their lower altitude magnetic mirror point and experience transverse heating which makes their distribution evolve into a conical shape. Eventually, they gain so much perpendicular kinetic energy that the associated mirror force is larger than the parallel electric field, and they can escape and stream anti-Earthward. *Hultqvist et al. (1988)* used Viking data to simultaneously observe these ion conics and upgoing energetic electrons on the same field line.

This simultaneous field-aligned evacuation of electrons and ions from low-altitude downward current regions leads to plasma depletion in the ionosphere, as viewed in Freja data by *Lundin et al. (1994)* and in the EISCAT radar data by *Aikio et al. (2004)*. A model by *Doe et al. (1995)* showed that these density cavities could develop in ~1 minute. As downward currents often flow for longer than this, it is obvious that they will need to broaden in latitude in order to obtain more ionospheric charge-carriers. This is exactly what was observed by *Johansson et al. (2004)* and *Marklund et al. (2001)* with Cluster. *Marklund et al. (2001)* found that when the first spacecraft flew through the region of interest, it observed a narrow region of strong current densities; as subsequent spacecraft passed through, they observed the region broadening out, current densities decreasing, with the same overall current being carried, over a timescale of ~200 s. Sometimes such a broadening will occur as more current-carriers are required to carry an increasing overall downward current. *Aikio et al. (2004)* used Cluster data and ground-based instruments to study a downward current region: the accelerating potential increased from 200 V to 1 kV in 70 s, and the current region was observed to widen during this time. *Marklund et al. (2006)* observed a similar growth phase

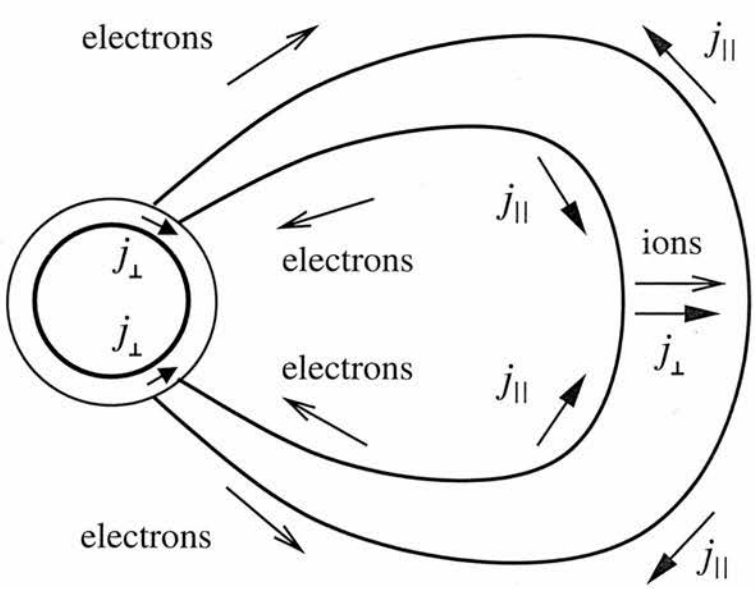

Figure 1.17: Schematic of global ULF Alfvén wave current circuit *(Wright et al. (2002))*.

using the Cluster satellites: the potential in the downward current region was seen to increase from < 1 to 3 kV over $\sim$100 s. A few minutes prior to this, the energy of the inverted-V ions in the adjacent upward current region was observed to decrease by roughly the same amount, offering intriguing circumstantial evidence for a potential redistribution between the upward and downward current regions.

1.7.3 Seasonal dependence of field-aligned currents

The first evidence that auroral activity is modulated by sunlight was given by *Newell et al. (1996)*, who presented nine years' worth of DMSP satellite data which showed that discrete auroral arcs occur preferentially in darkness (winter) compared to daylight (summer) by a factor of $\sim$3. This was followed by a wealth of other statistical surveys using a variety of techniques, which confirmed this result. *Collin et al. (1998)* used Polar satellite data to show that upflowing ion beams associated with the upward current in the evening sector occur much more frequently in winter than in summer. *Barth and Baker (2004)* made use of the fact that 3-4 keV electrons precipitating into the Earth's atmosphere excite atomic and molecular nitrogen to produce the visible aurora and nitric oxide, which fluoresces in solar UV radiation. Global observations of nitric oxide combined with a thermospheric model of its creation and loss processes show a minimum in electron flux at summer solstice. In the downward current region, *Hamrin et al. (2000)* used Freja data from 1700 km altitude on the nightside to show that transverse ion heating associated with the downward current is more common in dark ionospheric conditions than at sunlit times. The ions are also heated to substantially higher energies in darkness, yielding a greater stream of anti-Earthward moving ions and a larger resulting density cavity in the ionosphere.

The energies associated with upward currents also increase during darkness. *Deehr et al. (2005)* analysed the heights of auroral arcs over Alaska, and found that the altitude decreased from over 150 km at twilight to 100 km at midnight. Since more energetic electrons penetrate to lower altitudes in the ionosphere, it can be inferred that the energy of precipitating electrons is inversely proportional to the amount of sunlight on the ionosphere: in this case, the energy was found to increase from $\sim$100 eV to 3 keV during this time. The altitude of the auroral arcs increased again in the late morning, correlated with an increase in solar illumination. Results from the FAST satellite by *Cattell et al. (2006)* indicate that the characteristic energy of downgoing electron beams on the nightside is $\sim$2 times that of beams on the dayside. A statistical analysis of data from the Akebono satellite presented in *Morooka and Mukai (2003)* reveals that the average potential drop in upward current regions on the dayside is 600-800 V, rising to 4 kV in the pre-midnight sector.

Solar illumination has no great effect on magnetospheric plasma, but does result in greater photoionisation rates, and hence larger ion and electron number densities, in the ionosphere. The results outlined above suggest that field-aligned currents are carried by higher-energy electrons on field lines whose ionospheric end is in darkness, i.e. where the ionospheric density and conductivity are lower. Density further along the field line is also likely to be lower in dark conditions: Polar data in *Johnson et al. (2003)* show that the average plasma density at 1.9 to 2.5 R_E increases from 10 cm^{-3} in dark conditions to 60 cm^{-3} in sunlit conditions. In accordance with this, *Hultqvist et al. (1991)* found that upgoing ion beams associated with the upward current are favoured by low ambient plasma densities, and *Morooka and Mukai (2003)* found

that the acceleration region is found at lower altitudes in winter. In addition, *Lynch et al. (2002)* found that the current-voltage relationship in the downward current region is determined by the ambient ion density. This indicates that higher-voltage potential drops are more common in dark regions, and that ionospheric and near-Earth plasma conditions play a key role in the magnetosphere-ionosphere coupling mechanism. Thus, the ionosphere is not just a passive boundary, as assumed by *Knight (1973)* and others.

Dayside and nightside aurorae are seen to behave in different ways in Polar UV imagery taken from April to July, presented in *Liou et al. (1997)*. This data set highlighted three areas of optical intensification: one enhancement at pre-midnight associated with substorm activity, centred at 2230 MLT (Magnetic Local Time) at 68° MLAT (Magnetic LATitude) and extended for three hours in MLT; another in the post-noon sector at 1500 MLT and 75° MLAT, correlated with maximal upward Region 1 currents; and lastly, a weaker pre-noon enhancement, sometimes not visible in data, at 0900 MLT and 73° MLAT. The pre-midnight (nightside) enhancement was strongest in April, and weakened as the summer progressed, while the pre- and post-noon (dayside) enhancements grew. This indicated that nightside aurorae are suppressed by sunlight (as seen above), whilst dayside aurorae, although less frequent, are favoured by more sunlit conditions. This conclusion was verified by *Liou et al. (2001)*, who showed that the increase in aurorae in sunlit dayside summer conditions is due to a greater electron number flux, rather than higher precipitating electron energies. Finally, *Shue et al. (2001)* used Polar UV data to find the correlation between solar EUV Pedersen conductance and auroral brightness: negative and positive correlations were found in the pre-midnight and pre-noon sectors respectively, in agreement with the earlier findings of *Liou et al. (1997)*. The post-noon sector was discovered to be more complex, with other factors at work there as well, and no obvious correlation. Freja data analysed by *Marklund and Karlsson (2001)* showed the same asymmetry in the downward current region: in winter, most of the intense electric fields are concentrated at and after midnight, whilst in summer, the occurrence rate is lower overall, and the maxima are located near dawn and dusk.

1.7.4 Field-aligned currents on other planets

Earth is not the only planet in our solar system to exhibit aurorae - Jupiter, Saturn, Uranus and Neptune are all known to have permanent auroral ovals, as illustrated by global UV images *(Hill (2004))*. It is well-known that solar activity modulates and ultimately powers the aurora on Earth. *Gurnett et al. (2002)* found this to be true on Jupiter as well: as the Cassini-Huygens spacecraft approached Jupiter from upstream, it observed three solar wind shocks, followed by three brightenings of Jupiter's aurora and associated radio emissions after a suitable time delay. It is believed that aurorae on other planets are driven by similar current circuits to that observed at Earth. Circumstantial evidence for this is presented by *Frank and Paterson (2002)*, who show Galileo observations of intense field-aligned electron beams both parallel and anti-parallel to Jupiter's electric field $\sim$1-10 keV, which are energetic enough to cause bright Jovian aurorae. Other phenomena also seem to be similarly correlated: *Kurth et al. (2005)* have found an Earth-like correspondence between Saturn's kilometric radio emissions (similar to Earth's auroral kilometric radiation) observed by Cassini and bright auroral features observed by the Hubble Space Telescope.

Jupiter's aurora exhibits several interesting features missing at Earth. Jupiter is orbited by several moons

including Io, Ganymede and Europa. Whilst our moon has insufficient atmosphere or conductivity to interact with Earth's magnetic field, Jupiter's moons produce auroral footprints which are clearly visible on UV images *(Connerney et al. (1993), Clarke et al. (2002), Grodent et al. (2006))*. These are presumably caused by magnetic field line connections and resultant field-aligned currents between Jupiter and its moons: the current between Io and Jupiter is thought to be of the order of one million amperes.

Downward field-aligned currents have also been observed on other planets. *Kivelson et al. (2002)* reported Galileo observations of return currents ~6 MA into a $< 2^\circ$ band of latitude on Jupiter's dusk side, poleward of the main auroral oval. The Cassini spacecraft observed highly field-aligned anti-Saturnward electron beams, as presented by *Saur et al. (2006)*. These electron beams had similar energy spectra to those found on Earth, and they mapped back to Saturn's auroral region.

These observations suggest that the basic ingredients of auroral activity and field-aligned currents are not limited to Earth, but are a common feature of planetary magnetospheres. Whilst it is possible to make observations of aurorae on other planets, it is far more expensive and difficult than directly observing closer auroral features on Earth. Numerous satellites and rockets are continuing to provide us with a wealth of data from Earth's auroral region. When this data is analysed in detail and auroral features on Earth are clearly understood, the principles can be applied (with care) to other planets to gain understanding of their systems.

1.7.5 Quasi-neutrality in the field-aligned current region

The single fluid Magnetohydrodynamic (MHD) approximation, successful in many applications related to large-scale current systems, is not suitable for modelling all aspects of field-aligned currents, since this limit neglects electron mass compared with that of the ions, and thus neglects electron inertia. Massless electrons are infinitely mobile and move to wherever they are needed to carry any required current. Since this is not the case in the Earth's field-aligned current region, another approach is needed. Kinetic and fluid models have both been good tools for understanding this energisation, and quasi-neutrality is a primary modelling constraint. A plasma tends to exist in a quasi-neutral state; that is, it has roughly equal ion and electron number densities at each point in space. It is only roughly equal since small deviations in $\rho = e(n_i - n_e)$ are required by Maxwell's equation in (1.14) to generate electric fields in a plasma. If we take a static electric field such that it can be expressed as the gradient of the electrostatic potential, $\mathbf{E} = -\nabla\phi$, then equation (1.14) becomes

	Φ(V)	L(m)	N(m^{-3})	$\frac{\lvert n_i - n_e \rvert}{N}$	kT_e(eV)	λ_D(m)
Auroral region	10^3	10^6	10^6	5.5×10^{-8}	10^3	235
Boström et al. (1988) weak double layer	1	10^2	10^7	5.5×10^{-4}	10	7.4
Ergun et al. (2001) strong double layer	27	10^2	10^7	1.5×10^{-2}	10	7.4

Table 1.2: Plasma properties of the auroral acceleration region and weak and strong double layers: quasi-neutrality is obviously satisfied in the auroral region as a whole, but is not so well satisfied in double layers, which require a density deviation of up to 1.5 %.

$$\frac{\mathrm{d}^2\phi}{\mathrm{d}\ell^2} = -\frac{e\,(n_i - n_e)}{\epsilon_0} \tag{1.61}$$

where ℓ is the magnetic field-aligned coordinate. Then, in the auroral current region, we can do an order-of-magnitude analysis on this equation such that

$$|\, n_i - n_e \,| \approx \frac{\epsilon_0 \Phi}{eL^2} \tag{1.62}$$

where $\Phi = 10^3$ V is a typical overall potential increase on an auroral field line and $L = 10^6$ m is a typical distance over which the electron acceleration occurs. Thus, given that the ambient number density, N, is typically $10^6\ \mathrm{m}^{-3}$, we have that

$$\frac{|\, n_i - n_e \,|}{N} \approx 5 \times 10^{-8} \tag{1.63}$$

This implies that quasi-neutrality is a valid constraint in models of the overall electron acceleration region. Double layer theory is slightly different, and requires overall quasi-neutrality over the double layer, but significant density differences within it to produce large electric fields. This is illustrated by Table 1.2, in which the analysis carried out above for the overall auroral acceleration region is compared with results from equation (1.62) for the weak double layers in *Boström et al. (1988)*, and the strong layer in *Ergun et al. (2001)*: number density deviations of up to ~1-2 % are necessary for such localised acceleration. *Chiu and Schultz (1978)* and *Stern (1981)* both considered the generation of parallel electric fields along an auroral field line embedded in a cold, dense ionosphere near the Earth, and a hot, tenuous magnetosphere further away. *Chiu and Schultz (1978)* examined upward currents, and found potential differences of the order of 1 kV; in their examples, $E_{\parallel}$ maximised at an altitude of 2000-2500 km and extended to ~1 R_E. *Stern (1981)*'s model produced double layers for equilibria and upward and downward currents. More recently, *Ergun et al. (2000)*, *Rönnmark (2002)*, *Vedin and Rönnmark (2004)*, *Wright and Hood (2003)*, *Boström (2003)* and *Boström (2004)* have all modelled the upward current region.

Less attention has focused on modelling the downward current region. *Temerin and Carlson (1998)* present an ionospheric electron fluid model with fixed ion density, using quasi-neutrality to constrain the solution and obtain the required parallel potential drop. They obtain parallel potential drops of several kV for current densities of a few $\mu\mathrm{Am}^{-2}$. *Jasperse (1998)* uses a Vlasov model incorporating ion heating and wave effects, which explains the production of upward field-aligned electron beams, downward-pointing parallel electric fields and ion conics.

1.8 Outline of Thesis

The work presented in this Thesis aims to further understanding of the nature of electron acceleration in Earth's auroral field-aligned current region. In Chapter 2, we present a 1D Vlasov model of the downward

current region. The electrons are described via distribution functions, and the ion density profile is fixed along the field line; quasi-neutrality is invoked to solve for the potential variation along the field line. In Chapter 3, we use this model to derive an analytic current-voltage relation for the downward current region, analagous to the well-known *Knight (1973)* relation for upward currents. In Chapter 4, we present a similar Vlasov model for the upward current region, and use this to find the potential variation along the field line and to discover which factors contribute to the accelerating parallel electric field. The Appendix contains calculations of integrals used in this Chapter. In Chapter 5, we investigate how flow of downward current affects the number density of the ionospheric E region, using an Alfvén wave model of magnetosphere-ionosphere interaction. Finally, Chapter 6 presents the conclusions of the Thesis and possible further work.

Chapter 2

Downward field-aligned current model: Numerical results

2.1 Introduction

Downward field-aligned currents (FACs) are carried by upward-moving electron beams accelerated along field lines in the auroral region. Whilst analysis of recent FAST observations *(Ergun et al. (2003a))* has disclosed a rich variety of complex phenomena occurring in downward current regions, including turbulence, waves and indications of double layers, these same observations (e.g. *Carlson et al. (1998a))* also indicate a simpler overall picture, with correlated increases in electron energy and potential. This suggests the presence of stable accelerating potential structures at least on an electron acceleration timescale. An example of this is given in Figure 2.1, which shows FAST data for an upgoing electron beam event. The second panel shows that the satellite was passing through a strong downward current region between 45:55 and 46:20 UT, and the fourth panel indicates the associated upgoing energetic electron beams. The final panel shows the electric potential inferred from the integrated electric field (black line) compared with the characteristic energy of the electron beam (red line). The two are very similar. For this reason, a quasi-static model similar to *Knight (1973)*'s model for the upward current should yield considerable insight into the downward current region's large-scale behaviour.

In this work, we produce a one-dimensional model of this region by selecting a single auroral field line (with latitude of 70° to 72°) and examining the nature of the electron acceleration along it. The electron beams are observed to appear at altitutes within 1 R_E of the Earth *(Boehm et al. (1995), Carlson et al. (1998a)* and *Elphic et al. (2000))*. A keV electron traverses this distance in $\sim$1 s, whilst the period of a ULF standing Alfvén wave on a magnetic field line is hundreds of seconds, so we impose a steady state on our model by setting $\partial/\partial t = 0$. On this timescale, the reaction of ions to any parallel electric field along the field line will be negligible, since they are so much heavier than the electrons. Thus, we impose a fixed ion density profile along the field line to obtain the short-timescale solution to the problem.

The electron populations are described via distribution functions. We define a cold top-hat ionospheric distribution function at the base of the ionosphere, and a warm Maxwellian magnetospheric electron distribution at the equatorial end of the field line. In the ionosphere, this gives us a trapped electron population and a component which escapes to form the upgoing beam in the magnetosphere, whilst in the magnetosphere, we have warm mirroring magnetospheric electrons, and a cold current-carrying field-aligned electron beam of ionospheric origin. We can then equate the ion and electron number densities at each point along the field line to satisfy the plasma quasi-neutrality condition, giving the electric potential along the field line.

The model presented here extends the quasi-neutral electron fluid model by *Temerin and Carlson (1998)* via the use of electron distribution functions and the inclusion of electron behaviour in the F region of the ionosphere. Thus, an electron beam is extracted self-consistently from the ionosphere and is accelerated into the magnetosphere to carry the specified current. As with their fluid model, each of the electron populations is described separately, allowing us to track each of them along the field line, but using distribution functions also retains information about the spread of velocities in each population, rather than using average speeds. This model allows us to predict the height at which the electron beam emerges from the ionosphere and the extent of the energisation region. Both of these model features can then be compared with observational data to test their validity.

2.1.1 Dipolar field

We approximate the equilibrium magnetic field, $\mathbf{B}$, as being locally dipolar in the acceleration region, giving

$$B = \frac{B_0\sqrt{1+3\sin^2\theta}}{\cos^6\theta} \tag{2.1}$$

where B_0 is the equatorial field strength, θ is the latitude, and $r = LR_E\cos^2\theta$, where r is the radial distance from the centre of the Earth to a point on the field line and L is L shell. L is taken to be 10, giving $\cos\theta_m = \frac{1}{\sqrt{10}}$ at the ionospheric footpoint. This gives an invariant latitude of $\theta_m = 71.6°$ (where the field line enters the ionosphere). We model the acceleration region as having a dipole magnetic geometry; however, it is not necessary that the field line remains dipolar beyond this region. Now, in polar coordinates, the arc length element along $\mathbf{B}$ is

$$\mathrm{d}\ell = \mathrm{d}\theta\sqrt{r^2 + \left(\frac{\mathrm{d}r}{\mathrm{d}\theta}\right)^2} \tag{2.2}$$

Here, we have

$$\frac{\mathrm{d}r}{\mathrm{d}\theta} = -2LR_E\cos\theta\sin\theta \tag{2.3}$$

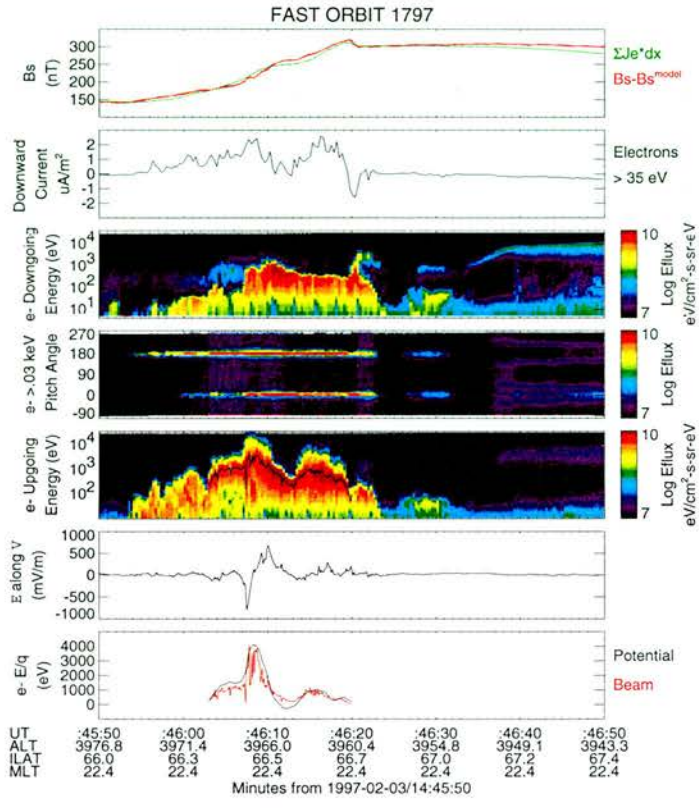

Figure 2.1: This is an example of FAST data taken from *Carlson et al. (1998a)*, Figure 2. Panel two shows the downward current region extending between 45:55 and 46:20 UT, and panel four indicates the presence of the characteristic field-aligned electron beams. The bottom panel is of most interest, as it shows the correlated increase in electic potential (black line) and beam energy (red line).

$$\begin{aligned} \Rightarrow \mathrm{d}\ell &= LR_E \cos\theta \sqrt{\cos^2\theta + 4\sin^2\theta}\ \mathrm{d}\theta \\ &= LR_E \cos\theta \sqrt{1 + 3\sin^2\theta}\ \mathrm{d}\theta \end{aligned} \tag{2.4}$$

So, the length along the field line, ℓ, which increases on approaching the ionosphere, is given by

$$\ell = \int_0^\theta LR_E \cos\theta' \sqrt{1 + 3\sin^2\theta'}\ \mathrm{d}\theta' \tag{2.5}$$

where θ is the angle at a general point along the field line. We can use the substitution $\sqrt{3}\sin\theta' = \sinh Y$ to obtain the upper limit $a = \sinh^{-1}\left(\sqrt{3}\sin\theta\right)$. The result is given by:

$$\ell = \frac{LR_E}{\sqrt{3}} \int_0^a \cosh Y \sqrt{1 + \sinh^2 Y}\ \mathrm{d}Y$$

$$
\begin{aligned}
&= \frac{LR_E}{\sqrt{3}} \int_0^a \cosh^2 Y \, \mathrm{d}Y \\
&= \frac{LR_E}{2\sqrt{3}} \int_0^a \cosh 2Y + 1 \, \mathrm{d}Y \\
&= \frac{LR_E}{2\sqrt{3}} \left[\frac{1}{2} \sinh 2Y + Y \right]_0^a \\
&= \frac{LR_E}{2\sqrt{3}} \left[\frac{1}{2} \sinh \left(2\sinh^{-1} \left(\sqrt{3} \sin\theta \right) \right) + \sinh^{-1} \left(\sqrt{3} \sin\theta \right) \right] \qquad (2.6) \\
& \qquad (2.7)
\end{aligned}
$$

The first term in this expression can be simplified using the substitution $Z = \sinh^{-1}(\sqrt{3}\sin\theta)$ and the hyperbolic identity $\sinh 2Z = 2\sinh Z \cosh Z$, since

$$
\begin{aligned}
\sinh \left(2\sinh^{-1} \left(\sqrt{3} \sin\theta \right) \right) &= \sinh 2Z \\
&= 2\sinh Z \sqrt{1 + \sinh^2 Z} \\
&= 2\sqrt{3} \sin\theta \sqrt{1 + 3\sin^2\theta} \qquad (2.8)
\end{aligned}
$$

Thus, we can write

$$
\ell = LR_E \left(\frac{1}{2} \sin\theta \sqrt{1 + 3\sin^2\theta} + \frac{\sqrt{3}}{6} \sinh^{-1} \left(\sqrt{3} \sin\theta \right) \right) \qquad (2.9)
$$

The model extends from a distant point in the magnetosphere, ℓ_0, whose exact location is unimportant, to the base of the F region, taken to be situated at a radial distance of 1 R_E. Since $\theta = \theta_m$ here, we know that $\cos\theta_m = \frac{1}{\sqrt{10}}$ and $\sin\theta_m = \frac{3}{\sqrt{10}}$, and we define $\ell_m = \ell(\theta_m)$. The coordinate ℓ is useful for global behaviour along the field line. However, we introduce a new field-aligned coordinate, $s = \ell_m - \ell$, which is measured from the ionospheric end. Thus, $s = 0$ at the base of the F region (ℓ_m) and increases with altitude. This coordinate is more useful for plotting acceleration features closer to the Earth. Using equation (2.9) and the fact that $\sinh^{-1} x = \ln\left(x + \sqrt{x^2 + 1}\right)$, we obtain the following expression for s:

$$
\begin{aligned}
s &= LR_E \left[\frac{3}{20}\sqrt{37} - \frac{1}{2} \sin\theta \sqrt{1 + 3\sin^2\theta} \right. \\
&\quad \left. + \frac{\sqrt{3}}{6} \ln \left(3\sqrt{\frac{3}{10}} + \sqrt{\frac{37}{10}} \right) - \frac{\sqrt{3}}{6} \ln \left(\sqrt{3}\sin\theta + \sqrt{1 + 3\sin^2\theta} \right) \right] \qquad (2.10)
\end{aligned}
$$

2.1.2 B/n curve

We impose the following fixed exponentially-decaying ion density profile along the field line

$$n = n_0 + (n_m - n_0) \exp\left[-\frac{(r - R_E)}{h}\right] \tag{2.11}$$

which gives a constant magnetospheric number density of n_0, and an ionospheric number density which is stratified by gravity with a scale height h, and a maximum n_m at the base. The scale height can vary, depending on the conditions. In the Introduction, we assumed that ionospheric ions are principally O^+ ions with temperature 2000 K, and calculated the scale height to be ~100 km. We can now find the variation of B/n along the field line. In this Chapter, the values that we take for the constants are $B_0 = 25$ nT, giving $B_m = 4.8 \times 10^4$ nT, $n_0 = 10^6$ m^{-3}, $n_m/n_0 = 10^6$, and $h = 100$ km, unless otherwise stated. We then obtain a characteristic B/n curve for the model, with a peak at 0.273 R_E, called ℓ_p, shown in Figure 2.2. For altitudes above ℓ_p, we have $n \approx n_0$ and $B \propto r^{-3}$, whilst Earthward of ℓ_p, $B \approx$ const, $n \propto \exp(-(r - R_E)/h)$.

The significance of the B/n ratio has been recognised for some time. *Swift (1975)* identified it as being proportional to the mean electron fluid speed, and subsequent studies, including *Wright and Hood (2003)*, show that the maximum energisation in the upward current region occurs where $\mathrm{d}(B/n)/\mathrm{d}\ell = 0$, i.e., at the B/n peak. In this model, we see that the properties of the B/n peak are also crucial in the downward current region.

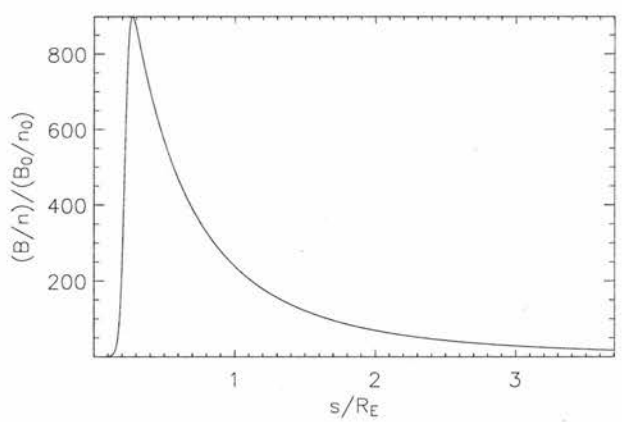

Figure 2.2: B/n variation along an $L = 10$ field line. The path length is measured from the base of the F region, taken to be at 1 R_E altitude. Earthward of the B/n peak, $B \approx$ constant and $n \propto \exp(-(r-R_E)/h)$, whilst beyond it, $B \propto r^{-3}$ and $n \approx n_0$.

2.1.3 Vlasov's Equation for Electrons

Following the approach of *Wright and Hood (2003)*, we model the ionospheric electron population via a gyro-averaged distribution function $f_I(\ell, v_\parallel, v_\perp, t)$, where $v_\parallel$ and $v_\perp$ are the parallel and perpendicular components of the electron velocity, and t is time. This distribution function satisfies the general guiding centre gyrotropic Vlasov equation,

$$\frac{\mathrm{d}f}{\mathrm{d}t} = \frac{\partial f}{\partial t} + \frac{\partial f}{\partial \ell}\frac{\mathrm{d}\ell}{\mathrm{d}t} + \frac{\partial f}{\partial v_\parallel}\frac{\mathrm{d}v_\parallel}{\mathrm{d}t} + \frac{\partial f}{\partial v_\perp}\frac{\mathrm{d}v_\perp}{\mathrm{d}t} = 0 \tag{2.12}$$

and we assume that the magnetic moment,

$$\mu = \frac{mv_\perp^2}{2B} \tag{2.13}$$

is conserved on an electron trajectory. We seek a solution of the form

$$f_I = F(\ell, v_\parallel, v_\perp, t)g(\mu) \tag{2.14}$$

where $g(\mu)$ is an arbitrary function of μ. Since f_I and μ are both conserved on an electron trajectory, we can deduce that F is also conserved on an electron trajectory. Following *Wright and Hood (2003)*, we substitute equation (2.14) into equation (2.12) to obtain

$$\begin{aligned} 0 &= g(\mu)\frac{\mathrm{d}F}{\mathrm{d}t} + F\frac{\mathrm{d}g}{\mathrm{d}t} \\ &= g(\mu)\frac{\mathrm{d}F}{\mathrm{d}t} + F\frac{\mathrm{d}g}{\mathrm{d}\mu}\frac{\mathrm{d}\mu}{\mathrm{d}t} \\ &= g(\mu)\frac{\mathrm{d}F}{\mathrm{d}t} \end{aligned} \tag{2.15}$$

since $\mathrm{d}\mu/\mathrm{d}t = 0$, $\mathrm{d}/\mathrm{d}t$ being the complete derivative following an electron trajectory. The forces included in this model are the parallel electric field ($-eE_\parallel$) and the magnetic mirror force ($-\mu\partial B/\partial\ell$), so our guiding centre equation of motion is

$$m\frac{\mathrm{d}v_\parallel}{\mathrm{d}t} = -eE_\parallel - \mu\frac{\partial B}{\partial \ell} \tag{2.16}$$

From μ-conservation, we obtain:

$$\begin{aligned} 0 &= \frac{\mathrm{d}\mu}{\mathrm{d}t} \\ &= \frac{mv_\perp}{B}\frac{\mathrm{d}v_\perp}{\mathrm{d}t} - \frac{mv_\perp^2}{2B^2}\frac{\mathrm{d}B}{\mathrm{d}t} \end{aligned} \tag{2.17}$$

From this, we can deduce $\mathrm{d}v_\perp/\mathrm{d}t$:

$$\frac{\mathrm{d}v_\perp}{\mathrm{d}t} = \frac{v_\perp}{2B}\frac{\partial B}{\partial \ell}\frac{\mathrm{d}\ell}{\mathrm{d}t}$$

$$= \frac{v_\parallel v_\perp}{2B}\frac{\partial B}{\partial \ell} \tag{2.18}$$

noting that $\mathrm{d}\ell/\mathrm{d}t = v_\parallel$. Then, Vlasov's equation becomes

$$g(\mu)\left[\frac{\partial F}{\partial t} + v_\parallel \frac{\partial F}{\partial \ell} - \left(\frac{eE_\parallel}{m} + \frac{v_\perp^2}{2B}\frac{\partial B}{\partial \ell}\right)\frac{\partial F}{\partial v_\parallel} + \frac{v_\parallel v_\perp}{2B}\frac{\partial B}{\partial \ell}\frac{\partial F}{\partial v_\perp}\right] = 0 \tag{2.19}$$

We take $g(\mu) = (m/\pi\bar{\mu})\delta(\mu/\bar{\mu})$, where δ is the Dirac delta function, and $\bar{\mu}$ is a normalising constant, to focus on field-aligned motion, since observations *(Carlson et al. (1998a))* and μ-conservation both give a highly-collimated upgoing electron beam. We can see that this is a good approximation, because if we consider the energy equation neglecting change in potential, and use equation (2.13):

$$\begin{aligned} W_0 &= \frac{m}{2}\left(v_\parallel^2 + v_\perp^2\right) \\ &= \frac{m}{2}v_\parallel^2 + \mu B \end{aligned} \tag{2.20}$$

Thus, we can write

$$v_\parallel = \sqrt{\frac{2}{m}\left(W_0 - \mu B\right)} \tag{2.21}$$

Thus, as the beam moves upwards and B decreases, $v_\parallel$ will increase, and $v_\perp$ will decrease, so the beam becomes more and more field-aligned. We note that $(v_\parallel, v_\perp)$-space is in fact analogous to cylindrical polar co-ordinates. Thus, we can integrate $g(\mu)$ over $v_\perp$ space by multiplying by $2\pi v_\perp \mathrm{d}v_\perp$ and integrating from $0 < v_\perp < \infty$ as follows

$$\begin{aligned} \int_0^\infty g(\mu) 2\pi v_\perp \ \mathrm{d}v_\perp &= \int_0^\infty \frac{m}{\pi\bar{\mu}}\delta\left(\frac{\mu}{\bar{\mu}}\right) 2\pi v_\perp \ \mathrm{d}v_\perp \\ &= 2B\int_0^\infty \delta\left(\frac{\mu}{\mu}\right)\mathrm{d}\left(\frac{\mu}{\bar{\mu}}\right) \\ &= B \end{aligned} \tag{2.22}$$

The first term in (2.19) can similarly be integrated over $v_\perp$ space, noting that $v_\perp = \sqrt{2B\mu/m}$ and that

$$\mathrm{d}\left(\frac{\mu}{\bar{\mu}}\right) = \frac{2}{\bar{\mu}}\sqrt{\frac{m\mu}{2B}}\,\mathrm{d}v_\perp \tag{2.23}$$

to give

$$\begin{aligned}\int g(\mu)\frac{\partial F}{\partial t}2\pi v_\perp \,\mathrm{d}v_\perp &= 2B\int \frac{\partial F}{\partial t}\delta\left(\frac{\mu}{\bar{\mu}}\right)\,\mathrm{d}\left(\frac{\mu}{\bar{\mu}}\right)\\ &= 2B\frac{\partial F}{\partial t}_{[v_\perp=0]}\end{aligned} \tag{2.24}$$

Similarly, the next two terms give

$$\begin{aligned}\int g(\mu)\left(v_\parallel\frac{\partial F}{\partial \ell}-\frac{eE_\parallel}{m}\frac{\partial F}{\partial v_\parallel}\right)2\pi v_\perp \,\mathrm{d}v_\perp &= 2B\int \delta\left(\frac{\mu}{\bar{\mu}}\right)\left(v_\parallel\frac{\partial F}{\partial \ell}-\frac{eE_\parallel}{m}\frac{\partial F}{\partial v_\parallel}\right)\,\mathrm{d}\left(\frac{\mu}{\bar{\mu}}\right)\\ &= 2Bv_{\parallel\,[v_\perp=0]}\frac{\partial F}{\partial \ell}_{[v_\perp=0]}-2B\frac{eE_\parallel}{m}\frac{\partial F}{\partial v_\parallel}_{[v_\perp=0]}\end{aligned} \tag{2.25}$$

The next term can be eliminated, since

$$\begin{aligned}\int g(\mu)\frac{v_\perp^2}{2B}\frac{\partial B}{\partial \ell}\frac{\partial F}{\partial v_\parallel}2\pi v_\perp \,\mathrm{d}v_\perp &= \int v_\perp^2\frac{\partial B}{\partial \ell}\frac{\partial F}{\partial v_\parallel}\delta\left(\frac{\mu}{\bar{\mu}}\right)\,\mathrm{d}\left(\frac{\mu}{\bar{\mu}}\right)\\ &= \left[v_\perp^2\frac{\partial B}{\partial \ell}\frac{\partial F}{\partial v_\parallel}\right]_{[v_\perp=0]}\\ &= 0\end{aligned} \tag{2.26}$$

Finally, we integrate the last term:

$$\begin{aligned}\int g(\mu)\frac{v_\parallel v_\perp}{2B}\frac{\partial B}{\partial \ell}\frac{\partial F}{\partial v_\perp}2\pi v_\perp \,\mathrm{d}v_\perp &= \int v_\parallel v_\perp\frac{\partial B}{\partial \ell}\frac{\partial F}{\partial v_\perp}\delta\left(\frac{\mu}{\bar{\mu}}\right)\,\mathrm{d}\left(\frac{\mu}{\bar{\mu}}\right)\\ &= \int v_\parallel\sqrt{\frac{2B\mu}{m}}\frac{\partial B}{\partial \ell}\frac{\partial F}{\partial\,(\mu/\bar{\mu})}\frac{2}{\bar{\mu}}\sqrt{\frac{m\mu}{2B}}\delta\left(\frac{\mu}{\bar{\mu}}\right)\,\mathrm{d}\left(\frac{\mu}{\bar{\mu}}\right)\\ &= \int 2v_\parallel\frac{\partial B}{\partial \ell}\frac{\partial F}{\partial\,(\mu/\bar{\mu})}\frac{\mu}{\bar{\mu}}\,\delta\left(\frac{\mu}{\bar{\mu}}\right)\,\mathrm{d}\left(\frac{\mu}{\bar{\mu}}\right)\end{aligned} \tag{2.27}$$

We can then use integration by parts, where

$$\int v\,\frac{\mathrm{d}u}{\mathrm{d}(\mu/\bar{\mu})}\,\mathrm{d}\left(\frac{\mu}{\bar{\mu}}\right)=[uv]-\int u\,\frac{\mathrm{d}v}{\mathrm{d}(\mu/\bar{\mu})}\,\mathrm{d}\left(\frac{\mu}{\bar{\mu}}\right) \tag{2.28}$$

We assign $v=\partial F/\partial(\mu/\bar{\mu})$, giving

$$\frac{\mathrm{d}v}{\mathrm{d}(\mu/\bar{\mu})} = \frac{\partial^2 F}{\partial(\mu/\bar{\mu})^2} \tag{2.29}$$

and

$$\frac{\mathrm{d}u}{\mathrm{d}(\mu/\bar{\mu})} = \frac{\mu}{\bar{\mu}}\delta\left(\frac{\mu}{\bar{\mu}}\right) \tag{2.30}$$

Now,

$$u = \int \frac{\mu}{\bar{\mu}}\,\delta\left(\frac{\mu}{\bar{\mu}}\right)\,\mathrm{d}\left(\frac{\mu}{\bar{\mu}}\right) = \left[\frac{\mu}{\bar{\mu}}\right]_{[\mu/\bar{\mu}=0]} = 0 \tag{2.31}$$

Thus, the integral in equation (2.27) reduces to zero.

Using these simplifications, we obtain

$$B\frac{\partial F}{\partial t} + v_{\parallel}B\frac{\partial F}{\partial \ell} - \frac{e}{m}E_{\parallel}B\frac{\partial F}{\partial v_{\parallel}} = 0, \tag{2.32}$$

where $F = F(\ell, v_{\parallel}, v_{\perp} = 0, t)$ in accord with *Wright and Hood (2003)*. F serves as a simplified distribution function for the ionospheric electrons and has units of $\mathrm{m}^{-4}\mathrm{s}\ \mathrm{T}^{-1}$. Equation (2.32) shows how our assumption of small μ (implicit in the choice of g) means the mirror force is not important for the ionospheric electrons. In equation (2.19), the coefficient of $\partial F/\partial v_{\parallel}$ represents the parallel components of the $\mathbf{E}$ and $-\mu\nabla\mathbf{B}$ forces. The latter is absent in equation (2.32). We assume steady fields, and thus describe the electric field in terms of ϕ, where $\mathbf{E} = -\nabla\phi$, giving

$$E_{\parallel} = -\frac{\partial \phi}{\partial \ell} \tag{2.33}$$

The magnetospheric electrons are assumed to be perfectly trapped, and are described separately via an isotropic Maxwellian distribution function given by

$$f_M = n_M\left(\frac{m}{2\pi kT}\right)^{\frac{3}{2}}\exp\left(-\frac{1}{kT}\left(\frac{m}{2}\left(v_{\parallel}^2 + v_{\perp}^2\right) - e\phi\right)\right) \tag{2.34}$$

where n_M is the Maxwellian electron number density at ℓ_0 (the point along the field line where $\theta = 0$), kT is the magnetospheric electron thermal energy and ϕ is the potential variation along the field line between ℓ_0 and ℓ. Thus, $\phi(\ell_0) = 0$ and we denote $\phi(\ell_m) = \phi_m$.

We obtain the following expressions for the electron number density (n) and field-aligned current (j) by integrating the total distribution function $f = f_I + f_M$ over perpendicular and parallel velocity space:

$$\frac{n(\ell)}{B(\ell)} = \int_{-\infty}^{\infty} F(\ell, v_{\parallel}) \ \mathrm{d}v_{\parallel} + \frac{n_M}{B(\ell)} \exp\left[\frac{e\phi}{kT}\right] \tag{2.35}$$

$$\frac{j(\ell)}{B(\ell)} = -e \int_{-\infty}^{\infty} v_{\parallel} F(\ell, v_{\parallel}) \ \mathrm{d}v_{\parallel} \tag{2.36}$$

Note that f_M does not contribute to j, since the Maxwellian is assumed to be perfectly trapped in the magnetosphere. The factor of $B(\ell)$ naturally arises, and is due to the fact that we are focusing on field-aligned motion.

2.1.4 Current Continuity Constraint

Another constraint on the solution is that of current continuity. All circuits must close - there must be no "end-points" to current density lines, since this would result in a build-up of charge, and our model is quasi-neutral and steady. This is expressed mathematically as

$$\nabla \cdot \mathbf{j} = 0 \tag{2.37}$$

Now, consider a flux tube section of area A_1, magnetic field strength B_1 and parallel current density j_1 at one end, and corresponding values of A_2, B_2 and j_2 at the other. Gauss's Divergence theorem tells us that

$$\int \mathbf{j} \cdot \mathrm{d}\mathbf{S} = \int \nabla \cdot \mathbf{j} \, \mathrm{d}^3V = 0 \tag{2.38}$$

and we also know that

$$\begin{aligned} \int \mathbf{j} \cdot \mathrm{d}\mathbf{S} &= j_1 A_1 - j_2 A_2 \\ \Rightarrow j_1 A_1 &= j_2 A_2 \end{aligned} \tag{2.39}$$

Similarly, it can be shown that the cross-sectional field strength of a flux tube is inversely proportional to the magnetic field strength, since

$$\int \mathbf{B} \cdot \mathrm{d}\mathbf{S} = \int \nabla \cdot \mathbf{B} \, \mathrm{d}^3V = 0 \tag{2.40}$$

Also,

$$\begin{aligned} \int \mathbf{B} \cdot \mathrm{d}\mathbf{S} &= B_1 A_1 - B_2 A_2 \\ \Rightarrow B_1 A_1 &= B_2 A_2 \end{aligned} \tag{2.41}$$

So, we can re-write the current continuity condition using equations (2.39) and (2.41) to give

$$\frac{j_1}{B_1} = \frac{j_2}{B_2} \tag{2.42}$$

From this, we can understand *Swift (1975)*'s observation that the mean electron drift speed, v_e, is proportional to B/n. The current density, j, is related to v_e and the electron number density, n_e, as follows

$$j = -n_e \, e \, v_e \tag{2.43}$$

Multiplying this expression by B/jn_e, we can see that

$$\frac{B}{n_e} = -\frac{eB}{j} v_e \tag{2.44}$$

and equation (2.42) tells us that eB/j is a constant along the field line, and thus

$$\frac{B}{n_e} \propto v_e \tag{2.45}$$

2.2 Model set-up

2.2.1 Boundary conditions

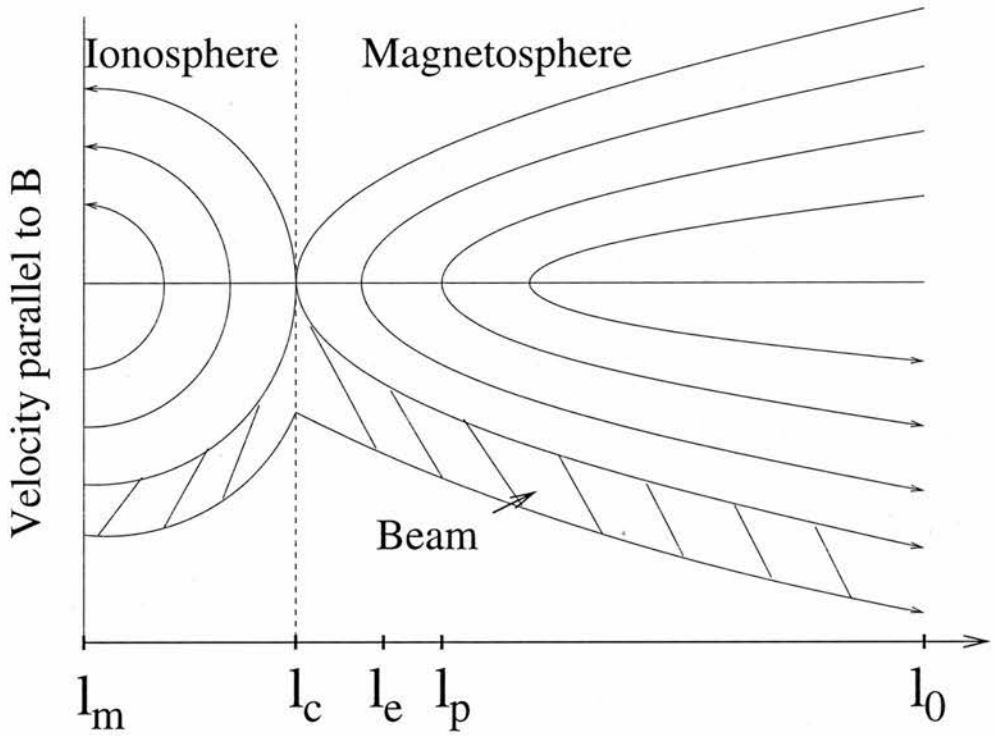

Figure 2.3: This is a schematic of the important locations in the solution along a dipolar field line of the Earth. The point l_m is at the base of the F region; l_c is the ionospheric trapping point, such that all ionospheric electrons except those constituting the beam are trapped between l_m and l_c; the maximum electric field occurs at l_e, below the B/n peak, ℓ_p; and l_0 is a distant point in the magnetosphere.

In this section, we give a brief overview of the model; a schematic of the different electron populations and important locations which emerge from model analysis is given in Figure 2.3. We consider a converging field-aligned flux tube, bounded at one end by the base of the F region, ℓ_m, taken to be at 1 R_E for convenience, and at the other by ℓ_0, a distant point in the magnetosphere taken to be in the equatorial plane. We define anti-Earthward electron populations at ℓ_m and the Earthward population at ℓ_0. The flux tube naturally divides into two regions separated by ℓ_c, the ionospheric electron trapping point contained within the F region. The ionospheric electron population is mostly trapped earthward of ℓ_c, in the region $\ell_c < \ell < \ell_m$, since the solution to the Vlasov equation produces a small ambipolar potential in this region. A small beam of the most energetic ionospheric electrons, although slowed by this ambipolar electric field, manages to escape into the magnetosphere. It penetrates the magnetospheric electron population between $\ell_0 < \ell < \ell_c$, taken to be a mirroring Maxwellian - this models the magnetic mirroring which takes place as a population enters an area of higher magnetic field strength.

The F region defined in terms of ion density extends to ~1000 km, well above ℓ_c, which typically occurs at altitudes of a few hundred km. However, the location of ℓ_c is a natural mathematical dividing

line in our model between the trapped ionospheric population and the mirroring Maxwellian where our two solutions must be matched, so we refer to the region $\ell_c < \ell < \ell_m$ as the "ionosphere", and $\ell_0 < \ell < \ell_c$ as the "magnetosphere".

We impose an ionospheric boundary condition on $F(\ell, v_\parallel)$ at ℓ_m: $F(\ell_m, v_\parallel)$ is a top-hat distribution such that $F(\ell_m, v_\parallel) = F_1, -a_m - \epsilon \leq v_\parallel \leq a_m$, where a_m corresponds to the ionospheric electron thermal velocity width. The section $-a_m \leq v_\parallel \leq a_m$ corresponds to the trapped ionospheric population, and $-a_m - \epsilon \leq v_\parallel < -a_m$ gives the current-carrying beam. We also impose a magnetospheric boundary condition such that $F = F_2$ at ℓ_0 for the mirroring Maxwellian population.

2.2.2 Equations

Ionospheric Equation

We make use of Liouville's theorem, which states that, for a distribution function, f,

$$\left[\frac{\mathrm{d}f}{\mathrm{d}t}\right]_{\text{orbit}} = 0, \tag{2.46}$$

that is, f is constant on an electron trajectory. Following *Temerin and Carlson (1998)*, we assume that a negligible fraction of the Maxwellian magnetospheric electrons penetrates beyond ℓ_c, and that the contribution of these electrons to the field-aligned current is also negligible. These assumptions are justified in Section 2.4.3. Now, the total energy (W_0) of an electron in the ionosphere is given by

$$\begin{aligned} \frac{W_0}{m} &= \frac{v_\parallel^2}{2} - \frac{e\phi(\ell)}{m} \\ &= \frac{v_\parallel^2}{2} - \Phi(\ell) \end{aligned} \tag{2.47}$$

where $\Phi = e\phi/m$ as before. So, if a particular electron has a speed $v_{\parallel m}$ at ℓ_m, where $\Phi = \Phi_m$, we can determine its speed, $v_\parallel$, at any other point:

$$\begin{aligned} \frac{W_0}{m} &= \frac{v_{\parallel m}^2}{2} - \Phi_m \\ &= \frac{v_\parallel^2}{2} - \Phi(\ell) \end{aligned}$$

$$\Rightarrow v_\parallel = \pm\sqrt{v_{\parallel m}^2 + 2\Delta\Phi(\ell)}, \tag{2.48}$$

where $\Delta\Phi(\ell) = \Phi(\ell) - \Phi(\ell_m)$, the change in scaled potential. Thus, if we set $\Delta\Phi(\ell_c) = \Delta\Phi_c = -a_m^2/2$, we trap all of the ionospheric electrons except the current-carrying beam component with $-a_m - \epsilon \leq v_{\parallel m} < -a_m$. At an arbitrary point between ℓ_m and ℓ_c, an electron with initial speed $-(a_m + \epsilon)$ will map to $v_\parallel(\ell) = -\sqrt{(a_m+\epsilon)^2 + 2\Delta\Phi(\ell)}$, and one with initial speed a_m will map to $v_\parallel(\ell) = \sqrt{a_m^2 + 2\Delta\Phi(\ell)}$. Thus, by Liouville's theorem, the distribution at each point is a top-hat distribution such that $F = F_1, -\sqrt{(a_m+\epsilon)^2 + 2\Delta\Phi} \leq v_\parallel \leq \sqrt{a_m^2 + 2\Delta\Phi}$. This is schematically illustrated in Figure 2.3. Since we assume that none of the magnetospheric Maxwellian population enters the ionosphere, we neglect this term in equation (2.35) in order to find the ionospheric number density relation. With the top-hat distribution function described above, the integral in equation (2.35) becomes trivial, and thus

$$\frac{n(\ell)}{B(\ell)} = F_1 \left[\sqrt{(a_m+\epsilon)^2 + 2\Delta\Phi} + \sqrt{a_m^2 + 2\Delta\Phi}\right]. \tag{2.49}$$

Magnetospheric equation

The magnetospheric equation contains a term corresponding to the mirroring isotropic Maxwellian population, and another corresponding to the emerging beam. The Maxwellian population gives a number density of $(F_2/B(\ell))\exp(e\phi/kT)$. The only ionospheric electrons to emerge above ℓ_c are those with velocities in the range $-a_m - \epsilon \leq v_{\parallel m} < -a_m$ at ℓ_m, so they contribute a number density divided by B of

$$\frac{n^*}{B} = F_1 \left[\sqrt{(a_m+\epsilon)^2 + 2\Delta\Phi} - \sqrt{a_m^2 + 2\Delta\Phi}\right], \tag{2.50}$$

giving the relation for charge neutrality in the magnetosphere ($\ell_0 < \ell < \ell_c$) as

$$\frac{n(\ell)}{B(\ell)} = \frac{F_2}{B(\ell)} \exp\left[\frac{m}{kT}(\Delta\Phi + \Phi_m)\right] + F_1 \left[\sqrt{(a_m+\epsilon)^2 + 2\Delta\Phi} - \sqrt{a_m^2 + 2\Delta\Phi}\right]. \tag{2.51}$$

Evaluating constants

We can use the equation for field-aligned current density (2.36) to evaluate the constant F_1 in the ionospheric equation. Now, the trapped ionospheric electrons contribute no net current, since the current carried by upflowing electrons is cancelled by corresponding downflowing ones. So, the only contribution to this current comes from the beam, since the beam electrons have no downflowing counterparts. Thus, at ℓ_m, electrons contributing to the current are those with speeds of $-a_m - \epsilon \leq v_{\parallel m} < -a_m$. So,

$$\begin{aligned} \frac{j_m}{B_m} &= -e \int_{-a_m-\epsilon}^{-a_m} v_\parallel F(\ell, v_\parallel)\, \mathrm{d}v_\parallel \\ &= -eF_1 \int_{-a_m-\epsilon}^{-a_m} v_\parallel\, \mathrm{d}v_\parallel \end{aligned}$$

$$= \frac{eF_1}{2}\left[(a_m+\epsilon)^2 - a_m^2\right] \tag{2.52}$$

From this, we can deduce that

$$F_1 = \frac{j_m}{eB_m\epsilon\left(a_m+\frac{\epsilon}{2}\right)} \tag{2.53}$$

We can find the magnetospheric constant F_2 by evaluating the magnetospheric equation at ℓ_0, where $\Delta\Phi(\ell_0) = -\Phi_m$, the normalised potential at ℓ_m:

$$\frac{n_0}{B_0} = \frac{F_2}{B_0} + F_1\left[\sqrt{(a_m+\epsilon)^2 - 2\Phi_m} - \sqrt{a_m^2 - 2\Phi_m}\right] \tag{2.54}$$

$$\Rightarrow F_2 = n_0 - \frac{j_m B_0}{eB_m\epsilon\left(a_m+\frac{\epsilon}{2}\right)}\left[\sqrt{(a_m+\epsilon)^2 - 2\Phi_m} - \sqrt{a_m^2 - 2\Phi_m}\right] \tag{2.55}$$

The above constitutes the exact solution. We can also obtain an accurate approximate expression by observing that $a_m^2 - 2\Phi_m \gg \epsilon a_m$. This tells us that

$$\sqrt{(a_m+\epsilon)^2 - 2\Phi_m} - \sqrt{a_m^2 - 2\Phi_m} \approx \frac{a_m\epsilon}{\sqrt{a_m^2 - 2\Phi_m}} \tag{2.56}$$

Thus,

$$F_2 \approx n_0 - \frac{j_m B_0}{eB_m\left(1+\frac{\epsilon}{2a_m}\right)\sqrt{a_m^2 - 2\Phi_m}} \tag{2.57}$$

So, we obtain the following exact solutions. In the ionosphere,

$$\frac{n(\ell)}{B(\ell)} = \frac{j_m}{eB_m\epsilon\left(a_m+\frac{\epsilon}{2}\right)}\left[\sqrt{(a_m+\epsilon)^2 + 2\Delta\Phi} + \sqrt{a_m^2 + 2\Delta\Phi}\right], \tag{2.58}$$

and in the magnetosphere,

$$\begin{aligned}\frac{n(\ell)}{B(\ell)} &= \frac{1}{B(\ell)}\left[n_0 - \frac{j_m B_0}{eB_m\left(1+\frac{\epsilon}{2a_m}\right)\sqrt{a_m^2 - 2\Phi_m}}\right]\exp\left[\frac{m}{kT}\left(\Delta\Phi + \Phi_m\right)\right] \\ &\quad + \frac{j_m}{eB_m\epsilon\left(a_m+\frac{\epsilon}{2}\right)}\left[\sqrt{(a_m+\epsilon)^2 + 2\Delta\Phi} - \sqrt{a_m^2 + 2\Delta\Phi}\right]\end{aligned} \tag{2.59}$$

Non-dimensionalising the equations

We wish to express the ionospheric and magnetospheric equations (2.58) and (2.59) in terms of dimensionless parameters. We substitute the expression for F_1 in equation (2.53) into (2.35) and evaluate it at ℓ_m, noting that we assume that there are no Maxwellian electrons in the ionosphere, to give

$$\frac{n_m}{B_m} = \frac{2j_m}{eB_m\epsilon} \tag{2.60}$$

From this, we can deduce an expression for the beam width, ϵ:

$$\epsilon = \frac{2j_m}{n_m e} \tag{2.61}$$

Thus, as the current density increases, so does the beam width, as more current-carrying electrons will be required; as the ionospheric number density increases, the beam width decreases proportionally to carry the same current.

There are four characteristic electron speeds or energies in this model: a_m and ϵ, the ionospheric background and beam thermal velocity widths at ℓ_m; kT, the thermal energy of the background magnetospheric population at ℓ_0; and $v^*(\ell_0) = -\sqrt{a_m^2 - 2\Phi_m}$, the parallel velocity of the beam at ℓ_0. These four characteristic speeds and energies can be expressed succinctly in terms of three dimensionless ratios with which we may reformulate our equations. Firstly, we define $\alpha = \epsilon/(2a_m)$, the ratio of the beam width in velocity space to the trapped ionospheric population width, $2a_m$. Thus, using equation (2.61),

$$\alpha = \frac{j_m}{n_m e a_m} \tag{2.62}$$

and α corresponds to a normalised current density. Now, we can use equations (2.50) and (2.53) to find a relation for n^*, the beam number density:

$$\frac{n^*}{B} = \frac{j_m}{eB_m\epsilon\left(a_m + \frac{\epsilon}{2}\right)}\left(\sqrt{(a_m+\epsilon)^2 + 2\Delta\Phi} - \sqrt{a_m^2 + 2\Delta\Phi}\right) \tag{2.63}$$

and v^*, the average velocity of the beam, using equation (2.48):

$$v^* = -\frac{1}{2}\left(\sqrt{(a_m+\epsilon)^2 + 2\Delta\Phi} + \sqrt{a_m^2 + 2\Delta\Phi}\right) \tag{2.64}$$

Now, the current density, j, can be expressed as

$$j(\ell) = -n^*(\ell)ev^*(\ell) \tag{2.65}$$

Evaluating this at ℓ_m tells us that $j_m \approx n_m^* e a_m$, where $n_m^* = n^*(\ell_m)$. Thus, we can deduce that $\alpha \approx n_m^*/n_m$, the ratio of the beam number density to the total ionospheric electron number density at ℓ_m. For downward currents, α is positive, and typically lies in the range 10^{-5}-10^{-3}. The second dimensionless parameter we introduce is

$$\eta = \frac{m a_m^2}{2kT} \tag{2.66}$$

representing the ratio of the kinetic energy of the ionospheric electron population to the thermal energy of the magnetospheric electron population. This again is a small parameter: ionospheric electron temperatures are generally $\sim$1 eV, whilst magnetospheric electron temperatures can vary from $\sim$100 eV to several keV. Thus, η is typically of the order of 10^{-4}-10^{-2}. Tables 2.1 and 2.2 below show how the dimensionless parameters α and η relate to the physical properties of the model. The third, and final, normalised parameter we define relates to the electric potential difference, so that

$$\Delta\tilde{\Phi} = \frac{\Delta\Phi}{a_m^2/2} \tag{2.67}$$

and

$$\tilde{\Phi} = \frac{2e\phi}{m a_m^2} \tag{2.68}$$

Thus, substituting the average beam velocity v^* into equation (2.48) with $v_{\parallel m}^* \approx a_m$, $\Delta\tilde{\Phi} \approx v^{*2}(\ell)/a_m^2 - 1$. Using these dimensionless parameters, we obtain the non-dimensionalised equations for the ionosphere and magnetosphere respectively:

$$\frac{n(\ell)}{B(\ell)} \Big/ \frac{n_0}{B_0} = A\left(\sqrt{(1+2\alpha)^2 + \Delta\tilde{\Phi}} + \sqrt{1+\Delta\tilde{\Phi}}\right) \tag{2.69}$$

$$\begin{aligned} \frac{n(\ell)}{B(\ell)} \Big/ \frac{n_0}{B_0} &= A\left(\sqrt{(1+2\alpha)^2 + \Delta\tilde{\Phi}} - \sqrt{1+\Delta\tilde{\Phi}}\right) \\ &\quad + \frac{B_0}{B(\ell)}(1 - AC)\exp\left(\eta\left(\Delta\tilde{\Phi} + \tilde{\Phi}_m\right)\right), \end{aligned} \tag{2.70}$$

where

$$A = \left(\frac{n_m}{n_0}\right)\left(\frac{B_0}{B_m}\right)\frac{1}{2(1+\alpha)}. \tag{2.71}$$

$$C = \sqrt{(1+2\alpha)^2 - \tilde{\Phi}_m} - \sqrt{1 - \tilde{\Phi}_m} \tag{2.72}$$

Table 2.1: Table showing variation of $\alpha = j_m/(n_m e a_m)$ with j_m and a_m. The current density j_m can vary between $\sim$1 and 10 $\mu\mathrm{Am}^{-2}$; n_m is generally 10^{12} m^{-3}; and $ma_m^2/2$ typically ranges from 1 to 5 eV.

$j_m(\mathrm{Am}^{-2})$	$ma_m^2/2$ (eV)	α (3sf)
1×10^{-6}	1	1.05×10^{-5}
1×10^{-6}	3	6.08×10^{-6}
1×10^{-6}	5	4.71×10^{-6}
5×10^{-6}	1	5.26×10^{-5}
5×10^{-6}	3	3.04×10^{-5}
5×10^{-6}	5	2.35×10^{-5}
1×10^{-5}	1	1.05×10^{-4}
1×10^{-5}	3	6.08×10^{-5}
1×10^{-5}	5	4.71×10^{-5}

Table 2.2: Table showing variation of η with a_m and kT. The ionospheric temperature, $ma_m^2/2$ generally ranges from 1 to 5 eV, whilst the magnetospheric temperature is significantly larger, ranging from $\sim$100 eV to 3 keV.

$ma_m^2/2$ (eV)	kT (eV)	η (3sf)
1	100	1×10^{-2}
3	100	3×10^{-2}
5	100	5×10^{-2}
1	1000	1×10^{-3}
3	1000	3×10^{-3}
5	1000	5×10^{-3}
1	3000	3.33×10^{-4}
3	3000	1×10^{-3}
5	3000	1.67×10^{-3}

2.3 Results

2.3.1 Potential variation

It is possible to solve the ionospheric and magnetospheric equations (2.69) and (2.70) numerically to obtain the variation of potential along the fieldline. To do this, we assume the following parameter values: $n_m = 10^{12}$ m^{-3}, $n_m/n_0 = 10^6$, $B_m/B_0 = 1923.54$, $ma_m^2/2 \sim 1$ eV (giving $a_m = 5.93 \times 10^5$ m/s), and $kT \sim 1$ keV. The current density j_m can vary from ~1-10 μAm^{-2}, giving a range for $\alpha = j_m/(n_m e a_m)$ of $\sim 1.05\times10^{-5}$-1.05×10^{-4}. The other dimensionless parameter $\eta = ma_m^2/2kT$ is the ratio of the thermal energies of the ionosphere and magnetosphere: we take this to range from 10^{-4}, where the ionospheric and magnetospheric thermal energies are 1 eV and 10 keV respectively, to 10^{-2}, where corresponding values are 1 eV and 100 eV.

As noted by *Temerin and Carlson (1998)*, the solution for $\Delta\tilde{\Phi}$ is multi-valued in the magnetosphere, but only the continuous, monotonically-increasing solution is physically viable. This is because it is the only solution to satisfy our boundary conditions, and it is the only profile for which the expression employed for the Maxwellian electron number density in equation (2.70) is valid. The solutions to magnetospheric equation (2.70) are discussed further in Chapter 3.

Figure 2.4 shows a typical potential variation for $\alpha = 5 \times 10^{-5}$ and $\eta = 10^{-3}$, which corresponds to ionospheric and magnetospheric temperatures of 1 eV and 1 keV respectively. The solution has some interesting characteristic features, which centre around the B/n peak and points we call ℓ_c and ℓ_e. The bound ionospheric electrons are trapped below ℓ_c, and above it we have the magnetospheric electrons and the current-carrying ionospheric beam component. Thus, l_c corresponds to the ionospheric trapping point. The maximum parallel electric field occurs at ℓ_e. In this case, ℓ_c is found at $s/R_E = 0.0826$, implying an ionospheric trapping point at an altitude of 526 km; ℓ_e is found at $s/R_E = 0.240$, giving a height of 1530 km; and the B/n peak, found from the equilibrium model, occurs at $s/R_E = 0.273$, at an altitude of 1740 km.

The numerical solutions of equations (2.69) and (2.70) are accurate to 10^{-6}. The roots of ionospheric equation (2.69) were found using the bisection method. The roots of magnetospheric equation (2.70) were generally found using the Newton-Raphson method, as this generally converges more quickly than the bisection method. However, the bisection method proved to be necessary beyond ℓ_c until $\Delta\tilde{\Phi} > -0.5$, since the gradients of the magnetospheric function in equation (2.70) were large in this region and the Newton-Raphson method failed to find the roots. This feature can be seen in Figure 3.3.

The potential increase in the magnetosphere performs two tasks in this model. At altitudes immediately above ℓ_c, the electrons are predominantly ionospheric upward beam electrons. In this region, significantly below the B/n peak, the ion number density decays exponentially with altitude, whereas the current density $j \propto B \propto r^{-3}$ decays more slowly. This information, along with equation (2.65), tells us that since the beam number density, n^*, is approximately equal to the ion number density here, the beam must travel more quickly to carry the required current. The potential increase continues to accelerate the electrons, whilst also having an effect on the magnetospheric Maxwellian electron population. The increasing magnetic field

strength experienced by the magnetospheric electrons as they travel Earthward does mirror some, but the existence of a large potential barrier has the effect of excluding almost all of them from the ionospheric ambipolar region. Obviously any electrons which do enter that region will precipitate and form a counterstreaming beam, neglected in this calculation. The effect is negligible in the vast majority of cases (see Section 2.4.3).

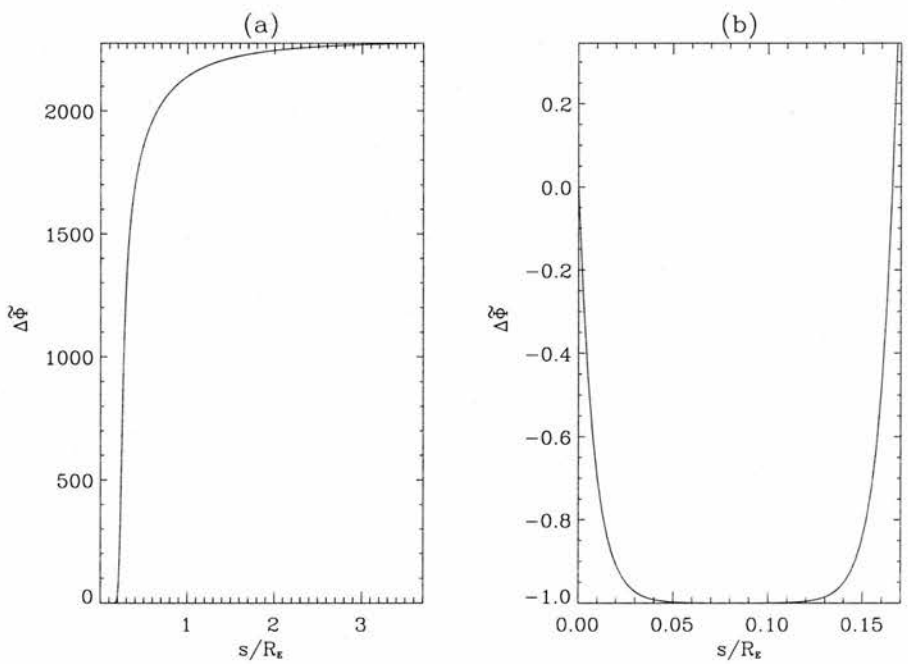

Figure 2.4: Solution curve for $\alpha = 5 \times 10^{-5}$, where $\Delta\tilde{\Phi} = -2283$. Graph (a) shows the total potential variation along the fieldline, while (b) focuses on the small ionospheric ambipolar potential.

2.3.2 Ionospheric trapping point, ℓ_c

One property that emerges naturally from this model is the ionospheric trapping point, ℓ_c, the point where the beam emerges from the ionosphere into the magnetosphere and Earthward of which all trapped ionospheric electrons are found. At ℓ_c, $\Delta\tilde{\Phi} = -1$, so, using the ionospheric equation (2.69), we obtain

$$\begin{aligned}\left(\frac{n_c}{B_c}\Big/\frac{n_0}{B_0}\right) &= \left(\frac{n_m}{n_0}\right)\left(\frac{B_0}{B_m}\right)\frac{1}{2(1+\alpha)}\sqrt{(1+2\alpha)^2-1} \\ &= \left(\frac{n_m}{n_0}\right)\left(\frac{B_0}{B_m}\right)\sqrt{\frac{\alpha}{\alpha+1}}\end{aligned} \tag{2.73}$$

For $\alpha \ll 1$, we can simplify this to

$$\left(\frac{n_c}{B_c}\Big/\frac{n_0}{B_0}\right) = \left(\frac{n_m}{n_0}\right)\left(\frac{B_0}{B_m}\right)\sqrt{\alpha} \tag{2.74}$$

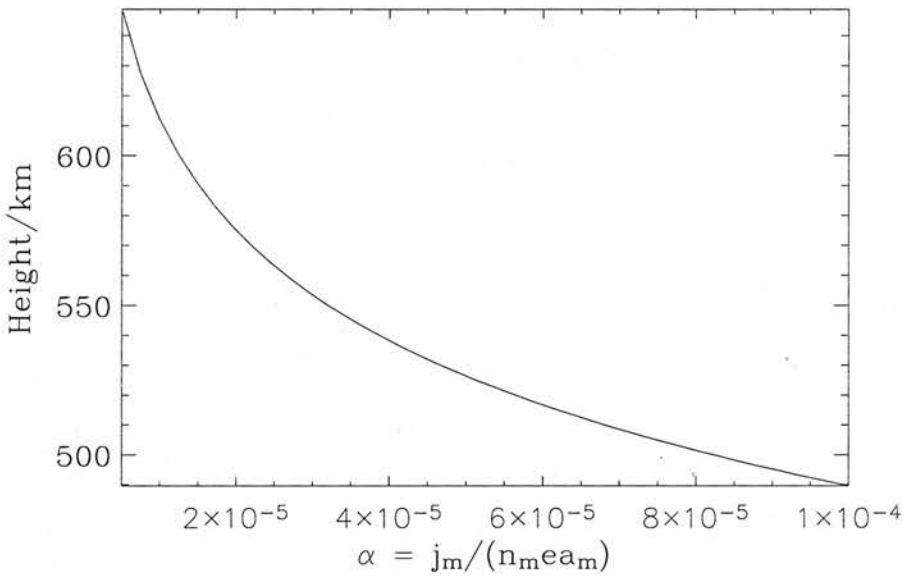

Figure 2.5: Variation of ionospheric trapping point, ℓ_c, for applicable values of α. Our model gives heights from 500-650 km.

From this equation, we can find the value of n_c/B_c for a given α, and then use the form of B/n (see Figure 2.2) to find the height to which this corresponds. There will always be two possible heights, one before and one after the B/n peak. However, we can show that ℓ_c always lies before the peak (see following section). Figure 2.5 shows that typical beam emergence heights obtained from our model range from 500-650 km. It is interesting to note that the location of ℓ_c is unaffected by η i.e. by the ratio of ionospheric to magnetospheric electron temperatures.

From equation (2.74), we can see that

$$\left(\frac{n_c}{B_c}\Big/\frac{n_0}{B_0}\right) = \frac{B_0}{B_m}\sqrt{\frac{j_m n_m}{e a_m n_0^2}} \tag{2.75}$$

So, as the ionospheric thermal velocity a_m increases, n_c/B_c decreases, giving a higher ionospheric trapping point, whilst as the current density j_m or ionospheric number density n_m increase, so does n_c/B_c, implying a lower ionospheric trapping point. This agrees with Temerin and Carlson's observation that for larger currents the ambipolar field must go to zero at larger ionospheric densities (i.e. at lower altitudes) to supply sufficient current-carrying electrons.

Proof that ℓ_c is Earthward of B/n peak

Earthward of ℓ_c, the ionospheric equation in (2.69) is valid. Taking the derivative of this equation with respect to s, we obtain

$$\frac{\mathrm{d}}{\mathrm{d}s}\left(\frac{n}{B}\Big/\frac{n_0}{B_0}\right) = \frac{A}{2}\left[\left((1+2\alpha)^2+\Delta\tilde{\Phi}\right)^{-1/2}+\left(1+\Delta\tilde{\Phi}\right)^{-1/2}\right]\frac{\mathrm{d}\Delta\tilde{\Phi}}{\mathrm{d}s} \tag{2.76}$$

We use s instead of ℓ as we are considering behaviour close to the Earth. Now, since $\Delta\tilde{\Phi}(\ell_c) = \Delta\tilde{\Phi}_c = -1$, we cannot evaluate this derivative directly at ℓ_c, so we expand around $\Delta\tilde{\Phi} = \Delta\tilde{\Phi}_c + \delta\tilde{\Phi} = -1 + \delta\tilde{\Phi}$. Substituting this into equation (2.76) yields

$$\frac{\mathrm{d}}{\mathrm{d}s}\left(\frac{n}{B}\Big/\frac{n_0}{B_0}\right) = \frac{A}{2}\left[\left(4\alpha(\alpha+1)+\delta\tilde{\Phi}\right)^{-1/2}+\delta\tilde{\Phi}^{-1/2}\right]\frac{\mathrm{d}\Delta\tilde{\Phi}}{\mathrm{d}s} \tag{2.77}$$

In all applicable cases, $\alpha > 0$, which tells us that $4\alpha(\alpha+1) > 0$. Also, since there is a minimum in the potential variation at ℓ_c, $\delta\tilde{\Phi} > 0$. So, the expression in square brackets in equation (2.77) is also positive. We also know that $\mathrm{d}\Delta\tilde{\Phi}/\mathrm{d}s < 0$, since we are slightly Earthward of the potential minimum. Thus, we can deduce that

$$\frac{\mathrm{d}}{\mathrm{d}s}\left(\frac{n}{B}\Big/\frac{n_0}{B_0}\right) < 0 \tag{2.78}$$

Earthward of ℓ_c.

Beyond ℓ_c, we must use the magnetospheric equation (2.70). If we again expand the expression around ℓ_c, we can use the fact the beam number density is much greater than the mirroring Maxwellian number density here, and simplify (2.70) to

$$\frac{n}{B}\Big/\frac{n_0}{B_0} \approx A\left(\sqrt{(1+2\alpha)^2+\Delta\tilde{\Phi}}-\sqrt{1+\Delta\tilde{\Phi}}\right) \tag{2.79}$$

Taking the derivative of this and using the same expansion as before,

$$\frac{\mathrm{d}}{\mathrm{d}s}\left(\frac{n}{B}\Big/\frac{n_0}{B_0}\right) \approx \frac{A}{2}\left[\left(4\alpha(\alpha+1)+\delta\tilde{\Phi}\right)^{-1/2}-\delta\tilde{\Phi}^{-1/2}\right]\frac{\mathrm{d}\Delta\tilde{\Phi}}{\mathrm{d}s} \tag{2.80}$$

It is still true that $4\alpha(\alpha+1) > 0$ and $\delta\tilde{\Phi} > 0$ (since we are now on the other side of the potential minimum), so we can see that as the minimum is approached ($\delta\tilde{\Phi} \to 0$)

$$\left(4\alpha(\alpha+1)+\delta\tilde{\Phi}\right)^{-1/2} < \delta\tilde{\Phi}^{-1/2}, \tag{2.81}$$

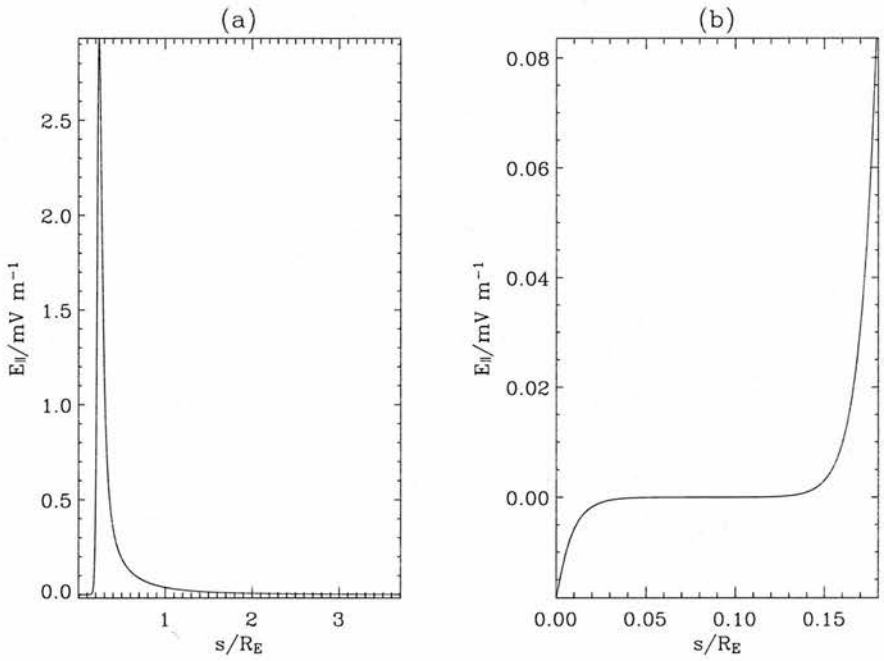

Figure 2.6: Variation of $E_\parallel$ along the field line for $\alpha = 5 \times 10^{-5}$, $\eta = 10^{-3}$ and an ionospheric temperature of 1 eV. $E_{\parallel \max}$ is 2.93 mV/m, and occurs between ℓ_c and the B/n peak at $s/R_E = 0.240$ (1530 km). Graph (b) shows the form of the small ambipolar electric field ($s/R_E < 0.03$) which traps most of the ionospheric electron population.

so

$$\left(4\alpha(\alpha+1) + \delta\tilde{\Phi}\right)^{-1/2} - \delta\tilde{\Phi}^{-1/2} < 0 \tag{2.82}$$

and the square bracket in equation (2.80) is negative. On this side of the minimum, $\mathrm{d}\Delta\tilde{\Phi}/\mathrm{d}s > 0$, and thus (2.80) yields

$$\frac{\mathrm{d}}{\mathrm{d}s}\left(\frac{n}{B}\Big/\frac{n_0}{B_0}\right) < 0 \tag{2.83}$$

beyond ℓ_c as well. Thus, we know that ℓ_c must lie Earthward of the B/n peak, since n/B is a decreasing function of s here.

2.3.3 $E_\parallel$ peak, ℓ_e

There is a maximum in the parallel electric field, $E_\parallel(\ell_e) = E_{\parallel \max}$, which occurs between ℓ_c and the B/n peak, near the start of the acceleration region: it is needed to provide acceleration over a scale comparable to the density scale height. Using equations (2.33) and (2.68), we know that

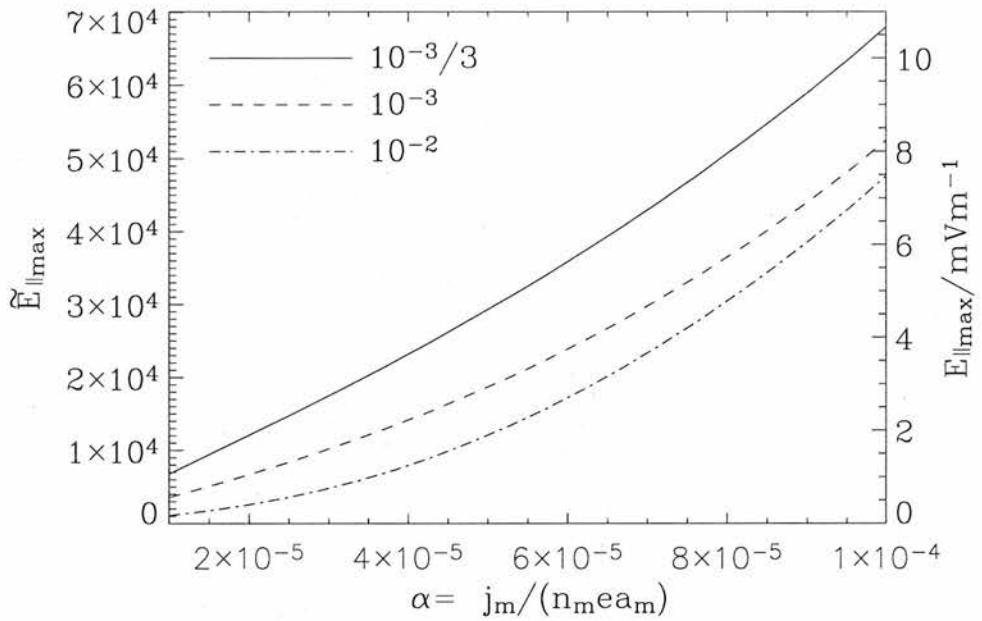

Figure 2.7: Variation of the maximum $\tilde{E}_{\parallel}$ with α and three different values of η. $E_{\parallel \max}$ is shown in mV/m for an ionospheric electron temperature of 1 eV. In this case, the magnetospheric electron temperatures are 3 keV (solid), 1 keV (dashed) and 100 eV (dot-dashed).

$$E_{\parallel} = -\frac{ma_m^2}{2eR_E}\frac{\partial \Delta\tilde{\Phi}}{\partial(\ell/R_E)}$$

From this, we can define a normalised parallel electric field, $\tilde{E}_{\parallel}$, such that

$$\tilde{E}_{\parallel} = \frac{2eR_E}{ma_m^2}E_{\parallel} = -\frac{\partial \Delta\tilde{\Phi}}{\partial(\ell/R_E)} \tag{2.84}$$

This electric field can be found numerically, and a typical result is shown in Figure 2.6. Figure 2.7 shows the variation of $\tilde{E}_{\parallel \max}$ with α and η, and the corresponding $E_{\parallel \max}$ variation for a specific ionospheric electron temperature of 1 eV, and three magnetospheric electron temperatures of 100 eV, 1 keV and 3 keV. $E_{\parallel \max}$ extends up to 10 mV/m. As the current density, or α, increases, more acceleration is needed; therefore $E_{\parallel \max}$ increases.

The location of ℓ_e is beyond the ionospheric trapping point, ℓ_c, and within three density scale heights of the B/n peak. As the current density increases, ℓ_e is found to move Earthward, as quasi-neutrality dictates that acceleration is needed closer to ℓ_c. As the magnetospheric electron temperature increases (causing a decrease in η), ℓ_e moves closer to the B/n peak, indicating the importance of the electric field for reflecting magnetospheric electrons to make room for the current-carrying ionospheric beam electrons.

2.3.4 Beam Characteristics

As seen from the potential curve in Figure 2.4, the acceleration takes place mainly around the B/n peak. The beam velocity, v^*, previously defined in equation (2.64), is the average velocity of the current-carrying ionospheric electrons, and can be expressed as

$$v^* = -\frac{a_m}{2}\left[\sqrt{(1+2\alpha)^2 + \Delta\tilde{\Phi}} + \sqrt{1+\Delta\tilde{\Phi}}\right], \tag{2.85}$$

where v^{*2} shows the same trend as the potential, as expected from energy conservation. The beam is slowed down by the small ambipolar potential as it travels through the ionosphere, but manages to escape to the magnetosphere and is quickly accelerated by the sharp potential increase around the B/n peak. The beam number density, however, shows a different trend. It peaks sharply at ℓ_c, since the beam is slowed down to its lowest speed here. This is the point where it just escapes being trapped like the remainder of the ionospheric electrons. At ℓ_c, $\Delta\tilde{\Phi} = -1$, and thus the average beam speed, v_c^*, is given by

$$\begin{aligned} v_c^* &= -\frac{a_m}{2}\sqrt{(1+2\alpha)^2 - 1} \\ &= -a_m\sqrt{\alpha(\alpha+1)} \end{aligned} \tag{2.86}$$

Since $\alpha \ll 1$, we can say that $v_c^* \approx -a_m\sqrt{\alpha}$. Thus, in our typical test case where $\alpha = 5\times10^{-5}$ and $\eta = 10^{-3}$, the beam is slowed down to $v_c^* = -0.00707\ a_m$. So, in order for the beam to carry its current, the number density of the beam must increase sharply to compensate for the lack of speed. We can show this from the equation for the beam number density given below. This is found by substituting equations (2.53), (2.61) and (2.62) into the expression in equation (2.50).

$$\frac{n^*}{B}\Big/\frac{n_0}{B_0} = \left(\frac{n_m}{n_0}\right)\left(\frac{B_0}{B_m}\right)\frac{1}{2(1+\alpha)}\left[\sqrt{(1+2\alpha)^2+\Delta\tilde{\Phi}} - \sqrt{1+\Delta\tilde{\Phi}}\right]. \tag{2.87}$$

From this, we can deduce that

$$\frac{\mathrm{d}}{\mathrm{d}s}\left(\frac{n^*}{B}\Big/\frac{n_0}{B_0}\right) = \frac{A}{2}\left[\left((1+2\alpha)^2+\Delta\tilde{\Phi}\right)^{-\frac{1}{2}} - \left(1+\Delta\tilde{\Phi}\right)^{-\frac{1}{2}}\right]\frac{\mathrm{d}\Delta\tilde{\Phi}}{\mathrm{d}s} \tag{2.88}$$

This cannot be directly evaluated at ℓ_c, since $\Delta\tilde{\Phi} = -1$ there, so we substitute in $\Delta\tilde{\Phi} = -1 + \delta\tilde{\Phi}$ to obtain

$$\frac{\mathrm{d}}{\mathrm{d}s}\left(\frac{n^*}{B}\Big/\frac{n_0}{B_0}\right) = \frac{A}{2}\left[\left(4\alpha(\alpha+1)+\delta\tilde{\Phi}\right)^{-\frac{1}{2}} - \delta\tilde{\Phi}^{-\frac{1}{2}}\right]\frac{\mathrm{d}\Delta\tilde{\Phi}}{\mathrm{d}s} \tag{2.89}$$

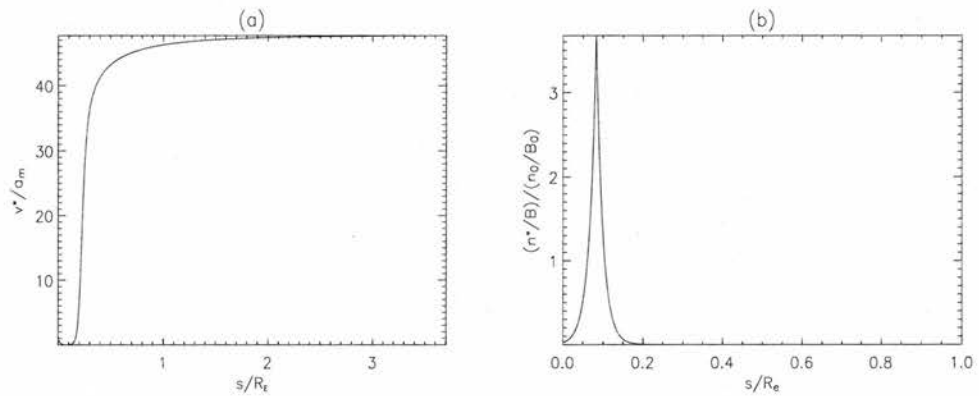

Figure 2.8: Beam characteristics for $\alpha = 5 \times 10^{-5}$ and $\eta = 10^{-3}$: (a) the beam velocity varies as the potential, as expected; and (b) the n^*/B curve shows a sharp peak at ℓ_c.

On either side of ℓ_c, $\alpha > 0$ and $\delta\tilde{\Phi} > 0$ since $\Delta\tilde{\Phi}$ has a minimum at ℓ_c; this tells us that the expression in square brackets is always negative. Earthward of ℓ_c, $\mathrm{d}\Delta\tilde{\Phi}/\mathrm{d}s < 0$, so the left hand side is positive. Beyond ℓ_c, $\mathrm{d}\Delta\tilde{\Phi}/\mathrm{d}s > 0$ and the left hand side is negative. Thus, n^*/B decreases on moving Earthward of ℓ_c and also decreases beyond it, indicating a maximum value, n_c^*/B, at ℓ_c given by

$$\frac{n_c^*}{B_c}\Big/\frac{n_0}{B_0} = \left(\frac{n_m}{n_0}\right)\left(\frac{B_0}{B_m}\right)\sqrt{\frac{\alpha}{\alpha+1}} \tag{2.90}$$

This can also be seen by substituting $\Delta\tilde{\Phi} = -1 + \delta\tilde{\Phi}$ into equation (2.87), assuming that $\delta\tilde{\Phi} \ll 4\alpha(\alpha+1)$, to obtain

$$\begin{aligned}
\frac{n^*}{B}\Big/\frac{n_0}{B_0} &= \left(\frac{n_m}{n_0}\right)\left(\frac{B_0}{B_m}\right)\frac{1}{2\,(1+\alpha)}\left(\sqrt{4\alpha(\alpha+1)+\delta\tilde{\Phi}} - \sqrt{\delta\tilde{\Phi}}\right) \\
&= \left(\frac{n_m}{n_0}\right)\left(\frac{B_0}{B_m}\right)\sqrt{\frac{\alpha}{\alpha+1}}\left(1 + \frac{\delta\tilde{\Phi}}{8\alpha(\alpha+1)} - \sqrt{\frac{\delta\tilde{\Phi}}{4\alpha(\alpha+1)}}\right) \\
&\approx \frac{n_c^*}{B_c}\Big/\frac{n_0}{B_0}\left(1 - \sqrt{\frac{\delta\tilde{\Phi}}{4\alpha(\alpha+1)}}\right)
\end{aligned} \tag{2.91}$$

This expression shows the local behaviour of n^*/B for small changes in potential: it shows that the beam number density (divided by B) maximises at ℓ_c.

The beam velocity increases all the way through the magnetosphere, as the current-carrying electrons are accelerated by the potential. It reaches its largest value, v_0^*, at the equatorial end of the field line, which is found by substituting $\Delta\tilde{\Phi} = -\tilde{\Phi}_m$ into equation (2.85) to give

$$v_0^* = -\frac{a_m}{2}\left[\sqrt{(1+2\alpha)^2 - \tilde{\Phi}_m} + \sqrt{1-\tilde{\Phi}_m}\right] \tag{2.92}$$

Now, since $\alpha \ll 1$ and $-\tilde{\Phi}_m \gg 1$, we can write

$$v_0^* \approx -a_m\sqrt{1-\tilde{\Phi}_m} \tag{2.93}$$

$$\Rightarrow v_0^* \approx -a_m\sqrt{-\tilde{\Phi}_m} \tag{2.94}$$

Hence, in our typical case, where $\tilde{\Phi}_m = -2283.0$, we have $v_0^* \approx 48.0\ a_m$, corresponding to an electron energy gain of 2283.0 eV.

2.3.5 Width of acceleration region, Ω

The distance over which the potential increase occurs depends on the parameters α and η. In order to get an idea of the trends involved, we define the acceleration region to start at the point where $\Delta\tilde{\Phi} = 0$ beyond ℓ_c (since the increase from ℓ_c, where $\Delta\tilde{\Phi} = -1$, to the point where $\Delta\tilde{\Phi} = 0$ is gradual) and to end where $\Delta\tilde{\Phi} = -0.8\ \tilde{\Phi}_m$. We define Ω to be the distance between these two points, giving a measure of the width of the acceleration region. This parameter gives an idea of how localised the potential increase is.

The results are shown in Figure 2.9. Typically, the acceleration occurs over a few thousand kilometres. As the current density increases, Ω decreases, despite the fact that the overall potential increase gets larger: this implies a much smaller, more concentrated acceleration region surrounding the B/n peak. As the magnetospheric electron temperature increases (indicating a decrease in η), Ω increases too. This implies that the acceleration region is not so concentrated. Much of the energisation will still occur over a small distance around the B/n peak, but some of it extends further into the magnetosphere. This performs a useful role: since the magnetospheric Maxwellian electrons are now more energetic, the presence of an increased potential difference in the magnetosphere has the effect of mirroring more of these electrons so that they do not penetrate too deeply into the acceleration region. This will enable matching of the electron and ion number densities along the field line.

Whilst observations do indicate the presence of double layers *(Ergun et al. (2003a))*, where considerable electron acceleration can occur over very small distances of $\sim$10 km, our model gives insight into the system as a whole. So, in reality, the potential distribution along the field line may be different to our theoretical potential variation, with sharp bursts of acceleration at several points along the field line, but the overall potential difference should be very similar.

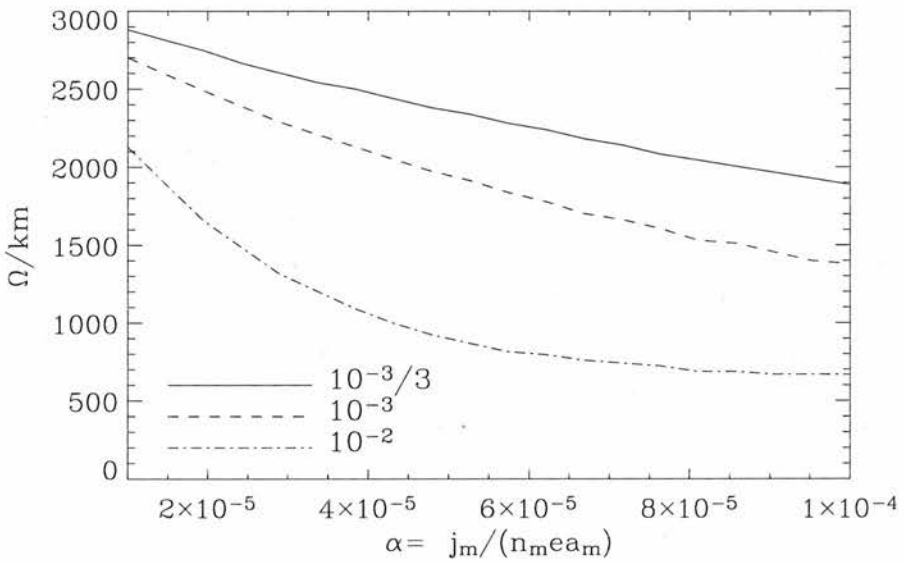

Figure 2.9: Variation of the width of the acceleration region, Ω, with α and three different values of η. Assuming an ionospheric electron temperature of 1 eV, these η values correspond to magnetospheric electron temperatures of 3 keV (solid), 1 keV (dashed) and 100 eV (dot-dashed). The density scale height is taken to be 100 km.

2.3.6 Significance of B/n peak

The ion number density profile chosen in this model is obviously vital to the solution of equations (2.69) and (2.70), since the total electron density must match this profile to satisfy quasi-neutrality. Hence, it would be reasonable to think that altering the ion number density profile must have an effect upon $\tilde{\Phi}_m$, the total potential difference along the field line. However, it turns out that only the number density in the vicinity of the B/n peak is vital to the overall solution of the equations, and hence, to $\tilde{\Phi}_m$.

To illustrate this, we altered the number density profile given in equation (2.11) on either side of the B/n peak, defining a new density profile, n_1. The alteration is shown in Figure 2.10, where $\delta n = \mid n_1 - n \mid$, the difference between the two number density profiles. The only constraint when changing the ion density profile is that it is necessary to preserve the single peak in the B/n curve and the boundary values at ℓ_m and ℓ_0. If the B/n curve has multiple peaks, the potential profile obtained from the model is no longer monotonic in the magnetosphere, giving an unphysical result. This constraint allows for large changes in number density Earthward of the B/n peak, but is more limiting beyond it. Hence, $\delta n/n \sim 10^{-3}$ is the largest change possible beyond the B/n peak, since n/n_0 only decreases from 1.04 to 1.00 between the B/n peak and ℓ_0. It is somewhat surprising that the total potential drop, $\tilde{\Phi}_m$, calculated for the original density profile and the modified one are identical to the accuracy of our numerical solution (at least 5 significant figures).

The change to the number density profile beyond the B/n peak may seem very small, suggesting that

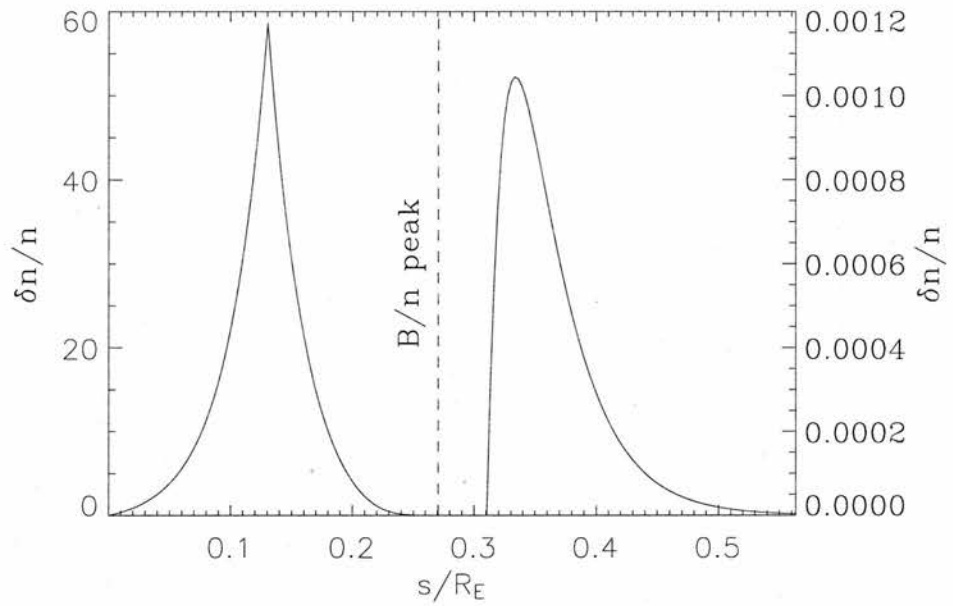

Figure 2.10: Alteration to ion number density. This alteration can be much larger on the Earthward side of the B/n peak whilst still retaining a single B/n peak, whereas the alteration beyond the B/n peak is more restricted by this condition. This change in density profile results in no change to $\tilde{\Phi}_m$, illustrating the importance of the region surrounding the B/n peak to finding this total potential difference.

no significant change in $\tilde{\Phi}_m$ will result. However, when we alter the number density at, rather than either side of, the B/n peak such that $\delta n/n \sim 10^{-3}$ in this region, we do obtain a significant relative change in $\tilde{\Phi}_m \sim 10^{-3}$-$10^{-2}$. These results demonstrate that the properties of the small region surrounding the B/n peak ($\sim$ a few density scale heights) are solely responsible for determining $\tilde{\Phi}_m$.

2.3.7 Comparison with Temerin and Carlson Model

Since our model is an extension of that by *Temerin and Carlson (1998)*, we tested our model using the example they cite, the results of which are given in their Figure 1. We used all of the same parameters, and an identical ion number density distribution. Our model starts at ℓ_m, the base of the F region, while the Temerin and Carlson model begins at ℓ_c, the point where the ambipolar electric field goes to zero. To compare with their model, we chose our boundary conditions and equilibrium between ℓ_m and ℓ_c such that our solution at ℓ_c coincides exactly with the boundary conditions that Temerin and Carlson imposed there.

The field-aligned coordinate used is $b = B/B_c$, where B_c represents the magnetic field strength at ℓ_c, and b extends from 0 (an idealised distant point in the magnetosphere) to 1 at ℓ_c. The number density is taken to be constant (1 cm^{-3}) between $b = 0$ and 0.5 (or $B = B_0 \rightarrow 0$ and $B_c/2$), and increases linearly thereafter up to $b = 1$ (ℓ_c), taken to be at an altitude of 3000 km. Figure 2.11 shows this variation in number density. We can extend the linear increase to find n_m, since when the magnetic field strength is greater than $B_c/2$, the number density is given by

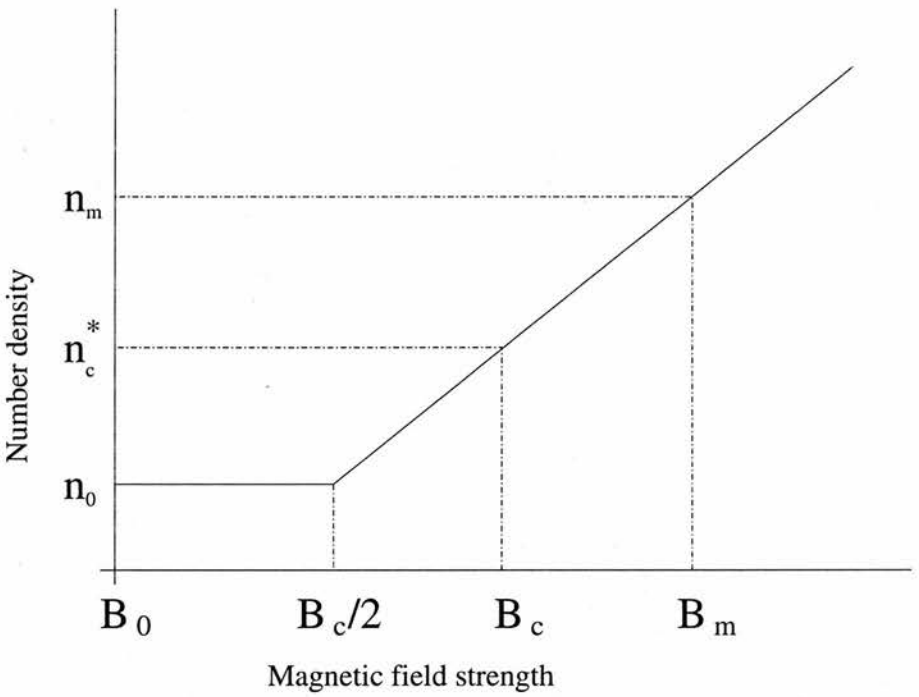

Figure 2.11: Temerin and Carlson used an idealised number density profile, with a constant value for magnetic field strengths between B_0 and $B_c/2$, and a linear increase for magnetic field strengths greater than $B_c/2$. Parameters are $n_0 = 10^6$ m^{-3}, $B_c/B_0 = 603$ and $n_c^* = 4.21 \times 10^7$ m^{-3}.

$$n(\ell) = \frac{G_n}{B_0}\left(B(\ell) - \frac{B_c}{2}\right) + n_0, \tag{2.95}$$

where G_n is the gradient of the line, given by

$$\begin{aligned} G_n &= \frac{n_c^* - n_0}{B_c/2B_0} \\ &= 1.36 \times 10^5 \text{ m}^{-3} \end{aligned} \tag{2.96}$$

Thus, for Temerin and Carlson's values of $n_c^* = 4.21 \times 10^7$ m^{-3} and $B_c/B_0 = 603$, we can substitute $B(\ell) = B_m$ into equation (2.95) to obtain $n_m = 2.23 \times 10^8$ m^{-3}. Finally, we need to satisfy our condition for the location of ℓ_c in equation (2.73), which tells us that

$$\sqrt{1 + \frac{1}{\alpha}}\left(\frac{n_c}{B_c}\Big/\frac{n_0}{B_0}\right) = \left(\frac{n_m}{n_0}\right)\left(\frac{B_0}{B_m}\right)$$

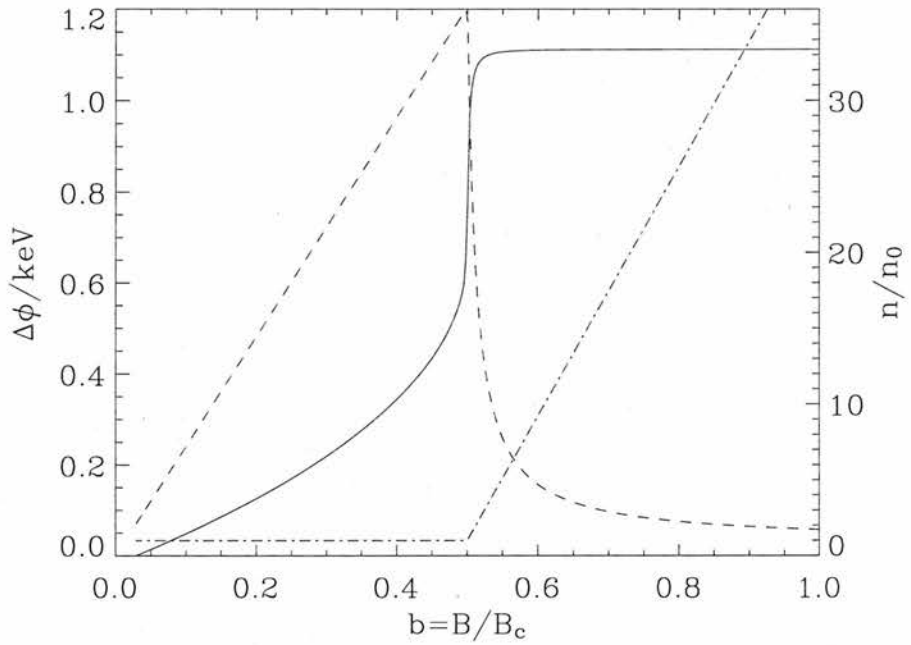

Figure 2.12: Our reproduction of the result in the work of *Temerin and Carlson (1998)*(Figure 1). Using all of their parameters and number density profile, we obtain $\tilde{\Phi}_m = -4073$, which gives a potential difference of 1.13 kV. The solid curve shows the potential variation, and the dot-dashed line shows the number density profile. The dashed plot is a scaled version of the B/n curve, $(B/n)/(250B_0/n_0)$, which clearly shows that the B/n peak occurs at $b = 0.5$. Note the large $E_\parallel$ (rapid change in $\Delta\phi$) which occurs where the density scale length is small (at the B/n peak).

$$\begin{aligned} \Rightarrow \alpha &= \left[\left(\frac{n_m}{n_0}\right)^2\left(\frac{n_0}{n_c}\right)^2\left(\frac{B_c}{B_0}\right)^2\left(\frac{B_0}{B_m}\right)^2 - 1\right]^{-1} \\ &= 0.576 \end{aligned} \tag{2.97}$$

This is an unusually large value, and is due to the linear rather than exponential ion density profile. From this, we can use our relation for α given in equation (2.62), to determine the characteristic ionospheric ionospheric velocity, $a_m = j_m/(n_m e\alpha) = 3.13\times10^5$ m/s. This gives an ionospheric temperature, $ma_m^2/2$, of 0.278 eV, which we can use to determine from equation (2.66) that $\eta = 2.78 \times 10^{-4}$. By taking these values, we have tuned our model to give a solution at ℓ_c that matches those values adopted by Temerin and Carlson exactly. Hence, our models should agree over the common "magnetospheric" domain $\ell_0 < \ell < \ell_c$. Using our model, we obtain a normalised potential difference $\tilde{\Phi}_m = -4073$. From equation (2.68), this corresponds to an actual poptential difference of 1.13 kV, identical to the value found by Temerin and Carlson. Our results are shown in Figure 2.12. The dot-dashed line shows the number density profile, the dashed line shows a scaled version of the B/n curve, and the solid curve shows the potential variation. It is interesting to note that the kink in ion number density at $b = 0.5$ has the effect of concentrating much of the electron acceleration over a very small region. We could have chosen a different extrapolated density for $\ell_c < \ell < \ell_m$ which would have given more typical values of n_m, α and η. What is important for the present comparison is that our values at ℓ_c match those of Temerin and Carlson, which serves to check the

validity of our model.

2.4 Total potential difference, $\tilde{\Phi}_m$

2.4.1 Properties of $\tilde{\Phi}_m$

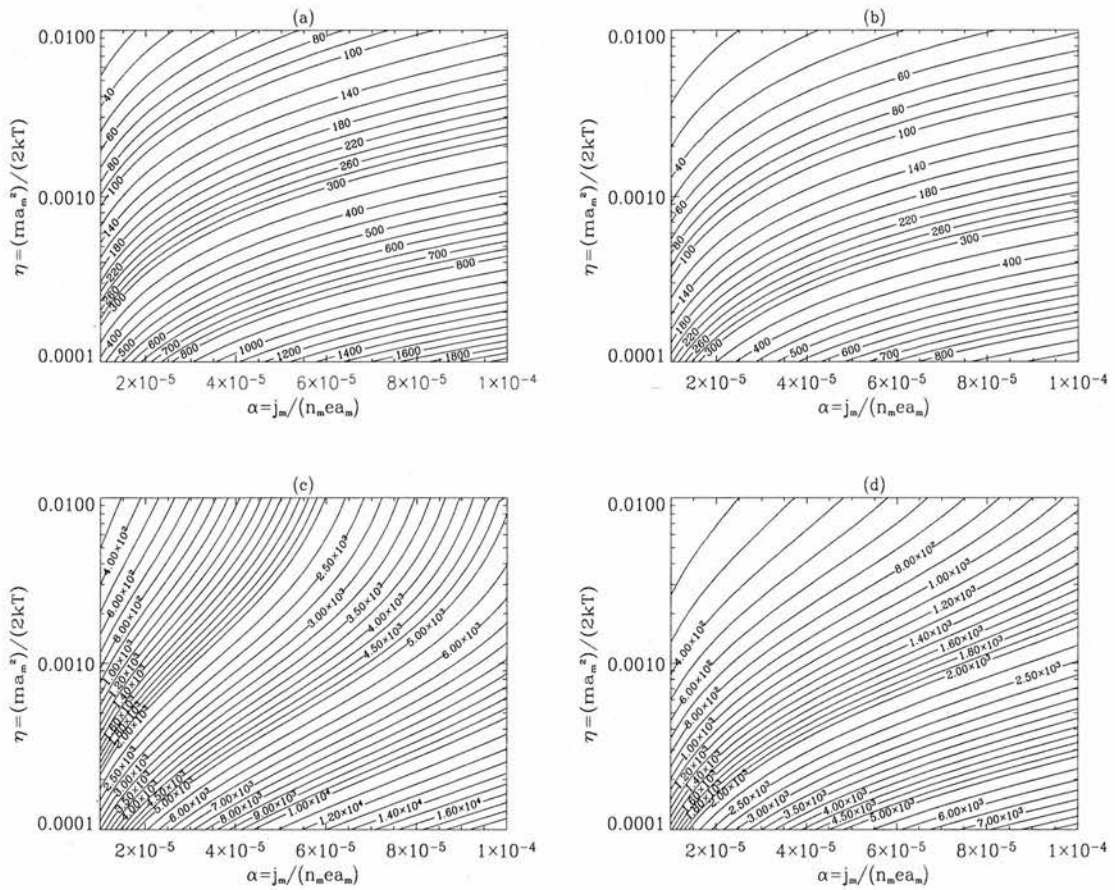

Figure 2.13: Four contour plots of -$\tilde{\Phi}_m$, the total potential increase along the field line, against α and η, for different ion number densities and scale heights: (a) and (b) are for $n_m/n_0 = 5 \times 10^4$, whilst (c) and (d) are for 10^6; (a) and (c) are for a scale height, h, of 50 km, whilst (b) and (d) are for 200 km.

Figure 2.13 shows the variation of $\tilde{\Phi}_m = 2e\phi_m/ma_m^2$ with α and η for scale heights of 50 and 200 km and n_m/n_0 values of 5×10^4 and 10^6. These range over typical values, and reveal various properties of $\tilde{\Phi}_m$. Although not clear in these plots, $\tilde{\Phi}_m$ is actually unaffected by equilibrium ionospheric parameters (n_m and a_m), a fact which will be justified in the analytical work in Chapter 3. The plots in Figure 2.13 change with n_m because this modifies the B/n curve, and the values of B and n at the B/n peak, which actually determine $\tilde{\Phi}_m$. In general, as α increases, implying a higher current density, so does the potential difference, $\mid \tilde{\Phi}_m \mid$, required to accelerate the current-carrying electrons. A decrease in η, caused by an increased

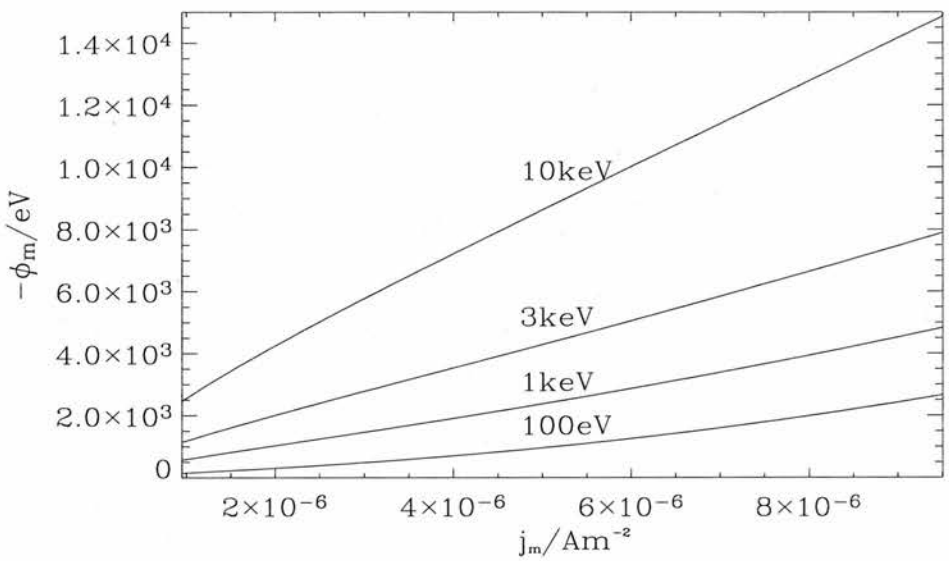

Figure 2.14: Current-voltage relationship for different magnetospheric electron temperatures, a scale height of 100 km and $\frac{1}{2}m_e a_m^2 \sim 1$ eV.

magnetospheric temperature, leads to an increase in $|\ \tilde{\Phi}_m\ |$: in this case, the increase in potential difference is required primarily to mirror the more energetic magnetospheric electrons. Comparisons between the contour plots also show that increasing the ion scale height, h, decreases $|\ \tilde{\Phi}_m\ |$. Increasing h has the effect of increasing the ion number density at higher altitudes, with the result that quasi-neutrality is a less stringent constraint on the beam number density, which can increase more to carry the required current, so the beam requires less acceleration overall.

The contour plots can be used to determine the total potential increase for a given downward current event as follows:

Step 1 Choose the equilibrium parameters of the event: the magnetospheric electron thermal energy (kT), the ionospheric electron thermal energy ($m_e a_m^2/2$), the ion number density at the base of the F region (n_m) and at ℓ_0 in the magnetosphere (n_0), the ion scale height (h), and the current density at the base of the F region (j_m). If you know the current density at a particular altitude, use the current continuity equation (2.42) to map this down to j_m.

Step 2 Calculate the dimensionless parameters α and η from equations (2.62) and (2.66) respectively.

Step 3 Use your α and η values to read off the required potential increase from the contour plot which has parameters closest to yours. Alternatively, if your value for h or n_m/n_0 lies between the ones we have shown, then read off two values of $\tilde{\Phi}_m$ and extrapolate between them. For example, if $h = 100$ km and $n_m/n_0 = 10^6$, then read off the required $\tilde{\Phi}_m$ values from both of the plots with $n_m/n_0 = 10^6$, giving $\tilde{\Phi}_m(50)$ and $\tilde{\Phi}_m(200)$ for scale heights of 50 and 200 km respectively. Then interpolate, so that

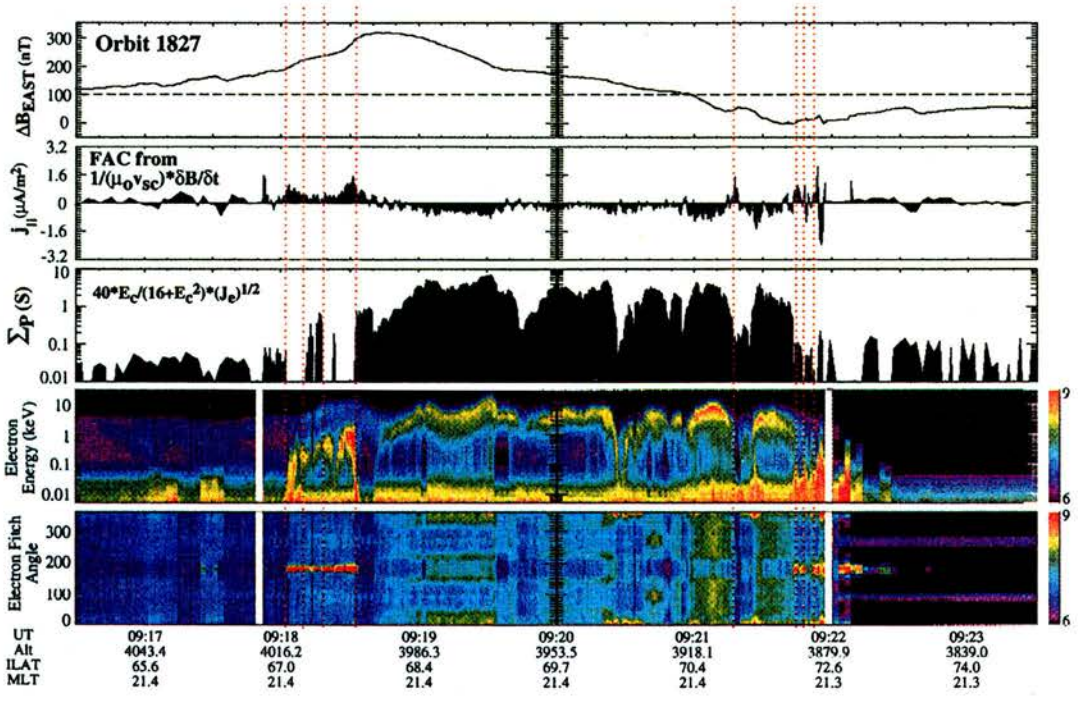

Figure 2.15: Data from *Elphic et al. (2000)*(Plate 1)

$$\tilde{\Phi}_m(100) = \frac{2}{3}\tilde{\Phi}_m(50) + \frac{1}{3}\tilde{\Phi}_m(200) \tag{2.98}$$

This gives an estimate of $\tilde{\Phi}_m(100)$, the total potential increase for a scale height of 100 km. Figure 2.14 illustrates specific current-voltage relations for a scale height of 100 km and different magnetospheric temperatures. These are weakly non-linear, but could be approximated well by linear functions.

2.4.2 Comparison with data

In order to test the validity of this model, we compare the results that it gives with FAST data presented in *Elphic et al. (2000)*, Plate 1, shown here in Figure 2.15. At the end of the first downward current phase (indicated by vertical dotted red lines starting at UT=09:18), an inferred current density, j_{FAST}, of 1.6 $\mu\mathrm{Am}^{-2}$ is observed at the altitude of FAST (second panel), and the associated electron energy is $\sim$2 keV (fourth panel).

Firstly, we need to calculate j_m using equation (2.42), noting that the altitude of FAST is $\sim$4000 km. This gives us $j_m = 6.94\ \mu\mathrm{Am}^{-2}$. The electron energy spectra suggest that we have typical ionospheric and magnetospheric electron temperatures of 1 eV and 1 keV respectively. Assuming $n_m/n_0 = 10^6$, we find that $\alpha = 7.30 \times 10^{-5}$ from equation (2.62) and $\eta = 10^{-3}$ from equation (2.66).

The ion scale height h can vary due to several factors, including the ion temperature, and the presence

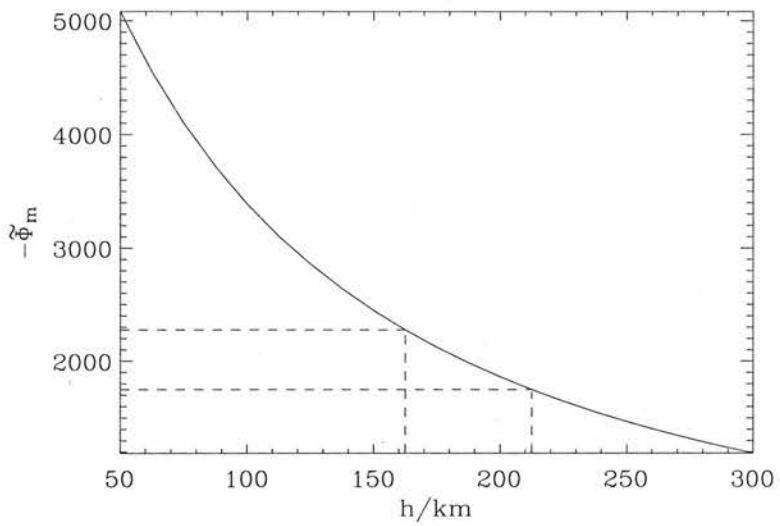

Figure 2.16: Comparison with FAST data in *Elphic et al. (2000)*, shown in Figure 2.15. The variation of $\tilde{\Phi}_m$ with h for $j_m = 6.94\ \mu\mathrm{Am}^{-2}$ and $j_{FAST} = 1.6\ \mu\mathrm{Am}^{-2}$ at an altitude of 4000 km is given. The data shows $\tilde{\Phi}_m \sim 2$ kV, implying an ion scale height of 160-210 km.

of additional features in the downward current region such as ion conics. We can use the information above to infer the value of h in this case. In Figure 2.16, we compute $\tilde{\Phi}_m$ for ion scale heights varying from 50 to 300 km. For $\tilde{\Phi}_m \sim 2$ kV, this corresponds to $h \sim$160-210 km, which is a very reasonable range.

2.4.3 Validity of assumptions

In this model, we assume that the magnetospheric number density is negligible at altitudes below ℓ_c, i.e. that no magnetospheric electrons penetrate into the ionosphere. In reality, because the distribution is Maxwellian, a few of the most energetic field-aligned magnetospheric electrons will be able to overcome the large potential barrier and mirror force to penetrate into the ionosphere, thus producing a downward electron population of magnetospheric origin and reducing the net upward flux. It is possible to calculate the neglected magnetospheric current density and number density at ℓ_c, and compare these with the beam current and number densities to check the validity of this assumption.

The neglected current density, $j_\parallel^u$, can be found by integrating the Maxwellian electron distribution given in equation (2.34) over $v_\parallel$ and $v_\perp$ space as follows with $n_M = n_0$

$$j_\parallel^u = -e \int_0^\infty \int_0^\infty v_\parallel f_M \ \mathrm{d}v_\parallel \ 2\pi v_\perp \mathrm{d}v_\perp \tag{2.99}$$

Using the following integrals

$$\int_0^\infty v_\perp \exp\left(-\frac{mv_\perp^2}{2kT}\right) \mathrm{d}v_\perp = \int_0^\infty v_\parallel \exp\left(-\frac{mv_\parallel^2}{2kT}\right) \mathrm{d}v_\parallel = \frac{kT}{m} \tag{2.100}$$

and the fact that $\Delta\tilde{\Phi} = -1$ at ℓ_c, we obtain

$$j_\parallel^u = -en_0\sqrt{\frac{kT}{2\pi m}} \exp\left(\eta\left(\tilde{\Phi}_m - 1\right)\right) \tag{2.101}$$

Using the current continuity condition in equation (2.42), we know that $j_c = B_c j_m / B_m$, giving

$$\left|\frac{j_\parallel^u}{j_c}\right| = \frac{1}{2\alpha}\left(\frac{B_m}{B_c}\right)\left(\frac{n_0}{n_m}\right)\sqrt{\frac{1}{\pi\eta}} \exp\left(\eta\left(\tilde{\Phi}_m - 1\right)\right) \tag{2.102}$$

Similarly, we can work out the ratio of number densities at ℓ_c. Here, the electron beam accounts for the total ionospheric electron number density. Thus, re-arranging equation (2.90)

$$\frac{n_c^*}{n_0} = \left(\frac{n_m}{n_0}\right)\left(\frac{B_c}{B_m}\right)\left(1 + \frac{1}{\alpha}\right)^{-\frac{1}{2}} \tag{2.103}$$

The magnetospheric number density at ℓ_c is determined by substituting $\Delta\tilde{\Phi} = -1$ into the second (Maxwellian) term on the RHS of equation (2.70) to yield

$$\frac{n_c^{\mathrm{mag}}}{n_0} = (1 - AC) \exp\left(\eta\left(\tilde{\Phi}_m - 1\right)\right) \tag{2.104}$$

where A and C are determined by equations (2.71) and (2.72) respectively. Thus, we obtain the ratio

$$\frac{n_c^{\mathrm{mag}}}{n_c^*} = (1 - AC)\left(\frac{n_0}{n_m}\right)\left(\frac{B_m}{B_c}\right)\sqrt{1 + \frac{1}{\alpha}} \exp\left(\eta\left(\tilde{\Phi}_m - 1\right)\right) \tag{2.105}$$

Contour plots of the ratios in equations (2.102) and (2.105) are given in Figure 2.17. These reveal that the neglected number density at ℓ_c is always negligible compared to the beam number density for relevant values of α and η. The neglected current density, however, is sometimes significant: when α and η are both very small, the neglected current density is comparable to the beam current density, but as either of these parameters increases (implying a larger beam current density or smaller difference between ionospheric and magnetospheric electron temperatures) the ratio becomes smaller, implying that the assumption becomes more accurate. These results make sense, as when j_m is small, j_c will also be small, so the magnetospheric component is more likely to yield a comparable upward current density. Also, a decrease in η implies

an increase in magnetospheric electron temperature, so more energetic electrons will be able to overcome the potential barrier and contribute to an upward current at ℓ_c. As an example, when the ionospheric and magnetospheric temperatures are 1 eV and 1 keV respectively (giving $\eta = 0.001$), the ratio in equation (2.102) falls to 0.1 (giving a 10 % error) for an ionospheric current density (j_m) of $\sim$3 μAm^{-2}. However, decreasing the magnetospheric temperature to 500 eV (and thus increasing η to 0.002), the ionospheric current density giving an error of 10 % falls to $\sim$2 μAm^{-2}.

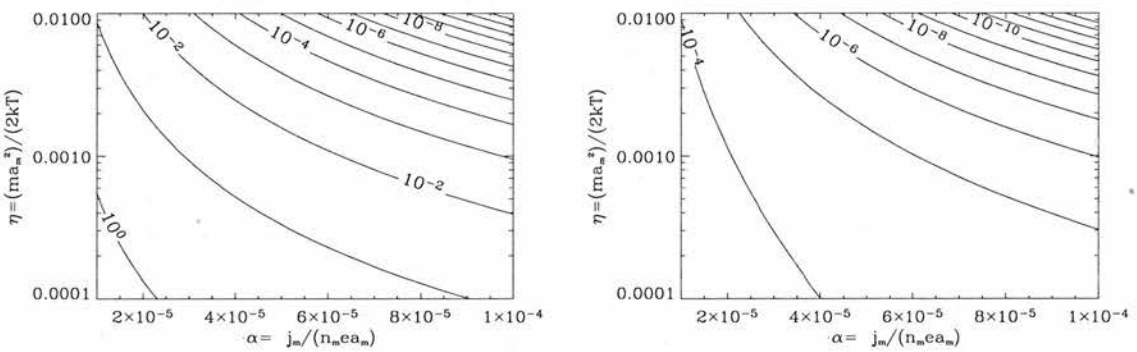

Figure 2.17: Contour plots showing (left) the ratio of neglected magnetospheric and beam current densities and (right) number densities at ℓ_c for $n_m/n_0 = 10^6$ and h =100 km. These plots reveal that the beam number density is always much greater than the magnetospheric contribution. The current densities, however, can be comparable for very small values of α and η. As either of these parameters increases, so does the accuracy of our assumption.

2.5 Instability of the electron beam

In this model, we do not concern ourselves with the stability of the current-carrying electron beam. After all the acceleration has taken place, the beam has a velocity given in equation (2.92) and a width in velocity space, W, of

$$\begin{aligned} W &= a_m \left(\sqrt{(1+2\alpha)^2 - \tilde{\Phi}_m} - \sqrt{1-\tilde{\Phi}_m} \right) \\ &\approx \frac{2a_m\alpha}{\sqrt{1-\tilde{\Phi}_m}} \end{aligned} \tag{2.106}$$

For our typical case, where $a_m = 5.93 \times 10^5$ m/s, $\alpha = 5 \times 10^{-5}$ and $\tilde{\Phi}_m = -2280$, the beam has a speed of 2.8×10^7 m/s and a width of only 1.2 m/s. This is clearly not a stable plasma configuration, and the beam would not remain in this form for long once accelerated. Data, such as that from *Carlson et al. (1998a)* shown in Figure 2.1, indicate a beam thermal width of $\sim$100 eV, which corresponds to $\sim 6 \times 10^6$ m/s.

2.5.1 Landau Damping

Landau damping is the term given to resonant wave-particle interactions leading to energy exchange in a plasma. If a plasma contains a wave with phase velocity v_{ph}, then particles with velocities close to v_{ph} will be able to interact strongly with it. The wave electric field accelerates those particles with velocities slightly lower than v_{ph}, and decelerates particles with velocities slightly higher than v_{ph}. The overall effect is to make all these interacting particles move at the wave phase velocity. The wave loses energy to the slower particles and gains energy from the faster ones.

In an equilibrium plasma, such as our magnetospheric Maxwellian electron population, there are more particles moving slower than v_{ph} than are moving faster. Thus, a wave loses energy overall and is damped, giving energy to the particle distribution. This situation is illustrated in Figure 2.18. We can see that the Maxwellian has a negative slope for positive velocities: it is this property which assures the stability of the distribution. If, however, a second more energetic population is added to the plasma, it becomes what is known as a "bump-on-tail" distribution (see Figure 2.19). This is an unstable configuration, as part of this "bump" in velocity space has a positive gradient: waves interacting with this part of the distribution will actually gain energy, since the particles travelling faster than the wave phase velocity and being decelerated outnumber those being accelerated. This has the effect of allowing small amplitude waves of the appropriate phase velocity to grow. This represents an instability that may eventually saturate after smoothing out the distribution function until the positive gradient is removed. This instability is a micro-instability, since it is localised in velocity space. The Penrose critereon, a necessary and sufficient condition for instability in this case, is given by

$$P = \int_{-\infty}^{\infty} \frac{F_0(v_\parallel) - F_0(v_{\parallel A})}{(v_\parallel - v_{\parallel A})^2} \mathrm{d}v_\parallel > 0 \tag{2.107}$$

where F_0 is the bump-on-tail distribution and $v_{\parallel A}$ is the speed at which the minimum in F_0 occurs *(Boyd and Sanderson (2003))*, as illustrated in Figure 2.19.

We wish to calculate this integral for the characteristic case of our model mentioned above when the beam has been fully accelerated into the magnetosphere (i.e. $\phi = 0$). Firstly, we have a three-dimensional Maxwellian which cannot as such be directly compared with the parallel beam. So, we integrate the Maxwellian distribution in equation (2.34), with $n_M = n_0$ and $\phi = 0$, over $v_\perp$ space to obtain F_M, the Maxwellian distribution in parallel velocity space:

$$\begin{aligned} F_M &= \int_0^\infty f_M \; 2\pi v_\perp \; \mathrm{d}v_\perp \\ &= n_0 \left(\frac{m}{2\pi kT}\right)^{3/2} \exp\left(-\frac{mv_\parallel^2}{2kT}\right) \int_0^\infty 2\pi v_\perp \exp\left(-\frac{mv_\perp^2}{2kT}\right) \; \mathrm{d}v_\perp \end{aligned}$$

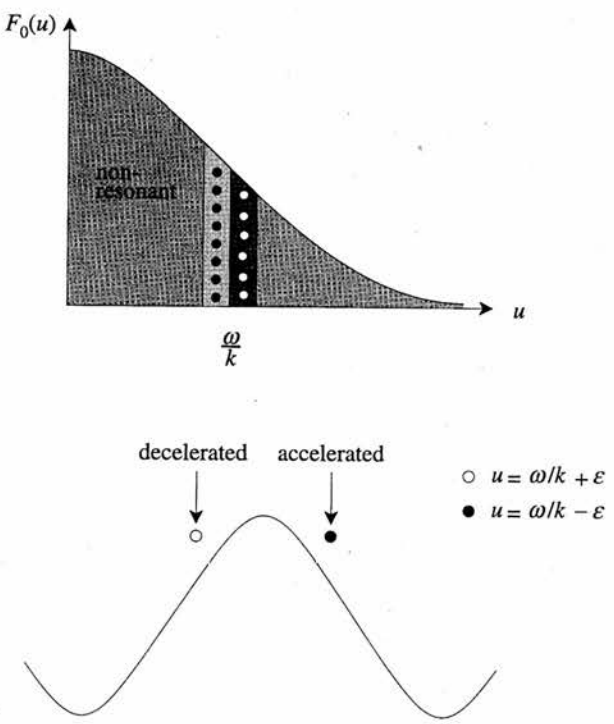

Figure 2.18: Picture illustrating the concept of Landau damping for an equilibrium distribution, where a wave of phase velocity $v_{ph} = \omega/k$ accelerates slightly slower particles (their speed $u = \omega/k - \epsilon$, where ϵ is small) and decelerates slightly faster ones ($u = \omega/k + \epsilon$). In an equilibrium such as a Maxwellian, the slower particles outnumber the faster ones, and so the wave loses energy on average and is damped. This Figure is included courtesy of *Boyd and Sanderson (2003)*.

$$= n_0\sqrt{\frac{m}{2\pi kT}}\exp\left(-\frac{mv_\parallel^2}{2kT}\right) \tag{2.108}$$

using the result in equation (2.100). Now, we need to deduce the beam distribution function, F_B, when $\Delta\tilde{\Phi} = -\tilde{\Phi}_m$ after all the acceleration has taken place, and the magnetic field strength is given by B. The number density of the beam, n^*, is given in equation (2.87), and, when evaluated at $\Delta\tilde{\Phi} = -\tilde{\Phi}_m$, this can be written in terms of the beam velocity width in equation (2.106) as

$$n^* = \frac{n_m}{2a_m(1+\alpha)}\frac{B}{B_m}W \tag{2.109}$$

Thus, since integrating over a distribution function yields the number density, we can deduce that

$$F_B = \frac{n_m}{2a_m(1+\alpha)}\frac{B}{B_m}, \quad -v_{\parallel B} \leq v_\parallel \leq -v_{\parallel A} \tag{2.110}$$

where

$$v_{\parallel A} = a_m\sqrt{1-\tilde{\Phi}_m}; \quad v_{\parallel B} = a_m\sqrt{(1+2\alpha)^2-\tilde{\Phi}_m} \tag{2.111}$$

are the smallest and largest beam speeds respectively. So, in order to calculate the Penrose integral, we need to use $F_0 = F_M + F_B$. In the specific case where $\alpha = 5\times10^{-5}$, the acceleration has mostly occurred at an altitude of 3 R_E, so we take $B/B_m = 0.015$ and find that $P = 15600$ m^{-5}s^2, telling us that our distribution is unstable.

2.5.2 Beam-plasma instability

If the energetic population forming the bump in the tail of the distribution function has a sufficiently large average velocity, then it is essentially totally separated from the equilibrium distribution function in velocity space. The two populations do not readily interact, the Penrose critereon in equation (2.107) is definitely satisfied as $F_0(v_{\parallel A}) \to 0$, and the system resembles what is known as a beam-plasma instability rather than a bump-on-tail instability. In order to examine this instability, we follow *Boyd and Sanderson (2003)* and take a steady-state plasma and allow perturbations to occur, such that for each population:

$$\begin{aligned} n &= n_0 + n_1 \\ \mathbf{u} &= \mathbf{u_0} + \mathbf{u_1} \\ \mathbf{E} &= \mathbf{E_1} \\ \mathbf{B} &= \mathbf{B_1} \end{aligned} \tag{2.112}$$

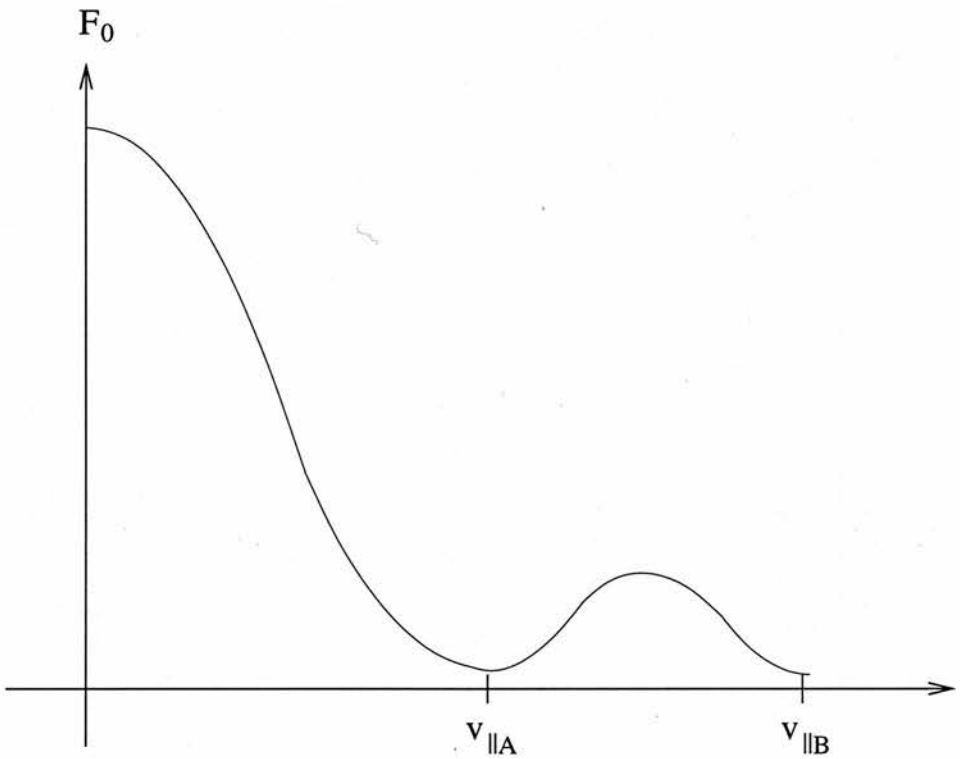

Figure 2.19: Picture of the "bump-on-tail" distribution function, where a flux of hot particles is added to an equilibrium distribution such as a Maxwellian.

where the subscript 0 denotes an equilibrium quantity, and 1 a small perturbation. The equations of continuity and motion for this fluid are given by

$$\frac{\partial n}{\partial t} + \nabla \cdot (n\mathbf{u}) = 0 \tag{2.113}$$

$$\frac{\partial \mathbf{u}}{\partial t} + (\mathbf{u} \cdot \nabla)\,\mathbf{u} = \frac{q}{m}(\mathbf{E} + \mathbf{u} \times \mathbf{B}) \tag{2.114}$$

Linearising these equations, we obtain

$$\frac{\partial n_1}{\partial t} + \nabla \cdot (n_0\mathbf{u_1} + n_1\mathbf{u_0}) = 0 \tag{2.115}$$

$$\frac{\partial \mathbf{u_1}}{\partial t} + (\mathbf{u_0} \cdot \nabla)\,\mathbf{u_1} = \frac{q}{m}(\mathbf{E_1} + \mathbf{u_0} \times \mathbf{B_1}) \tag{2.116}$$

If we look solely for longitudinal waves, then $\nabla \times \mathbf{E} = 0$, and by Maxwell's equation in (1.13), $\mathbf{B_1} = 0$. Assuming that all small quantities vary as $\exp i\,(\mathbf{k} \cdot \mathbf{r} - \omega t)$ yields algebraic results. Equation (2.116) tells us that

$$\mathbf{u_1} = \frac{iq\mathbf{E_1}}{m\left(\omega - \mathbf{k}\cdot\mathbf{u_0}\right)} \tag{2.117}$$

Combining this result with the algebraic version of equation (2.115) yields

$$n_1 = \frac{iqn_0kE_1}{m\left(\omega - \mathbf{k}\cdot\mathbf{u_0}\right)^2} \tag{2.118}$$

where $\mathbf{k}\cdot\mathbf{E_1} = kE_1$, since we are looking for longitudinal waves. Then, if we have N plasma populations interacting, Poisson's equation becomes

$$\nabla\cdot\mathbf{E_1} = \frac{1}{\epsilon_0}\sum_{\alpha=1}^{N} q_\alpha n_{1\alpha} \tag{2.119}$$

where q_α is the charge of species α. We substitute equation (2.118) into this with $n_0 = n_\alpha$ and $\mathbf{u_0} = \mathbf{u}_\alpha$ to give the dispersion relation for longitudinal waves in a plasma containing moving particle streams:

$$\sum_{\alpha=1}^{N} \frac{\omega_{p\alpha}^2}{\left(\omega - \mathbf{k}\cdot\mathbf{u}_\alpha\right)^2} = 1 \tag{2.120}$$

where $\omega_{p\alpha}$ is the plasma frequency for each species, given by

$$\omega_{p\alpha} = \sqrt{\frac{q^2 n_\alpha}{\epsilon_0 m}} \tag{2.121}$$

and $\mathbf{u}_\alpha$ is the zero-order velocity of the population α.

In our case, we essentially have an electron beam (since it has such a narrow width in velocity space) penetrating a cold electron population of frequency ω_p, with a uniform background of positive charge. If this beam has a number density of n^*, a speed of v^* and a plasma frequency of ω^*, the dispersion relation in equation (2.120) becomes

$$\frac{\omega_p^2}{\omega^2} + \frac{\omega^{*2}}{\left(\omega - kv^*\right)^2} = 1 \tag{2.122}$$

which can be rearranged to give

$$\left(\omega^2 - \omega_p^2\right)\left[\left(\omega - kv^*\right)^2 - \omega^{*2}\right] = \omega_p^2\omega^{*2} \tag{2.123}$$

The homogeneous equivalent to this has solutions

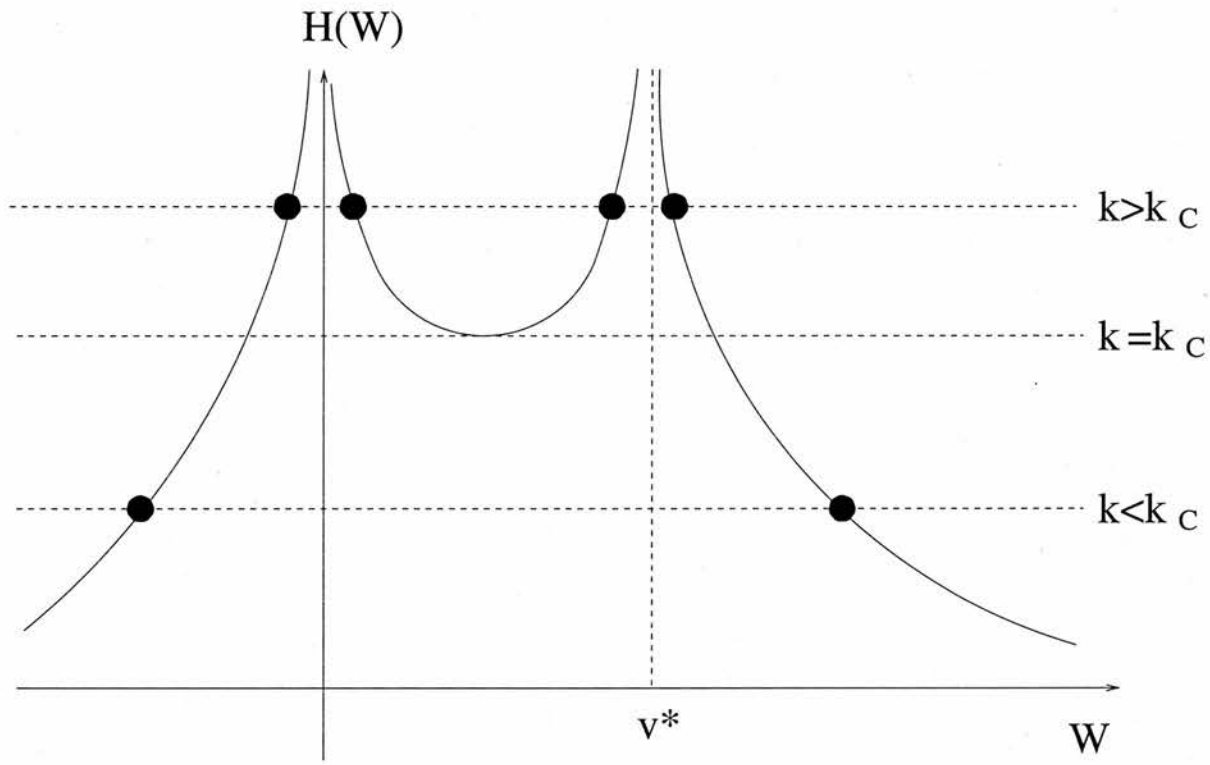

Figure 2.20: Schematic illustrating the form of $H(W)$ for the beam-plasma instability. If $k > k_c$ then there are four real solutions to the quartic equation in (2.123); if $k < k_c$, there are only two, implying the existence of a conjugate pair of imaginary solutions, one of which must necessarily lead to instability.

$$\begin{aligned} \omega_{1,2} &= \pm\omega_p \\ \omega_{3,4} &= kv^* \pm \omega^* \end{aligned} \tag{2.124}$$

which in this case are coupled by the term on the RHS of equation (2.123). Substituting $W = \omega/k$ into equation (2.122) gives

$$H(W) = \frac{\omega_p^2}{W^2} + \frac{\omega^{*2}}{(W - v^*)^2} = k^2 \tag{2.125}$$

Figure 2.20 shows a plot of $H(W)$: for $k > k_c$ there are four real solutions, but for $k < k_c$ there are only two, implying the existence of two imaginary solutions in a conjugate pair, one of which must lead to wave growth and instability. Thus, we find k_c by setting $\mathrm{d}H/\mathrm{d}W = 0$ to give

$$W = \frac{\omega_p^{2/3} v^*}{\omega_p^{2/3} + \omega^{*2/3}} \tag{2.126}$$

Substituting this into equation (2.125) yields

$$k_c = \left(\frac{\omega_p}{v^*}\right)\left[1+\left(\frac{\omega^*}{\omega_p}\right)^{2/3}\right]^{3/2} \tag{2.127}$$

In our model, the number density of the accelerated beam is much smaller than that of the Maxwellian magnetospheric electron distribution, i.e. $n^* \ll n_0$, which also implies that $\omega^* \ll \omega_p$. In this limit,

$$k_c \approx \frac{\omega_p}{v^*} \tag{2.128}$$

and the wave solutions in equation (2.124) become $\omega_1 = -\omega_p$, $\omega_2 = \omega_p$ and $\omega_{3,4} = \omega_p \pm \omega^*$. Thus ω_1 decouples from the other closely-associated waves which have very similar frequencies and can thus interact strongly. Setting

$$\begin{aligned} \delta\omega &= \omega - \omega_p \\ \delta k &= k - \frac{\omega_p}{v^*} \end{aligned} \tag{2.129}$$

and noting that

$$\omega^{*2} = \omega_p^2\left(\frac{n^*}{n_0}\right) \tag{2.130}$$

equation (2.123) becomes

$$\delta\omega\left(\delta\omega - v^*\delta k\right)^2 = \omega_p^3\left(\frac{n^*}{2n_0}\right) \tag{2.131}$$

Substituting $\delta\omega = \omega_r + i\omega_i$ into equation (2.131), we wish to maximise the wave growth rate, i.e. set $\mathrm{d}\omega_i/\mathrm{d}k = 0$. The real part of equation (2.131) is

$$\omega_r^3 - 3\omega_r\omega_i^2 + 2v^*\delta k\left(\omega_i^2 - \omega_r^2\right) + \omega_r v^{*2}\delta k^2 = \omega_p^3\left(\frac{n^*}{2n_0}\right) \tag{2.132}$$

which can be differentiated with $\mathrm{d}\omega_i/\mathrm{d}k = 0$ to give

$$\frac{\mathrm{d}\omega_r}{\mathrm{d}k} = \frac{2v^*\left(\omega_r^2 - \omega_i^2 - \omega_r v^*\delta k\right)}{3\left(\omega_r^2 - \omega_i^2\right) - 4\omega_r v^*\delta k + v^{*2}\delta k^2} \tag{2.133}$$

We can also obtain the imaginary part of equation (2.131), which yields $\omega_i = 0$ (no instability) or

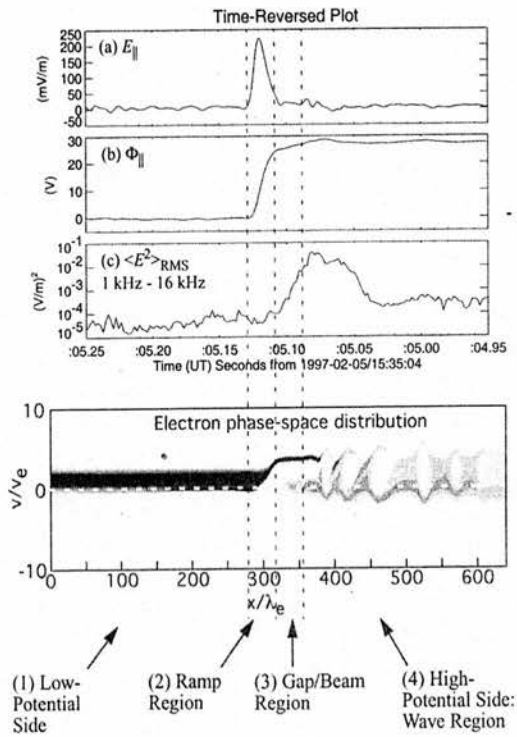

Figure 2.21: Figure from *Ergun et al. (2003a)* comparing FAST data of upgoing electron beam acceleration and thermalisation with a 1D numerical simulation. The distance in the simulation is normalised by the Debye length, λ_e, on the low-potential side $\sim$1 m. The narrow acceleration "ramp" region is followed by an equally small gap region where the beam propagates undisturbed before it is stabilised by intense electrostatic wave activity. This produces electron phase-space holes, seen as vortices in the numerical simulation.

$$\omega_i^2 = 3\omega_r^2 - 4\omega_r v^* \delta k + {v^*}^2 \delta k^2 \tag{2.134}$$

which can be differentiated to give

$$\frac{\mathrm{d}\omega_r}{\mathrm{d}k} = \frac{v^* \left(2\omega_r - v^* \delta k\right)}{3\omega_r - 2v^* \delta k} \tag{2.135}$$

Now, substituting equation (2.134) into (2.133) yields

$$\frac{\mathrm{d}\omega_r}{\mathrm{d}k} = \frac{v^* \left(2\omega_r - v^* \delta k\right)}{3\omega_r - v^* \delta k} \tag{2.136}$$

and comparing this with equation (2.135) tells us that $\delta k = 0$. We can now simplify equation (2.134) to give

$$\omega_r = \pm\frac{\omega_i}{\sqrt{3}} \tag{2.137}$$

which can be substituted into equation (2.132) with $\delta k = 0$ to yield

$$\omega_i = \pm\frac{\sqrt{3}\omega_p}{2^{4/3}}\sqrt[3]{\frac{n^*}{n_0}} \tag{2.138}$$

The positive sign gives the maximum growth rate of the beam-plasma instability. In our example, assuming that all the acceleration has taken place at $\sim$3 R_E where $B/B_m = 0.015$, this corresponds to a growth rate of $\sim$9700 s^{-1}. Thus, the instability grows on a short timescale of $\sim 1.0\times10^{-4}$ s. The accelerated beam electrons have an energy of $\sim$2280 eV, and so will travel $\sim$2.9 km in this time. Thus, the electron beam will be thermalised very quickly on the onset of instability.

2.5.3 Observations of beam thermalisation

Recent high resolution FAST observations of the downward current region have provided examples of upward beam acceleration and subsequent thermalisation. They show a narrow acceleration "ramp" region of $\sim$10 Debye lengths, then a similarly small "gap" region where the unstable beam can be detected, followed by a thermalisation region where intense electrostatic waves stabilise the electron beam. *Ergun et al. (2003a)* present an example of this which is shown in Figure 2.21: a section of FAST data showing evidence of these three regions is compared with a 1D numerical Vlasov simulation by *Newman et al. (2001)*. The top two panels show the parallel electric field and potential, which indicate the narrowly-confined ramp region. The third panel is a measure of electrostatic wave activity, which increases dramatically after the small beam region to stabilise the beam.

Above these confined double layers, the intense wave turbulence thermalises the beam to such an extent that some electrons end up moving back towards the double layer *(Ergun et al. (2003a))*. This gives rise to a two-stream instability rather than the beam-plasma instability which would occur in our model. This instability leads to the formation of persistent structures of depleted electron density which are observed to be rotating vortices of trapped particles around phase-space "holes": these electron phase-space holes can be seen in the thermalisation region of the numerical simulation in Figure 2.21. Thus, the electron beam is accelerated by a potential as in our model, travels a short distance unmodified, and is then thermalised into a stable plasma configuration via the two-stream instability.

2.6 Discussion and Conclusions

We have presented a distribution function solution for ionospheric electrons accelerated into the magnetosphere to form an upflowing beam which carries the downward field-aligned current coupling both regions. This formulation is advantageous as it is possible to isolate the different electron populations involved:

the trapped ionospheric population, the mirroring Maxwellian magnetospheric population, and the current-carrying beam. The ionospheric population (except the beam) is found to be trapped below ℓ_c, which lies earthward of the B/n peak at altitudes of 300-700 km. Above this, the beam emerges into the magnetosphere. $E_{\parallel}$ maximises beyond ℓ_c, within three density scale heights of the B/n peak; this is near the beginning of the acceleration region, which extends for between 500 and 3000 km around the B/n peak.

We have demonstrated that, for given boundary conditions, the exact form of the ion number density profile is unimportant except within a few density scale heights around the B/n peak. It is the properties of this region which define the overall solution, including $\tilde{\Phi}_m$. This highlights that the properties of this model are general, and not just confined to the specific density profiles used in this chapter. Different density profiles could include those produced by the presence of ion conics trapped Earthward of the acceleration region, as discussed by *Temerin and Carlson (1998)*, which have the effect of increasing the ion number density along the field line, thus increasing the ion scale height. These ion conics will modify the ion distribution. The ion scale height, h, and ion number density, n_m/n_0, are the main factors which affect the location of the B/n peak. Studies of FAST data by *Cattell et al. (2004)* and *Carlson et al. (1998a)* show that upward-accelerated electron beams are much more prevalent in the winter or midnight sectors than they are in regions where the ionosphere is sunlit. This implies a strong dependence on scale height and ionospheric number density (n_m).

From observations (e.g. *Ergun et al. (2003a)*), it is apparent that the acceleration in the downward current region can occur over a very small distance (a double layer). In this case, it is obvious that the change in potential occurs over a very small region, which could be thought of as an extreme version of our model with a compacted acceleration width. This can be achieved via a sharp fall or sudden change in ion number density at the required altitude. *Temerin and Carlson (1998)* used such a profile, and obtained a sharp increase in potential. This type of feature in the ion density could evolve from the motion of ions along the field line in a time-dependent model. We neglected ion motion in this model, since a keV electron traverses 1 R_E in ~0.34 s, whilst a hygdrogen ion takes ~40 times as long. However, on longer timescales, this slower ion motion would cause a redistribution of the ion density profile along the field line, modifying the overall potential. This is not dissimilar to our model, where the result is also determined by the properties of a very small region around the B/n peak, which in the compacted case would occur within the double layer. Thus, the results should not be radically different, except that more of the potential increase would occur over a shorter distance: a feature seen very clearly in our reproduction of $\phi(B)$ for *Temerin and Carlson (1998)*'s density profile.

Although observations of double layers show that they may move upward with the ion acoustic speed of a few 10s of km/s *(Andersson et al. (2002))*, this is small compared to the electron speeds, suggesting that the quasi-steady potential viewpoint presented in our calculation is still appropriate. We neglect the evolution of ions, and only address the stability of the beam qualitatively. Any related thermalisation may well require additional energisation: simulations by *Ergun et al. (2003a)* show that there is a rich variety of physics operating here. Their results also show that about 80% of the potential drop is associated with stable acceleration as described in our model, with the remainder occurring in a turbulent thermalising region downstream.

Typical values for $\tilde{\Phi}_m$ obtained from this model are consistent with those obtained by *Temerin and*

Carlson (1998), and range from several 100 V to a few kV. This agrees very well with typically observed values, and we have shown good agreement with a specific data set from *Elphic et al. (2000)* (Plate 1). It will be worthwhile to compare results from our model more closely with observational data over a wider range of conditions to check validity.

Chapter 3

Downward field-aligned current model: Analytical results

3.1 Introduction

Satellite data have established that quasi-static electric fields accelerate electrons both up and down auroral field lines (e.g. *Ergun et al. (2003a)*). *Knight (1973)* recovered a linear current-voltage relation from his upward current model, and this linearity has since been confirmed in several studies including *Weimer et al. (1987)*. This has not been achieved for the downward current region, although a statistical study by *Lynch et al. (2002)* has shown that the downward current-voltage relation is controlled by the local ion density. This idea will be upheld in this chapter, where we use our model to obtain two non-linear current-voltage relations for the downward current region, valid in different regimes. In Chapter 2, we touched on the fact that the magnetospheric equation (2.70) is multi-valued. This is a purely mathematical property which will be explored further in this Chapter, since it leads to an analytical method for determining $\tilde{\Phi}_m$, the total potential drop along the field line.

3.2 Multi-valued solutions in the magnetosphere

We know the value of n/B along the field line from equations (2.1) and (2.11), so in the ionosphere, we can solve equation (2.69) at each point between ℓ_m and ℓ_c to find the potential, $\Delta\tilde{\Phi}(\ell)$. Solving equation (2.70) to find the potential variation in the magnetosphere is not so straightforward, as the equation contains a free parameter $\tilde{\Phi}_m$ (the total potential drop along the field line), where $\Delta\tilde{\Phi}(\ell_0) = -\tilde{\Phi}_m$. Varying this parameter produces a family of curves of the roots of $\Delta\tilde{\Phi}$ in equation (2.70); *Temerin and Carlson (1998)* also noted the multi-valued nature of their solution.

In general, the solutions to this equation are described by two branches, or curves, for a given $\tilde{\Phi}_m$, as

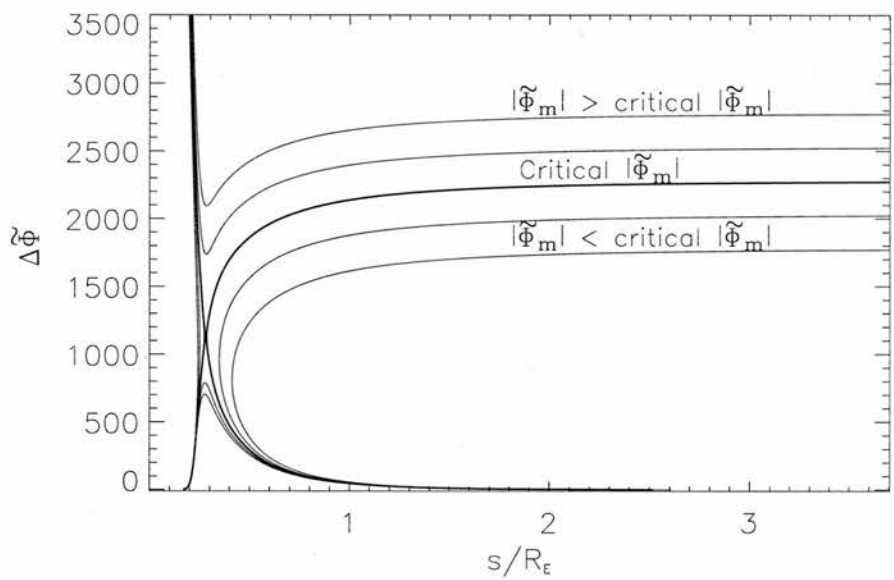

Figure 3.1: Plot showing the form of the two roots of magnetospheric equation (2.70) for different values of the parameter $\tilde{\Phi}_m$, where $\alpha = 5 \times 10^{-5}$, $\eta = 10^{-3}$ and $s = \ell - \ell_m$. These branches are contours of $\tilde{\Phi}_m$. If $\mid \tilde{\Phi}_m \mid$ is larger than the critical value, then upper and lower branches of $\Delta\tilde{\Phi}$ exist all the way along the field line (above and below the x-point), but do not meet at any point, and neither curve satisfies our boundary conditions. If $\mid \tilde{\Phi}_m \mid$ is smaller than the critical value, then there are again two branches of $\Delta\tilde{\Phi}$, one to the right and the other to the left of the x-point. Thus, there are points along the field line between these two curves for which no root of $\Delta\tilde{\Phi}$ exists. All of these curves are unphysical, but there is a unique critical value of $\tilde{\Phi}_m$ for which the two curves of $\Delta\tilde{\Phi}$ meet at a stationary x-point. The solution which satisfies our boundary conditions is the monotonically increasing one, which switches from the lower to the upper branch as it passes through the x-point.

shown in Figure 3.1. For one particular critical value of $\tilde{\Phi}_m$, these branches touch at a stationary point. If we take $\mid \tilde{\Phi}_m \mid <$ critical $\mid \tilde{\Phi}_m \mid$, then there are two branches, one to the right of the x-point, and another to the left. Clearly, there are points along the field line between these two curves for which no root exists, so we exclude these values of $\tilde{\Phi}_m$ as being unphysical. On taking $\mid \tilde{\Phi}_m \mid >$ critical $\mid \tilde{\Phi}_m \mid$, we again find two branches, this time above and below the x-point. Both of these curves are continuous: however, we assume in the derivation of equation (2.70) that the Maxwellian electron distribution at ℓ_0 remains Maxwellian throughout the magnetosphere. This is only the case for a monotonically decreasing potential from the magnetospheric end, since any increase will lead to a hole in velocity space around $v_{\parallel} = 0$, giving a non-Maxwellian distribution. Thus, these curves are mathematical roots of equation (2.70), but this equation no longer describes our system accurately, and so these curves must be discounted. Thus, we choose the monotonically increasing continuous curve which passes through the stationary point as the physically relevant solution for this problem. Numerically, this involves finding the roots of $g(\Delta\tilde{\Phi}, \ell, \tilde{\Phi}_m) = 0$ at every point along the fieldline, where

$$g(\Delta\tilde{\Phi}, \ell, \tilde{\Phi}_m) = \frac{B_0}{B(\ell)}[1 - AC]\exp\left[\eta\left(\Delta\tilde{\Phi} + \tilde{\Phi}_m\right)\right] + A\left[\sqrt{(1+2\alpha)^2 + \Delta\tilde{\Phi}} - \sqrt{1+\Delta\tilde{\Phi}}\right] - \frac{n(\ell)}{B(\ell)}\Big/\frac{n_0}{B_0}, \quad (3.1)$$

The definitions of A and C are given in equations (2.71) and (2.72) respectively. We search for the value of $\tilde{\Phi}_m$ for which the branches touch at a stationary point we label ℓ_q, and choose the lower solution Earthward of ℓ_q, and the upper solution beyond ℓ_q. Figure 3.2 shows the contours of $G(\Delta\tilde{\Phi}, \ell, \tilde{\Phi}_m = -2280)$ for $\alpha = 5 \times 10^{-5}$ and $\eta = 10^{-3}$, whilst figure 3.3 plots $G(\Delta\tilde{\Phi}, \ell, \tilde{\Phi}_m = -2280)$ for the same parameters for four representative points along the field line, showing the nature of the roots.

Figure 3.4 shows a schematic of the important locations in the model, including ℓ_q. Two different field-aligned coordinates are used in this model: ℓ, defined in equation (2.9), is useful for global behaviour along a field line ($\ell = \ell_0$ at the magnetospheric end and increases as the Earth is approached); $s = \ell_m - \ell$ is measured from the ionospheric end and is useful for plotting features closer to the Earth ($s = 0$ at the base of the F region and increases with altitude).

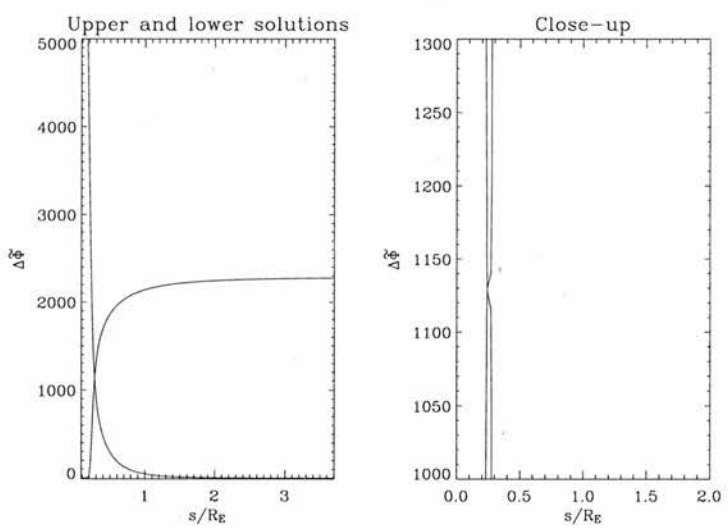

Figure 3.2: Close-up of the two magnetospheric solutions where $\alpha = 5 \times 10^{-5}$, $\eta = 10^{-3}$ and the critical $\tilde{\Phi}_m = -2280$. The upper and lower solutions touch at one point, ℓ_q.

3.3 Stationary point analysis

In Chapter 2, we showed numerically that the B/n peak determined the solution; altering the ion number density on either side of the peak resulted in no difference to $\tilde{\Phi}_m$. This can be explained by describing the stationary point outlined above mathematically. To do this, we make a small simplification to equation (2.70) to allow solution of the resulting equations, by using the approximation

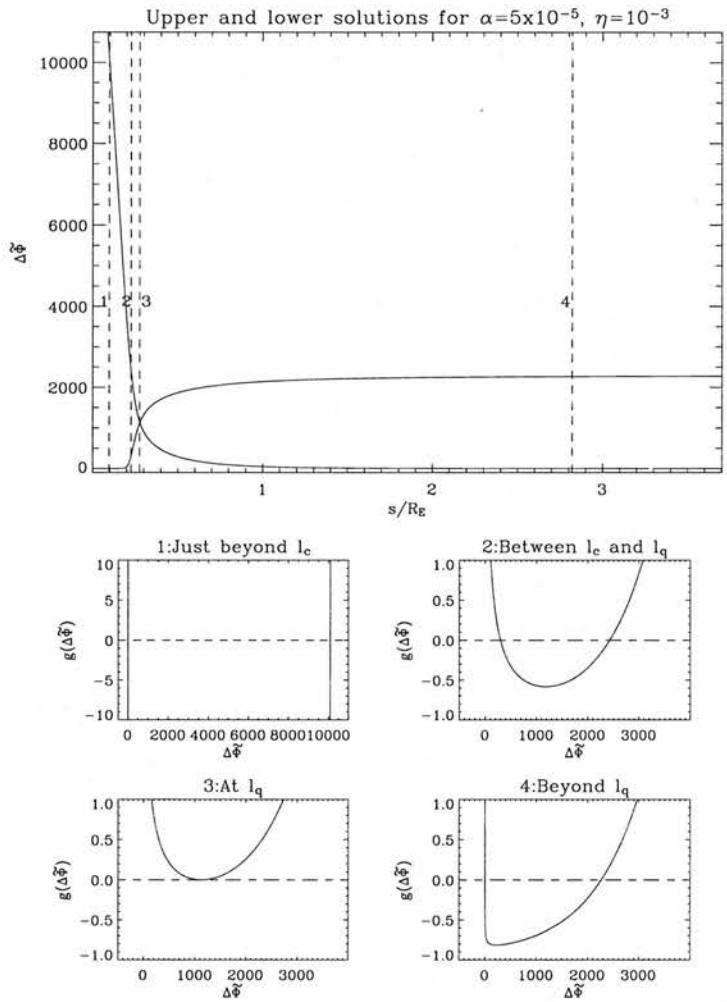

Figure 3.3: In this figure, $\alpha = 5\times10^{-5}$, $\eta = 10^{-3}$ and the critical $\tilde{\Phi}_m = -2280$. In order to solve equation (2.70), we must find the roots of the magnetospheric equation $g(\Delta\tilde{\Phi}, \ell, \tilde{\Phi}_m = -2280)$ at each point along the field line. Here, we plot $g(\Delta\tilde{\Phi}, \ell, \tilde{\Phi}_m = -2280)$ at four different points along the field line, illustrating the nature of the roots.

$$\sqrt{(1+2\alpha)^2 + \Delta\tilde{\Phi}} - \sqrt{1+\Delta\tilde{\Phi}} \approx \frac{2\alpha(\alpha+1)}{\sqrt{1+\Delta\tilde{\Phi}}} \tag{3.2}$$

valid when $1 + \Delta\tilde{\Phi} \gg 4\alpha(\alpha+1)$. Since $\alpha \ll 1$, typically $\sim 10^{-5}$-10^{-3}, and our stationary point ℓ_q lies in the middle of the acceleration region where $\Delta\tilde{\Phi}$ is large, this is an excellent approximation. Indeed, for typical parameters, $4\alpha(\alpha+1)/(1+\Delta\tilde{\Phi}) \sim 10^{-7}$-$10^{-6}$. From this approximation, we obtain

$$\begin{aligned}\frac{n(\ell)}{B(\ell)}\Big/\frac{n_0}{B_0} &= \left(\frac{n_m}{n_0}\right)\left(\frac{B_0}{B_m}\right)\frac{\alpha}{\sqrt{1+\Delta\tilde{\Phi}}} \\ &\quad + \frac{B_0}{B(\ell)}(1-AC)\exp\left(\eta\left(\Delta\tilde{\Phi}+\tilde{\Phi}_m\right)\right)\end{aligned} \tag{3.3}$$

Evaluating this relation at the stationary point, ℓ_q, where $n(\ell) = n_q$, $B(\ell) = B_q$ and $\Delta\tilde{\Phi} = \Delta\tilde{\Phi}_q$, we obtain our first stationary point equation

$$\frac{n_q}{n_0} = \left(\frac{n_m}{n_0}\right)\left(\frac{B_q}{B_m}\right)\frac{\alpha}{\sqrt{1+\Delta\tilde{\Phi}_q}} + (1-AC)\exp\left(\eta\left(\Delta\tilde{\Phi}_q + \tilde{\Phi}_m\right)\right) \tag{3.4}$$

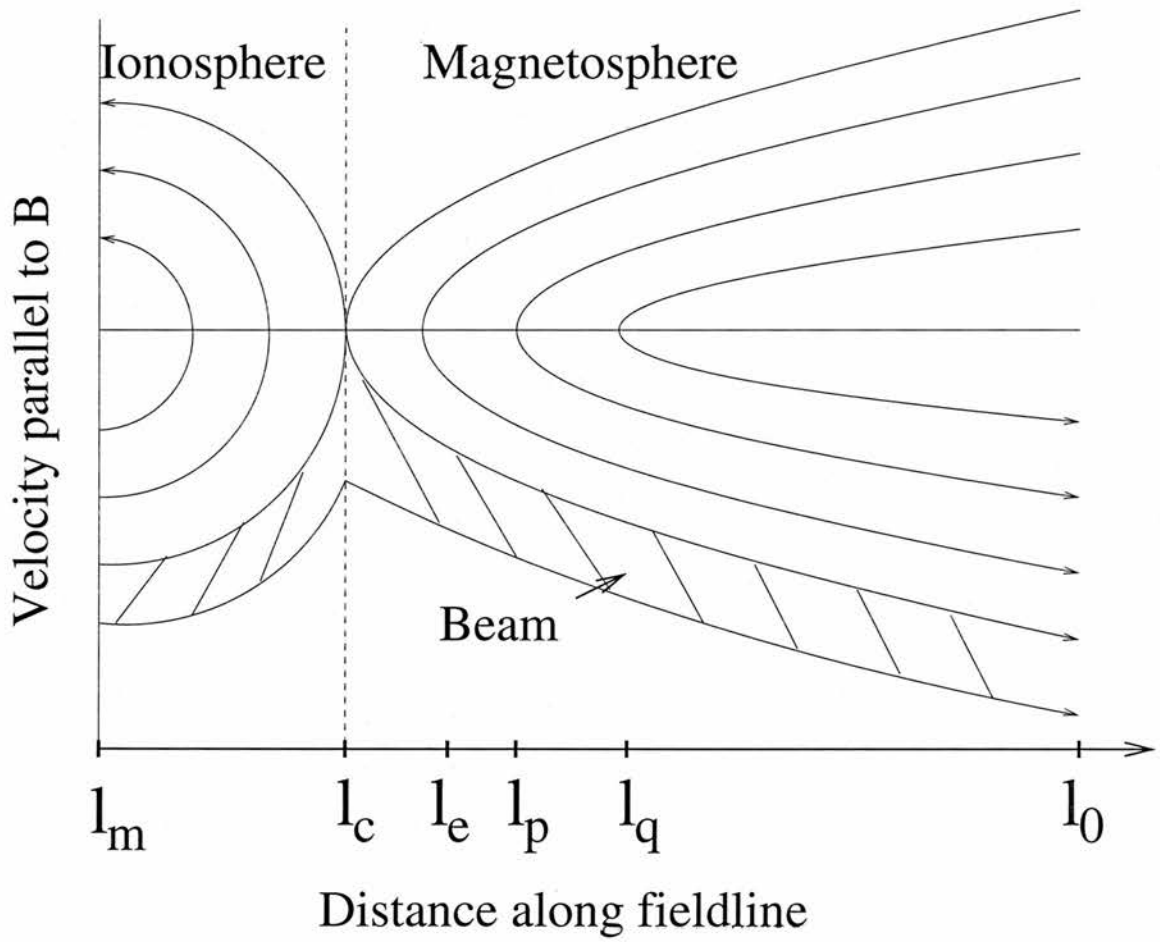

Figure 3.4: This is a schematic of the important locations in the solution along a field line. The point ℓ_m is at the base of the F region; ℓ_c is the ionospheric trapping point; the electric field maximises at ℓ_e, just Earthward of the B/n peak, ℓ_p; the stationary point ℓ_q lies just beyond the B/n peak; and ℓ_0 is a distant point in the magnetosphere. The field-aligned coordinate ℓ, defined in equation (2.9), increases from $\ell_0 = \ell(\theta = 0)$ at a distant point in the magnetosphere to ℓ_m at the base of the F region. Our other field-aligned coordinate, $s = \ell_m - \ell$, is useful for studying features closer to the Earth.

The stationary point at ℓ_q is a standard two-variable saddle point. At a stationary point of a general function $g(x, y)$, $\partial g/\partial x = \partial g/\partial y = 0$ *(Salas et al. (2003))*. From equation (3.3), we know that $G(B, \Delta\tilde{\Phi}, \tilde{\Phi}_m) = 0$, where n is a known function of B and all other parameters are given, but $\tilde{\Phi}_m$ is not

(hence it is retained as a variable). Setting $G = 0$ implictly defines $\tilde{\Phi}_m$ given B and $\Delta\tilde{\Phi}$, which we can express as $\tilde{\Phi}_m = g(B, \Delta\tilde{\Phi})$. We see how B and $\Delta\tilde{\Phi}$ play the roles of x and y in a textbook two-variable stationary point analysis. Indeed, the contours of $\tilde{\Phi}_m$ in Figure 3.1 were calculated from just this expression (except it uses s rather than B as the field-aligned coordinate). The requirements $\partial g/\partial x = \partial g/\partial y = 0$ become $(\partial g/\partial B)_{\Delta\tilde{\Phi}} = \partial g/\partial B + (\partial g/\partial n)(\mathrm{d}n/\mathrm{d}B) = 0$ and $(\partial g/\partial \Delta\tilde{\Phi})_B = 0$ at ℓ_q, giving us two more equations for the stationary point:

$$0 = -\frac{1}{2}\left(\frac{n_m}{n_0}\right)\left(\frac{B_q}{B_m}\right)\frac{\alpha}{\left(1+\Delta\tilde{\Phi}_q\right)^{\frac{3}{2}}} + \eta\left(1 - AC\right)\exp\left(\eta\left(\Delta\tilde{\Phi}_q + \tilde{\Phi}_m\right)\right) \tag{3.5}$$

$$B_0\frac{\mathrm{d}}{\mathrm{d}B}\left(\frac{n(B)}{n_0}\right)_q - \left(\frac{n_m}{n_0}\right)\left(\frac{B_0}{B_m}\right)\frac{\alpha}{\sqrt{1+\Delta\tilde{\Phi}_q}} = 0 \tag{3.6}$$

Thus, we have three equations at the stationary point (3.4,3.5, and 3.6), and four unknowns (n_q, B_q, $\Delta\tilde{\Phi}_q$, and $\tilde{\Phi}_m$). In principle, we could solve this system of equations by introducing a fourth equation relating n_q and B_q. However, this proves to be unnecessary, as we shall show in section 3.4.1 that it is possible to get good estimates of n_q and B_q by another route. We do not use equation (3.6) in our derivation of an analytical expression for $\tilde{\Phi}_m$, but we have included it for completeness, since it would be necessary to use it if n_q and B_q were unknown. Substituting for the exponential in equation (3.4) using equation (3.5) we obtain

$$\frac{n_q}{n_0} = \frac{n_m}{n_0}\frac{B_q}{B_m}\frac{\alpha}{\sqrt{1+\Delta\tilde{\Phi}_q}} + \frac{\alpha}{2\eta}\frac{n_m}{n_0}\frac{B_q}{B_m}\left(1+\Delta\tilde{\Phi}_q\right)^{-3/2} \tag{3.7}$$

This can be re-arranged to give the cubic

$$X^3 - \alpha c_q X^2 - \frac{\alpha c_q}{2\eta} = 0 \tag{3.8}$$

where

$$X = \sqrt{1+\Delta\tilde{\Phi}_q} \tag{3.9}$$

and

$$c_q = \left(\frac{n_m}{n_q}\right)\left(\frac{B_q}{B_m}\right) \tag{3.10}$$

3.3.1 Solving the cubic

There is a general solution for the cubic equation, but it proved difficult to use in this case because we are only interested in the real root of equation (3.8), and it is hard to extract that from the general solution. There is another technique for finding a real root of a general cubic. This technique works for any cubic of the form

$$X^3 + pX + q = 0 \tag{3.11}$$

We substitute

$$p = 3st; \;\; q = t^3 - s^3 \tag{3.12}$$

into equation (3.11), and it is then the case that $X = s - t$ is a real solution to the cubic. This can be shown by factorising:

$$\begin{aligned} X^3 + 3stX + (t^3 - s^3) &= (X - (s-t))(X^2 + (s-t)X + st + s^2 + t^2) \\ &= 0 \end{aligned} \tag{3.13}$$

It is possible to convert our cubic in equation (3.8) into the form in equation (3.11), as shown below:

$$X^3 + aX^2 + c = \left(X + \frac{a}{3}\right)^3 - \frac{a^2}{3}\left(X + \frac{a}{3}\right) + \left(c + \frac{2a^3}{27}\right) \tag{3.14}$$

where $a = -\alpha c_q$ and $c = -\alpha c_q / 2\eta$. Using this transformation, we have that

$$p = -\frac{\alpha^2 c_q^2}{3} \tag{3.15}$$

and

$$q = -\frac{\alpha c_q}{2\eta} - \frac{2\alpha^3 c_q^3}{27} \tag{3.16}$$

Substituting equation (3.12) into (3.15) tells us that

$$t = -\frac{\alpha^2 c_q^2}{9s} \tag{3.17}$$

We can then substitute equations (3.16) and (3.17) into the expression for q in equation (3.12) to obtain

$$\frac{\alpha^6 c_q^6}{729 s^3} + s^3 = \frac{\alpha c_q}{2\eta} + \frac{2\alpha^3 c_q^3}{27} \tag{3.18}$$

which can be re-arranged to give a quadratic equation in s^3:

$$s^6 - \left(\frac{\alpha c_q}{2\eta} + \frac{2\alpha^3 c_q^3}{27}\right) s^3 + \frac{\alpha^6 c_q^6}{729} = 0 \tag{3.19}$$

We can use the quadratic formula on this to get an expression for s^3:

$$\begin{aligned} s^3 &= \frac{1}{2}\left[\frac{\alpha c_q}{2\eta} + \frac{2\alpha^3 c_q^3}{27} \pm \sqrt{\left(\frac{\alpha c_q}{2\eta} + \frac{2\alpha^3 c_q^3}{27}\right)^2 - \frac{4\alpha^6 c_q^6}{729}}\right] \\ &= \frac{1}{2}\left[\frac{\alpha c_q}{2\eta} + \frac{2\alpha^3 c_q^3}{27} \pm \sqrt{\frac{\alpha^2 c_q^2}{4\eta^2} + \frac{2\alpha^4 c_q^4}{27\eta}}\right] \\ &= \frac{\alpha c_q}{4\eta} + \frac{\alpha^3 c_q^3}{27} \pm \frac{\alpha c_q}{4\eta}\sqrt{1 + \frac{8\eta\alpha^2 c_q^2}{27}} \end{aligned} \tag{3.20}$$

Finally, substituting equations (3.16) and (3.20) into the expression for q in equation (3.12) gives us t^3:

$$\begin{aligned} t^3 &= q + s^3 \\ &= -\frac{\alpha c_q}{4\eta} - \frac{\alpha^3 c_q^3}{27} \pm \frac{\alpha c_q}{4\eta}\sqrt{1 + \frac{8\eta\alpha^2 c_q^2}{27}} \end{aligned} \tag{3.21}$$

It can be demonstrated that the root $X + a/3 = s - t$ is the same irrespective of which sign one chooses in equations (3.20) and (3.21). Taking the positive sign and substituting $a = -\alpha c_q$ gives

$$\begin{aligned} X &= \sqrt[3]{\frac{\alpha c_q}{4\eta} + \frac{\alpha^3 c_q^3}{27} + \frac{\alpha c_q}{4\eta}\sqrt{1 + \frac{8\eta\alpha^2 c_q^2}{27}}} \\ &\quad - \sqrt[3]{-\frac{\alpha c_q}{4\eta} - \frac{\alpha^3 c_q^3}{27} + \frac{\alpha c_q}{4\eta}\sqrt{1 + \frac{8\eta\alpha^2 c_q^2}{27}}} + \frac{\alpha c_q}{3} \\ &= \sqrt[3]{\frac{\alpha c_q}{4\eta} + \frac{\alpha^3 c_q^3}{27} + \frac{\alpha c_q}{4\eta}\sqrt{1 + \frac{8\eta\alpha^2 c_q^2}{27}}} \end{aligned}$$

$$+\sqrt[3]{\frac{\alpha c_q}{4\eta}+\frac{\alpha^3 c_q^3}{27}-\frac{\alpha c_q}{4\eta}\sqrt{1+\frac{8\eta\alpha^2 c_q^2}{27}}}+\frac{\alpha c_q}{3} \tag{3.22}$$

Thus, using equations (3.9) and (3.22) we can write that

$$\begin{aligned}\sqrt{1+\Delta\tilde{\Phi}_q} &= \sqrt[3]{\frac{\alpha c_q}{4\eta}+\frac{\alpha^3 c_q^3}{27}+\frac{\alpha c_q}{4\eta}\sqrt{1+\frac{8\eta\alpha^2 c_q^2}{27}}} \\ &\quad +\sqrt[3]{\frac{\alpha c_q}{4\eta}+\frac{\alpha^3 c_q^3}{27}-\frac{\alpha c_q}{4\eta}\sqrt{1+\frac{8\eta\alpha^2 c_q^2}{27}}}+\frac{\alpha c_q}{3} \\ &= \left(\frac{\alpha c_q}{4\eta}\right)^{1/3}\left[\sqrt[3]{1+\frac{4\alpha^2 c_q^2\eta}{27}+\sqrt{1+\frac{8\alpha^2 c_q^2\eta}{27}}}\right. \\ &\quad \left.+\sqrt[3]{1+\frac{4\alpha^2 c_q^2\eta}{27}-\sqrt{1+\frac{8\alpha^2 c_q^2\eta}{27}}}+\frac{4^{1/3}}{3}\alpha^{2/3}c_q^{2/3}\eta^{1/3}\right]\end{aligned} \tag{3.23}$$

We are now in a position to derive an expression for $\tilde{\Phi}_m(\alpha,\eta,n_q,B_q)$. Re-arranging equation (3.5) gives us

$$\tilde{\Phi}_m=\frac{1}{\eta}\ln\left[\frac{\alpha}{2\eta}\frac{n_m}{n_0}\frac{B_q}{B_m}(1-AC)^{-1}\left(1+\Delta\tilde{\Phi}_q\right)^{-3/2}\right]-\Delta\tilde{\Phi}_q \tag{3.24}$$

We can substitute for $\Delta\tilde{\Phi}_q$ using equation (3.23) and for c_q using equation (3.10) in this to obtain

$$\tilde{\Phi}_m=\frac{1}{\eta}\ln\left(\frac{2n_q}{n_0(1-AC)}\right)-\frac{3}{\eta}\ln\left[y(\Psi)\right]-\left(\frac{\alpha c_q}{4\eta}\right)^{2/3}\left[y(\Psi)\right]^2+1, \tag{3.25}$$

where

$$y(\Psi)=\sqrt[3]{1+\frac{4\Psi^3}{27}+\sqrt{1+\frac{8\Psi^3}{27}}}+\sqrt[3]{1+\frac{4\Psi^3}{27}-\sqrt{1+\frac{8\Psi^3}{27}}}+\frac{4^{1/3}}{3}\Psi \tag{3.26}$$

and

$$\Psi=\alpha^{2/3}c_q^{2/3}\eta^{1/3} \tag{3.27}$$

The constant C, contained in our expression for $\tilde{\Phi}_m$ in equation (3.25) and defined in equation (2.72), depends on $\tilde{\Phi}_m$. However, we can split up the first term on the RHS of equation (3.25) as follows:

$$\frac{1}{\eta}\ln\left(\frac{2n_q}{n_0(1-AC)}\right) = \frac{1}{\eta}\ln\left(2\frac{n_q}{n_0}\right) - \frac{1}{\eta}\ln(1-AC) \tag{3.28}$$

where typically, $\eta^{-1}\ln(1-AC)/\tilde{\Phi}_m \sim 10^{-4}$. Thus, we can safely neglect this term to obtain a more useful expression for $\tilde{\Phi}_m$:

$$\tilde{\Phi}_m = \frac{1}{\eta}\ln\left(2\frac{n_q}{n_0}\right) - \frac{3}{\eta}\ln[y(\Psi)] - \left(\frac{\alpha c_q}{4\eta}\right)^{2/3}[y(\Psi)]^2 + 1 \tag{3.29}$$

When $\tilde{\Phi}_m$ is evaluated using equation (3.29) with the exact values of n_q, B_q and ℓ_q, taken from a numerical solution, we find exact agreement with the numerically-derived value of $\tilde{\Phi}_m$, as expected. The expression in equation (3.29) is helpful because although $\tilde{\Phi}_m$ is a function of two variables, α and η, the expression contains $y(\Psi)$, a function of one variable which is easy to expand in a Taylor series to simplify the expression.

3.4 Taylor Series Approximations

3.4.1 ℓ_p and ℓ_q

It is very hard to pinpoint the exact location of ℓ_q analytically by solving the stationary point equations. However, the numerical solutions of Chapter 2 can be used to show that ℓ_q always lies very close to the B/n peak. The results of these numerical solutions are shown in Figure 3.5 for varying ion scale heights (h), current densities and electron temperatures. The ion scale height varies with ion temperature, which can range from 10^3 K to a few thousand K: this gives ion scale heights from 50 to a few hundred km. The values of the two small parameters, α and η, do have a small effect on the location of ℓ_q: as α (the normalised current density) increases, ℓ_q moves closer to the B/n peak; and as the ratio of ionospheric and magnetospheric electron temperatures, η, increases (implying a lower magnetospheric temperature), ℓ_q again moves closer to the B/n peak. However, in all applicable cases, the difference in height is no more than 10%. As a result of this, we can make the approximations $n_q \approx n_p$ and $B_q \approx B_p$ in the analytical solution, and obtain a very accurate approximation to $\tilde{\Phi}_m$. Thus, we can approximate the exact solution by replacing c_q, defined in equation (3.10), with

$$c_p = \left(\frac{n_m}{n_p}\right)\left(\frac{B_p}{B_m}\right) \tag{3.30}$$

Figure 3.5 shows an almost linear relationship between the B/n location and ion scale height, h. This work illustrates that, not surprisingly, the ion scale height plays the major role in determining the position of the B/n peak, and hence of ℓ_q. This agrees with work on the prevalence of beams in the winter auroral region *(Carlson et al. (1998), Cattell et al. (2004))*, which indicate the important role played by the scale height and number density.

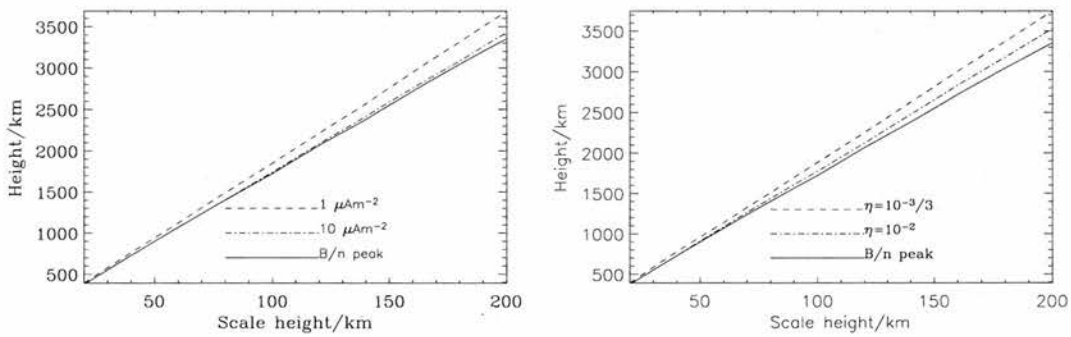

Figure 3.5: The location of ℓ_q (the stationary point, dashed and dot-dashed lines) and ℓ_p (the B/n peak, solid line) plotted against ion scale height for different values of α (left) and η (right). In the left graph, η is taken to be 10^{-3}, which corresponds, for example, to ionospheric and magnetospheric electron temperatures of 1 eV and 1 keV respectively. In the right graph, α is fixed at 1×10^{-5}, corresponding to a downward current density at ℓ_m of 1 μAm^{-2}. This figure shows that ℓ_q is always close to the B/n peak, so we can make the assumption that $n_q \approx n_p$ and $B_q \approx B_p$ in our analytical solution.

3.4.2 Taylor series: $\Psi \ll 0$

Firstly, we assume that $\Psi = \alpha^{2/3} c_p^{2/3} \eta^{1/3}$ is small, which corresponds to cases where α and η are both small, implying small current densities and moderate to high magnetospheric temperatures. It is possible to derive a Taylor series of $y(\Psi)$ in equation (3.26) about $\Psi = 0$. Firstly, we note that

$$y(0) = 2^{1/3} \tag{3.31}$$

It is convenient to write

$$y(\Psi) = a_1^{1/3} + a_2^{1/3} + \frac{4^{1/3}}{3}\Psi \tag{3.32}$$

where

$$\begin{aligned} a_1 &= 1 + \frac{4\Psi^3}{27} - \sqrt{1 + \frac{8\Psi^3}{27}} \\ a_2 &= 1 + \frac{4\Psi^3}{27} + \sqrt{1 + \frac{8\Psi^3}{27}} \end{aligned} \tag{3.33}$$

Expanding a_1 and a_2 for small Ψ yields

Table 3.1: Table of derivatives of a_1 and a_2. These can be used to calculate the values of the derivatives of $y(\Psi)$ at $\Psi = 0$.

a_1	$8\Psi^6/729 + O(\Psi^9)$	a_2	$2 + 8\Psi^3/27 + O(\Psi^6)$
a_1'	$48\Psi^5/729 + O(\Psi^8)$	a_2'	$8\Psi^2/9 + O(\Psi^5)$
a_1''	$240\Psi^4/729 + O(\Psi^7)$	a_2''	$16\Psi/9 + O(\Psi^4)$
a_1'''	$960\Psi^3/729 + O(\Psi^6)$	a_2'''	$16/9 + O(\Psi^3)$

$$\begin{aligned} a_1 &= 1 + \frac{4\Psi^3}{27} - \left[1 + \frac{1}{2}\frac{8\Psi^3}{27} - \frac{1}{8}\left(\frac{8\Psi^3}{27}\right)^2 + O(\Psi^9)\right] \\ &= \frac{8\Psi^6}{729} + O(\Psi^9) \end{aligned} \tag{3.34}$$

Similarly,

$$\begin{aligned} a_2 &= 1 + \frac{4\Psi^3}{27} + \left[1 + \frac{1}{2}\frac{8\Psi^3}{27} + O(\Psi^6)\right] \\ &= 2 + \frac{8\Psi^3}{27} + O(\Psi^6) \end{aligned} \tag{3.35}$$

Thus, we can calculate the leading order of the derivatives of a_1 and a_2, as shown in Table 3.1. Care must be taken with the order of neglected terms, as different expressions end up being added together in this analysis.

Taking the derivative of equation (3.32), we write

$$y'(\Psi) = \frac{1}{3}a_1^{-2/3}a_1' + \frac{1}{3}a_2^{-2/3}a_2' + \frac{4^{1/3}}{3} \tag{3.36}$$

We can examine the limit of the first term:

$$\lim_{\Psi\to 0}\left[a_1^{-2/3}a_1'\right] = \lim_{\Psi\to 0}\left[\left(\frac{8\Psi^6}{729} + O(\Psi^9)\right)^{-2/3}\left(\frac{48\Psi^5}{729} + O(\Psi^8)\right)\right]$$

$$\begin{aligned}
&= \lim_{\Psi\to 0}\left[\frac{81\Psi^{-4}}{4}\left(1+O(\Psi^3)\right)^{-2/3}\left(\frac{48\Psi^5}{729}+O(\Psi^8)\right)\right]\\
&= \lim_{\Psi\to 0}\left[\frac{81\Psi^{-4}}{4}\left(1+O(\Psi^3)\right)\left(\frac{48\Psi^5}{729}+O(\Psi^8)\right)\right]\\
&= \lim_{\Psi\to 0}\left[\frac{4\Psi}{3}+O(\Psi^4)\right]\\
&= 0
\end{aligned} \tag{3.37}$$

The same can be done for the second term:

$$\begin{aligned}
\lim_{\Psi\to 0}\left[a_2^{-2/3}a_2'\right] &= \lim_{\Psi\to 0}\left[\left(2+\frac{8\Psi^3}{27}+O(\Psi^6)\right)^{-2/3}\left(\frac{8\Psi^2}{9}+O(\Psi^5)\right)\right]\\
&= \lim_{\Psi\to 0}\left[2^{-2/3}\left(1+\frac{4\Psi^3}{27}+O(\Psi^6)\right)^{-2/3}\left(\frac{8\Psi^2}{9}+O(\Psi^5)\right)\right]\\
&= \lim_{\Psi\to 0}\left[2^{-2/3}\left(1+O(\Psi^3)\right)\left(\frac{8\Psi^2}{9}+O(\Psi^5)\right)\right]\\
&= \lim_{\Psi\to 0}\left[\frac{8\left(2^{-2/3}\right)\Psi^2}{9}+O(\Psi^5)\right]\\
&= 0
\end{aligned} \tag{3.38}$$

Thus, substituting the limits in equations (3.37) and (3.38) into the expression in (3.36), we see that

$$y'(\Psi) = \frac{4^{1/3}}{3} \tag{3.39}$$

Now we need to examine the second derivative of $y(\Psi)$, by differentiating equation (3.36):

$$y''(\Psi) = -\frac{2}{9}a_1^{-5/3}(a_1')^2 + \frac{1}{3}a_1^{-2/3}a_1'' - \frac{2}{9}a_2^{-5/3}(a_2')^2 + \frac{1}{3}a_2^{-2/3}a_2'' \tag{3.40}$$

We now find the limit of each term in turn:

$$\begin{aligned}
\lim_{\Psi\to 0}\left[-\frac{2}{9}a_1^{-5/3}(a_1')^2\right] &= \lim_{\Psi\to 0}\left[-\frac{2}{9}\left(\frac{8\Psi^6}{729}+O(\Psi^9)\right)^{-5/3}\left(\frac{48\Psi^5}{729}+O(\Psi^8)\right)^2\right]\\
&= \lim_{\Psi\to 0}\left[-\frac{2}{9}\left(\frac{8\Psi^6}{729}\right)^{-5/3}\left(1+O(\Psi^3)\right)^{-5/3}\left(\frac{48\Psi^5}{729}\right)^2\left(1+O(\Psi^3)\right)^2\right]\\
&= \lim_{\Psi\to 0}\left[-\frac{16}{9}\Psi^{-10}\Psi^{10}\left(1+O(\Psi^3)\right)\left(1+O(\Psi^3)\right)\right]
\end{aligned}$$

$$\begin{aligned} &= \lim_{\Psi\to 0}\left[-\frac{16}{9}\left(1+O(\Psi^3)\right)\right] \\ &= -\frac{16}{9} \end{aligned} \tag{3.41}$$

$$\begin{aligned} \lim_{\Psi\to 0}\left[\frac{1}{3}a_1^{-2/3}a_1''\right] &= \lim_{\Psi\to 0}\left[\frac{1}{3}\left(\frac{8\Psi^6}{729}+O(\Psi^9)\right)^{-2/3}\left(\frac{240\Psi^4}{729}+O(\Psi^7)\right)\right] \\ &= \lim_{\Psi\to 0}\left[\frac{1}{3}\left(\frac{8\Psi^6}{729}\right)^{-2/3}\left(1+O(\Psi^3)\right)^{-2/3}\left(\frac{240\Psi^4}{729}\right)\left(1+O(\Psi^3)\right)\right] \\ &= \lim_{\Psi\to 0}\left[\frac{20}{9}\left(1+O(\Psi^3)\right)\left(1+O(\Psi^3)\right)\right] \\ &= \lim_{\Psi\to 0}\left[\frac{20}{9}\left(1+O(\Psi^3)\right)\right] \\ &= \frac{20}{9} \end{aligned} \tag{3.42}$$

$$\begin{aligned} \lim_{\Psi\to 0}\left[-\frac{2}{9}a_2^{-5/3}\left(a_2'\right)^2\right] &= \lim_{\Psi\to 0}\left[-\frac{2}{9}\left(2+\frac{8\Psi^3}{27}+O(\Psi^6)\right)^{-5/3}\left(\frac{8\Psi^2}{9}+O(\Psi^5)\right)^2\right] \\ &= \lim_{\Psi\to 0}\left[-\frac{2}{9}(2^{-5/3})\left(1+\frac{4\Psi^3}{27}+O(\Psi^6)\right)^{-5/3}\left(\frac{8\Psi^2}{9}\right)^2\left(1+O(\Psi^3)\right)^2\right] \\ &= \lim_{\Psi\to 0}\left[-\frac{128\left(2^{-5/3}\right)\Psi^4}{729}\left(1+O(\Psi^3)\right)\left(1+O(\Psi^3)\right)\right] \\ &= \lim_{\Psi\to 0}\left[-\frac{128\left(2^{-5/3}\right)\Psi^4}{729}\left(1+O(\Psi^3)\right)\right] \\ &= 0 \end{aligned} \tag{3.43}$$

$$\begin{aligned} \lim_{\Psi\to 0}\left[\frac{1}{3}a_2^{-2/3}a_2''\right] &= \lim_{\Psi\to 0}\left[\frac{1}{3}\left(2+\frac{8\Psi^3}{27}+O(\Psi^6)\right)^{-2/3}\left(\frac{16\Psi}{9}+O(\Psi^4)\right)\right] \\ &= \lim_{\Psi\to 0}\left[\frac{1}{3}\left(2^{-2/3}\right)\left(1+\frac{4\Psi^3}{27}+O(\Psi^6)\right)^{-2/3}\left(\frac{16\Psi}{9}\right)\left(1+O(\Psi^3)\right)\right] \\ &= \lim_{\Psi\to 0}\left[\frac{16\left(2^{-2/3}\right)\Psi}{27}\left(1+O(\Psi^3)\right)\left(1+O(\Psi^3)\right)\right] \\ &= \lim_{\Psi\to 0}\left[\frac{16\left(2^{-2/3}\right)\Psi}{27}\left(1+O(\Psi^3)\right)\right] \\ &= 0 \end{aligned} \tag{3.44}$$

By adding these four limits, we obtain

$$y''(0) = \frac{4}{9} \tag{3.45}$$

Thus, we can use equations (3.31), (3.39) and (3.45) to see that the Taylor series expansion of $y(\Psi)$ about $\Psi = 0$ is

$$y(\Psi) = 2^{1/3} + \frac{4^{1/3}}{3}\Psi + \frac{2}{9}\Psi^2 + O(\Psi^3) \tag{3.46}$$

Substituting this into equation (3.29), and assuming that $c_p \approx c_q$ since $n_q \approx n_p$ and $B_q \approx B_p$

$$\begin{aligned}
\tilde{\Phi}_m(\alpha,\eta) &\approx \frac{1}{\eta}\ln\left(\frac{2n_p}{n_0}\right) - \frac{3}{\eta}\ln\left(2^{1/3} + \frac{4^{1/3}}{3}\Psi + \frac{2}{9}\Psi^2\right) \\
&\quad - \left(\frac{\alpha c_p}{4\eta}\right)^{2/3}\left(2^{1/3} + \frac{4^{1/3}}{3}\Psi + \frac{2}{9}\Psi^2\right)^2 + 1 \\
&\approx \frac{1}{\eta}\ln\left(\frac{2n_p}{n_0}\right) - \frac{1}{\eta}\ln 2 - \frac{3}{\eta}\ln\left(1 + \frac{2^{1/3}}{3}\Psi + \frac{2^{2/3}}{9}\Psi^2\right) \\
&\quad - \left(\frac{\alpha c_p}{4\eta}\right)^{2/3}\left(2^{2/3} + \frac{2(2^{1/3})(4^{1/3})}{3}\Psi + \left(\frac{4^{2/3}}{9} + \frac{4(2^{1/3})}{9}\right)\Psi^2\right) + 1
\end{aligned} \tag{3.47}$$

Noting that $\ln(1+x) \approx x - x^2/2$ for small x, we can simplify the above expression to give

$$\tilde{\Phi}_m(\alpha,\eta) \approx \frac{1}{\eta}\ln\left(\frac{n_p}{n_0}\right) - 3\left(\frac{\alpha c_p}{2\eta}\right)^{\frac{2}{3}} - \frac{1}{2^{1/3}}\left(\frac{\alpha^{4/3}c_p^{4/3}}{\eta^{1/3}}\right) - \frac{\alpha^2 c_p^2}{3} + O\left(\alpha^{8/3}c_p^{8/3}\eta^{1/3}\right) \tag{3.48}$$

Finally, it is possible to neglect the first term on the right hand side, since $n_p \approx n_0$. (When $h = 100$ km and $n_m/n_0 = 10^6$, $n_p = 1.038 n_0$.) Thus, the expansion can be simplified to

$$\tilde{\Phi}_m(\alpha,\eta) \approx -3\left(\frac{\alpha c_p}{2\eta}\right)^{\frac{2}{3}} - \frac{1}{2^{1/3}}\left(\frac{\alpha^{4/3}c_p^{4/3}}{\eta^{1/3}}\right) - \frac{\alpha^2 c_p^2}{3} \tag{3.49}$$

3.4.3 Taylor series: $\Psi \gg 1$

The other possibility is that Ψ is large, which implies large values of α and η i.e. large current densities and low magnetospheric temperatures. Performing a Taylor expansion of equation (3.26) about $\Psi = \infty$ is equivalent to expanding $y(1/\Psi)$ about $1/\Psi = \zeta = 0$. So, we can manipulate equation (3.26) to obtain

$$\begin{aligned}\zeta y(\zeta) &= \sqrt[3]{\frac{4}{27}+\zeta^3-\sqrt{\frac{8}{27}}\zeta^{3/2}\sqrt{1+\frac{27}{8}\zeta^3}} \\ &\quad +\sqrt[3]{\frac{4}{27}+\zeta^3+\sqrt{\frac{8}{27}}\zeta^{3/2}\sqrt{1+\frac{27}{8}\zeta^3}}+\frac{4^{\frac{1}{3}}}{3}\end{aligned} \tag{3.50}$$

Letting $\zeta y(\zeta) = Y(\zeta)$, it is convenient to write

$$Y(\zeta) = b_1^{1/3} + b_2^{1/3} + \frac{4^{1/3}}{3} \tag{3.51}$$

where

$$\begin{aligned}b_1 &= \frac{4}{27}+\zeta^3-\sqrt{\frac{8}{27}}\zeta^{3/2}\sqrt{1+\frac{27}{8}\zeta^3} \\ b_2 &= \frac{4}{27}+\zeta^3+\sqrt{\frac{8}{27}}\zeta^{3/2}\sqrt{1+\frac{27}{8}\zeta^3}\end{aligned} \tag{3.52}$$

Expanding b_1 and b_2 tells us their leading order terms, which will aid us when we find the Taylor series of $Y(\zeta)$. So,

$$\begin{aligned}b_1 &= \frac{4}{27}+\zeta^3-\sqrt{\frac{8}{27}}\zeta^{3/2}\left(1+\frac{27}{16}\zeta^3+O(\zeta^6)\right) \\ &= \frac{4}{27}-\frac{2}{3}\sqrt{\frac{2}{3}}\zeta^{3/2}+\zeta^3+O(\zeta^{9/2})\end{aligned} \tag{3.53}$$

Similarly,

$$\begin{aligned}b_2 &= \frac{4}{27}+\zeta^3+\sqrt{\frac{8}{27}}\zeta^{3/2}\left(1+\frac{27}{16}\zeta^3+O(\zeta^6)\right) \\ &= \frac{4}{27}+\frac{2}{3}\sqrt{\frac{2}{3}}\zeta^{3/2}+\zeta^3+O(\zeta^{9/2})\end{aligned} \tag{3.54}$$

Using the same methodology as in the previous section, we can calculate the leading order of the derivatives of b_1 and b_2, shown in table 3.2.

Firstly, we can substitute $\zeta = 0$ into equation (3.51) using equation (3.52) to see that

Table 3.2: Table of derivatives of b_1 and b_2. These can be used to calculate the values of the derivatives of $Y(\zeta)$ at $\zeta = 0$.

b_1	$\frac{4}{27} - \frac{2}{3}\sqrt{\frac{2}{3}}\zeta^{3/2} + \zeta^3 + O(\zeta^{9/2})$	b_2	$\frac{4}{27} + \frac{2}{3}\sqrt{\frac{2}{3}}\zeta^{3/2} + \zeta^3 + O(\zeta^{9/2})$
b_1'	$-\sqrt{\frac{2}{3}}\zeta^{1/2} + 3\zeta^2 + O(\zeta^{7/2})$	b_2'	$\sqrt{\frac{2}{3}}\zeta^{1/2} + 3\zeta^2 + O(\zeta^{7/2})$
b_1''	$-\frac{1}{2}\sqrt{\frac{2}{3}}\zeta^{-1/2} + 6\zeta + O(\zeta^{5/2})$	b_2''	$\frac{1}{2}\sqrt{\frac{2}{3}}\zeta^{-1/2} + 6\zeta + O(\zeta^{5/2})$
b_1'''	$\frac{1}{4}\sqrt{\frac{2}{3}}\zeta^{-3/2} + 6 + O(\zeta^{3/2})$	b_2'''	$-\frac{1}{4}\sqrt{\frac{2}{3}}\zeta^{-3/2} + 6 + O(\zeta^{3/2})$

$$Y(0) = 4^{1/3} \tag{3.55}$$

Taking the derivative of equation (3.51), we find that

$$Y'(\zeta) = \frac{1}{3}b_1^{-2/3}b_1' + \frac{1}{3}b_2^{-2/3}b_2' \tag{3.56}$$

Examining the limit of the first term,

$$\begin{aligned}
\lim_{\zeta\to 0}\left[b_1^{-2/3}b_1'\right] &= \lim_{\zeta\to 0}\left[\left(\frac{4}{27} + O(\zeta^{3/2})\right)^{-2/3}\left(-\sqrt{\frac{2}{3}}\zeta^{1/2} + O(\zeta^2)\right)\right] \\
&= \lim_{\zeta\to 0}\left[-\left(\frac{27}{4}\right)^{2/3}\sqrt{\frac{2}{3}}\zeta^{1/2} + O(\zeta^2)\right] \\
&= 0
\end{aligned} \tag{3.57}$$

Similarly,

$$\lim_{\zeta\to 0}\left[b_2^{-2/3}b_2'\right] = 0 \tag{3.58}$$

Substituting equations (3.57) and (3.58) into (3.56), we see that

$$Y'(0) = 0 \tag{3.59}$$

We now need to examine the second derivative of $Y(\zeta)$, obtained by differentiating equation (3.56):

$$Y''(\zeta) = -\frac{2}{9}b_1^{-5/3}(b_1')^2 + \frac{1}{3}b_1^{-2/3}b_1'' - \frac{2}{9}b_2^{-5/3}(b_2')^2 + \frac{1}{3}b_2^{-2/3}b_2'' \tag{3.60}$$

Using the same methods as above, it can be shown that

$$\begin{aligned} \lim_{\zeta\to 0}\left[b_1^{-5/3}(b_1')^2\right] &= \lim_{\zeta\to 0}\left[b_2^{-5/3}(b_2')^2\right] \\ &= 0 \end{aligned} \tag{3.61}$$

It is not possible to find the limits of the second and fourth terms on the right hand side of equation (3.60) separately, since both $\sim \zeta^{-1}$. However, we can find the limit of the sum of these two terms:

$$\begin{aligned} \lim_{\zeta\to 0}\left[b_1^{-2/3}b_1'' + b_2^{-2/3}b_2''\right] &= \lim_{\zeta\to 0}\left[\left(\frac{4}{27}+O(\zeta^{3/2})\right)^{-2/3}\left(\left(-\frac{1}{2}\sqrt{\frac{2}{3}}\zeta^{-1/2}+6\zeta+O(\zeta^{5/2})\right)\right.\right. \\ &\quad \left.\left.+\left(\frac{1}{2}\sqrt{\frac{2}{3}}\zeta^{-1/2}+6\zeta+O(\zeta^{5/2})\right)\right)\right] \\ &= \lim_{\zeta\to 0}\left[\frac{9}{4^{2/3}}\left(1+O(\zeta^{3/2})\right)\left(12\zeta+O(\zeta^{5/2})\right)\right] \\ &= \lim_{\zeta\to 0}\left[\frac{108}{4^{2/3}}\zeta+O(\zeta^{5/2})\right] \\ &= 0 \end{aligned} \tag{3.62}$$

Thus, it is clear that

$$Y''(0) = 0 \tag{3.63}$$

So, we need to look at the third derivative of Y, obtained by differentiating equation (3.60) again with respect to ζ:

$$\begin{aligned} Y'''(\zeta) &= \frac{10}{27}b_1^{-8/3}(b_1')^3 - \frac{2}{3}b_1^{-5/3}b_1'b_1'' + \frac{1}{3}b_1^{-2/3}b_1''' \\ &+ \frac{10}{27}b_2^{-8/3}(b_2')^3 - \frac{2}{3}b_2^{-5/3}b_2'b_2'' + \frac{1}{3}b_2^{-2/3}b_2''' \end{aligned} \tag{3.64}$$

Terms 1 and 4 on the RHS of equation (3.64) have limit 0. Examining the limit of term 2, we can see that

$$\begin{aligned}\lim_{\zeta\to 0}\left[-\frac{2}{3}b_1^{-5/3}\right] &= -\frac{2}{3}\lim_{\zeta\to 0}\left[\left(\frac{4}{27}+O(\zeta^{3/2})\right)^{-5/3}\right] \\ &= -\frac{3^4}{8}2^{2/3} \end{aligned} \tag{3.65}$$

Also,

$$\begin{aligned}\lim_{\zeta\to 0}[b_1' b_1''] &= \lim_{\zeta\to 0}\left[\left(-\sqrt{\frac{2}{3}}\zeta^{1/2}+O(\zeta^2)\right)\left(-\frac{1}{2}\sqrt{\frac{2}{3}}\zeta^{-1/2}+O(\zeta)\right)\right] \\ &= \lim_{\zeta\to 0}\left[\frac{1}{3}+O(\zeta^{3/2})\right] \\ &= \frac{1}{3} \end{aligned} \tag{3.66}$$

Using these two limits, we can see that

$$\lim_{\zeta\to 0}\left[-\frac{2}{3}b_1^{-5/3}b_1' b_1''\right] = -\frac{27}{8}2^{2/3} \tag{3.67}$$

Similarly, the limit of term 5 can also be found to be

$$\lim_{\zeta\to 0}\left[-\frac{2}{3}b_2^{-5/3}b_2' b_2''\right] = -\frac{27}{8}2^{2/3} \tag{3.68}$$

Terms 3 and 6 both have a leading order of $b^{-3/2}$, but when added together this term cancels, and we find that

$$\lim_{\zeta\to 0}\left[\frac{1}{3}b_1^{-2/3}b_1''' + \frac{1}{3}b_2^{-2/3}b_2'''\right] = \frac{39}{4}2^{2/3} \tag{3.69}$$

Using these limits, we can deducc that

$$Y'''(0) = 3(2^{2/3}) \tag{3.70}$$

Using equations (3.55), (3.59), (3.63) and (3.70), we can see that the Taylor expansion for $Y(\zeta)$ is

$$Y(\zeta) = 4^{1/3} + \frac{\zeta^3}{2^{1/3}} + O(\zeta^4) \tag{3.71}$$

Thus, the Taylor expansion of equation (3.26) in terms of Ψ is

$$y(\Psi) = 4^{1/3}\Psi + \frac{1}{2^{1/3}\Psi^2} + O(\Psi^{-3}) \tag{3.72}$$

Now, we can substitute expansion (3.72) into equation (3.29), noting that $c_q \approx c_p$ since $n_q \approx n_p$ and $B_q \approx B_p$:

$$\begin{aligned}
\tilde{\Phi}_m(\alpha,\eta) &\approx \frac{1}{\eta}\ln\left(2\frac{n_p}{n_0}\right) - \frac{3}{\eta}\ln\left(4^{1/3}\Psi + \frac{1}{2^{1/3}\Psi^2} + O(\Psi^{-3})\right) \\
&\quad - \left(\frac{\alpha c_p}{4\eta}\right)^{2/3}\left(4^{1/3}\Psi + \frac{1}{2^{1/3}\Psi^2} + O(\Psi^{-3})\right)^2 + 1 \\
&\approx \frac{1}{\eta}\ln\left(2\frac{n_p}{n_0}\right) - \frac{1}{\eta}\ln\left(4\Psi^3\right) - \frac{3}{\eta}\ln\left(1 + \frac{1}{2\Psi^3} + 0(\Psi^{-4})\right) \\
&\quad - \left(\frac{\alpha c_p}{4\eta}\right)^{2/3}\left(4^{2/3}\Psi^2 + \frac{2(4^{1/3})}{2^{1/3}\Psi} + O(\Psi^{-2})\right) + 1
\end{aligned} \tag{3.73}$$

Now, we can simplify this by noting that $\ln(1+x) \approx x + 0(x^2)$ for small x, and by substituting in equation (3.27) to see that

$$\tilde{\Phi}_m(\alpha,\eta) \approx \frac{1}{\eta}\ln\left(\frac{n_p}{n_0}\right) - \frac{1}{\eta}\ln\left(2\alpha^2 c_p^2\eta\right) - \alpha^2 c_p^2 - \frac{1}{\eta} + 1 + O\left(\alpha^{-2/3}c_p^{-2/3}\eta^{-4/3}\right) \tag{3.74}$$

We can simplify this still further by noting that we can drop the first term on the RHS, since $n_p \approx n_0$, to give

$$\tilde{\Phi}_m(\alpha,\eta) \approx -\frac{1}{\eta}\ln\left(2\alpha^2 c_p^2\eta\right) - \alpha^2 c_p^2 - \frac{1}{\eta} \tag{3.75}$$

3.5 Dimensional expressions

Whilst it is useful to work in terms of dimensionless quantities (α, η and $\Delta\tilde{\Phi}$) to obtain expressions for $\tilde{\Phi}_m$ (the total normalised potential increase along the field line) it can be informative to return to dimensional quantities in order to gain further physical insight. Substituting equations (2.62) and (2.66) into the small-Ψ expression for $\tilde{\Phi}_m$ in equation (3.49), noting that $\tilde{\Phi}_m = 2e\phi_m/ma_m^2$ and $\phi(\ell_0) = 0$, we obtain:

$$-\phi_m = \frac{3}{2}\left(\frac{m^{1/2}j_m B_p kT}{e^{5/2}n_p B_m}\right)^{\frac{2}{3}} + \frac{1}{2}\left(\frac{m^2 j_m^4 B_p^4 kT}{e^7 n_p^4 B_m^4}\right)^{\frac{1}{3}} + \frac{m}{6e^3}\frac{j_m^2 B_p^2}{n_p^2 B_m^2} \tag{3.76}$$

We can obtain a similar expression for $\tilde{\Phi}_m$ for large Ψ using equation (3.75):

$$-\phi_m = \frac{kT}{e} \ln\left(\frac{j_m^2 B_p^2}{n_p^2 e^2 B_m^2} \frac{m}{kT}\right) + \frac{m}{2e^3} \frac{j_m^2 B_p^2}{n_p^2 B_m^2} + \frac{kT}{e} \tag{3.77}$$

It is interesting to note that both of these expressions for ϕ_m are independent of the ionospheric temperature, a_m, and ionospheric electron number density, n_m. This highlights the fact that the precise properties of the ionosphere are unimportant to the acceleration of the field-aligned electrons: the ionosphere is simply the reservoir from which the necessary electrons are extracted. It is the properties of the B/n peak which determine the solution.

3.5.1 Potential drop in terms of speeds

We can derive expressions for ϕ_m, the actual potential increase along the field line, in terms of two characteristic speeds: the mean electron drift speed at the B/n peak, u_p, defined as

$$u_p = \frac{j_p}{n_p e} \tag{3.78}$$

where $j_p = j_m B_p / B_m$, and the magnetospheric thermal velocity, v_{th}, given by

$$v_{th}^2 = \frac{2kT}{m} \tag{3.79}$$

If we substitute equations (3.78) and (3.79) into equation (3.27), we find that

$$\Psi^3 = \left(\frac{u_p}{v_{th}}\right)^2 \tag{3.80}$$

Thus, the small-Ψ expression for $\tilde{\Phi}_m$ in equation (3.49) corresponds to cases where $u_p \ll v_{th}$, i.e. for relatively small current densities and moderate to high magnetospheric electron temperatures. We substitute equations (3.78) and (3.79) into (3.76) to obtain an expression for ϕ_m in this regime:

$$-\phi_m = \frac{m}{2e}\left(3\left(\frac{u_p}{2}\right)^{2/3} v_{th}^{4/3} + \frac{u_p^{4/3} v_{th}^{2/3}}{2^{1/3}} + \frac{u_p^2}{3}\right) \tag{3.81}$$

In the alternative regime, where $\Psi > 1$ or $u_p \gg v_{th}$, implying higher current densities and lower magnetospheric electron temperatures, we substitute equations (3.78) and (3.79) into (3.77) to obtain:

$$-\phi_m = \frac{m}{2e}\left(v_{th}^2 \ln\left(2\frac{u_p^2}{v_{th}^2}\right) + u_p^2 + v_{th}^2\right) \tag{3.82}$$

3.5.2 Potential drop in terms of current densities

Alternatively, we can derive $\tilde{\Phi}_m$ in terms of two characteristic current densities: the beam current density at the B_n peak, written using equation (2.42) as

$$j_p = j_m \frac{B_p}{B_m} \tag{3.83}$$

and the field-aligned thermal current density, j_{th}, due to the downgoing component of the Maxwellian electron distribution (i.e. $0 < v_\parallel < \infty$, $0 < v_\perp < \infty$) at ℓ_0:

$$\begin{aligned} j_{th} &= -e\int_0^\infty v_\parallel f_M \, \mathrm{d}v_\parallel \int_0^\infty 2\pi v_\perp \, \mathrm{d}v_\perp \\ &= -en_0\sqrt{\frac{kT}{2\pi m}} \end{aligned} \tag{3.84}$$

where f_M is defined in equation (2.34) and we take $n_M = n_0$. This is identical to the current density carried by magnetospheric electrons at the ionosphere in the absence of a potential drop. Of course, we assume that these electrons mirror, so this population does not carry a net current. The parameter Ψ in equation (3.27) can now be written as

$$\Psi^3 = \frac{1}{4\pi}\frac{j_p^2}{j_{th}^2}\frac{n_0^2}{n_p^2}, \tag{3.85}$$

So, the small-Ψ expression (3.76), valid when $j_p \ll \mid j_{th} \mid$, can be written in terms of (3.83) and (3.84) to give

$$-\phi_m = \frac{m}{2e^3}\left(3\left(\frac{2\pi}{n_0^2 n_p}\right)^{2/3} j_p^{2/3} \mid j_{th} \mid^{4/3} + \left(\frac{2\pi}{n_0^2 n_p^4}\right)^{1/3} j_p^{4/3} \mid j_{th} \mid^{2/3} + \frac{j_p^2}{3n_p^2}\right) \tag{3.86}$$

A further simplification can be made to equation (3.86) by noting that $n_p \approx n_0$, giving

$$-\phi_m = \frac{m}{2e^3 n_0^2}\left(3\,(2\pi)^{2/3} j_p^{2/3} \mid j_{th} \mid^{4/3} + (2\pi)^{1/3} j_p^{4/3} \mid j_{th} \mid^{2/3} + j_p^2\right) \tag{3.87}$$

Similarly, the large-Ψ expression in equation (3.77), valid when $\mid j_{th} \mid \ll j_p$, can be written as

$$-\phi_m = \frac{m}{e^3}\left(\frac{2\pi}{n_0^2} j_{th}^2 \ln\left(\frac{j_p^2}{j_{th}^2}\frac{n_0^2}{2\pi n_p^2}\right) + \frac{j_p^2}{2n_p^2} + \frac{2\pi j_{th}^2}{n_0^2}\right) \tag{3.88}$$

We can make the same simplification ($n_p \approx n_0$) to equation (3.88) to obtain

$$-\phi_m = \frac{m}{e^3 n_0^2}\left(2\pi j_{th}^2 \ln\left(\frac{1}{2\pi}\frac{j_p^2}{j_{th}^2}\right) + \frac{j_p^2}{2} + 2\pi j_{th}^2\right) \tag{3.89}$$

3.6 Accuracy of Approximations

Equations (3.29), (3.26) and (3.27) give the analytical form of $\tilde{\Phi}_m$ if c_q is known. However, finding this parameter is awkward and involves numerical work, since the location of ℓ_q changes with α and η for a given equilibrium model. If we let $c_q \approx c_p$, which is easier to calculate (a range of values are given in Table 3.3), we obtain approximate relations for $\tilde{\Phi}_m$ which are easy to use.

The relative accuracy of the two approximations is shown in Figure 3.6 for two different values of η. In each case, $\Psi < 1$ for small current densities and the first approximation in equation (3.49) is accurate. Many relevant scenarios in the downward current region with low to moderate current densities and average ionospheric and magnetospheric electron temperatures satisfy $\Psi \ll 1$, so this approximation is valid. Even as α increases and Ψ approaches 1 and exceeds it, this approximation remains very accurate. Then, at some value of $\Psi \sim 1$, the first approximation loses accuracy as we enter a different regime where the second approximation in equation (3.75) should be adopted. In all cases for the standard parameters we have chosen, the appropriate approximation is valid to within 6.4% of the exact numerically-determined potential increase.

3.6.1 An example

In order to estimate the potential increase for a given event in the downward current region, the following steps should be carried out.

Step 1: Choose the parameters for the equilibrium model: the magnetospheric thermal electron energy (kT), the ionospheric electron thermal energy ($m_e a_m^2/2$), the ion number density at the base of the F region (n_m) and at ℓ_0 in the magnetosphere (n_0), the ion scale height (h), and the current density at the base of the F region (j_m). From these, calculate the dimensionless parameters α and η, from equations (2.62) and (2.66) respectively.

Step 2: Determine the parameter c_p given in equation (3.30). This can be done by using Table 3.3. Also determine the value of Ψ in equation (3.27), replacing c_q with c_p.

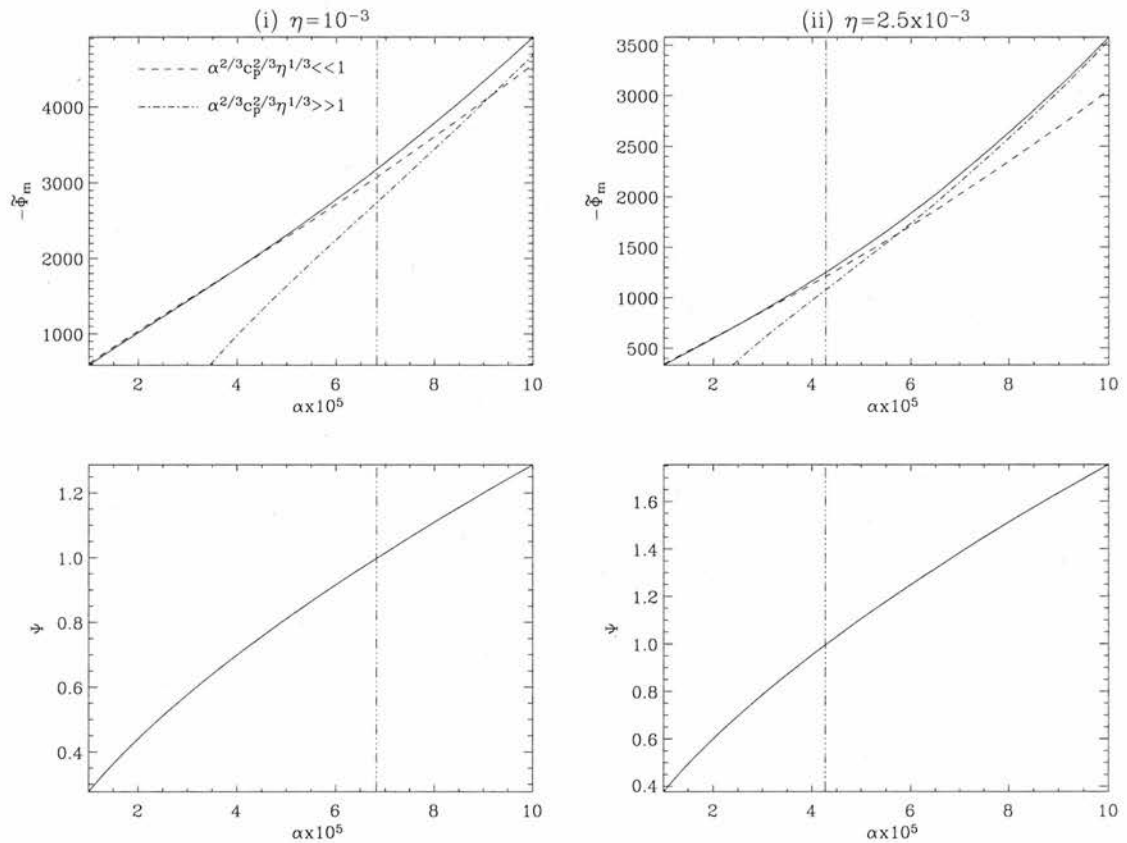

Figure 3.6: Graphs showing the regions of validity of the two Taylor expansions. The current densities run from ~1 to 10 μAm^{-2} (corresponding to α values of 1×10^{-5} to 1×10^{-4}); for an ionospheric electron temperature of 1 eV, η values of 10^{-3} and 2.5×10^{-3} correspond to magnetospheric electron temperatures of 1 keV and 400 eV respectively. In the top two figures, the solid line represents the actual values of $\tilde{\Phi}_m$ found by solving equation (2.70) numerically, or using the numerically determined values of n_q and B_q in equation (3.29). The dashed line shows the approximation given in equation (3.49), which is most accurate for small α and η, whilst the dotted-dashed line shows the approximation given in equation (3.75), most accurate for larger values of α and η. The bottom two graphs plot the corresponding values of Ψ, defined in equation (3.27), which is the variable in which we derive the Taylor series. The vertical dashed line indicates the point at which $\Psi = 1$ in each case. The first approximation is more accurate for $\Psi \leq 1.2$. When $\Psi \geq 1.2$, the second approximation should be adopted.

Step 3: Now there are two options. The first is to use equation (3.26) to determine $y(\Psi)$ and substitute into equation (3.29), using $n_q \approx n_0$ and $c_q \approx c_p$ to obtain $\tilde{\Phi}_m$. The second is to use the approximation in equation (3.49) if $\Psi < 1$, or the one in equation (3.75) if $\Psi > 1$. Note that $\tilde{\Phi}_m$ is negative for downward currents, and -$\tilde{\Phi}_m$ gives the total potential increase along the field line.

We now use this approach to approximate the potential in the FAST data given in Figure 2 of *Carlson et al. (1998a)*, shown here in Figure 2.1. This is taken at an altitude of around 3965 km, which we denote by ℓ_{FAST}. The current density at this altitude, j_{FAST}, varies from 1 to 2.5 μAm^{-2}, so we consider both of these cases. We use the current continuity condition in equation (2.42) to obtain corresponding values for j_m, which are 4.29 (case 1) and 10.7 (case 2) μAm^{-2}. These are high current densities, so this is a

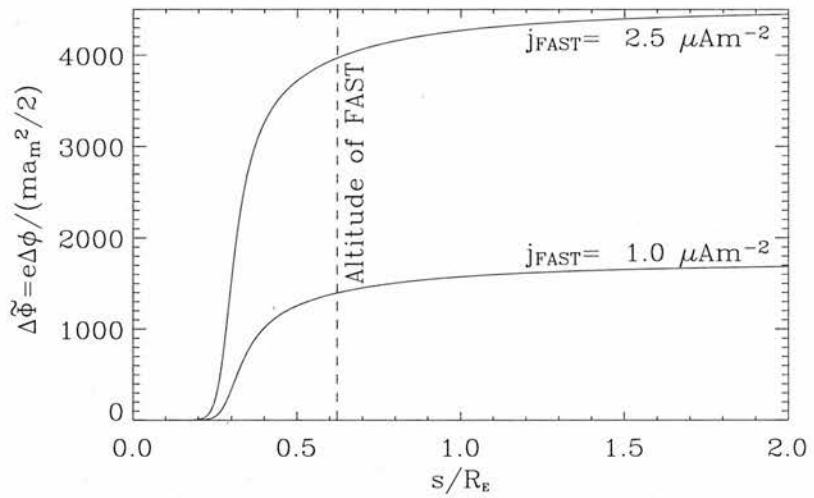

Figure 3.7: Comparison with data in *Carlson et al. (1998a)*, shown in Figure 2.1. Taking $j_m = 4.29$ and 10.7 μAm^{-2} gives current densities at FAST of 1 and 2.5 μAm^{-2} respectively. Taking $\eta = 10^{-3}$, an ionospheric temperature of 1 eV, $n_m/n_0 = 10^5$ and $h = 150$ km, we obtain $\Delta\tilde{\Phi}_{FAST}$ values of 1400 and 3970 V for each case, which correspond well with the bottom panel of their figure.

strong downward current event. We take typical ionospheric and magnetospheric electron temperatures of 1 eV and 1 keV, giving $\eta = 10^{-3}$; n_m is taken to be 10^{11} m^{-3}, slightly lower than used previously to account for the fact that this event occurred at night, giving $n_m/n_0 = 10^5$; finally, the ion scale height is taken to be 150 km, slightly larger than before to account for transverse ion heating effects which modify the distribution of ions. The results are shown in Figure 3.7; the total potential increase is 1730 V for case 1, and 4510 V for case 2. Most of the acceleration has taken place by ℓ_{FAST}, giving $\Delta\phi_{FAST} = 1400$ V for case 1, and 3970 V for case 2. These values show excellent agreement with the bottom panel of Figure 2 in *Carlson et al. (1998a)*, where ϕ_{FAST} was inferred from $\int \mathbf{E} \cdot \mathrm{ds}$ along the satellite trajectory. The potential in this figure varies from ~ 1 to ~ 4 kV.

The Taylor series expansions can be used for this example, where the B/n peak lies at 2200 km, and $c_p = 3.89 \times 10^4$.

Case 1: Here, $j_{FAST} = 1\ \mu\mathrm{Am}^{-2}$, giving $\alpha = 4.51 \times 10^{-4}$ and $\Psi = 0.675 < 1$. Thus, we use the expansion in equation (3.49) to give $\tilde{\Phi}_m \approx -1730$, which is accurate to 0.8%.

Case 2: Now, $j_{FAST} = 2.5\ \mu\mathrm{Am}^{-2}$, giving $\alpha = 1.13 \times 10^{-3}$ and $\Psi = 1.25$. Since this value is around 1, either expansion should give a good approximation. From equation (3.49), we obtain $\tilde{\Phi}_m = -4220$ eV, accurate to 6.4%; equation (3.75) yields $\tilde{\Phi}_m = -4270$ eV, accurate to 5.2%. This illustrates that both approximations still work well in the region $\Psi \approx 1$.

3.7 Discussion and Conclusions

The analysis presented in this chapter reveals that the B/n peak is central to the solution of the downward current region. Mathematically, the equations contain a stationary point which lies slightly beyond the B/n peak. Examination of this stationary point yields a near-exact solution for $\tilde{\Phi}_m$, the total potential increase along the field line (given the model parameters, and n_q and B_q). Taylor series expansions of the exact solution can be carried out to give two simplified non-linear current-voltage relations. Since the stationary point is so close to the B/n peak, approximations can be derived for which we use the number density and magnetic field strength at the B/n peak. One approximation is valid for lower current densities and moderate to high magnetospheric temperatures ($\sim$1 keV), whilst the other takes over for higher current densities and lower magnetospheric temperatures. Typically, the first expansion will be more useful for most downward current regions in the Earth's magnetosphere, except for events with particularly high current densities. Both of these expansions, when written in dimensional form, are independent of ionospheric equilibrium parameters, illustrating that the exact properties of the ionosphere are unimportant in this model.

Observations such as those in *Ergun et al. (2003a)* suggest that acceleration in the downward current region can occur over a very small distance (i.e. a double layer). A double layer does not satisfy quasi-neutrality, so in our model, it would be seen as a discontinuity. This can be achieved via a sharp decrease or change in ion number density at a certain altitude. We showed this in Chapter 2 using the number density profile from *Temerin and Carlson (1998)*. Just as *Knight (1973)*'s model of the upward current provides a good overview of the region as a whole, neglecting double layers, we describe the downward current region on a similarly large scale. Thus, we find a smooth transition in potential, but it is quite possible that this overall change is confined to sharp increases in potential contained within several double layers *(Andersson et al. (2002))*. In any case, the overall change in potential is likely to be similar in both cases. In Chapter 2, we find that it is the properties of the small region surrounding the B/n peak (containing the stationary point ℓ_q) which solely determine the total potential change $\tilde{\Phi}_m$. This has been corroborated by the analytical work presented in this Chapter, which shows that we can determine $\tilde{\Phi}_m$ simply by solving the stationary point equations at ℓ_q. If we were to include ion motion in this model, it is possible that the ion distribution would steepen into a double layer, which would preserve the single B/n peak and effectively move ℓ_q even closer to it: thus, our analysis should still be appropriate.

The location of the B/n peak is principally dependent upon the ion scale height and number density,

	5×10^4	1.0×10^5	5.0×10^5	1.0×10^6
50 km	3.514×10^4	6.924×10^4	3.346×10^5	6.595×10^5
100 km	2.621×10^4	5.103×10^4	2.398×10^5	4.671×10^5
150 km	2.019×10^4	3.890×10^4	1.786×10^5	3.446×10^5
200 km	1.593×10^4	3.041×10^4	1.369×10^5	2.619×10^5
250 km	1.281×10^4	2.426×10^4	1.073×10^5	2.039×10^5
300 km	1.046×10^4	1.967×10^4	8.571×10^4	1.619×10^5

Table 3.3: Values of the constant c_p for different ion number densities (n_m/n_0) and scale heights (h). The first row shows values of n_m/n_0, and the first column gives different values of h.

n_m/n_0. In *Cattell et al. (2004)*'s statistical survey of the occurrence of upward-accelerated electron beams, many more beams were observed on field lines where the ionospheric footpoint is in darkness than when it is illuminated. This makes sense in terms of the model, since at night time, the number density and scale height will be smaller due to lack of photoionisation. These two factors cause the B/n peak, and hence the stationary point, to move Earthward. With a smaller number density, the ionosphere will provide fewer charge carriers which, on encountering lower ion number densities due to the decreased scale height, will need to be accelerated at lower altitudes to meet the demands of quasi-neutrality and carry the required current.

The current-voltage relations derived here show good agreement with observational data. Qualitatively, our model predicts potential increases of $\sim$100 V to $\sim$1 kV, which tally well with observations of downward current regions. Quantitatively, our model agrees very well with the FAST data from *Carlson et al. (1998a)*, Figure 2. It will be desirable to make further comparisons with data to check consistency over a range of current densities.

Chapter 4

Upward field-aligned current model

4.1 Introduction

The upward current region has been more extensively observed and modelled than its downward counterpart, but there are still several outstanding issues to be resolved. Electrons of magnetospheric origin penetrate into the ionosphere the carry the current: to do this, they must have enough parallel kinetic energy to overcome the magnetic mirror force as they encounter higher and higher magnetic field strengths on approaching the Earth. To model this region, we must consider both the kinetics of motion and quasi-neutrality. Firstly, if we ignore the constraint of quasi-neutrality and set the electrostatic potential equal to zero along a field line, then magnetic moment conservation alone determines which electrons of a given magnetospheric electron distribution make it into the ionosphere without being mirrored, and hence form the source cone: these electrons carry a net current called the random thermal current. If we require a higher current density, an attractive electrostatic potential is needed to achieve this: it widens the source cone by allowing more of the magnetospheric electrons to overcome the magnetic mirror force and carry current.

Knight (1973) used kinetic theory to derive an overall linear current-voltage relation which has generally been verified by observational data. However, one big question remains: how is the potential distributed along the field line, and what controls its variation? Quasi-neutrality provides one key to answering this question. Just as in our downward current model of Chapter 2, this fundamental plasma property constrains the electrons to have the same number density profile as the heavier ions, which enables us to derive the potential variation along a field line. In this Chapter, we extend work by *Boström (2003)* and *Boström (2004)* to obtain potential variations for the upward current region; this enables us to find the location of the parallel electric field along the field line, and to determine which factors contribute to this electric field at different altitudes.

4.2 *Boström (2003)* model

Boström (2003) and *(2004)* describe the auroral current region by considering an auroral flux tube from the base of the F region in the ionosphere to an end-point in the magnetosphere, along which particles experience electrostatic and magnetic mirror forces. Böstrom considers motion of electrons and ions, but for our model, we concentrate solely on the former. Electron velocity (v), kinetic energy ($mv^2/2$), electrostatic potential (ϕ), current density (j), number density (n), and magnetic field strength (B) are normalised as follows:

$$u = v\sqrt{\frac{m}{kT_M}} \tag{4.1}$$

$$\tilde{u} = v\sqrt{\frac{m}{kT_I}} \tag{4.2}$$

$$W = \frac{mv^2}{2kT_M} = \frac{u^2}{2} \tag{4.3}$$

$$\tilde{W} = \frac{mv^2}{2kT_I} = \frac{\tilde{u}^2}{2} \tag{4.4}$$

$$U = \frac{e\phi}{kT_M} \tag{4.5}$$

$$i = \frac{j}{n_0 e}\sqrt{\frac{m}{kT_M}} \tag{4.6}$$

$$N = \frac{n}{n_0} \tag{4.7}$$

$$\zeta = \frac{B_I}{B} \tag{4.8}$$

where e and m are electron charge and mass, respectively, T_M is magnetospheric electron temperature, k is Boltzmann's constant, n_0 is magnetospheric number density, and B_I is the magnetic field strength at the ionospheric boundary. For ionospheric electrons, velocity and energy will be normalised by the ionospheric electron temperature, T_I, but the potential U will still be normalised by T_M throughout the solution for consistency. The subscripts I and M denote that a given quantity is to be evaluated at the ionospheric and magnetospheric ends, respectively. The electrostatic potential, U, is defined to be zero at the ionospheric end of the field line, and U_M at the magnetospheric end ($U_M < 0$ for upward currents), whilst ζ can serve as a field-aligned co-ordinate, where $\zeta_I = 1$ and $\zeta_M = B_I/B_M > 1$. Electron velocity

can be further subdivided into parallel velocity ($v_{\parallel}$) and perpendicular velocity ($v_{\perp}$), from which we obtain the following normalised velocities:

$$u_{\parallel} = v_{\parallel}\sqrt{\frac{m}{kT_M}} \tag{4.9}$$

$$u_{\perp} = v_{\perp}\sqrt{\frac{m}{kT_M}} \tag{4.10}$$

$$\tilde{u}_{\parallel} = v_{\parallel}\sqrt{\frac{m}{kT_I}} \tag{4.11}$$

$$\tilde{u}_{\perp} = v_{\perp}\sqrt{\frac{m}{kT_I}} \tag{4.12}$$

From these, normalised kinetic energies are obtained such that

$$W_{\parallel} = \frac{u_{\parallel}^2}{2};\ \tilde{W}_{\parallel} = \frac{\tilde{u}_{\parallel}^2}{2} \tag{4.13}$$

and

$$W_{\perp} = \frac{u_{\perp}^2}{2};\ \tilde{W}_{\perp} = \frac{\tilde{u}_{\perp}^2}{2} \tag{4.14}$$

Conservation of total energy for an electron tells us that

$$W_{\parallel}(\zeta) + W_{\perp}(\zeta) - U(\zeta) = W_{\parallel M} + W_{\perp M} - U_M \tag{4.15}$$

Conservation of the magnetic moment, μ, defined in equation (2.13), can be recast as

$$\zeta W_{\perp} = \zeta_M W_{\perp M} \tag{4.16}$$

4.3 Davisson accessibility condition

A given magnetospheric electron with initial parallel and perpendicular kinetic energies of $W_{\parallel M}$ and $W_{\perp M}$ only contributes to the current if it travels all the way down to the ionosphere, that is if $W_{\parallel}(\zeta) > 0,\ 1 < \zeta < \zeta_M$. Substituting equation (4.16) into (4.15) and rearranging yields an expression for $W_{\parallel}(\zeta)$; this must be positive for an electron to reach the point ζ:

$$W_{\parallel}(\zeta) = W_{\parallel M} + \left(1 - \frac{\zeta_M}{\zeta}\right) W_{\perp M} - U_M + U(\zeta) > 0 \tag{4.17}$$

Rearranging the expression on the RHS tells us that an electron reaches the point ζ if

$$W_{\parallel M} > \max \begin{cases} \Psi\left(W_{\perp M}, \zeta\right) = \left(\frac{\zeta_M}{\zeta} - 1\right) W_{\perp M} + U_M - U(\zeta) \\ 0 \end{cases} \tag{4.18}$$

The bottom line on the RHS is necessary, since the top expression may be negative, and we need to ensure that energy is a positive quantity. The above constitutes a necessary and sufficient condition for a magnetospheric electron to reach the ionosphere and form part of the source cone, if it is satisfied for all points along the field line, i.e. for $1 < \zeta < \zeta_M$. Now, evaluating equation (4.17) at the ionospheric end gives

$$W_{\parallel I} = W_{\parallel M} + (1 - \zeta_M) W_{\perp M} - U_M > 0 \tag{4.19}$$

which can be rearranged to tell us that an electron is part of the source cone if

$$W_{\parallel M} > \max \begin{cases} \Psi_I\left(W_{\perp M}\right) = \left(\zeta_M - 1\right) W_{\perp M} + U_M \\ 0 \end{cases} \tag{4.20}$$

This is a necessary condition for a magnetospheric electron to be part of the source cone, but not a sufficient one, since we do not know from (4.20) that (4.18) is satisfied at every point along the field line. This means that, in general, the particular distribution of the potential along the field line determines which electrons form the source cone, and hence how much current flows. Thus, in general, there is no unique current-voltage relation for the upward current region, since the same overall potential increase, U_M, can be distributed in different ways to modify the source cone and, hence, the current. If certain limitations are placed on the form of $U(\zeta)$, then condition (4.20) is just as restrictive as (4.18), with the result that the source cone population is independent of the potential variation, and a unique current-voltage relation does exist. In the upward current region where $U_M < 0$, we can find this condition when the top line of equation (4.18) is valid by rearranging it for $W_{\perp M}$.

$$W_{\perp M} < \frac{W_{\parallel M} + U(\zeta) - U_M}{\frac{\zeta_M}{\zeta} - 1} \tag{4.21}$$

which is most restrictive when $W_{\parallel M} = 0$, giving

$$W_{\perp M} < \frac{U(\zeta) - U_M}{\frac{\zeta_M}{\zeta} - 1} \tag{4.22}$$

When the bottom line of equation (4.18) is valid, the top line must be negative, and the same result follows. Similarly, rearranging the top line of equation (4.20) for $W_{\perp M}$ when $W_{\parallel M} = 0$ yields

$$W_{\perp M} < -\frac{U_M}{\zeta_M - 1} = k \tag{4.23}$$

Again, the same result follows when the bottom line of equation (4.20) is valid, since this implies that the top line must be negative. In order that the inequality in (4.23) is just as restrictive as that in (4.22) at every point along the field line, we require that

$$\begin{aligned} -\frac{U_M}{\zeta_M - 1} &< \frac{U(\zeta) - U_M}{\frac{\zeta_M}{\zeta} - 1} \\ \Rightarrow U(\zeta) &> \frac{1 - \frac{1}{\zeta}}{1 - \frac{1}{\zeta_M}} U_M = U_D \end{aligned} \tag{4.24}$$

which is known as the Davisson accessibility condition, after *Davisson (1925)*. This is a powerful result, since when this condition is satisfied, the source cone and hence the current are uniquely determined by the total potential drop along the field line (U_M), with no exact prior knowledge of the potential distribution, $U(\zeta)$, required. Having identified the source cone, the electron distribution can be mapped along the field line and its number density found.

In this Chapter, we seek to find the potential variation in the upward current region by fixing the ion number density profile as we did for the downward current in Chapters 2 and 3, and constraining the solution via quasi-neutrality by matching the electron number density to the fixed ion density at each point along the field line: this derives the potential variation. We will seek only continuous solutions, discarding those with a discontinuous jump in potential.

4.4 Source Cones

4.4.1 Magnetospheric electrons

Assuming *a priori* that the potential variation we obtain will satisfy the Davisson condition in equation (4.24), the source cone of precipitating, current-carrying electrons is determined by U_M, and is shown in Figure 4.1(a). The geometric cone of electrons which would penetrate when $U_M = 0$ is widened by an attractive potential drop to carry more current. The limiting line, Ψ_I, is defined in equation (4.20), and the unshaded region above the $W_{\perp M}$ axis represents those electrons which will be mirrored at some point along the field line, preventing them from reaching the ionosphere. Using conservation of energy, the regions of precipitating and mirroring electrons can be mapped to a general point along the field line, where the potential is U, as shown in Figure 4.1(b). The region above line Γ_b represents those electrons which can arrive at this general point i.e. with $W_\parallel \geq 0$ and $W_{\parallel M} \geq 0$. Substituting equation (4.16) into (4.17) tells us

that

$$W_{\parallel} = W_{\parallel M} + \left(\frac{\zeta}{\zeta_M} - 1\right) W_{\perp} - U_M + U(\zeta) \tag{4.25}$$

$$\Rightarrow W_{\parallel} \geq \left(\frac{\zeta}{\zeta_M} - 1\right) W_{\perp} - U_M + U(\zeta) \tag{4.26}$$

This inequality defines regions A_1 and A_2 in Figure 4.1(a), and line Γ_b is given by

$$W_{\parallel} = \left(\frac{\zeta}{\zeta_M} - 1\right) W_{\perp} - U_M + U(\zeta) \tag{4.27}$$

Line Γ_c separates those electrons which will precipitate to the ionosphere from those that will mirror. In order to precipitate, an electron must have $W_{\parallel I} \geq 0$; by conservation of energy,

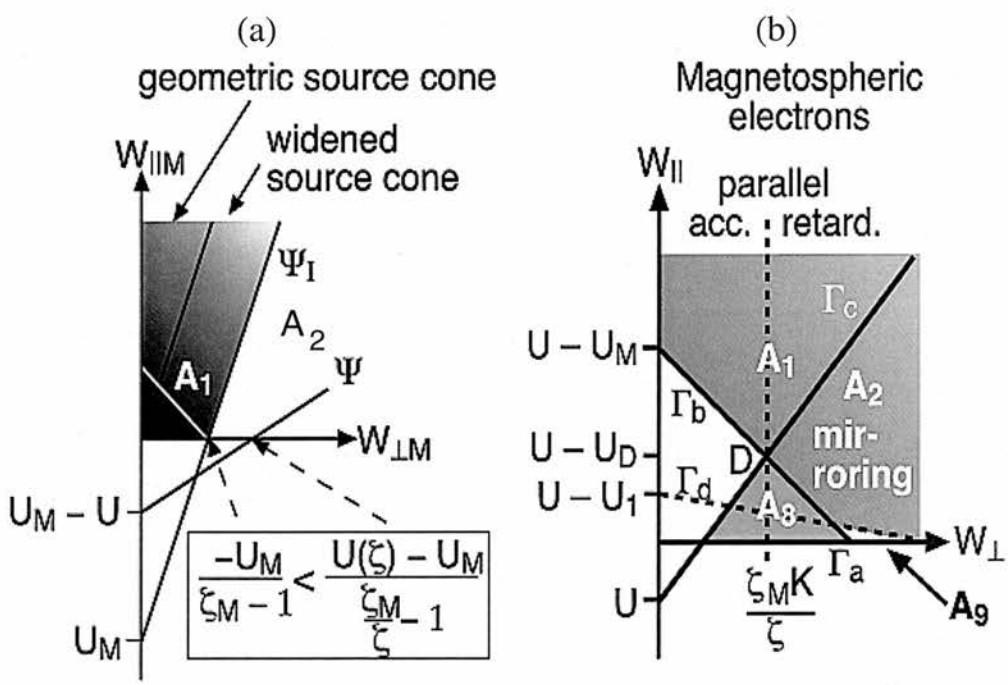

Figure 4.1: (a) This velocity-space plot, taken from *Boström (2003)*, illustrates the magnetospheric electron source cone (shaded) in terms of initial parallel and perpendicular kinetic energies, $W_{\parallel M}$ and $W_{\perp M}$, for an upward current with accelerating potential $U_M < 0$, as defined in equation (4.20). The geometric source cone represents those electrons which would penetrate into the ionosphere with no potential variation. This source cone is widened by the attractive potential, U_M, to provide more charge-carriers to carry the required upward current. The unshaded region above the $W_{\perp M}$-axis (area A_2) represents mirroring electrons. (b) This phase-space plot is taken from *Boström (2004)*, and shows how the source cone (area A_1) and mirroring electron population (area A_2) map at a general point along the field line with potential U and magnetic field ratio ζ. Areas A_8 and A_9 are not pertinent to this work.

$$W_{\|I} + W_{\perp I} = W_{\|} + W_{\perp} - U(\zeta) \tag{4.28}$$

Substituting equation (4.16) into this and rearranging tells us that

$$W_{\|I} = W_{\|} + (1-\zeta)\,W_{\perp} - U(\zeta) \geq 0 \tag{4.29}$$

$$\Rightarrow W_{\|} \geq (\zeta - 1)\,W_{\perp} + U(\zeta) \tag{4.30}$$

This inequality tells us that the area above line Γ_c (and above line Γ_b) defines the source cone electron population. The limiting line, Γ_c, is thus given by

$$W_{\|} = (\zeta - 1)\,W_{\perp} + U(\zeta) \tag{4.31}$$

4.4.2 Ionospheric electrons

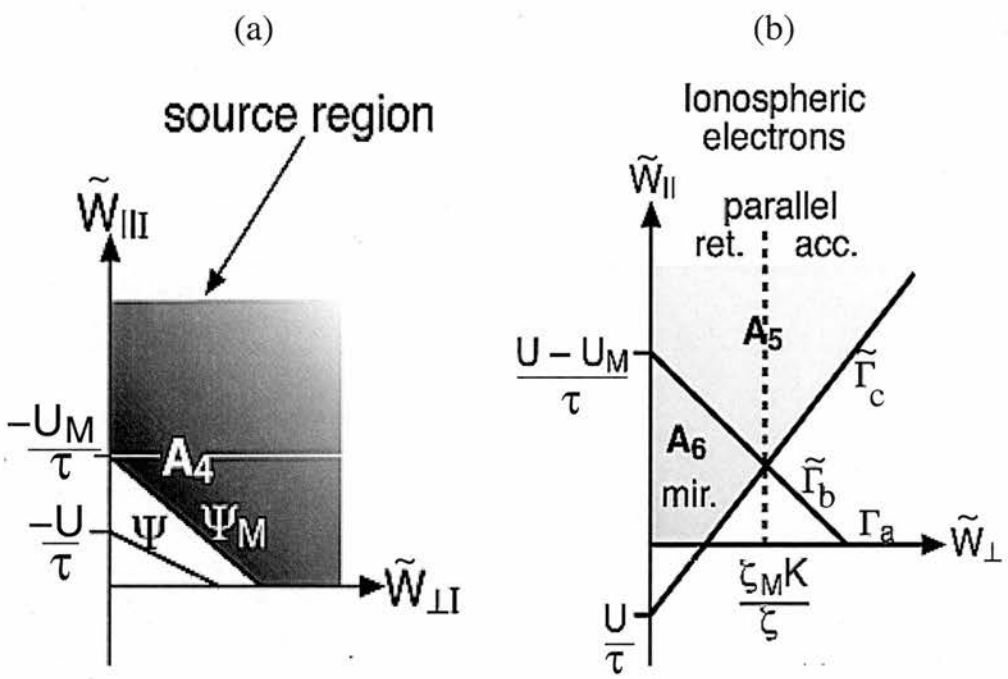

Figure 4.2: (a) This velocity-space plot, adapted from *Boström (2003)*, shows the ionospheric electron source cone (shaded) in terms of $\tilde{W}_{\|I}$ and $\tilde{W}_{\perp I}$, given in equation (4.35). (b) This plot, adapted from *Boström (2004)*, shows how the source cone (area A_5) and mirroring population (area A_6) map at a general point with potential U/τ and magnetic field ratio ζ.

We also require ionospheric electrons to populate the F region. The energetics of this population can be considered in just the same way as in the previous section, noting that the ionospheric and magnetospheric

electron temperatures are very different in this model, and their ratio,

$$\tau = \frac{T_I}{T_M} \tag{4.32}$$

is small. Thus, an ionospheric electron will feel a normalised potential of

$$\tilde{U} = \frac{e\phi}{kT_I} = \frac{U}{\tau} \tag{4.33}$$

In order to reach the magnetosphere, an electron must have $\tilde{W}_{\parallel M} \geq 0$; rearranging equation (4.19) with U_M replaced by U_M/τ, and substituting $\zeta_M \tilde{W}_{\perp M} = \tilde{W}_{\perp I}$ by equation (4.16), gives

$$\tilde{W}_{\parallel M} = \tilde{W}_{\parallel I} + \left(1 - \frac{1}{\zeta_M}\right)\tilde{W}_{\perp I} + \frac{U_M}{\tau} > 0 \tag{4.34}$$

$$\Rightarrow \tilde{W}_{\parallel I} > \max\begin{cases} \Psi_M\left(\tilde{W}_{\perp I}\right) = \left(\frac{1}{\zeta_M} - 1\right)\tilde{W}_{\perp I} - \frac{U_M}{\tau} \\ 0 \end{cases} \tag{4.35}$$

This source cone is illustrated in Figure 4.2(a). Figure 4.2(b) shows a phase-space plot of a general point along the field line with a potential of U/τ. In order to reach a general point with potential U, an electron must have $\tilde{W}_{\parallel} \geq 0$ and $\tilde{W}_{\parallel I} \geq 0$. Conservation of energy gives the equivalent of equation (4.28) with U replaced by U/τ, and thus the area above line $\tilde{\Gamma}_c$, given by

$$\tilde{W}_{\parallel} = (\zeta - 1)\,\tilde{W}_{\perp} + \frac{U(\zeta)}{\tau} \tag{4.36}$$

in Figure 4.2(b) denotes those electrons which populate this point on the field line. In order to escape, an ionospheric electron must have $\tilde{W}_{\parallel M} \geq 0$; conservation of energy yields the equivalent of equation (4.25) with potentials scaled by τ, and thus the area above line $\tilde{\Gamma}_b$, given by

$$\tilde{W}_{\parallel} = \left(\frac{\zeta}{\zeta_M} - 1\right)\tilde{W}_{\perp} - \frac{U_M}{\tau} + \frac{U(\zeta)}{\tau} \tag{4.37}$$

denotes those electrons which escape into the magnetosphere. Those electrons beneath $\tilde{\Gamma}_b$ and above $\tilde{\Gamma}_c$ mirror before this (due to the decelerating potential U_M, rather than magnetic mirroring, which actually serves to accelerate ionospheric electrons up along a field line). In practice, the decelerating potential in our model will be so large as to mirror all of the ionospheric electron population.

4.5 Potential Variation

In this model, we take magnetospheric and ionospheric Maxwellian electron populations of

$$f_M = n_0 \left(\frac{m}{2\pi k T_M}\right)^{\frac{3}{2}} \exp\left[-\frac{m}{2kT_M}\left(v_\parallel^2 + v_\perp^2\right) + \frac{e}{kT_M}\left(\phi - \phi_M\right)\right] \tag{4.38}$$

and

$$f_I = n_I \left(\frac{m}{2\pi k T_I}\right)^{\frac{3}{2}} \exp\left[-\frac{m}{2kT_I}\left(v_\parallel^2 + v_\perp^2\right) + \frac{e\phi}{kT_I}\right] \tag{4.39}$$

where n_I is the number density at the ionospheric end where $\zeta = 1$. There is in fact a small correction term to n_I in equation (4.39) to account for the presence of the precipitating magnetospheric electrons, but since this correction is typically $\sim 1 \times 10^{-4}\%$ for $n_I/n_0 = 10^6$, it can safely be neglected. The expressions in equations (4.38) and (4.39) can be recast in terms of dimensionless variables as

$$\begin{aligned} \bar{f}_M &= \left(\frac{kT_M}{m}\right)^{3/2} \frac{f_M}{n_0} \\ &= (2\pi)^{-3/2} \exp\left[-W_\parallel - W_\perp + U - U_M\right] \end{aligned} \tag{4.40}$$

and

$$\begin{aligned} \bar{f}_I &= \left(\frac{kT_I}{m}\right)^{3/2} \frac{f_I}{n_0} \\ &= \nu\,(2\pi)^{-3/2} \exp\left[-\tilde{W}_\parallel - \tilde{W}_\perp + \frac{U}{\tau}\right] \end{aligned} \tag{4.41}$$

where

$$\nu = \frac{n_I}{n_0} \tag{4.42}$$

is the ratio of ionospheric and magnetospheric number densities, and generally lies in the range $10^3 \leq \nu \leq 10^6$. Number density is found by integrating a distribution function over velocity space, so in this case

$$n = \int f_M \mathrm{d}\mathbf{v} + \int f_I \mathrm{d}\mathbf{v} \tag{4.43}$$

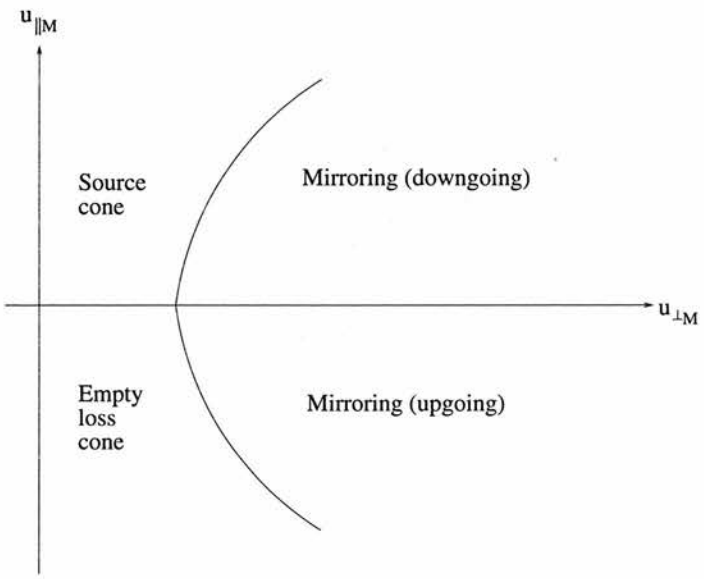

Figure 4.3: Magnetospheric source cone in $u_{\|M}$-$u_{\perp M}$ space; since the source cone electrons penetrate into the ionosphere, they do not return to the magnetosphere, and so the corresponding loss cone is necessarily empty.

where

$$\begin{aligned} \mathrm{d}\mathbf{v} &= \mathrm{d}v_{\|}\, 2\pi v_{\perp}\mathrm{d}v_{\perp} \\ &= \left(\frac{kT_M}{m}\right)^{3/2} \mathrm{d}u_{\|}\, 2\pi u_{\perp}\mathrm{d}u_{\perp} \\ &= \left(\frac{kT_M}{m}\right)^{3/2} \mathrm{d}\mathbf{u} \end{aligned} \tag{4.44}$$

for the magnetospheric number density. Thus, integrating the normalised magnetospheric distribution function over normalised velocity (u) space gives

$$\begin{aligned} \int \bar{f}_M \mathrm{d}\mathbf{u} &= \frac{1}{n_0}\left(\frac{kT_M}{m}\right)^{3/2} \int f_M \mathrm{d}\mathbf{v} \left(\frac{m}{kT_M}\right)^{3/2} \\ &= \frac{1}{n_0}\int f_M \mathrm{d}\mathbf{v} \\ &= \frac{n}{n_0} \\ &= N \end{aligned} \tag{4.45}$$

which is the normalised number density. Similarly, in the ionosphere,

$$\mathrm{d}\mathbf{v} = \left(\frac{kT_I}{m}\right)^{3/2} \mathrm{d}\tilde{\mathbf{u}} \tag{4.46}$$

leading to

$$\int \bar{f}_I \mathrm{d}\tilde{\mathbf{u}} = N \tag{4.47}$$

Recasting equation (4.20) in terms of $u_\parallel$ and $u_\perp$ as defined in equations (4.9) and (4.10), the magnetospheric source cone limiting line is defined as

$$u_\parallel^2 = (\zeta_M - 1)\, u_\perp^2 + 2U_M \tag{4.48}$$

giving a hyperbolic line in $u_{\parallel M}$-$u_{\perp M}$ space, as shown in Figure 4.3. The source cone electrons penetrate into the ionosphere and are lost, thus leaving the loss cone, which is the image of the source cone in the $u_{\perp M}$-axis, devoid of electrons. The downgoing mirroring electrons do return, and thus the image of this region in the $u_{\perp M}$-axis is populated with magnetospheric electrons. We assume that the source cone is constantly replenished at the magnetospheric end. Thus, the total electron number density along the field line is given by

$$N_e = \int\limits_{A_1+2A_2} \bar{f}_M \ \mathrm{d}\mathbf{u} + \int\limits_{A_5+2A_6} \bar{f}_I \ \mathrm{d}\tilde{\mathbf{u}} \tag{4.49}$$

The integration elements can be recast in terms of $W_\parallel$ and $W_\perp$, since we know from equation (4.3) that

$$\mathrm{d}W_\parallel = u_\parallel \mathrm{d}u_\parallel; \quad \mathrm{d}W_\perp = u_\perp \mathrm{d}u_\perp \tag{4.50}$$

so that the first integration element in equation (4.49) becomes

$$\mathrm{d}\mathbf{u} = \frac{\mathrm{d}W_\parallel}{\sqrt{W_\parallel}} \sqrt{2}\pi \ \mathrm{d}W_\perp \tag{4.51}$$

Similarly, for the second integration element in equation (4.49)

$$\mathrm{d}\tilde{\mathbf{u}} = \frac{\mathrm{d}\tilde{W}_\parallel}{\sqrt{\tilde{W}_\parallel}} \sqrt{2}\pi \ \mathrm{d}\tilde{W}_\perp \tag{4.52}$$

Following *Boström (2004)*, we use these integration elements and the normalised Maxwellians in equations (4.40) and (4.41) to obtain

$$\int\limits_{A_1+2A_2} \bar{f}_M \mathrm{d}\mathbf{u} = \frac{1}{2\sqrt{\pi}} \int\limits_{A_1+2A_2} \frac{\mathrm{e}^{-W_\parallel - W_\perp + U - U_M}}{\sqrt{W_\parallel}} \, \mathrm{d}W_\parallel \, \mathrm{d}W_\perp \tag{4.53}$$

and

$$\int\limits_{A_5+2A_6} \bar{f}_I \mathrm{d}\tilde{\mathbf{u}} = \frac{\nu}{2\sqrt{\pi}} \int\limits_{A_5+2A_6} \frac{\mathrm{e}^{-\tilde{W}_\parallel - \tilde{W}_\perp + \frac{U}{\tau}}}{\sqrt{\tilde{W}_\parallel}} \, \mathrm{d}\tilde{W}_\parallel \, \mathrm{d}\tilde{W}_\perp \tag{4.54}$$

4.5.1 Magnetospheric electron number density

In this section, we follow *Boström (2004)* and compute the magnetospheric electron number density; for this, we need to know the limits of integration for area $A_1 + 2A_2$, as shown in Figure 4.1(b). Line Γ_b, given in equation (4.27), cuts the $W_\parallel$ axis at

$$A = (0, U - U_M) \tag{4.55}$$

and the $W_\perp$ axis at

$$C = \left(\frac{U_M - U}{\frac{\zeta}{\zeta_M} - 1}, 0 \right) \tag{4.56}$$

The other crucial point is the intersection, $D = (W_{\perp D}, W_{\parallel D})$, of lines Γ_b and Γ_c, given in equation (4.31). Eliminating $W_\parallel$ from equations (4.27) and (4.31) tells us that

$$W_{\perp D} = -\frac{U_M}{\zeta - \frac{\zeta}{\zeta_M}} \tag{4.57}$$

which can then be substituted back into equation (4.27) to obtain

$$W_{\parallel D} = U - \frac{1 - \frac{1}{\zeta}}{1 - \frac{1}{\zeta_M}} U_M = U - U_D \tag{4.58}$$

where U_D is the Davisson limit, as shown in equation (4.24). The easiest way to compute the number density over $A_1 + 2A_2$ is

$$N_e^M = \int\limits_{A_1+A_2} \bar{f}_M \, \mathrm{d}\mathbf{u} + \int\limits_{A_2} \bar{f}_M \, \mathrm{d}\mathbf{u} = N_a + N_b \tag{4.59}$$

where

$$N_a = \int_{W_\parallel=0}^{\infty}\int_{W_\perp=0}^{\infty} \bar{f}_M \; \mathrm{d}\mathbf{u} - \int_{W_\parallel=0}^{U-U_M}\int_{W_\perp=0}^{\frac{W_\parallel-U+U_M}{\zeta/\zeta_M-1}} \bar{f}_M \; \mathrm{d}\mathbf{u} = N_{a1} - N_{a2} \tag{4.60}$$

and

$$N_b = \int_{W_\parallel=0}^{U-U_D}\int_{W_\perp=\frac{W_\parallel-U+U_M}{\zeta/\zeta_M-1}}^{\infty} \bar{f}_M \; \mathrm{d}\mathbf{u} + \int_{W_\parallel=U-U_D}^{\infty}\int_{W_\perp=\frac{W_\parallel-U}{\zeta-1}}^{\infty} \bar{f}_M \; \mathrm{d}\mathbf{u} = N_{b1} + N_{b2} \tag{4.61}$$

We now need to evaluate each of these integrals in turn, starting with N_{a1}, using the Maxwellian in equation (4.40) and the integration element in terms of $W_\parallel$ and $W_\perp$ given in equation (4.51). So,

$$\begin{aligned}
N_{a1} &= \int_{W_\parallel=0}^{\infty}\int_{W_\perp=0}^{\infty} (2\pi)^{-3/2} \exp\left[-W_\parallel - W_\perp + U - U_M\right] \; \frac{\mathrm{d}W_\parallel}{\sqrt{W_\parallel}}\sqrt{2}\pi \; \mathrm{d}W_\perp \\
\Rightarrow 2\sqrt{\pi}N_{a1} &= e^{U-U_M} \int_{W_\parallel=0}^{\infty}\int_{W_\perp=0}^{\infty} \frac{e^{-W_\parallel}}{\sqrt{W_\parallel}} \; e^{-W_\perp} \; \mathrm{d}W_\perp \; \mathrm{d}W_\parallel \\
&= e^{U-U_M} \int_{W_\parallel=0}^{\infty} \frac{e^{-W_\parallel}}{\sqrt{W_\parallel}} \; \left[-e^{-W_\perp}\right]_{W_\perp=0}^{\infty} \; \mathrm{d}W_\parallel \\
&= e^{U-U_M} \int_{W_\parallel=0}^{\infty} \frac{e^{-W_\parallel}}{\sqrt{W_\parallel}} \; \mathrm{d}W_\parallel \\
&= e^{U-U_M} \int_{x=0}^{\infty} 2e^{-x^2} \; \mathrm{d}x, \quad \text{where } x = \sqrt{W_\parallel}
\end{aligned} \tag{4.62}$$

We can now make use of the error function, where

$$\mathrm{erf}(X) = \frac{2}{\sqrt{\pi}} \int_{x=0}^{X} e^{-x^2} \; \mathrm{d}x \tag{4.63}$$

and $\mathrm{erf}(0) = 0$ and $\mathrm{erf}(\infty) = 1$. Thus,

$$N_{a1} = \frac{e^{U-U_M}}{2} \tag{4.64}$$

Secondly,

$$\begin{aligned} 2\sqrt{\pi}N_{a2} &= e^{U-U_M} \int_{W_\parallel=0}^{U-U_M} \int_{W_\perp=0}^{\frac{W_\parallel - U + U_M}{\zeta/\zeta_M - 1}} \frac{e^{-W_\parallel}}{\sqrt{W_\parallel}}\, e^{-W_\perp}\, \mathrm{d}W_\perp\, \mathrm{d}W_\parallel \\ &= e^{U-U_M} \int_{W_\parallel=0}^{U-U_M} \frac{e^{-W_\parallel}}{\sqrt{W_\parallel}} \left[1 - \exp\left(\frac{U-U_M}{\frac{\zeta}{\zeta_M}-1}\right) \exp\left(-\frac{W_\parallel}{\frac{\zeta}{\zeta_M}-1}\right)\right] \mathrm{d}W_\parallel \end{aligned} \tag{4.65}$$

Here, we let

$$1 + \frac{1}{\frac{\zeta}{\zeta_M} - 1} = -\frac{\zeta}{\zeta_M - \zeta} = -s \tag{4.66}$$

Thus,

$$\begin{aligned} 2\sqrt{\pi}N_{a2} &= e^{U-U_M} \int_{W_\parallel=0}^{U-U_M} \frac{e^{-W_\parallel}}{\sqrt{W_\parallel}}\, \mathrm{d}W_\parallel - e^{-s(U-U_M)} \int_{W_\parallel=0}^{U-U_M} \frac{e^{sW_\parallel}}{\sqrt{W_\parallel}}\, \mathrm{d}W_\parallel \\ &= 2e^{U-U_M} \int_{x=0}^{\sqrt{U-U_M}} e^{-x^2}\, \mathrm{d}x - \frac{2}{\sqrt{s}} e^{-s(U-U_M)} \int_{y=0}^{\sqrt{s(U-U_M)}} e^{y^2}\, \mathrm{d}y \end{aligned} \tag{4.67}$$

where $x = \sqrt{W_\parallel}$ and $y = \sqrt{sW_\parallel}$. We now make use of Dawson's integral, where

$$D(X) = e^{-X^2} \int_{y=0}^{X} e^{y^2}\, \mathrm{d}y \tag{4.68}$$

Thus,

$$N_{a2} = \frac{e^{U-U_M}}{2} \mathrm{erf}\left[\sqrt{U-U_M}\right] - \frac{\mathrm{D}\left[\sqrt{s(U-U_M)}\right]}{\sqrt{s\pi}} \tag{4.69}$$

So, using the contributions to N_a from equations (4.64) and (4.69), and the complementary error func-

tion, where

$$\operatorname{erfc}(X) = \frac{2}{\sqrt{\pi}} \int_{x=X}^{\infty} e^{-x^2} \, \mathrm{d}x = 1 - \operatorname{erf}(X) \tag{4.70}$$

we have that

$$N_a = \frac{e^{U-U_M}}{2} \operatorname{erfc}\left[\sqrt{U-U_M}\right] + \frac{\mathrm{D}\left[\sqrt{s(U-U_M)}\right]}{\sqrt{s\pi}} \tag{4.71}$$

Thirdly, we need to compute N_{b1} in equation (4.61), given by

$$\begin{aligned}
2\sqrt{\pi}N_{b1} &= e^{U-U_M} \int_{W_\parallel=0}^{U-U_D} \int_{W_\perp=\frac{W_\parallel - U + U_M}{\zeta/\zeta_M - 1}}^{\infty} \frac{e^{-W_\parallel}}{\sqrt{W_\parallel}} e^{-W_\perp} \, \mathrm{d}W_\perp \, \mathrm{d}W_\parallel \\
&= e^{U-U_M} \int_{W_\parallel=0}^{U-U_D} \frac{e^{-W_\parallel}}{\sqrt{W_\parallel}} \exp\left(-\frac{W_\parallel}{\frac{\zeta}{\zeta_M} - 1}\right) \exp\left(\frac{U-U_M}{\frac{\zeta}{\zeta_M} - 1}\right) \, \mathrm{d}W_\parallel \\
&= e^{-s(U-U_M)} \int_{W_\parallel=0}^{U-U_D} \frac{e^{sW_\parallel}}{\sqrt{W_\parallel}} \, \mathrm{d}W_\parallel, \text{ using equation (4.66)} \\
&= \frac{2}{\sqrt{s}} e^{-s(U-U_M)} \int_{y=0}^{\sqrt{s(U-U_D)}} e^{y^2} \, \mathrm{d}y
\end{aligned} \tag{4.72}$$

where $y = \sqrt{sW_\parallel}$. To simplify this answer, we can make use of the result that

$$\begin{aligned}
e^{-s(U-U_M)} \, e^{s(U-U_D)} &= e^{s(U_M-U_D)} \\
&= \exp\left[\left(\frac{\zeta U_M}{\zeta_M - \zeta}\right)\left(1 - \frac{1-\frac{1}{\zeta}}{1-\frac{1}{\zeta_M}}\right)\right] \\
&= \exp\left[\left(\frac{\zeta U_M}{\zeta_M - \zeta}\right)\left(\frac{\zeta_M - \zeta}{\zeta(\zeta_M - 1)}\right)\right] \\
&= \exp\left(\frac{U_M}{\zeta_M - 1}\right) \\
&= e^{-k}
\end{aligned} \tag{4.73}$$

where k is defined in equation (4.23), to give

$$N_{b1} = \frac{e^{-k}}{\sqrt{s\pi}} \mathrm{D}\left[\sqrt{s(U-U_D)}\right] \tag{4.74}$$

Finally, we need to compute N_{b2} in equation (4.61):

$$\begin{aligned} 2\sqrt{\pi}N_{b2} &= e^{U-U_M} \int_{W_\parallel=U-U_D}^{\infty} \int_{W_\perp=\frac{W_\parallel-U}{\zeta-1}}^{\infty} \frac{e^{-W_\parallel}}{\sqrt{W_\parallel}} e^{-W_\perp} \, \mathrm{d}W_\perp \, \mathrm{d}W_\parallel \\ &= e^{U-U_M} \int_{W_\parallel=U-U_D}^{\infty} \frac{e^{-W_\parallel}}{\sqrt{W_\parallel}} \exp\left(-\frac{W_\parallel}{\zeta-1}\right) \exp\left(\frac{U}{\zeta-1}\right) \, \mathrm{d}W_\parallel \end{aligned} \tag{4.75}$$

We define

$$1 + \frac{1}{\zeta-1} = \frac{\zeta}{\zeta-1} = t \tag{4.76}$$

to give

$$\begin{aligned} 2\sqrt{\pi}N_{b2} &= e^{tU-U_M} \int_{W_\parallel=U-U_D}^{\infty} \frac{e^{-tW_\parallel}}{\sqrt{W_\parallel}} \, \mathrm{d}W_\parallel \\ &= \frac{2}{\sqrt{t}} e^{tU-U_M} \int_{z=\sqrt{t(U-U_D)}}^{\infty} e^{-z^2} \, \mathrm{d}z, \text{ where } z = \sqrt{tW_\parallel} \\ \Rightarrow N_{b2} &= \frac{e^{tU-U_M}}{2\sqrt{t}} \mathrm{erfc}\left[\sqrt{t(U-U_D)}\right] \end{aligned} \tag{4.77}$$

In a final simplification, we note that

$$\begin{aligned} e^{tU-U_M} \; e^{-t(U-U_D)} &= e^{tU_D-U_M} \\ &= \exp\left(U_M\left(\left(\frac{\zeta}{\zeta-1}\right)\left(\frac{1-\frac{1}{\zeta}}{1-\frac{1}{\zeta_M}}\right)-1\right)\right) \\ &= \exp\left(U_M\left(\frac{\zeta_M-(\zeta_M-1)}{\zeta_M-1}\right)\right) \\ &= \exp\left(\frac{U_M}{\zeta_M-1}\right) \\ &= e^{-k} \end{aligned} \tag{4.78}$$

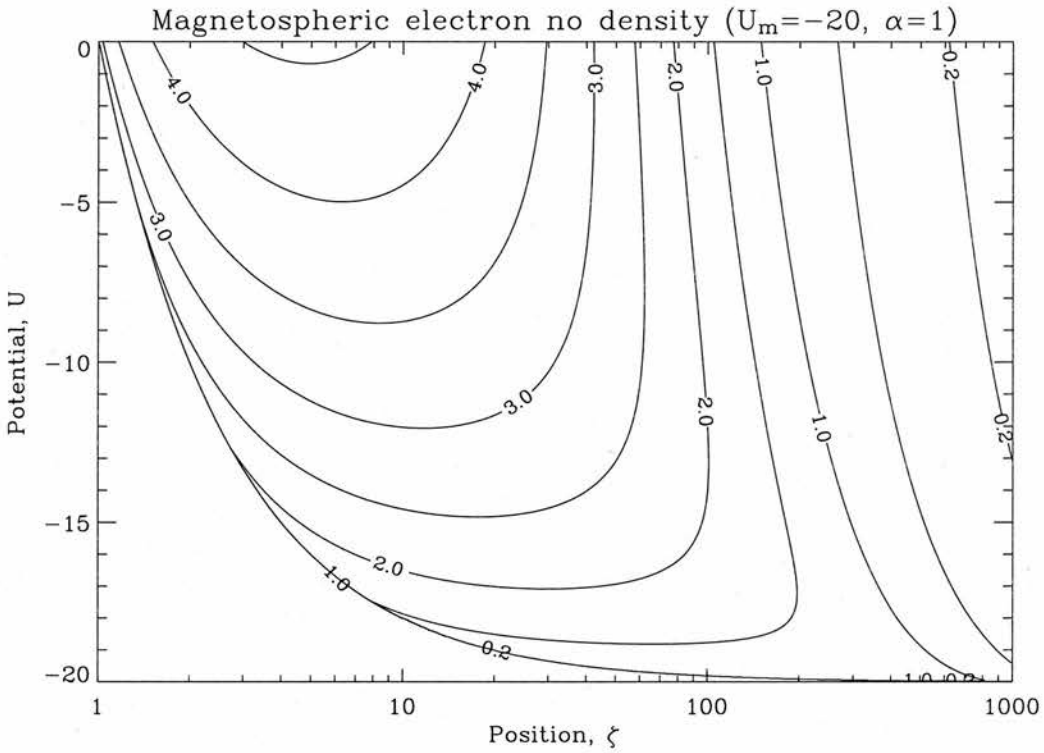

Figure 4.4: Recalculation of Figure 3(c) of *Boström (2004)*, showing a contour plot of N_e^M, given in equation (4.81), against U and ζ, where $\zeta_M = 1000$ and $U_M = -20$ in this example.

Thus, we can write that

$$N_{b2} = \frac{e^{-k}}{2\sqrt{t}} e^{t(U-U_D)} \mathrm{erfc}\left[\sqrt{t(U-U_D)}\right] \tag{4.79}$$

We can now find N_b by adding the contributions from equations (4.74) and (4.79) to obtain

$$N_b = e^{-k}\left(\frac{\mathrm{D}\left[\sqrt{s(U-U_D)}\right]}{\sqrt{s\pi}} + \frac{e^{t(U-U_D)}}{2\sqrt{t}} \mathrm{erfc}\left[\sqrt{t(U-U_D)}\right]\right) \tag{4.80}$$

Finally, the magnetospheric electron number density can be written using the contributions from equations (4.71) and (4.80) as

$$N_e^M = \frac{e^{U-U_M}}{2} \mathrm{erfc}\left[\sqrt{U-U_M}\right] + \frac{\mathrm{D}\left[\sqrt{s(U-U_M)}\right]}{\sqrt{s\pi}}$$

$$+e^{-k}\left(\frac{\mathrm{D}\left[\sqrt{s(U-U_D)}\right]}{\sqrt{s\pi}}+\frac{e^{t(U-U_D)}}{2\sqrt{t}}\mathrm{erfc}\left[\sqrt{t(U-U_D)}\right]\right) \tag{4.81}$$

Using this expression for the magnetospheric electron number density, we reproduced Figure 3(c) from *Boström (2004)*, shown in Figure 4.4. This is a contour plot of N_e^M against potential, U, and position, ζ, where ζ_M is taken to be 1000. When we fix the ion number density along the field line and impose quasi-neutrality, the electron and ion number densities must be equal at each value of ζ. This number density will correspond to a particular value of the potential, U, which can be found using the contour plot. When this procedure is carried out at every point along the field line, we will be able to trace out a specific potential profile and hence determine the electric field.

4.5.2 Ionospheric electron number density

We also follow *Boström (2004)* to work out the ionospheric electron number density, given in equation (4.54), where areas A_5 and A_6 are illustrated in Figure 4.2(b). The simplest way to do this is as follows:

$$N_e^I=\int\limits_{2(A_5+A_6)}\bar{f}_I\ \mathrm{d}\tilde{\mathrm{u}}-\int\limits_{A_5}\bar{f}_I\ \mathrm{d}\tilde{\mathrm{u}}=2N_c-N_d \tag{4.82}$$

Area A_5 is identical to A_1, where the precipitating magnetospheric electron number density is given by N_a-N_b, where N_a and N_b are given in equations (4.71) and (4.80), respectively. Thus, the number density of escaping ionospheric electrons gives the same answer with potentials scaled by τ, and a factor of $\nu e^{U_M/\tau}$ due to the difference between $\bar{f}_M$ and $\bar{f}_I$ i.e.

$$\begin{aligned}N_d &= \nu e^{\frac{U_M}{\tau}}\left(\frac{1}{2}\exp\left(\frac{U-U_M}{\tau}\right)\mathrm{erfc}\left[\sqrt{\frac{U-U_M}{\tau}}\right]+\frac{1}{\sqrt{s\pi}}\mathrm{D}\left[\sqrt{\frac{s(U-U_M)}{\tau}}\right]\right.\\ &- \left.\frac{e^{-\frac{k}{\tau}}}{\sqrt{s\pi}}\mathrm{D}\left[\sqrt{\frac{s(U-U_D)}{\tau}}\right]-\frac{e^{-\frac{k}{\tau}}}{2\sqrt{t}}\exp\left(\frac{t(U-U_D)}{\tau}\right)\mathrm{erfc}\left[\sqrt{\frac{t(U-U_D)}{\tau}}\right]\right)\end{aligned} \tag{4.83}$$

Now,

$$\begin{aligned}\frac{2\sqrt{\pi}}{\nu}N_c &= e^{\frac{U}{\tau}}\int\limits_{\tilde{W}_\parallel=0}^{\infty}\int\limits_{\tilde{W}_\perp=0}^{\frac{\tilde{W}_\parallel-\frac{U}{\tau}}{\zeta-1}}\frac{e^{-\tilde{W}_\parallel}}{\sqrt{\tilde{W}_\parallel}}e^{-\tilde{W}_\perp}\ \mathrm{d}\tilde{W}_\perp\mathrm{d}\tilde{W}_\parallel\\ &= e^{\frac{U}{\tau}}\int\limits_{\tilde{W}_\parallel=0}^{\infty}\frac{e^{-\tilde{W}_\parallel}}{\sqrt{\tilde{W}_\parallel}}\left[1-\exp\left(-\frac{\tilde{W}_\parallel}{\zeta-1}\right)\exp\left(\frac{U/\tau}{\zeta-1}\right)\right]\ \mathrm{d}\tilde{W}_\parallel\end{aligned}$$

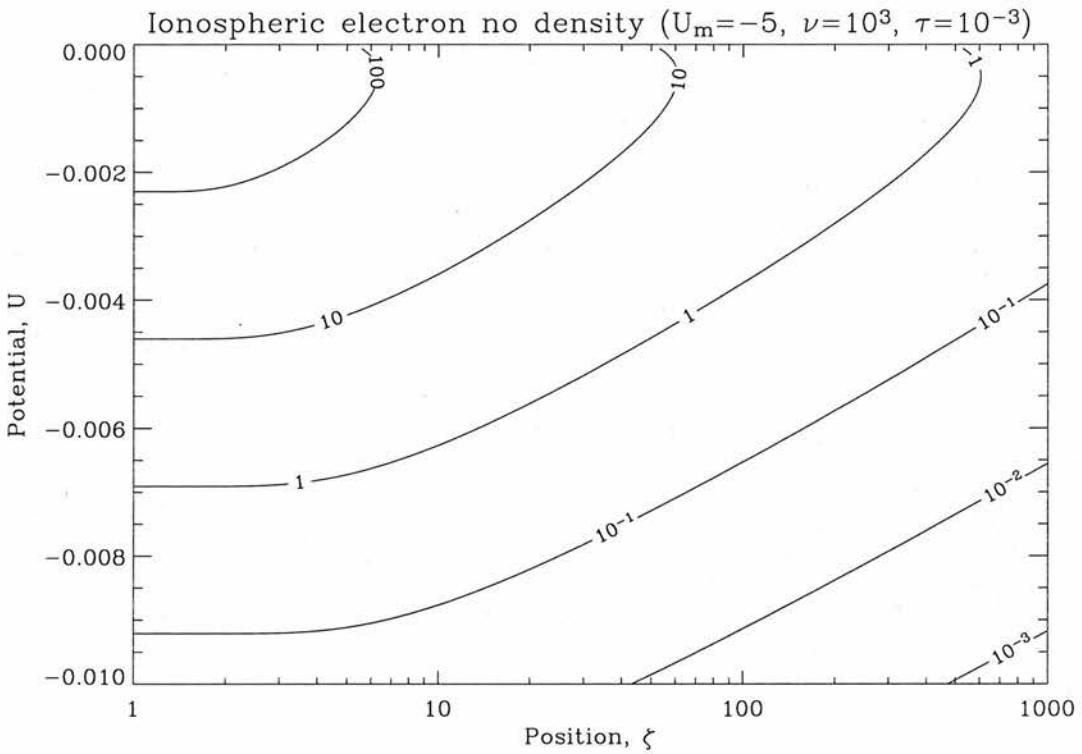

Figure 4.5: Recalculation of Figure 7(a) of *Boström (2004)*, showing a contour plot of N_e^I, given in equation (4.86), against U and ζ, where $\zeta_M = 1000$, $U_M = -5$, $\nu = 10^3$ and $\tau = 10^{-3}$ in this example. Note the small scale of U ($-0.01 \leq U \leq 0$) compared to $U_M = -5$. The cool ionospheric electrons are easily excluded from the magnetosphere by a fraction of the overall potential.

$$
\begin{aligned}
&= e^{\frac{U}{\tau}} \int_{\tilde{W}_\parallel=0}^{\infty} \frac{e^{-\tilde{W}_\parallel}}{\sqrt{\tilde{W}_\parallel}}\, \mathrm{d}\tilde{W}_\parallel - e^{\frac{tU}{\tau}} \int_{\tilde{W}_\parallel=0}^{\infty} \frac{e^{-t\tilde{W}_\parallel}}{\sqrt{\tilde{W}_\parallel}}\, \mathrm{d}\tilde{W}_\parallel, \text{ using equation (4.76)} \\
&= 2e^{\frac{U}{\tau}} \int_{x=0}^{\infty} e^{-x^2}\, \mathrm{d}x - \frac{2}{\sqrt{t}} e^{\frac{tU}{\tau}} \int_{z=0}^{\infty} e^{-z^2}\, \mathrm{d}z \qquad (4.84)
\end{aligned}
$$

where $x = \sqrt{\tilde{W}_\parallel}$ and $z = \sqrt{t\tilde{W}_\parallel}$. Thus,

$$
N_c = \frac{\nu}{2}\left(e^{\frac{U}{\tau}} - \frac{e^{\frac{tU}{\tau}}}{\sqrt{t}}\right) \qquad (4.85)
$$

In practice, since our potential will be large and the ionospheric temperature small, $N_d \to 0$. (In our numerical calculations, $N_d < 10^{-13}$ at all times). Thus, we can say that the ionospheric electron number density contribution, N_e^I, is given by

$$N_e^I \approx \nu \left(e^{\frac{U}{\tau}} - \frac{e^{\frac{tU}{\tau}}}{\sqrt{t}} \right) \tag{4.86}$$

Using this expression for the ionospheric electron number density, we reproduced Figure 7(a) of *Boström (2004)*, shown in Figure 4.5. The ionospheric electrons are really only dominant for very small potentials i.e. close to the ionosphere, and their main role is to populate the F region, with its exponentially-decaying number density profile.

4.5.3 Potential solutions

In order to find the potential variation along the field line, we choose a fixed ion density profile. We take an exponentially-decaying ionospheric component, such that the normalised ion number density is

$$N_i = 1 + (\nu - 1) \exp \left[-\frac{R_E}{h} \left(L \cos^2 \theta - 1 \right) \right] \tag{4.87}$$

where ν is the ratio of ionospheric and magnetospheric number densities, as defined in equation (4.42), h is the ion scale height, L denotes L shell and θ is the usual polar latitudinal coordinate. In Chapter 2, we took a scale height of 100 km, and ionospheric and magnetospheric number densities of 10^{12} m^{-3} and 10^6 m^{-3} respectively, giving $\nu = 10^6$. We found that the curve of B/N has a characteristic peak, which in this case occurs at 0.273 R_E, or 1740 km.

Firstly, we must choose a value for U_M, the total potential drop along the field line. As we are searching for potential solutions which satisfy the Davisson condition in equation (4.24), this potential drop defines both the source cone and the field-aligned current. We can find the unique current-voltage relation for a Maxwellian magnetospheric source as follows. Firstly, we note that j/B is constant along a field line, as shown in equation (2.42). In our present notation, this translates to

$$i_\parallel \zeta = \text{constant} \tag{4.88}$$

and, more specifically, that

$$i_{\parallel I} = \zeta_M i_{\parallel M} \tag{4.89}$$

where $i_{\parallel M}$ is found by integrating $u_\parallel \bar{f}_M$ over the source cone in Figure 4.1(a):

$$i_{\parallel M} = \int_{\text{source cone}} \int u_\parallel \bar{f}_M \, \mathrm{d}\mathbf{u} \tag{4.90}$$

Using the integration element in equation (4.51), the definition of W in equation (4.3) and the definition of $\bar{f}_M$ in equation (4.40), we can write that

$$\begin{aligned} i_{\|I} &= \frac{\zeta_M}{\sqrt{2\pi}} \int_{\text{source}} \int_{\text{cone}} e^{-W_{\|M}} e^{-W_{\perp M}} \, \mathrm{d}W_{\perp M} \mathrm{d}W_{\|M} \\ &= \frac{\zeta_M - (\zeta_M - 1)\, e^{\frac{U_M}{\zeta_M - 1}}}{\sqrt{2\pi}} \end{aligned} \tag{4.91}$$

Details of this integration may be found in the Appendix. When the magnetic mirror ratio, ζ_M, is large compared to U_M,

$$e^{\frac{U_M}{\zeta_M - 1}} \approx 1 + \frac{U_M}{\zeta_M - 1} \tag{4.92}$$

yielding the familiar linear Knight relation for the upward current region, where

$$i_{\|I} \approx \frac{1 - U_M}{\sqrt{2\pi}} \tag{4.93}$$

Using equations (4.5) and (4.6), we can write this linear current-voltage relation in dimensional quantities, where

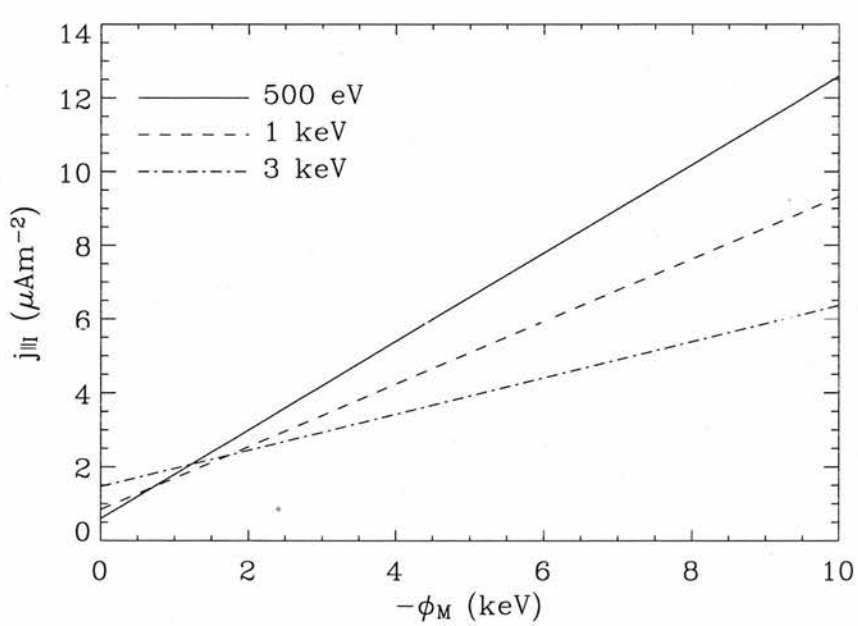

Figure 4.6: Knight relation for varying magnetospheric temperatures

$$j_{\|I} \approx n_0 e \sqrt{\frac{kT_M}{2\pi m}} \left(1 - \frac{e\phi_M}{kT_M}\right) \tag{4.94}$$

This relation is shown in Figure 4.6 for varying magnetospheric temperatures. When there is no potential drop, that is $\phi_M = 0$, the thermal current (j_{th}) flows, with a current density at the ionosphere of

$$j_{thI} \approx n_0 e \sqrt{\frac{kT_M}{2\pi m}} \tag{4.95}$$

This value corresponds to the y intercepts of the lines in Figure 4.6. As the magnetospheric temperature increases, so does the random thermal current, since more energetic electrons are able to overcome the mirror force and precipitate into the ionosphere. The slopes in Figure 4.6 correspond to $j_{thI}/(kT_M/e) \propto (kT_M)^{-1/2}$, and so an increased magnetospheric temperature results in a smaller slope. This is due to the fact that a more energetic magnetospheric population will experience a greater mirror force $\propto v_\perp^2$.

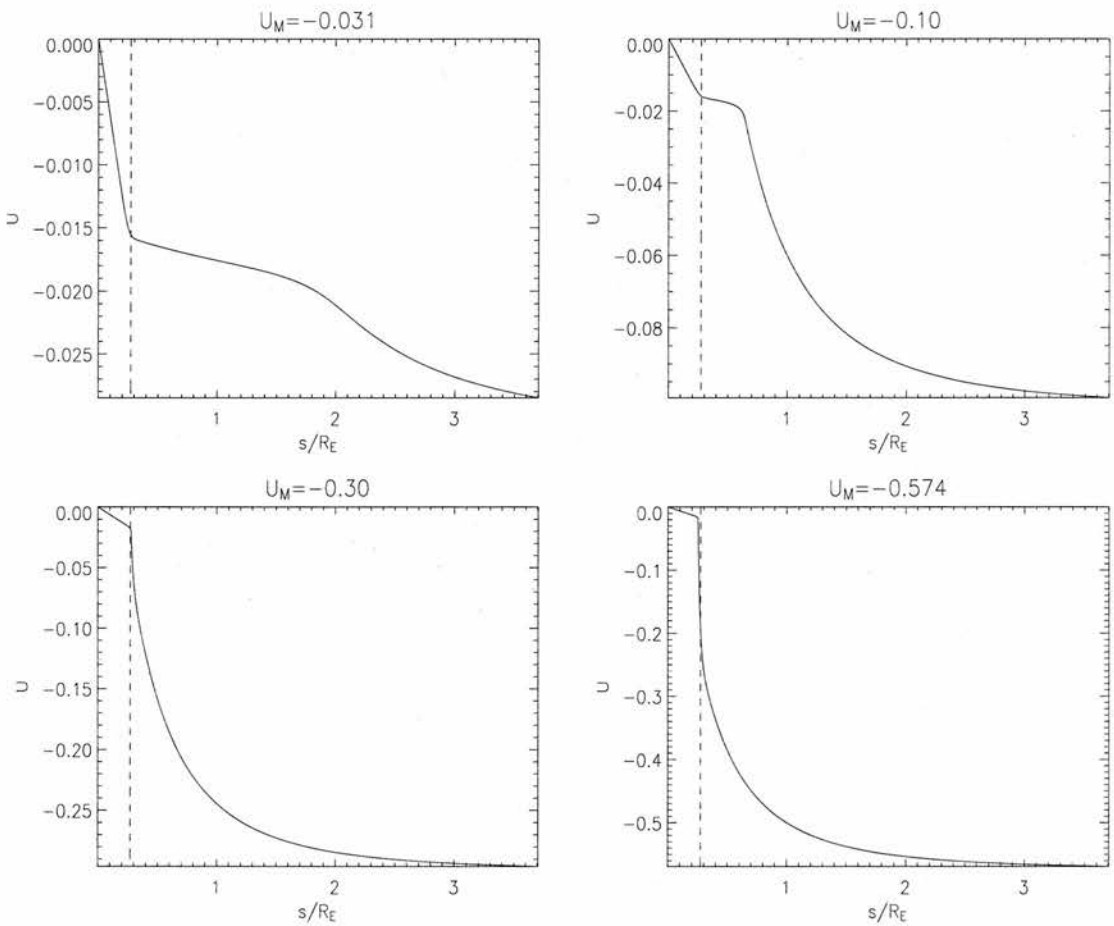

Figure 4.7: Examples of continuous potential variation; note how a potential "shoulder" extends to higher altitudes for small U_M, whilst the solution steepens up around the B/N peak (dashed lines) as $\mid U_M \mid$ is increased.

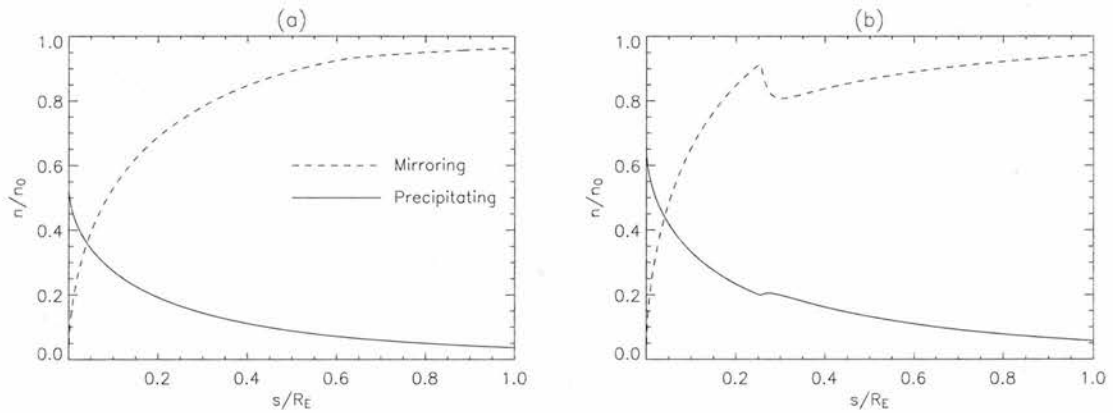

Figure 4.8: Precipitating and mirroring magnetospheric electron number densities for (a) $U_M = -0.1$ and (b) $U_M = -0.5$.

Having chosen U_M, and hence the current density, we then impose quasi-neutrality by setting

$$N_i = N_e^M + N_e^I \tag{4.96}$$

where N_e^M and N_e^I are found in equations (4.81) and (4.86) respectively. This uniquely defines the potential variation along the field line.

4.5.4 Continuous Potentials

It is only possible to find continuous potential solutions for a relatively small range of values of U_M; taking $\nu = 10^6$, $\tau = 10^{-3}$ and $h = 100$ km, we can find continuous solutions for $-0.574 \leq U_M \leq -0.031$, which for $n_0 = 10^6$ m^{-3} and $T_M \sim 1$ keV corresponds to $8.74 \times 10^{-7} \leq j_{\|I} \leq 1.33 \times 10^{-6}$. This is a narrow range, but insight can nonetheless be gleaned as to the nature of potential variation seen. We show four examples of potential curves in Figure 4.7. For small U_M, a potential "shoulder" extends out to higher altitudes ~2-3 R_E: since the overall potential is small, a significant proportion of it is required at these higher altitudes to allow the precipitating electrons to overcome the mirror force there. As $\mid U_M \mid$ is incrcased, this shoulder moves towards the B/N peak (dashed lines) until it no longer exists: some acceleration is still required at higher altitudes to counteract the mirror force, but a significant proportion of it is now concentrated around the B/N peak where, since $B/N \propto \bar{v}_{\|}$ (the mean electron drift speed), the electrons must travel most quickly to carry the current. When $\mid U_M \mid$ is increased further, there are points along the field line for which we can no longer find a quasi-neutral solution: in order to generate such a solution, we would either need to change the ion number density profile, or introduce moving ions, which could lead to the formation of double layers.

Figure 4.8 shows the precipitating and mirroring magnetospheric electron number densities for $U_M = -0.1$ and -0.5. Note that while the mirroring electrons carry no current, their presence is vital to the solution, since their large number density in much of the magnetosphere plays a major role in matching the

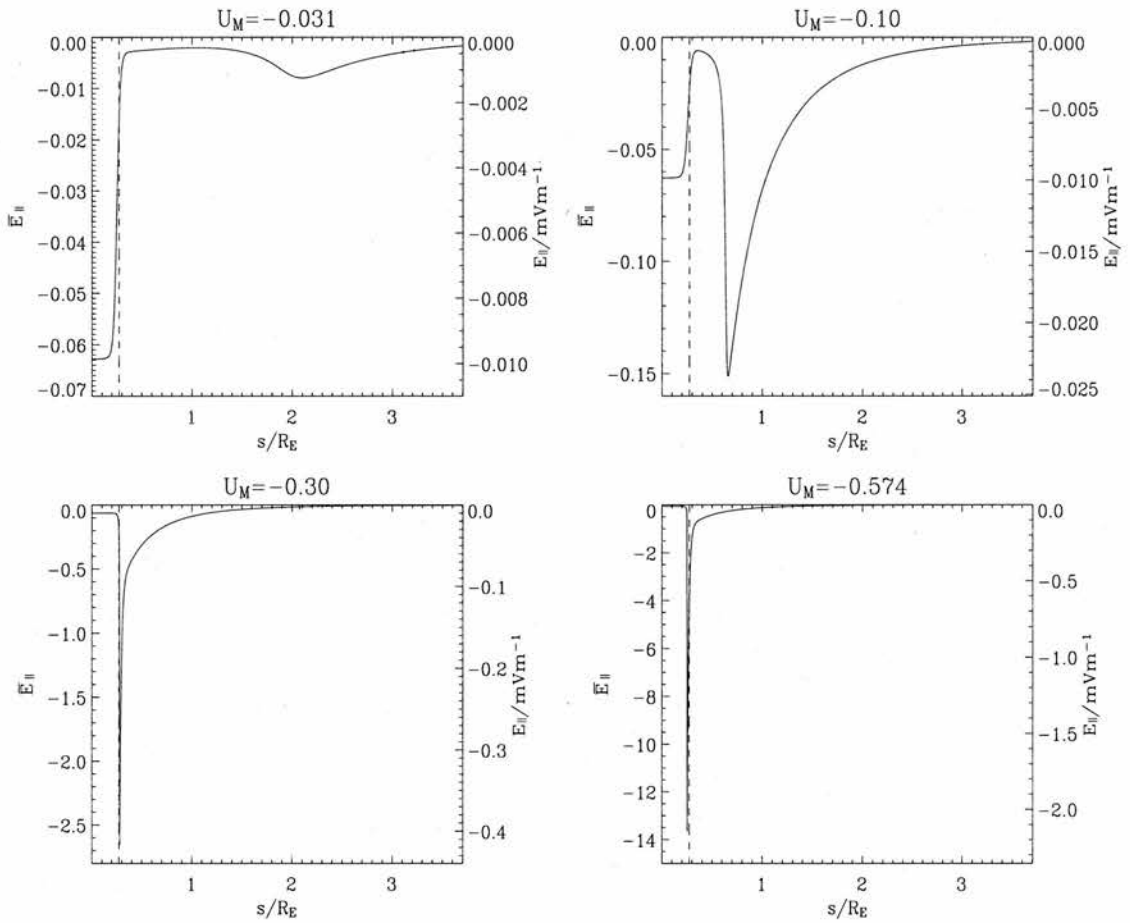

Figure 4.9: Examples of $\bar{E}_{\|}$ for four different values of U_M. Note how, for smaller U_M values, $\bar{E}_{\|}$ extends to higher altitudes, whilst as $\mid U_M \mid$ increases, it moves to an increasingly narrow region around the B/N peak (dashed lines). Actual $E_{\|}$ values are also plotted in the specific case were $T_M \sim 1$ keV.

ion number density to satisfy quasi-neutrality. In both cases, the precipitating number density only matches the mirroring number density at $s/R_E = 0.04 \sim 260$ km altitude. This is a robust feature independent of the value of U_M. The importance of the mirroring electrons to the solution will be discussed further in later sections.

4.5.5 Parallel electric field

The parallel electric field, $E_{\|}$, is given by

$$\begin{aligned} E_{\|} &= -\frac{\partial \phi}{\partial \ell} \\ &= -\frac{kT_M}{eR_E}\frac{\partial U}{\partial\left(\ell/R_E\right)} \end{aligned} \tag{4.97}$$

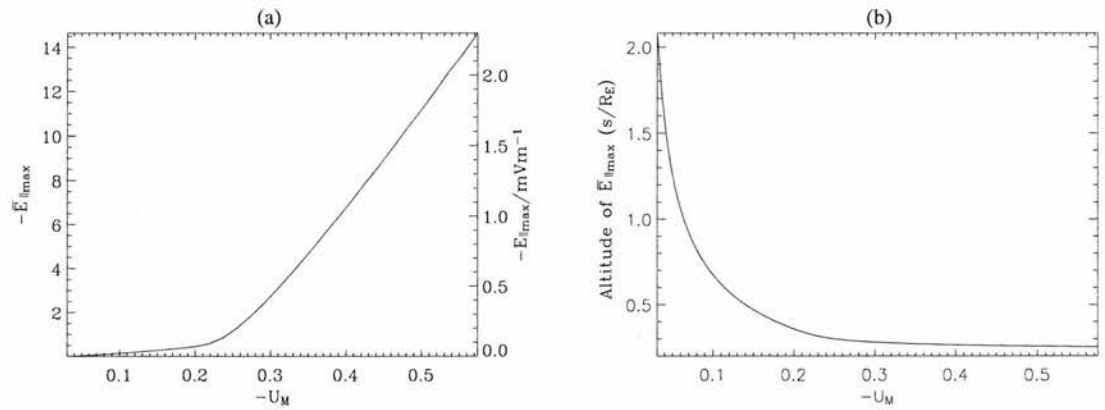

Figure 4.10: (a) Plot of the $\bar{E}_{\parallel}$ peak ($\bar{E}_{\parallel \max}$) against U_M, showing a definite increase as $\mid U_M \mid$ (and hence, the required current density) increases. A dimensional $E_{\parallel \max}$ scale is also shown for $T_M \sim 1$ keV. (b) Plots of the altitude of $\bar{E}_{\parallel \max}$ against U_M: the peak can be as high as 2 R_E for low current densities, but asymptotes to the B/N peak at $s = 0.27 R_E$ for $-U_M \geq 0.3$.

where we define a second dimensionless distance along the field line, ξ, such that

$$\xi = \frac{\ell}{R_E} \tag{4.98}$$

Thus,

$$\begin{aligned} \bar{E}_{\parallel} &= -\frac{\partial U}{\partial \xi} \\ &= \frac{eR_E}{kT_M} E_{\parallel} \end{aligned} \tag{4.99}$$

serves as a normalised parallel electric field. We plot $\bar{E}_{\parallel}$ in Figure 4.9 for the same four values that we plotted the potential for in Figure 4.7. For small U_M-values, $\bar{E}_{\parallel}$ extends to higher altitudes and over a larger distance, again showing that its main role is to allow the precipitating electrons to overcome the mirror force. The characteristic $\bar{E}_{\parallel}$ peak ($\bar{E}_{\parallel \max}$) in the magnetosphere occurs at $\sim$2 R_E for $U_M = -0.031$, moves earthward to 0.65 R_E for $U_M = -0.1$, and is within a few density scale heights of the B/N peak for $\mid U_M \mid \geq 0.3$.

Note that the ambipolar electric field, $\bar{E}_{\rm amb}$, which constrains the ionospheric electrons close to the Earth, is the same in each case (-0.063): this is most visible in the first two cases. In fact, for $U_M = -0.031$, $\bar{E}_{\rm amb}$ is far larger than $\bar{E}_{\parallel \max}$; in the majority of cases, $\bar{E}_{\rm amb} \ll \bar{E}_{\parallel \max}$. More will be said of $\bar{E}_{\rm amb}$ later. In Figure 4.9, a dimensional $E_{\parallel}$ scale has also been included for reference, for the case when $T_M \sim 1$ keV. These show very small $E_{\parallel}$ values of $\sim$0.001 and 0.01 mV/m for $U_M = -0.031$ and -0.1 respectively, with larger values of $\sim$1 mV/m for higher U_M values or current densities.

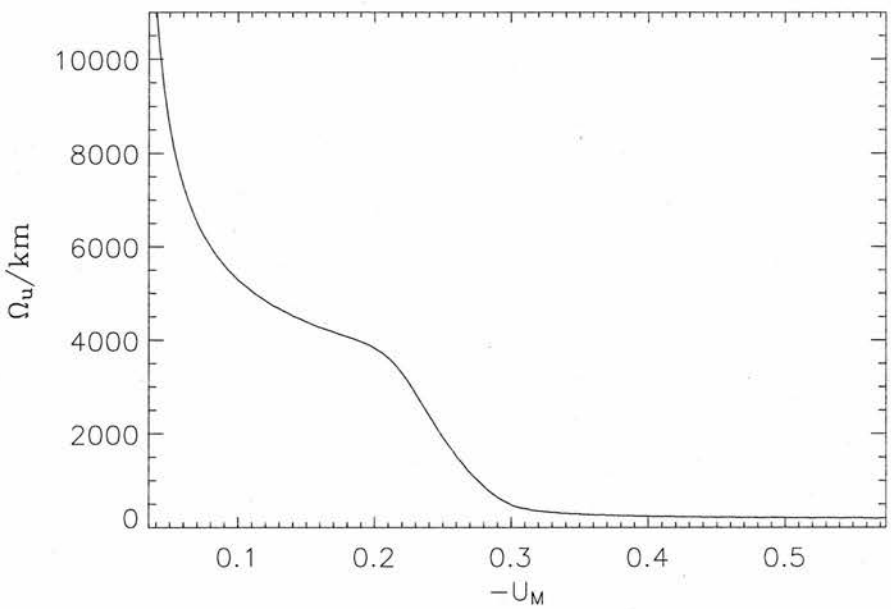

Figure 4.11: A plot of the acceleration width, Ω_u, against U_M, showing that smaller U_M-values require acceleration over larger distances ~1-2 R_E, whilst for larger U_M-values, Ω_u contracts to ~200 km.

Figure 4.10(a) shows the variation of $\bar{E}_{\parallel \max}$ with U_M. As anticipated, as $\mid U_M \mid$, or the required current density, increases, the maximum $\bar{E}_{\parallel}$ required to accelerate the precipitating electrons increases. Figure 4.10(b) shows that the altitude of this peak occurs at relatively high altitudes ~1-2 R_E for small U_M, but asymptotes to the B/N peak at $s = 0.27R_E$ for $\mid U_M \mid \geq 0.3$.

4.5.6 Acceleration width, Ω_u

As with our downward current model in Chapter 2, we define an acceleration width, Ω_u, for this upward current model to get an idea of the extent of the acceleration region. In this case, we define Ω_u in terms of $\bar{E}_{\parallel}$, since this is easier to use than the potential: it is defined to be

$$\Omega_u = s_h - s_l \tag{4.100}$$

where

$$\bar{E}_{\parallel}(s_h) = \bar{E}_{\parallel}(s_l) = 0.2\bar{E}_{\parallel \max} \tag{4.101}$$

A plot of Ω_u against U_M is shown in Figure 4.11. This illustrates points noted earlier from the potential and $\bar{E}_{\parallel}$ variations in Figures 4.7 and 4.9: smaller U_M-values require acceleration over larger distances ~1-

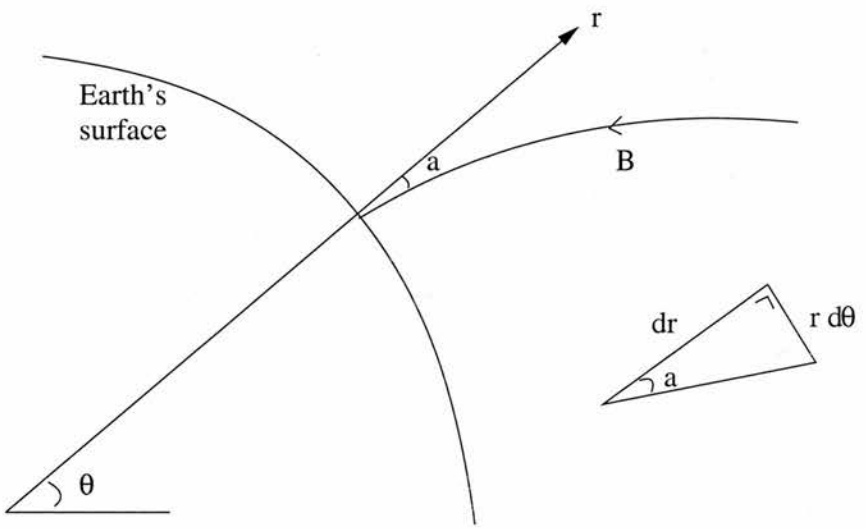

Figure 4.12: Diagram showing the angle, a, between $\mathbf{r}$ and $\mathbf{B}$ at the ionosphere.

2 R_E to overcome the mirror force, whilst for larger U_M-values, the bulk of the acceleration is required at the B/N peak, so Ω_u ~200 km. This plot illustrates how, for higher current densities, the potential could steepen into a thin double layer at the B/N peak, as found by *Boström (2004)*.

4.5.7 Ambipolar electric field, $\bar{E}_{\rm amb}$

As mentioned in the Introduction, the escape velocity from the ionosphere is $\sim 1.12\times10^4$ m/s. Given an ionospheric temperature of 1 eV, the electron speed is $\sim 5.93\times10^5$ m/s, so ionospheric electrons are not gravitationally bound to the Earth. Thus, a small ambipolar electric field is required. Its form can be deduced by examining the hydrodynamic equation of motion for ionospheric electrons in a steady state with no flow velocity:

$$-enE_{\rm amb} - \nabla p_e = 0 \tag{4.102}$$

where $E_{\rm amb}$ is the ambipolar electric field, and $p_e = nkT_I$ is the ionospheric electron pressure. We take T_I to be fixed and $n \sim n_I \exp\left((\ell - \ell_m)/h_\parallel\right)$, where $h_\parallel$ is the scale height along the field line, which is slightly different to the scale height, h, in the radial direction. This difference in direction between $\mathbf{r}$ and $\mathbf{B}$ is shown in Figure 4.12. From this, we can see that the angle, a, between the two can be written as

$$\tan a = \frac{r\mathrm{d}\theta}{\mathrm{d}r} \tag{4.103}$$

At Earth's surface, $r = R_E$, and we can use equation (2.3) to see that

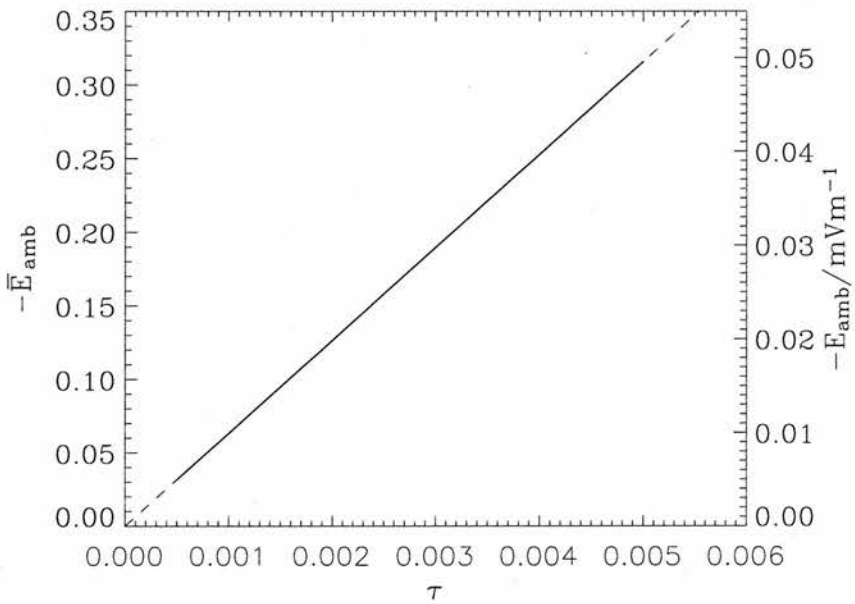

Figure 4.13: A plot of the effect of τ on $\bar{E}_{\text{amb}}$, keeping h fixed at 100 km. The model gives a linear relationship (solid line) with gradient 62.8, extended (dashed line) to show that it passes through the origin.

$$\tan a = \frac{1}{2L \cos\theta_m \sin\theta_m} \tag{4.104}$$

For our typical case where $L = 10$ and $\theta_m = 71.6°$, $a = 9.48°$. Thus, $h_{\parallel} = h/\cos a = 1.01h$. Our number density variation gives us $\nabla n \approx n/h_{\parallel}$, and we obtain

$$E_{\text{amb}} \approx -\frac{kT_I}{eh_{\parallel}} \tag{4.105}$$

This relation suggests that E_{amb} is only affected by the ion scale height, h, and the ionospheric electron temperature T_I (via τ); it is not, however, affected by changes in n_M via ν. We can check this relation using our numerical results. Figure 4.13 shows the effect of τ on $\bar{E}_{\text{amb}}$ with h fixed at 100 km: this gives a linear relation, as expected, such that

$$\bar{E}_{\text{amb}} = -62.8\tau \tag{4.106}$$

Figure 4.14 shows the effect of h on $\bar{E}_{\text{amb}}$ with τ fixed at 10^{-3}. As h decreases, $\bar{E}_{\text{amb}}$ is required to increase, as the ion number density falls off more quickly with altitude, so a larger parallel electric field is required to constrain the ionospheric electrons over a shorter distance. Figure 4.14(b) confirms a linear relationship between $\bar{E}_{\text{amb}}$ and h^{-1}, such that

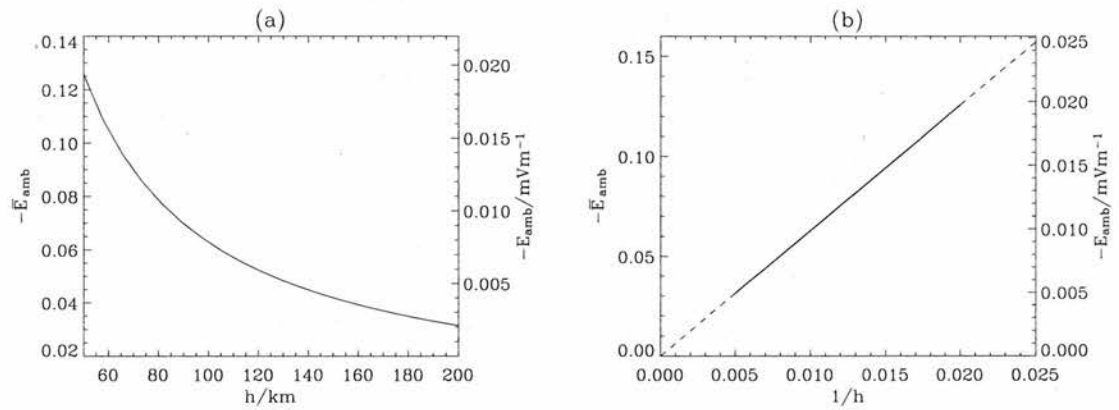

Figure 4.14: (a) A plot of the effect of h on $\bar{E}_{\rm amb}$, keeping τ fixed at 0.001. (b) Plotting $\bar{E}_{\rm amb}$ against $1/h$ shows a linear relationship (solid line) with gradient 6280, extended (dashed line) to show that it passes through the origin.

$$\bar{E}_{\rm amb} = -\frac{6280}{h} \tag{4.107}$$

The two results in equations (4.106) and (4.107) can be combined to give

$$\bar{E}_{\rm amb} = -\frac{6.28 \times 10^6 \tau}{h} \tag{4.108}$$

Using equations (4.32) and (4.99), this gives a dimensional expression of

$$\begin{aligned} E_{\rm amb} &= -\frac{6.28 \times 10^6 k}{eR_E}\left(\frac{T_I}{h}\right) \\ &= -\frac{kT_I}{eh_\parallel} \end{aligned} \tag{4.109}$$

which confirms the theoretical result derived in equation (4.105). It can be seen from Figure 4.9(a) that this ambipolar electric field extends almost to the B/N peak, so we can integrate $E_{\rm amb}$ from the base of the field line (ℓ_m) to the B/N peak (ℓ_p) to find the ambipolar potential, $\phi_{\rm amb}$, as follows:

$$\begin{aligned} \phi_{\rm amb} &\approx -\int_{\ell_m}^{\ell_p} E_{\rm amb}\, {\rm d}\ell \\ &= \frac{kT_I}{e}\left(\frac{\ell_p - \ell_m}{h_\parallel}\right) \end{aligned} \tag{4.110}$$

Thus, in this case, where $h = 100$ km and the distance from ℓ_m to the B/N peak is $\sim$17 scale heights,

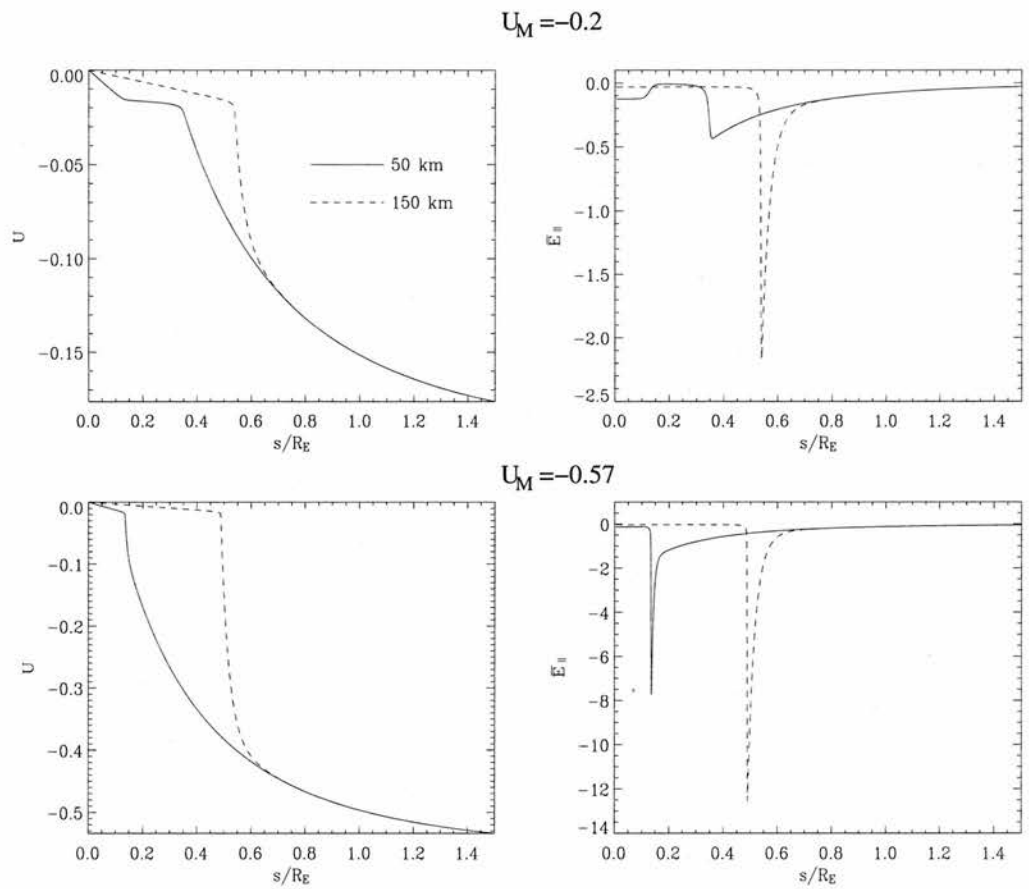

Figure 4.15: Plots illustrating the effect of ion scale height, h, on potential distribution and $\bar{E}_{\|}$. The potential, U, and parallel electric field, $\bar{E}_{\|}$, are plotted for two scale heights of 50 km (solid) and 150 km (dashed), in two cases where $U_M = -0.2$ (top) and -0.57 (bottom).

the ambipolar potential is $\sim$17 times kT_I/e. Using equation (4.5), we can see that the normalised ambipolar potential, U_{amb}, can be expressed as

$$U_{\mathrm{amb}} \approx \tau \left(\frac{\ell_p - \ell_m}{h_{\|}} \right) \tag{4.111}$$

4.5.8 Effect of scale height on potential distribution

For potential solutions such as ours which satisfy the Davisson condition in equation (4.24), the total potential drop, U_M, uniquely defines the source cone and hence current density, so altering the ion scale height, h, cannot affect the overall potential required for a prescribed current density. It will, however, affect the distribution of that potential along the field line due to the quasi-neutrality constraint, and hence the parallel electric field will also be affected.

Figure 4.15 illustrates the effect on potential, U, and parallel electric field, $\bar{E}_{\|}$, of increasing the scale

height from 50 to 150 km in two cases where U_M is -0.2 and -0.57. Increasing the scale height results in higher ion number densities at higher altitudes, and thus moves the B/N peak to higher altitudes: for scale heights of 50 and 150 km, the B/N peak lies at 0.141 R_E (898 km) and 0.400 R_E (2550 km), respectively. Thus, for a larger scale height, the ambipolar region extends to higher altitudes, as can be seen in both examples. At higher altitudes > 0.663 R_E (4220 km), the ion number densities for the two scale heights only vary by $< 1 \times 10^{-6}$, so the two potential and parallel electric field curves coincide for a given value of U_M, as can be seen in the examples plotted in Figure 4.15. The combination of these two effects is that a larger scale height forces the electron acceleration to occur at higher altitudes over a narrower region, resulting in a higher parallel electric field spike.

These examples illustrate that, whilst the overall current-voltage relation may be linear and uniquely defined, the distribution of potential along the field line, and hence the parallel electric field, are highly dependent on the ion density distribution which constrains this solution via quasi-neutrality.

4.6 Parallel electric field

4.6.1 Derivation of electron fluid equation

In this section, we seek to obtain the single electron fluid equation involving the parallel electric field, $E_\parallel$, from the guiding centre Vlasov equation. This is similar to work done by *Comfort (1988)*. The general Vlasov equation is

$$\frac{\partial f}{\partial t} + \mathbf{v} \cdot \frac{\partial f}{\partial \mathbf{r}} + \frac{\mathbf{F}}{m} \cdot \frac{\partial f}{\partial \mathbf{v}} = 0 \tag{4.112}$$

where f is the electron distribution function, t is time, $\mathbf{r}$ is position, $\mathbf{v}$ is electron velocity, and $\mathbf{F}$ is a general force which may include a parallel electric field. In our case, we are considering a steady state (so $\partial/\partial t = 0$), and ℓ is our field-aligned coordinate, as defined in equation (2.9). The forces we include are the parallel electric field ($-eE_\parallel$) and the magnetic mirror force ($-\mu \partial B/\partial \ell$), where $\mu = mv_\perp^2/2B$ is the magnetic moment, which is conserved along an electron trajectory. Thus our gyrotropic Vlasov equation becomes

$$v_\parallel \frac{\partial f}{\partial \ell} - \left(\frac{eE_\parallel}{m} + \frac{v_\perp^2}{2B} \frac{\partial B}{\partial \ell} \right) \frac{\partial f}{\partial v_\parallel} + \frac{\mathrm{d}v_\perp}{\mathrm{d}t} \frac{\partial f}{\partial v_\perp} = 0 \tag{4.113}$$

Finally, we can use equation (2.18) to obtain

$$v_\parallel \frac{\partial f}{\partial \ell} - \left(\frac{eE_\parallel}{m} + \frac{v_\perp^2}{2B} \frac{\partial B}{\partial \ell} \right) \frac{\partial f}{\partial v_\parallel} + \frac{v_\parallel v_\perp}{2B} \frac{\partial B}{\partial \ell} \frac{\partial f}{\partial v_\perp} = 0 \tag{4.114}$$

In order to establish the fluid equations for the electrons, we must take moments of equation (4.114). Moments for the general Vlasov equation can be found in textbooks, but no full derivation was found for gyrotropic, magnetic moment conserving particles, so we derive these results ourselves here.

Zero-order moment

Taking the zero-order moment produces the mass-conservation law, in terms of the electron number density, n, and the electron fluid velocity, $\bar{v}_\parallel$, where

$$\bar{v}_\parallel = \frac{1}{n} \int v_\parallel f \ \mathrm{d}\mathbf{v} \tag{4.115}$$

Firstly, we take the zero-order moment of the first term in equation (4.114).

$$\begin{aligned}\int v_{\parallel}\frac{\partial f}{\partial \ell}\ \mathrm{d}\mathbf{v} &= \frac{\partial}{\partial \ell}\int v_{\parallel} f\ \mathrm{d}\mathbf{v} \\ &= \frac{\partial}{\partial \ell}\left(n\bar{v}_{\parallel}\right)\end{aligned} \tag{4.116}$$

The second term vanishes, since

$$-\int\left(\frac{eE_{\parallel}}{m}+\frac{v_{\perp}^2}{2B}\frac{\partial B}{\partial \ell}\right)\frac{\partial f}{\partial v_{\parallel}}\ \mathrm{d}v_{\parallel} = -\left(\frac{eE_{\parallel}}{m}+\frac{v_{\perp}^2}{2B}\frac{\partial B}{\partial \ell}\right)[f]_{-\infty}^{\infty} \tag{4.117}$$

where we assume that the distribution function f behaves such that

$$\lim_{|v_{\parallel}|\to\infty}(f) = 0 \tag{4.118}$$

In computing the final term of the mass-conservation law, we need to use the following result, where $A(v_{\parallel})$ is an arbitrary function of $v_{\parallel}$, achieved by using integration by parts twice:

$$\begin{aligned}\int A(v_{\parallel})v_{\perp}\frac{\partial f}{\partial v_{\perp}}\ \mathrm{d}\mathbf{v} &= \int A(v_{\parallel})\left(\int v_{\perp}\frac{\partial f}{\partial v_{\perp}}\left(2\pi v_{\perp}\ \mathrm{d}v_{\perp}\right)\right)\ \mathrm{d}v_{\parallel} \\ &= \int A(v_{\parallel})\int\frac{\partial}{\partial v_{\perp}}\left(f v_{\perp}\right)\left(2\pi v_{\perp}\ \mathrm{d}v_{\perp}\right)\ \mathrm{d}v_{\parallel} - \int A(v_{\parallel})\int f\left(2\pi v_{\perp}\ \mathrm{d}v_{\perp}\right)\ \mathrm{d}v_{\parallel} \\ &= \int A(v_{\parallel})\left(\left[2\pi v_{\perp}\left(f v_{\perp}\right)\right]_{v_{\perp}=0}^{\infty} - \int 2\pi f v_{\perp}\ \mathrm{d}v_{\perp} - \int f 2\pi v_{\perp}\ \mathrm{d}v_{\perp}\right)\ \mathrm{d}v_{\parallel} \\ &= -2\int A(v_{\parallel})f\left(2\pi v_{\perp}\right)\ \mathrm{d}v_{\perp}\ \mathrm{d}v_{\parallel} \\ &= -2\int A(v_{\parallel})f\ \mathrm{d}\mathbf{v}\end{aligned} \tag{4.119}$$

Using this, we can take the zero-order moment of the final term in equation (4.114), where $A(v_{\parallel}) = v_{\parallel}$:

$$\begin{aligned}\int\frac{v_{\parallel}v_{\perp}}{2B}\frac{\partial B}{\partial \ell}\frac{\partial f}{\partial v_{\perp}}\ \mathrm{d}\mathbf{v} &= -\frac{1}{B}\frac{\partial B}{\partial \ell}\int v_{\parallel} f\ \mathrm{d}\mathbf{v} \\ &= -\frac{n\bar{v}_{\parallel}}{B}\frac{\partial B}{\partial \ell}\end{aligned} \tag{4.120}$$

Using the contributions from equations (4.116) and (4.120), we can see that the mass conservation equation is

$$\frac{\partial}{\partial \ell}\left(n\bar{v}_{\parallel}\right) - \frac{n\bar{v}_{\parallel}}{B}\frac{\partial B}{\partial \ell} = 0, \tag{4.121}$$

which can also be written as

$$\frac{\partial}{\partial \ell}\left(\frac{n\bar{v}_{\parallel}}{B}\right) = 0 \tag{4.122}$$

We can also define the parallel current density, $j_{\parallel}$, as

$$j_{\parallel} = -ne\bar{v}_{\parallel} \tag{4.123}$$

Substituting equation (4.123) into (4.122) tells us that

$$\frac{\partial}{\partial \ell}\left(\frac{j_{\parallel}}{B}\right) = 0, \tag{4.124}$$

that is, $j_{\parallel}/B$ is conserved along a flux tube, as expected.

First-order moment

Taking the first-order moment of equation (4.114) involves multiplying it by $mv_{\parallel}$ and integrating over velocity space. Doing this to the first term of equation (4.114) gives

$$\int mv_{\parallel}^2 \frac{\partial f}{\partial \ell}\ \mathrm{d}\mathbf{v} = m\frac{\partial}{\partial \ell}\int v_{\parallel}^2 f\ \mathrm{d}\mathbf{v} \tag{4.125}$$

Now we perform the same operation on the second term of equation (4.114), where we use integration by parts and assume that

$$\lim_{|v_{\parallel}|\to\infty}\left(fv_{\parallel}\right) = 0 \tag{4.126}$$

to obtain the result:

$$\begin{aligned} -\frac{eE_{\parallel}}{m}\int mv_{\parallel}\frac{\partial f}{\partial v_{\parallel}}\ \mathrm{d}\mathbf{v} &= -eE_{\parallel}\int\left(\left[fv_{\parallel}\right]_{v_{\parallel}=-\infty}^{\infty} - \left(\int f\ \mathrm{d}v_{\parallel}\right)\right)\ 2\pi v_{\perp}\ \mathrm{d}v_{\perp} \\ &= eE_{\parallel}\int f\ \mathrm{d}\mathbf{v} \\ &= enE_{\parallel} \end{aligned} \tag{4.127}$$

We can use the same result to show that the third term yields

$$-\frac{1}{2B}\frac{\partial B}{\partial \ell}\int mv_\perp^2 v_\parallel \frac{\partial f}{\partial v_\parallel}\ \mathrm{d}\mathbf{v} = \frac{m}{2B}\frac{\partial B}{\partial \ell}\int v_\perp^2 f\ \mathrm{d}\mathbf{v} \tag{4.128}$$

Finally, we can take the first moment of the final term of equation (4.114) using the result in equation (4.119):

$$\int \frac{mv_\parallel^2}{2B}\frac{\partial B}{\partial \ell} v_\perp \frac{\partial f}{\partial v_\perp}\ \mathrm{d}\mathbf{v} = -\frac{m}{B}\frac{\partial B}{\partial \ell}\int v_\parallel^2 f\ \mathrm{d}\mathbf{v} \tag{4.129}$$

Using all of the contributions from equations (4.125), (4.127), (4.128) and (4.129), the first-order moment reads

$$-\frac{en}{m}E_\parallel = \frac{\partial}{\partial \ell}\int v_\parallel^2 f\ \mathrm{d}\mathbf{v} + \frac{1}{2B}\frac{\partial B}{\partial \ell}\int v_\perp^2 f\ \mathrm{d}\mathbf{v} - \frac{1}{B}\frac{\partial B}{\partial \ell}\int v_\parallel^2 f\ \mathrm{d}\mathbf{v} \tag{4.130}$$

We can recast this equation in terms of parallel pressure, $p_\parallel$, where

$$\frac{p_\parallel}{mn} = \frac{1}{n}\int v_\parallel^2 f\ \mathrm{d}\mathbf{v} - \bar{v}_\parallel^2 \tag{4.131}$$

and perpendicular pressure, $p_\perp$. In Cartesian coordinates, there are two orthogonal perpendicular directions, x and y say, such that the pressures in these two directions are

$$p_{xx} = m\int v_x^2 f\ \mathrm{d}\mathbf{v};\quad p_{yy} = m\int v_y^2 f\ \mathrm{d}\mathbf{v} \tag{4.132}$$

since there is no average fluid speed $\bar{v}$ in the perpendicular direction. We also have that

$$v_\perp^2 = v_x^2 + v_y^2 \tag{4.133}$$

and that

$$p_\perp = \frac{1}{2}\left(p_{xx} + p_{yy}\right) \tag{4.134}$$

Thus, using these three equations, we see that

$$\begin{aligned} p_\perp &= \frac{m}{2}\int \left(v_x^2 + v_y^2\right) f \mathrm{d}\mathbf{v} \\ &= \frac{m}{2}\int v_\perp^2 f \mathrm{d}\mathbf{v} \end{aligned} \tag{4.135}$$

Using equation (4.131), we can express the first term on the RHS of equation (4.130) in terms of $p_{\|}$ as

$$\begin{aligned}\frac{\partial}{\partial \ell}\int v_{\|}^2 f \ \mathrm{d}\mathbf{v} &= \frac{\partial}{\partial \ell}\left(\frac{p_{\|}}{m}+n\bar{v}_{\|}^2\right)\\ &= \frac{1}{m}\frac{\partial p_{\|}}{\partial \ell}+\bar{v}_{\|}\frac{\partial}{\partial \ell}\left(n\bar{v}_{\|}\right)+n\bar{v}_{\|}\frac{\partial \bar{v}_{\|}}{\partial \ell}\end{aligned} \tag{4.136}$$

Similarly, we can use equation (4.135) to express the second term of equation (4.130) as

$$\frac{1}{2B}\frac{\partial B}{\partial \ell}\int v_{\perp}^2 f \ \mathrm{d}\mathbf{v} = \frac{p_{\perp}}{mB}\frac{\partial B}{\partial \ell} \tag{4.137}$$

Finally, the third term can be written as

$$-\frac{1}{B}\frac{\partial B}{\partial \ell}\int v_{\|}^2 f \ \mathrm{d}\mathbf{v} = -\frac{1}{B}\frac{\partial B}{\partial \ell}\left(\frac{p_{\|}}{m}+n\bar{v}_{\|}^2\right) \tag{4.138}$$

Substituting these expressions into equation (4.130) and simplifying using the mass conservation law in equation (4.121) yields

$$E_{\|} = -\frac{1}{en}\left(\frac{\partial p_{\|}}{\partial \ell}+mn\bar{v}_{\|}\frac{\partial \bar{v}_{\|}}{\partial \ell}+\frac{p_{\perp}-p_{\|}}{B}\frac{\partial B}{\partial \ell}\right) \tag{4.139}$$

Thus, there are contributions to $E_{\|}$ from three distinct sources: the first term on the RHS represents the parallel gradient in parallel pressure, the second term is a measure of electron fluid acceleration, whilst the third term represents the effect of the mirror force, and its size gives a measure of the anisotropy of the plasma in question.

4.6.2 Dimensionless contributions to $\bar{E}_{\|}$

Since our model has ionospheric and magnetospheric Maxwellian distribution functions given in equations (4.41) and (4.40) respectively, both of these will contribute to the parallel electric field, as shown in equations (4.130) and (4.139). We wish to evaluate these contributions in order to discover which factors are most important in supporting the parallel electric field along the field line. To accomplish this, it is useful to transform some of the definitions in the previous section into the dimensionless quantities in equations (4.1) to (4.8). As such, the LHS of equation (4.130) can be written as

$$-\frac{enE_{\|}}{m} = -\frac{n_0 kT_M}{mR_E}N\bar{E}_{\|} \tag{4.140}$$

Firstly, we examine the contributions to the parallel electric field from the magnetospheric electrons.

The first term on the RHS of equation (4.130) can be expressed in terms of the magnetospheric Maxwellian distribution function, $\bar{f}_M$, in equation (4.40) using equations (4.44) and (4.99) to give

$$\frac{\partial}{\partial \ell}\int v_\parallel^2 f_M \ \mathrm{d}\mathbf{v} = \frac{n_0 k T_M}{m R_E}\frac{\partial}{\partial \xi}\int u_\parallel^2 \bar{f}_M \ \mathrm{d}\mathbf{u} \tag{4.141}$$

The other two terms can be transformed in a similar manner by noting that

$$\frac{1}{B}\frac{\partial B}{\partial \ell} = -\frac{1}{\zeta R_E}\frac{\partial \zeta}{\partial \xi} \tag{4.142}$$

Using these results, we can transform equation (4.130) to find the parallel electric field, $\bar{E}_\parallel^{\mathrm{mag}}$, caused by the magnetospheric electrons

$$N\bar{E}_\parallel^{\mathrm{mag}} = -\frac{\partial}{\partial \xi}\int u_\parallel^2 \bar{f}_M \ \mathrm{d}\mathbf{u} + \frac{1}{2\zeta}\frac{\partial \zeta}{\partial \xi}\int u_\perp^2 \bar{f}_M \ \mathrm{d}\mathbf{u} - \frac{1}{\zeta}\frac{\partial \zeta}{\partial \xi}\int u_\parallel^2 \bar{f}_M \ \mathrm{d}\mathbf{u} \tag{4.143}$$

This can be further subdivided into the parallel electric field, $\bar{E}_\parallel^p$, caused by the precipitating magnetospheric electrons,

$$N\bar{E}_\parallel^p = -\frac{\partial}{\partial \xi}\int_{A_1} u_\parallel^2 \bar{f}_M \ \mathrm{d}\mathbf{u} + \frac{1}{2\zeta}\frac{\partial \zeta}{\partial \xi}\int_{A_1} u_\perp^2 \bar{f}_M \ \mathrm{d}\mathbf{u} - \frac{1}{\zeta}\frac{\partial \zeta}{\partial \xi}\int_{A_1} u_\parallel^2 \bar{f}_M \ \mathrm{d}\mathbf{u} \tag{4.144}$$

and the field, $\bar{E}_\parallel^m$, caused by the mirroring electrons,

$$N\bar{E}_\parallel^m = -\frac{\partial}{\partial \xi}\int_{2A_2} u_\parallel^2 \bar{f}_M \ \mathrm{d}\mathbf{u} + \frac{1}{2\zeta}\frac{\partial \zeta}{\partial \xi}\int_{2A_2} u_\perp^2 \bar{f}_M \ \mathrm{d}\mathbf{u} - \frac{1}{\zeta}\frac{\partial \zeta}{\partial \xi}\int_{2A_2} u_\parallel^2 \bar{f}_M \ \mathrm{d}\mathbf{u} \tag{4.145}$$

where areas A_1 and A_2 are illustrated in Figure 4.1(b). In a similar way, we can find the parallel electric field, $\bar{E}_\parallel^{\mathrm{iono}}$, caused by the ionospheric electrons. Examining the first term on the RHS of equation (4.130) for f_I leads to

$$\frac{\partial}{\partial \ell}\int v_\parallel^2 f_I \ \mathrm{d}\mathbf{v} = \frac{n_0 k T_I}{m R_E}\frac{\partial}{\partial \xi}\int \tilde{u}_\parallel^2 \bar{f}_I \ \mathrm{d}\tilde{\mathbf{u}} \tag{4.146}$$

Thus, the final answer is very similar, this time incorporating a factor of τ due to the T_I present in the above equation:

$$\frac{N}{\tau}\bar{E}_\parallel^{\mathrm{iono}} = -\frac{\partial}{\partial \xi}\int_{A_5+2A_6} \tilde{u}_\parallel^2 \bar{f}_I \ \mathrm{d}\tilde{\mathbf{u}} + \frac{1}{2\zeta}\frac{\partial \zeta}{\partial \xi}\int_{A_5+2A_6} \tilde{u}_\perp^2 \bar{f}_I \ \mathrm{d}\tilde{\mathbf{u}} - \frac{1}{\zeta}\frac{\partial \zeta}{\partial \xi}\int_{A_5+2A_6} \tilde{u}_\parallel^2 \bar{f}_I \ \mathrm{d}\tilde{\mathbf{u}} \tag{4.147}$$

4.6.3 Dimensionless pressure terms

It is also possible to define dimensionless parallel and perpendicular pressure terms, related to the dimensional $p_{\parallel}$ and $p_{\perp}$ in equations (4.131) and (4.135). Firstly, examining the average velocity in equation (4.115), we can use equations (4.40) and (4.44) to see that

$$\begin{aligned} \bar{v}_{\parallel} &= \frac{1}{n}\int v_{\parallel} f_M \ \mathrm{d}\mathbf{v} \\ &= \sqrt{\frac{kT_M}{m}}\frac{1}{N}\int u_{\parallel}\bar{f}_M \ \mathrm{d}\mathbf{u} \\ &= \sqrt{\frac{kT_M}{m}}\bar{u}_{\parallel} \end{aligned} \tag{4.148}$$

where

$$\bar{u}_{\parallel} = \frac{1}{N}\int u_{\parallel}\bar{f}_M \ \mathrm{d}\mathbf{u} \tag{4.149}$$

Thus, examining the expression in equation (4.131), we can write an expression for the contribution to the parallel pressure, $p_{\parallel}^{\mathrm{mag}}$, from the magnetospheric electrons

$$\begin{aligned} p_{\parallel}^{\mathrm{mag}} &= kT_M n_0 \left(\int u_{\parallel}^2 \bar{f}_M \ \mathrm{d}\mathbf{u} - N\bar{u}_{\parallel}^2\right) \\ &= kT_M n_0 \bar{p}_{\parallel}^{\mathrm{mag}} \end{aligned} \tag{4.150}$$

where

$$\bar{p}_{\parallel}^{\mathrm{mag}} = \int u_{\parallel}^2 \bar{f}_M \ \mathrm{d}\mathbf{u} - N\bar{u}_{\parallel}^2 \tag{4.151}$$

is the normalised contribution to parallel pressure from the magnetospheric electrons. Similarly, the magnetospheric contribution to the perpendicular pressure in equation (4.135) can be written as

$$\bar{p}_{\perp}^{\mathrm{mag}} = \frac{1}{2}\int u_{\perp}^2 \bar{f}_M \ \mathrm{d}\mathbf{u} \tag{4.152}$$

The magnetospheric parallel pressure in equation (4.151) can be further subdivided into the contribution, $\bar{p}_{\parallel}^{p}$, from the precipitating electrons,

$$\bar{p}_{\parallel}^{p} = \int_{A_1} u_{\parallel}^2 \bar{f}_M \ \mathrm{d}\mathbf{u} - N\bar{u}_{\parallel}^2 \tag{4.153}$$

and the contribution, $\bar{p}_{\parallel}^{m}$, from the mirroring electrons,

$$\bar{p}_{\parallel}^{m} = \int_{2A_2} u_{\parallel}^2 \bar{f}_M \ \mathrm{d}\mathbf{u} \tag{4.154}$$

where the mirroring electrons have a zero average drift velocity. In a similar fashion, the contribution to parallel pressure, $\bar{p}_{\parallel}^{\mathrm{iono}}$, from the ionospheric electrons can be found to be

$$\begin{aligned} \bar{p}_{\parallel}^{\mathrm{iono}} &= \int_{A_5+2A_6} \tilde{u}_{\parallel}^2 \bar{f}_I \ \mathrm{d}\tilde{\mathbf{u}} \\ &= kT_I n_0 p_{\parallel}^{\mathrm{iono}} \end{aligned} \tag{4.155}$$

Similarly, the perpendicular pressure for the precipitating, mirroring and ionospheric electrons can be found by using integration areas of A_1, $2A_2$ and $A_5 + 2A_6$ respectively in equation (4.152). We can substitute the normalised forms in equations (4.99), (4.142), (4.148), (4.151) and (4.155) into equation (4.139) to yield

$$\begin{aligned} \bar{E}_{\parallel} = & -\frac{1}{N}\left(\frac{\partial \bar{p}_{\parallel}^{\mathrm{mag}}}{\partial \xi} + N\bar{u}_{\parallel}\frac{\partial \bar{u}_{\parallel}}{\partial \xi} + \frac{\bar{p}_{\parallel}^{\mathrm{mag}} - \bar{p}_{\perp}^{\mathrm{mag}}}{\zeta}\frac{\partial \zeta}{\partial \xi}\right) \\ & -\frac{\tau}{N}\left(\frac{\partial \bar{p}_{\parallel}^{\mathrm{iono}}}{\partial \xi} + \frac{\bar{p}_{\parallel}^{\mathrm{iono}} - \bar{p}_{\perp}^{\mathrm{iono}}}{\zeta}\frac{\partial \zeta}{\partial \xi}\right) \end{aligned} \tag{4.156}$$

where

$$\bar{p}_{\parallel}^{\mathrm{mag}} = \bar{p}_{\parallel}^{p} + \bar{p}_{\parallel}^{m} \tag{4.157}$$

and

$$\bar{p}_{\perp}^{\mathrm{mag}} = \bar{p}_{\perp}^{p} + \bar{p}_{\perp}^{m} \tag{4.158}$$

4.6.4 Calculation of magnetospheric pressure terms

We can calculate the contribution to $\bar{E}_{\parallel}$ from the magnetospheric precipitating electrons, $\bar{E}_{\parallel}^{p}$ (equation (4.144)), and the magnetospheric mirroring electrons, $\bar{E}_{\parallel}^{m}$ (equation (4.145)), by integrating over the appropriate areas in Figures 4.1(b). Details of all of these integrals may be found in the Appendix. Firstly,

$$\begin{aligned}\int\limits_{A_1+2A_2} u_{\parallel}^2 \bar{f}_M \ \mathrm{d}\mathbf{u} &= \int\limits_{A_1+A_2} u_{\parallel}^2 \bar{f}_M \ \mathrm{d}\mathbf{u} + \int\limits_{A_2} u_{\parallel}^2 \bar{f}_M \ \mathrm{d}\mathbf{u} \\ &= \eta_1 + \eta_2 \end{aligned} \tag{4.159}$$

where

$$\begin{aligned}\eta_1 &= \int\limits_{W_{\parallel}=0}^{\infty}\int\limits_{W_{\perp}=0}^{\infty} u_{\parallel}^2 \bar{f}_M \ \mathrm{d}\mathbf{u} - \int\limits_{W_{\parallel}=0}^{U-U_M}\int\limits_{W_{\perp}=0}^{\frac{W_{\parallel}-U+U_M}{\zeta/\zeta_M-1}} u_{\parallel}^2 \bar{f}_M \ \mathrm{d}\mathbf{u} \\ &= \frac{e^{U-U_M}}{2}\mathrm{erfc}\left(\sqrt{U-U_M}\right) - \frac{s^{-3/2}}{\sqrt{\pi}}\mathrm{D}\left(\sqrt{s(U-U_M)}\right) + \frac{\zeta_M}{\zeta}\sqrt{\frac{U-U_M}{\pi}} \end{aligned} \tag{4.160}$$

and

$$\begin{aligned}\eta_2 &= \int\limits_{W_{\parallel}=0}^{U-U_D}\int\limits_{W_{\perp}=\frac{W_{\parallel}-U+U_M}{\zeta/\zeta_M-1}}^{\infty} u_{\parallel}^2 \bar{f}_M \ \mathrm{d}\mathbf{u} + \int\limits_{W_{\parallel}=U-U_D}^{\infty}\int\limits_{W_{\perp}=\frac{W_{\parallel}-U}{\zeta-1}}^{\infty} u_{\parallel}^2 \bar{f}_M \ \mathrm{d}\mathbf{u} \\ &= e^{-k}\left[\left(\frac{\zeta_M-1}{\zeta}\right)\sqrt{\frac{U-U_D}{\pi}} + \frac{t}{2}^{-3/2} e^{t(U-U_D)}\mathrm{erfc}\left(\sqrt{t(U-U_D)}\right)\right. \\ &\left. -\frac{s^{-3/2}}{\sqrt{\pi}}D\left(\sqrt{s(U-U_D)}\right)\right] \end{aligned} \tag{4.161}$$

The contribution to this integral from the precipitating electrons is given by

$$\int\limits_{A_1} u_{\parallel}^2 \bar{f}_M \ \mathrm{d}\mathbf{u} = \eta_1 - \eta_2 \tag{4.162}$$

whilst the contribution from the mirroring electrons is

$$\int_{2A_2} u_\parallel^2 \bar{f}_M \ \mathrm{d}\mathbf{u} = 2\eta_2 \tag{4.163}$$

Now we can carry out the same procedure for the perpendicular pressure term, i.e.

$$\begin{aligned}\int_{A_1+2A_2} u_\perp^2 \bar{f}_M \ \mathrm{d}\mathbf{u} &= \int_{A_1+A_2} u_\perp^2 \bar{f}_M \ \mathrm{d}\mathbf{u} + \int_{A_2} u_\perp^2 \bar{f}_M \ \mathrm{d}\mathbf{u} \\ &= \mu_1 + \mu_2\end{aligned} \tag{4.164}$$

where

$$\begin{aligned}\mu_1 &= \int_{W_\parallel=0}^{\infty}\int_{W_\perp=0}^{\infty} u_\perp^2 \bar{f}_M \ \mathrm{d}\mathbf{u} - \int_{W_\parallel=0}^{U-U_M}\int_{W_\perp=0}^{\frac{W_\parallel-U+U_M}{\zeta/\zeta_M-1}} u_\perp^2 \bar{f}_M \ \mathrm{d}\mathbf{u} \\ &= e^{U-U_M}\,\mathrm{erfc}\left(\sqrt{U-U_M}\right) - \frac{\zeta_M}{\zeta}\sqrt{\frac{U-U_M}{\pi}} \\ &\quad + \frac{2}{\sqrt{s\pi}}\left(1+\frac{\zeta_M}{2\zeta}-\frac{U-U_M}{\frac{\zeta}{\zeta_M}-1}\right)\mathrm{D}\left(\sqrt{s(U-U_M)}\right)\end{aligned} \tag{4.165}$$

and

$$\begin{aligned}\mu_2 &= \int_{W_\parallel=0}^{U-U_D}\int_{W_\perp=\frac{W_\parallel-U+U_M}{\zeta/\zeta_M-1}}^{\infty} u_\perp^2 \bar{f}_M \ \mathrm{d}\mathbf{u} + \int_{W_\parallel=U-U_D}^{\infty}\int_{W_\perp=\frac{W_\parallel-U}{\zeta-1}}^{\infty} u_\perp^2 \bar{f}_M \ \mathrm{d}\mathbf{u} \\ &= e^{-k}\left[\left(\frac{1-\zeta_M}{\zeta}\right)\sqrt{\frac{U-U_D}{\pi}} + \frac{e^{t(U-U_D)}}{\sqrt{t}}\left(1-\frac{U}{\zeta-1}+\frac{1}{2\zeta}\right)\mathrm{erfc}\left(\sqrt{t(U-U_D)}\right)\right. \\ &\quad \left. + \frac{2}{\sqrt{s\pi}}\left(1-\frac{U-U_M}{\frac{\zeta}{\zeta_M}-1}+\frac{\zeta_M}{2\zeta}\right)D\left(\sqrt{s(U-U_D)}\right)\right]\end{aligned} \tag{4.166}$$

The contribution to this integral from the precipitating electrons is given by

$$\int_{A_1} u_\perp^2 \bar{f}_M \ \mathrm{d}\mathbf{u} = \mu_1 - \mu_2 \tag{4.167}$$

whilst the contribution from the mirroring electrons is

$$\int_{2A_2} u_\perp^2 \bar{f}_M \, \mathrm{d}\mathbf{u} = 2\mu_2 \tag{4.168}$$

Using the results in equations (4.162), (4.163), (4.167) and (4.168), we can obtain expressions for the contributions to $\bar{E}_\parallel$ by the precipitating electrons in equation (4.144),

$$\bar{E}_\parallel^p = \frac{1}{N}\left(-\frac{\partial}{\partial\xi}(\eta_1 - \eta_2) + \frac{1}{\zeta}\frac{\partial\zeta}{\partial\xi}\left(\frac{1}{2}(\mu_1 - \mu_2) + \eta_2 - \eta_1\right)\right) \tag{4.169}$$

and by the mirroring electrons in equation (4.145),

$$\bar{E}_\parallel^m = \frac{1}{N}\left(-\frac{\partial}{\partial\xi}(2\eta_2) + \frac{1}{\zeta}\frac{\partial\zeta}{\partial\xi}(\mu_2 - 2\eta_2)\right) \tag{4.170}$$

4.6.5 Calculation of ionospheric pressure terms

We can also calculate the contribution to $\bar{E}_\parallel$ by the ionospheric electrons, $\bar{E}_\parallel^{\text{iono}}$ (equation (4.147)). Details of these integrals may also be found in the Appendix. We consider the parallel term first:

$$\begin{aligned}\int_{A_5+2A_6} \tilde{u}_\parallel^2 \bar{f}_I \, \mathrm{d}\tilde{\mathbf{u}} &= \int_{2(A_5+A_6)} \tilde{u}_\parallel^2 \bar{f}_I \, \mathrm{d}\tilde{\mathbf{u}} - \int_{A_5} \tilde{u}_\parallel^2 \bar{f}_I \, \mathrm{d}\tilde{\mathbf{u}} \\ &= 2\gamma_1 - \gamma_2\end{aligned} \tag{4.171}$$

where

$$\begin{aligned}\gamma_1 &= \int_{\tilde{W}_\parallel=0}^{\infty} \int_{\tilde{W}_\perp=0}^{\frac{\tilde{W}_\parallel - U/\tau}{\zeta-1}} \tilde{u}_\parallel^2 \bar{f}_I \, \mathrm{d}\tilde{\mathbf{u}} \\ &= \frac{\nu e^{\frac{U}{\tau}}}{2} - \frac{\nu e^{\frac{tU}{\tau}}}{2t^{3/2}}\end{aligned} \tag{4.172}$$

Since area A_5 is identical to area A_1 with potentials scaled by τ, γ_2 can be found by substituting $U = U/\tau$, $U_M = U_M/\tau$ and $U_D = U_D/\tau$ into $\eta_1 - \eta_2$ (given in equations (4.160) and (4.161)) and multiplying by $\nu e^{U_M/\tau}$ due to the difference in $\bar{f}_M$ and $\bar{f}_I$ to give

$$\begin{aligned}\frac{\gamma_2}{\nu} &= \frac{e^{\frac{U}{\tau}}}{2}\operatorname{erfc}\left(\sqrt{\frac{U-U_M}{\tau}}\right) - \frac{s^{-3/2}}{\sqrt{\pi}}e^{\frac{U_M}{\tau}}\mathrm{D}\left(\sqrt{\frac{s}{\tau}(U-U_M)}\right)\\ &+e^{\frac{U_M}{\tau}}\frac{\zeta_M}{\zeta}\sqrt{\frac{U-U_M}{\pi\tau}} - \left(\frac{\zeta_M-1}{\zeta}\right)e^{\frac{tU_D}{\tau}}\sqrt{\frac{U-U_D}{\pi\tau}}\\ &-\frac{t^{-3/2}}{2}e^{\frac{tU}{\tau}}\operatorname{erfc}\left(\sqrt{\frac{t}{\tau}(U-U_D)}\right) + s^{-3/2}e^{\frac{tU_D}{\tau}}\mathrm{D}\left(\sqrt{\frac{s}{\tau}(U-U_D)}\right)\end{aligned} \tag{4.173}$$

Similarly, we can work out the perpendicular terms as follows:

$$\begin{aligned}\int\limits_{A_5+2A_6}\tilde{u}_\perp^2\bar{f}_I\ \mathrm{d}\tilde{\mathbf{u}} &= \int\limits_{2(A_5+A_6)}\tilde{u}_\perp^2\bar{f}_I\ \mathrm{d}\tilde{\mathbf{u}} - \int\limits_{A_5}\tilde{u}_\perp^2\bar{f}_I\ \mathrm{d}\tilde{\mathbf{u}}\\ &= 2\delta_1 - \delta_2\end{aligned} \tag{4.174}$$

where

$$\begin{aligned}\delta_1 &= \int\limits_{\tilde{W}_\parallel=0}^{\infty}\int\limits_{\tilde{W}_\perp=0}^{\frac{\tilde{W}_\parallel-U/\tau}{\zeta-1}}\tilde{u}_\perp^2\bar{f}_I\ \mathrm{d}\tilde{\mathbf{u}}\\ &= \nu\left(e^{\frac{U}{\tau}} + \frac{e^{\frac{tU}{\tau}}}{\sqrt{t}}\left(\frac{U/\tau}{\zeta-1} - 1 - \frac{1}{2\zeta}\right)\right)\end{aligned} \tag{4.175}$$

As in the parallel integral case, we can find δ_2 simply by substituting $U = U/\tau$, $U_M = U_M/\tau$ and $U_D = U_D/\tau$ into $\mu_1 - \mu_2$ (found in equations (4.165) and (4.166)), and multiplying the answer by $\nu e^{\frac{U_M}{\tau}}$ to obtain

$$\begin{aligned}\frac{\delta_2}{\nu} &= e^{\frac{U}{\tau}}\operatorname{erfc}\left(\sqrt{\frac{U-U_M}{\tau}}\right) - \frac{\zeta_M}{\zeta}e^{\frac{U_M}{\tau}}\sqrt{\frac{U-U_M}{\pi\tau}} + \left(\frac{\zeta_M-1}{\zeta}\right)e^{\frac{tU_D}{\tau}}\sqrt{\frac{U-U_D}{\pi\tau}}\\ &+\frac{2}{\sqrt{s\pi}}\left(1+\frac{\zeta_M}{2\zeta} - \frac{U-U_M}{\tau\left(\frac{\zeta}{\zeta_M}-1\right)}\right)\left(e^{\frac{U_M}{\tau}}\mathrm{D}\left(\sqrt{\frac{s}{\tau}(U-U_M)}\right) - e^{\frac{tU_D}{\tau}}\mathrm{D}\left(\sqrt{\frac{s}{\tau}(U-U_D)}\right)\right)\\ &+\frac{e^{\frac{tU}{\tau}}}{\sqrt{t}}\left(\frac{U}{\tau(\zeta-1)} - 1 - \frac{1}{2\zeta}\right)\operatorname{erfc}\left(\sqrt{\frac{t}{\tau}(U-U_D)}\right)\end{aligned} \tag{4.176}$$

In reality, the integrals over area A_5 tend to zero in our model, since the ionospheric temperature is so much smaller than the magnetospheric one that no electrons actually overcome the potential barrier to

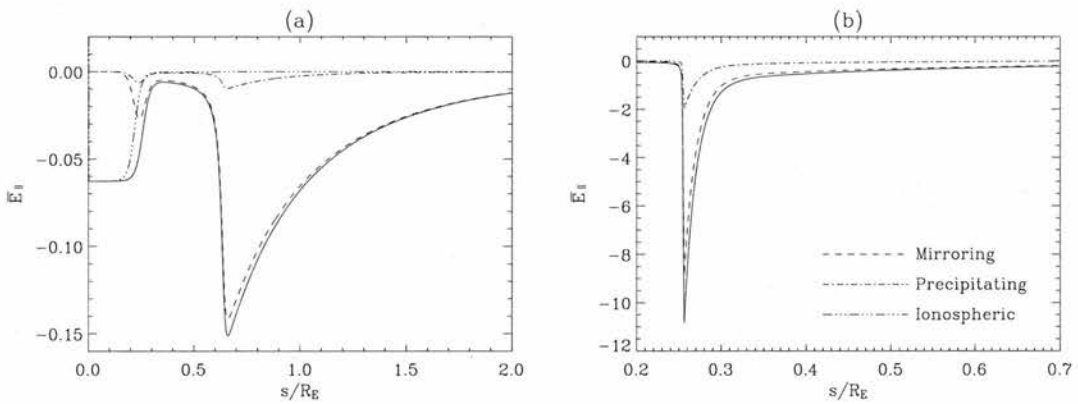

Figure 4.16: Contributions to $\bar{E}_{\parallel}$ (solid line) from precipitating, mirroring and ionospheric electron populations for (a) $U_M = -0.1$ and (b) $U_M = -0.5$. These plots clearly show that while it is the precipitating electrons that carry the current, the mirroring electrons balance most of the parallel electric field which enables this current to be carried.

escape into the magnetosphere. Thus, the contribution to $\bar{E}_{\parallel}$ in equation (4.147) can be expressed as

$$\bar{E}_{\parallel}^{\text{iono}} = \frac{\tau}{N}\left(-\frac{\partial}{\partial\xi}(2\gamma_1) + \frac{1}{\zeta}\frac{\partial\zeta}{\partial\xi}(\delta_1 - 2\gamma_1)\right) \tag{4.177}$$

4.6.6 Contributions to $\bar{E}_{\parallel}$

We now have two methods to calculate the parallel electric field. Firstly, we can find the potential and take its derivative along the field line, as in Section 4.5.5, which was based upon mapping electron trajectories along $\mathbf{B}$ whilst conserving total energy and magnetic moment, and applying Liouville's theorem. Secondly, given the potential variation and the magnetospheric and ionospheric distribution functions, we can take moments to find the parallel electric field. Thus, the contributions from equations (4.169), (4.170) and (4.177) should add up to give the same result as taking the derivative of the normalised potential in equation (4.99). This is an important confirmation of much algebra; if a mistake is made, the two results will not agree. In fact, the two methods agree to at least $\sim 5 \times 10^{-5}$, confirming the results of the previous sections.

Using the expressions in equations (4.169), (4.170) and (4.177), we can find the contributions to $\bar{E}_{\parallel}$ from the precipitating, mirroring and ionospheric electron populations respectively. Two examples of this are given in Figure 4.16 for $U_M = -0.1$ (left) and -0.5 (right). From these graphs, it is clear that the ionospheric electrons support the ambipolar electric field close to the Earth, as expected. Out in the magnetosphere, it can be seen that although the precipitating electrons carry the current, the mirroring electrons actually balance the bulk of the parallel electric field which accelerates the current-carrying electrons. This emphasizes the importance of the mirroring electron population in sustaining the system, since even though it does not actually carry any current, the mirroring electrons play a dominant role in quasi-neutrality constraints. In Figure 4.17, we plot the ratio of mirroring and precipitating contributions to $E_{\parallel\max}$ against U_M: we see that for small potentials, the precipitating population is so small that it hardly supports any of the parallel electric field; as the potential increases, the source cone becomes larger and the precipitating

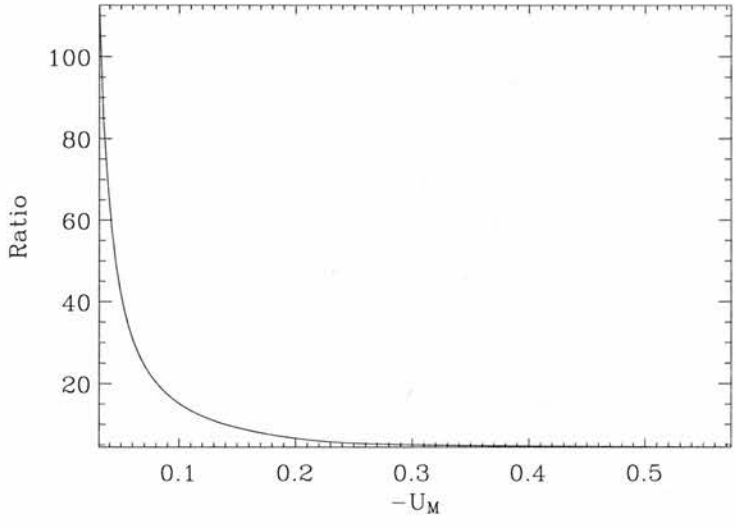

Figure 4.17: Ratio of mirroring and precipitating contributions to $\bar{E}_{\parallel \max}$ plotted against U_M.

electrons make a bigger contribution to the parallel electric field which accelerates them. The ratio asymptotes to ∼5, so that the mirroring electrons support ∼5/6 of the electric field, and the precipitating electrons ∼1/6.

We can also consider the contributions to $\bar{E}_{\parallel}$ from the terms in equation (4.156), corresponding to parallel pressure gradient, electron fluid acceleration and mirroring coupled with plasma anisotropy. For low values of U_M, no term is dominant, and no particular insight is gained into the support of the system. However, for higher values of $\mid U_M \mid \geq 0.3$, the parallel pressure gradient term provides the bulk of $\bar{E}_{\parallel \max}$, as shown for $U_M = -0.4$ in Figure 4.18, while the mirroring term is dominant at higher altitudes. This makes sense, as mirroring is the dominant feature at high altitudes, and the acceleration which occurs at $\bar{E}_{\parallel \max}$ gives all the magnetospheric electrons more parallel velocity, resulting in a parallel velocity and hence parallel pressure gradient.

These results are further illustrated by Figure 4.19, which plots the magnetospheric parallel and perpendicular pressures for $U_M = -0.1$ and -0.5. In both cases, the plasma is isotropic at high altitudes, with equal parallel and perpendicular pressures of 1; as the magnetospheric plasma approaches the Earth, mirroring converts some parallel pressure into perpendicular pressure, resulting in the anisotropy which makes the third term in equation (4.156) dominant at high altitudes. When $U_M = -0.1$, the parallel pressure never has a strong negative gradient, as the source cone of precipitating electrons is small for such a small current, and not much acceleration is required. However, for a higher potential of $U_M = -0.5$, a sharp negative gradient in the parallel pressure can be seen around the B/N peak (0.27 R_E), where the bulk of the acceleration occurs. This makes the parallel pressure gradient the primary contribution to $\bar{E}_{\parallel}$ around the B/N peak.

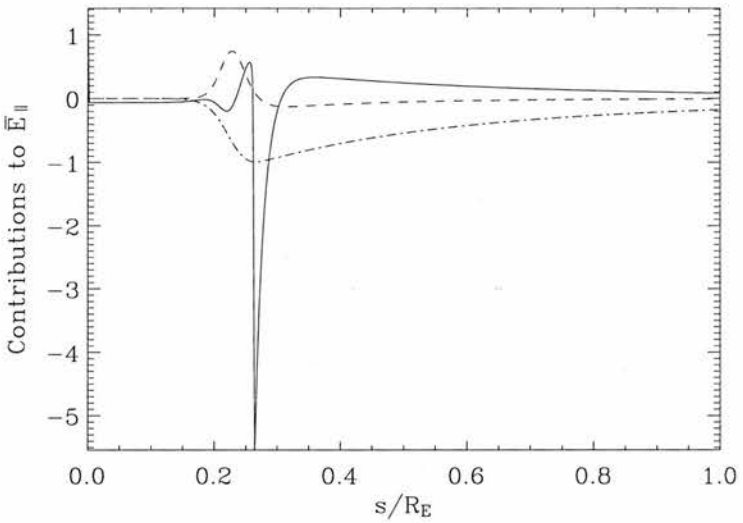

Figure 4.18: Contributions to $\bar{E}_\parallel$ from the parallel pressure gradient (solid line), electron fluid acceleration (dashed line) and mirroring/anisotropy (dot-dashed).

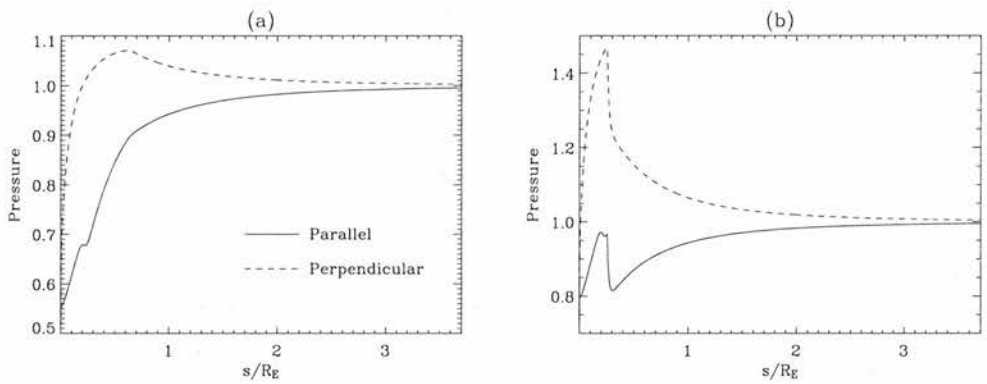

Figure 4.19: Magnetospheric parallel and perpendicular pressures plotted for (a) $U_M = -0.1$ and (b) -0.5.

4.7 Auroral acceleration altitudes

Observations by *Marklund (1993)* suggest that downward-pointing electric fields, and hence electron energisation in the downward current region, occur at altitudes below 4000 km, whilst their upward-pointing counterparts, associated with electron acceleration in the upward current region, are found at altitudes above 4000 km. In both our upward and downward current models, the B/n peak plays a key role in the acceleration region: in the upward current model, acceleration begins at the peak and extends above it for $\sim$1 R_E, whilst in the downward current model, acceleration begins several density scale heights Earthward of the peak, and again extends above it by $\sim$1 R_E. This gives a difference in altitude of several hundred kilometres, but is not quite enough to explain the observed difference of $\sim$1000 km. This indicates that there is a general difference in the ion number density variations with altitude in each region.

Anti-earthward ion flow is a feature of both regions: in the upward current region, the parallel potential accelerates ions upwards, whilst in the downward current region, ions trapped between the low-altitude end of the potential structure and their lower-altitude mirror point are transversely-heated by waves until they are able to overcome the potential and form upward-moving ion conics. This ion outflow is more efficient and extends to lower altitudes in the downward current region, resulting in topside ionospheric cavities *(Moore et al. (1999))*; in the upward current region, higher-altitude plasma density cavities are observed at ~4000 km, with number densities of 0.5-1 cm^{-3} *(Carlson et al. (1998a))*.

In order to model this difference, we take an exponentially-decaying ion number density profile with a scale height of 250 km in the upward current region, shown in Figure 4.20 (dashed line); this profile accounts for the high-altitude density cavity, since the number density is ~1 cm^{-3} at 4000 km altitude. *Lundin et al. (1994)* show that, at Freja altitudes of ~1700 km, strong transverse ion heating causes the ambient ion number density to decrease by over two orders of magnitude from ~1000 cm^{-3} to 10 cm^{-3}. Thus, to produce the ion number density profile in the downward current region, we take the exponentially-decaying profile and drop the number density from ~1000 cm^{-3} to 10 cm^{-3} between 1500 and 1700 km; at higher altitudes, the number density decays to 1 cm^{-3}, as in the upward current region. This modified profile for the downward current region is shown in Figure 4.20 (solid line).

Using these number density profiles, the accelerating potentials and electric fields can be found for upward and downward current densities of 1 μAm^{-2}. These results are shown in Figure 4.21. In the upward current region (dashed lines), a potential of ~180 V is required to carry this current, and the maximum parallel electric field of 0.31 mV/m occurs at ~4270 km. In the downward current region (solid lines), a larger potential of ~590 V is needed to carry the same current, and the correspondingly larger maximum parallel electric field of 1.4 mV/m is located at an altitude of only ~1860 km. Defining the acceleration

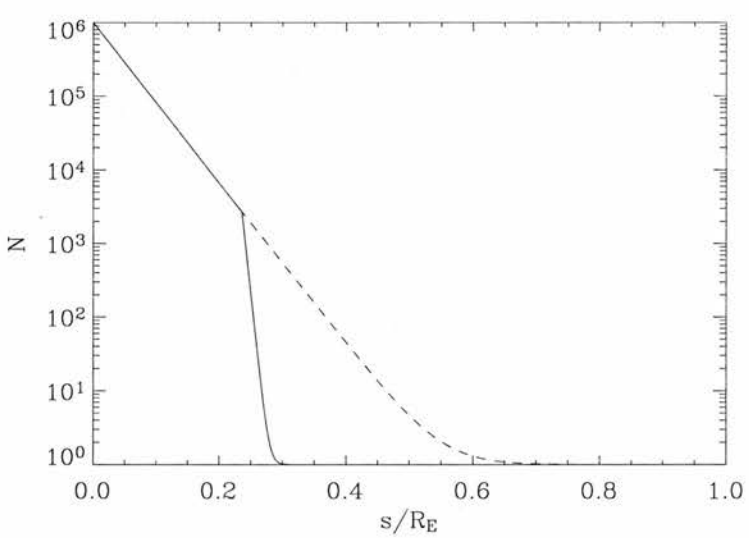

Figure 4.20: Number density profiles in upward (dashed line) and downward (solid line) current regions. The number density decreases more rapidly in the downward current region at ~1500 km (0.24 R_E) due to strong transverse ion heating and outflow in the topside ionosphere.

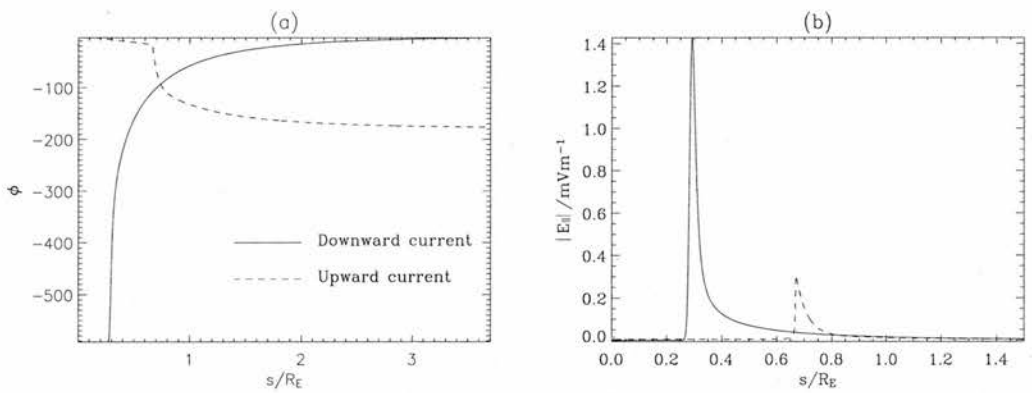

Figure 4.21: Accelerating potentials (a) and electric fields (b) in upward (dashed) and downward (solid) current regions.

width as in Section 2.3.5 for the downward current region and as in equations (4.100) and (4.101) for the upward current region, it is found that acceleration in the downward current region extends from ~1760 km to ~2140 km, whilst in the upward current region, acceleration mainly occurs from ~4230 km to ~4750 km. These numbers agree well with the data in *Marklund (1993)*, and distinctly demonstrate the possibility of enhanced ion outflow in the downward current region reducing the ion density and resulting in a lower altitude acceleration region.

4.8 Discussion and Conclusions

We have presented an upward current model along an auroral flux tube where the ion distribution is fixed and the electrons are described via distribution functions. The ions are much heavier, and so will not react appreciably to an electric field on a typical electron transit time of ~1 s along the flux tube. As such, this model gives the short-timescale solution to the problem. The system is constrained via quasi-neutrality, which enables us to find the potential variation along the field line.

We are only able to find continuous potential solutions for a range of smaller current densities of ~1 μAm^{-2}. At the lower end of this range, the potential is distributed over a large distance of up to ~2-3 R_E, but as the current density becomes larger, the potential is increasingly concentrated immediately above the B/N peak until most of the acceleration occurs over a small distance ~100 km. This gives an indication that if the current density were to be increased further and moving ions were introduced, the solution could steepen into a double layer, such as those observed by *Ergun et al. (2004)* using FAST data at 4000 km altitude. *Ergun et al. (2004)* have found that these stationary double layers have amplitudes of up to ~100 mV/m, extend for ~100 m, and can account for 10 to 50% of the total field-aligned potential. This is similar to the upper limit for continuous potential solutions in our model, where $U_M = -0.574$ in Figure 4.7: here, 42% of the potential occurs around the B/N peak (dashed line), and the rest extends to higher altitudes of up to 3 R_E, to maintain quasi-neutrality. We have also demonstrated that, although the current-voltage relation is independent of the ion number density profile along the field line, the exact nature of that profile will determine the location and magnitude of the parallel electric field. An order of magnitude density

gradient is generally colocated with double layers *(Ergun et al. (2004))*: such a sharp change in density would have the effect of concentrating much of the potential over a very small region in our model.

We found the contributions to the parallel electric field from the plasma anisotropy and magnetic field gradient, electron fluid acceleration and parallel pressure gradient. It was found that for the largest potentials in our continuous range, the parallel pressure gradient supports most of the parallel electric field concentrated at the B/N peak. This is in agreement with results from simulations of shear Alfvén waves by *Vedin and Rönnmark (2005)*, and with observations from the Polar satellite presented by *Hull et al. (2003b)*. At higher altitudes, the plasma anisotropy and magnetic field gradient term is dominant. This is in qualitative agreement with *Mozer and Hull (2001)*, who find that high-altitude acceleration is required up to $\sim$3 R_E to overcome the mirror force, mid-altitude acceleration is required to maintain quasi-neutrality, and a much stronger narrow sheath field exists at low altitudes. Moreover, we discovered that although the precipitating electrons are responsible for carrying the current, the presence of the mirroring electrons is essential to their acceleration, as the mirroring electrons support the majority of the parallel electric field. The mirroring electrons are also vital to the system in that they play a major role in satisfying quasi-neutrality along the flux tube.

Our model uses energy conservation considerations coupled with the magnetic mirror force to determine the source cone of precipitating electrons: our solutions satisfy the linear *Knight (1973)* relation. Several observational studies have been carried out to test this current-voltage relation. *Shiokawa et al. (1990)* used the S-310 sounding rocket at 200 km to collect data which satisfied the Knight relation, and *Lu et al. (1991)* used particle data from the DE-1 at DE-2 satellites at high (10,000-14,000 km) and low (600-800 km) altitudes on auroral field lines to estimate parallel potential, coupled with ground-based magnetometer readings of current density, which also supported a linear relationship. Other studies are not so conclusive: *Haerendel et al. (1994)* and *Frey et al. (1998)* used Freja and ground-based instruments to conclude that the Knight relation is sometimes tenuous, whilst *Sakanoi et al. (1995)* and *Morooka et al. (2004)* used data from the Akebono satellite to show that the Knight relation often significantly underestimates the amount of current that flows with a given potential. This led them to suggest that lower-energy secondary and trapped electrons in the adiabatically "forbidden" area of phase-space must also precipitate and contribute to the current, possibly due to a time-varying parallel electric field at high altitudes. However, *Olsson et al. (1998)* used the Freja satellite to study stronger substorm-related currents: here, the linear Knight relationship is satisfied, showing that low-energy electrons are not important in these energetic cases.

Thus, our steady state model identifies the high-energy electrons which can precipitate subject to energy constraints. The observational studies above generally show that this is at least a good first approximation to the upward current region, and we have demonstrated that, although the linear current-voltage relation itself is simple, the accompanying potential distribution and parallel electric field variation are heavily dependent on the ion density profile along the flux tube. Finally, we discussed the differences in the density profile in the upward and downward current regions: ion outflow occurs in both regions, but is stronger and extends to lower altitudes in the downward current region. Modelling this difference, we found that acceleration occurs at $\sim$2000 km altitude in the downward current region, and at $\sim$4000 km altitude in the upward current region, consistent with observations *(Marklund (1993))*. We would wish to extend this work in the future to include study of the discontinuities, or double layers, which may well occur in our model for larger current densities.

Chapter 5

Ionospheric depletion in downward current regions

5.1 Introduction

In our models of upward and downward field-aligned currents presented thus far, we have assumed a steady state. In the downward current region, for example, we have assumed that the electrons accelerated upwards from the ionosphere to carry the current are continuously replaced. In reality, however, as electrons are accelerated upwards, ions travel horizontally through the E region to carry the Pedersen current: thus, the E region electron and ion number densities quickly erode. Such suppressed densities have been observed by EISCAT radar data in downward current regions by *Aikio et al. (2002)* and *Aikio et al. (2004)*. In a simple calculation, a steady downward current density of 1 μAm^{-2} leads to an outflow of electrons of 6.24×10^{12} m^{-2}s^{-1}. The nightside E region typically has a number density of 10^{10} m^{-3} and a height of 20 km, resulting in a height-integrated number density of 2×10^{14} m^{-2}. Thus, the upward electron flow will result in total E region density erosion in $\sim$32 s. This illustrates that if a modest downward current is to flow for longer than $\sim$1 minute, the region will need to broaden in order to access more current-carriers in the E region. *Aikio et al. (2004)* observed exactly this phenomenon with Cluster: the downward current region widened over a period of $\sim$70 s in order to continue to carry the required current.

A similar situation has also been observed by *Marklund et al. (2001)* using the four Cluster spacecraft; Figure 3 of that paper, reproduced in Figure 5.1, shows the event which took place at 0336 MLT on 14 January 2001 at $\sim$21,000 km altitude and at a magnetic latitude of 69.8°. When the first spacecraft flew through, it detected a compact downward current region with a peak current density of $\sim$0.16 μAm^{-2} (middle panel, Rumba). As subsequent spacecraft flew through the same region over a period of 280 s, a broadening of the downward current region was seen, with lower current densities but roughly the same overall current being carried. The associated bipolar perpendicular electric field signature, indicative of an accelerating potential beneath the spacecraft, initially grew to $\sim$25 mV/m and then disappeared altogether by the final crossing. This data supports the idea that evacuation of the E region during a downward current

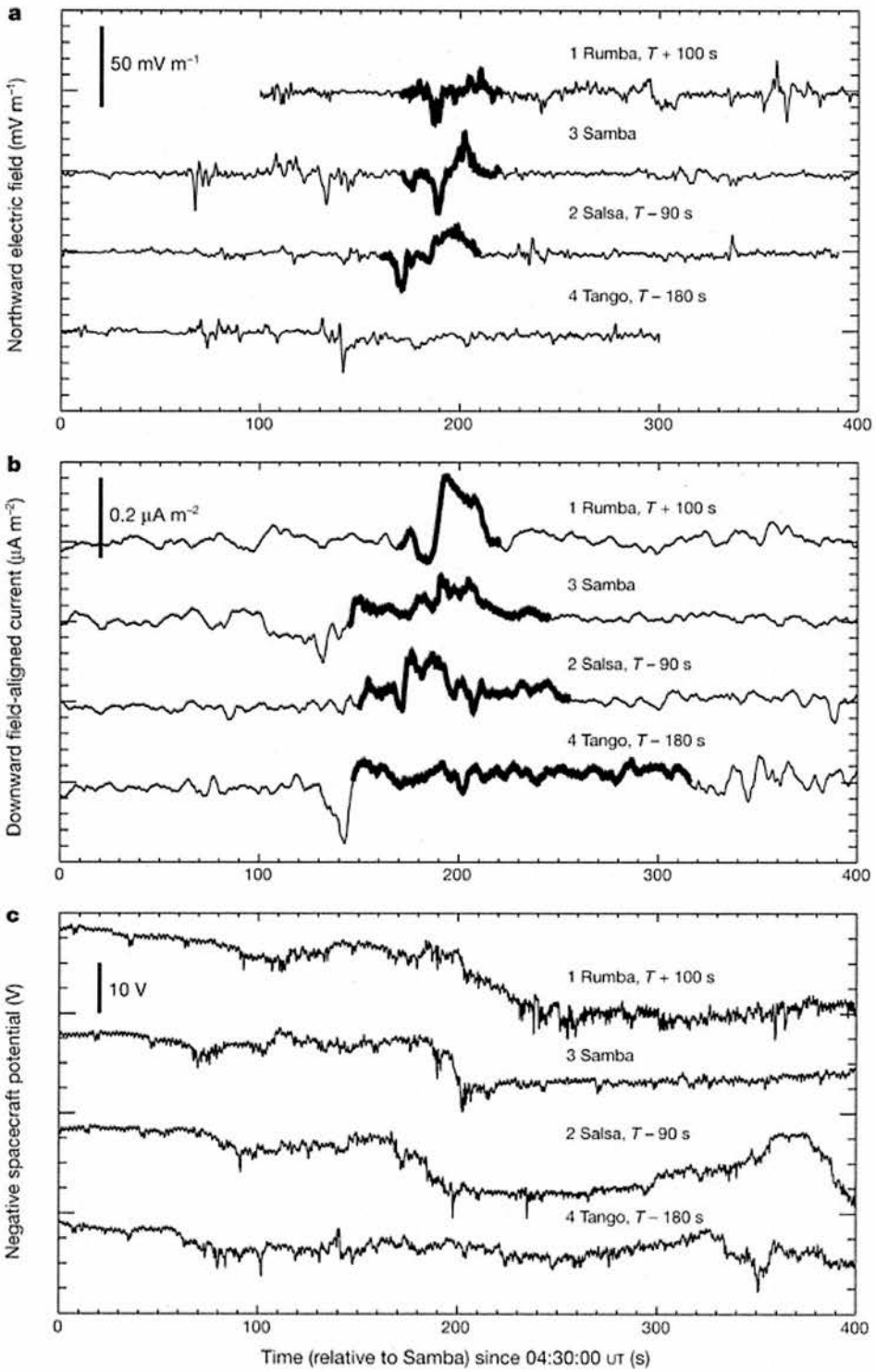

Figure 5.1: Cluster data of (a) northward electric field; (b) downward field-aligned current; and (c) negative spacecraft potential at ~21,000 km altitude and 69.8° magnetic latitude on 14 January 2001 at 0336 MLT. This comes from Figure 3 of *Marklund et al. (2001)* and shows the four satellites flying through a broadening downward current region over a period of ~280 s.

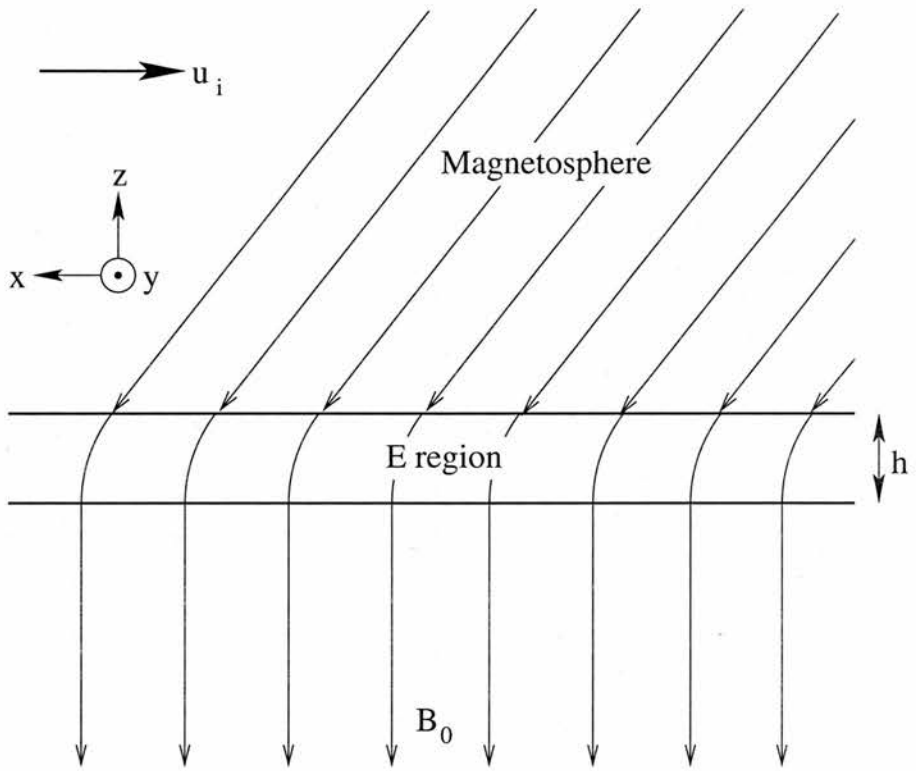

Figure 5.2: Diagram of the x-z plane of the model, adapted from *Wright (1996)*. Incoming Alfvén waves in the magnetosphere have velocity $-u_i\hat{\mathbf{x}}$ and magnetic field perturbation $b_i\hat{\mathbf{x}}$. These waves are partially reflected at the magnetosphere-E region interface.

forces the current region to broaden in time in order to continue to carry the same current. *Karlsson and Marklund (1998)* have modelled this phenomenon by imposing current closure on a small-scale (~10 km) field-aligned current pair, and found that current densities of the order of 10 μAm^{-2} created deep density cavities in the E and lower F regions on timescales of the order of seconds.

The dynamics of propagating Alfvén waves coupling the magnetosphere and ionosphere have been extensively studied in the upward current region, where electron precipitation leads to conductivity enhancements and gradients in the ionosphere. These drive a nonlinear feedback process that produces small-scale auroral arcs (*Pokhotelov et al. (2002)*, *Lysak and Song (2002)* and *Streltsov and Lotko (2005)*). In this Chapter, we model the evacuation of electrons from the E region for a downward current using the ideas of Alfvén wave propagation and reflection at the magnetosphere-ionosphere boundary, which lead to decreased conductivities and a necessary broadening of the current region, which we see is achieved through a change in reflection coefficient.

5.2 Introducing the model

We use a 2D Cartesian system with no x variation to model the E region electron evacuation in the downward current region. Figure 5.2 shows a slice of the model in the x-z plane: incoming Alfvén waves with

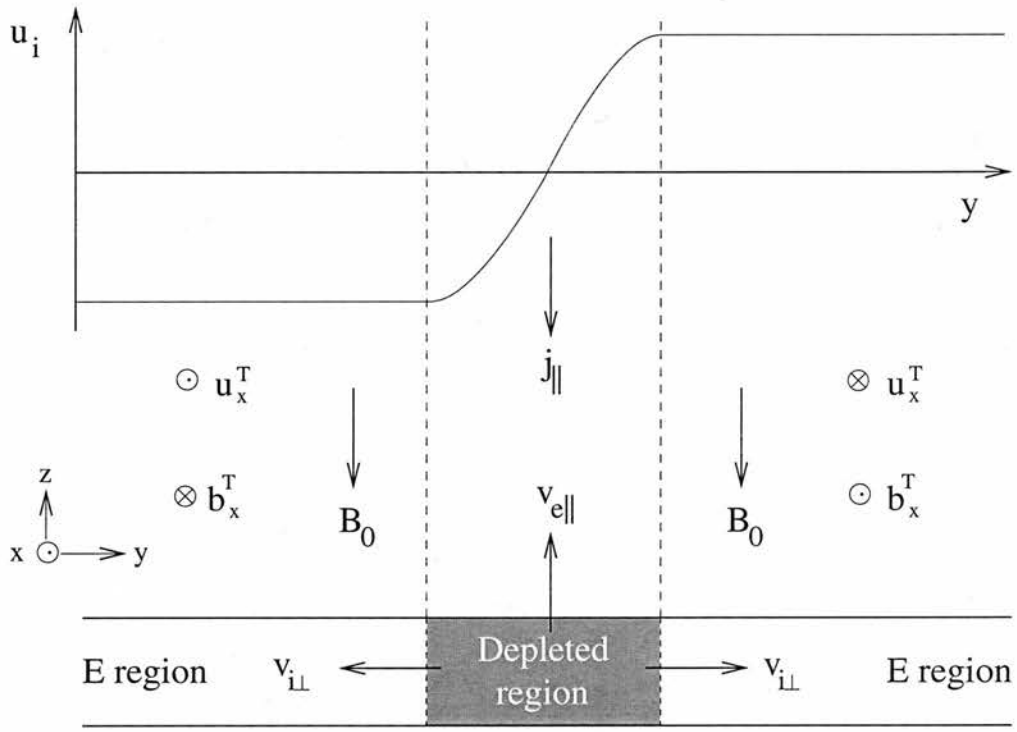

Figure 5.3: Diagram of the y-z plane of the model: a shear in the incident Alfvén velocity ($-u_i\hat{\mathbf{x}}$) in the y direction generates a downward field-aligned current. This draws electrons upwards from the E region, whilst ions travel away horizontally to carry the Pedersen current, leaving a region of depleted number density. The total Alfvén speed (u_x^T) and magnetic field perturbation (b_x^T) change sign over the incident velocity shear.

velocity in the x direction partially reflect at the magnetosphere-E region interface, and the extent of this reflection is governed by a reflection coefficient. The E region, of height h, is initially undepleted. The E region number density is subject to gain due to photoionisation and loss due to recombination. At equilibrium when no current is drawn, these two effects balance one another in a steady state.

Figure 5.3 shows the y-z plane of the model: a shear in the incident Alfvén speed (u_i) in the y direction leads to the formation of a downward field-aligned current ($j_\parallel$), such that electrons are drawn up from the E region with velocity $v_{e\parallel}\hat{\mathbf{z}}$ and ions travel away horizontally with velocity $\pm v_{i\perp}\hat{\mathbf{y}}$ to carry the Pedersen current. Thus, the downward field-aligned current acts as another loss mechanism to the E region number density, causing the formation of a depleted region. The resulting decrease in conductivity in this depleted region modifies the reflection coefficient and hence affects the reflected Alfvén waves. The evolution of the system is modelled via a number density continuity equation in the E region, which incorporates changes to the number density due to photoionisation, recombination and downward field-aligned current caused by the shear flow in the magnetosphere.

5.2.1 Continuity equation

In the E region, which has height h, the plasma continuity equation can be written as

$$\frac{\mathrm{D}n}{\mathrm{D}t} = S - L \tag{5.1}$$

where n is the electron number density, $\mathrm{D}n/\mathrm{D}t$ is defined as $\partial n/\partial t + \nabla \cdot (n\mathbf{v})$ for a velocity $\mathbf{v}$, and S and L represent ion source and loss terms, respectively. The main ions in the E region are NO^+ and O_2^+, and their dissociative recombination in equation (1.9) represents the main loss term, which can be modelled by $-\alpha n^2$, where α is the recombination coefficient which generally takes the value $\sim 3 \times 10^{-13}$ $\mathrm{m^3 s^{-1}}$ *(Ulich et al. (2000))*. When the ionosphere is in equilibrium, equation (5.1) reduces to

$$S = \alpha n_e^2 \tag{5.2}$$

where n_e is the equilibrium E region electron number density. S represents UV photoionisation, and is modulated by n_e, which can range from 10^{10} $\mathrm{m^{-3}}$ at night to at least 10^{11} $\mathrm{m^{-3}}$ during the day: thus, this term implies that more photoionisation occurs during the day than at night, which is logical, as photoionisation will be inhibited at night when the ionosphere is not directly sunlit. This term also indicates that the photoionisation rate is constant; this can be justified, since the rate depends on the incident radiation and E region neutral number density, both of which can be taken to be constant on the timescales involved in this model ($\sim$minutes). Thus, our continuity equation becomes

$$\frac{\partial n}{\partial t} + \nabla \cdot (n\mathbf{v}) = \alpha \left(n_e^2 - n^2\right) \tag{5.3}$$

Assuming that n and $\mathbf{v} = v_z \hat{\mathbf{z}}$ vary only in the y and z directions, this equation can be written as

$$\frac{\partial n}{\partial t} + \frac{\partial}{\partial z}\left(n\left(y,z\right) v_z\left(y,z\right)\right) = \alpha \left(n_e^2 - n^2\right) \tag{5.4}$$

We can integrate this equation in the z direction over the height, h, of the ionosphere, such that

$$\frac{\partial}{\partial t}\int_0^h n \,\mathrm{d}z + \int_0^h \frac{\partial}{\partial z}\left(n\left(y,z\right) v_z\left(y,z\right)\right) \,\mathrm{d}z = \int_0^h \alpha \left(n_e^2 - n^2\right) \,\mathrm{d}z \tag{5.5}$$

Assuming further that n does not vary in the z direction, such that

$$\int_0^h n(y) \,\mathrm{d}z = n(y)h = N(y) \tag{5.6}$$

where $N(y)$ is the height-integrated number density of the E region, and $N_e = n_e h$ is the equilibrium value, equation (5.5) simplifies to

$$\frac{\partial N}{\partial t} + [n(y)v_z(y,z)]_0^h = \frac{\alpha}{h}\left(N_e^2 - N^2\right) \tag{5.7}$$

Finally, we use the relation $j_z = -n(y)ev_z(y,z)$, coupled with the fact that, since the field-aligned and horizontal ionospheric Pedersen currents close within the E region, $j_z = 0$ (i.e. $v_z = 0$) at the base of the E region, to write that

$$\frac{\partial N}{\partial t} - \frac{j_z(y,h)}{e} = \frac{\alpha}{h}\left(N_e^2 - N^2\right) \tag{5.8}$$

This is the continuity equation used by *Pokhotelov et al. (2002)*, *Lysak and Song (2002)* and *Streltsov and Lotko (2005)* to study the dynamics of the upward current region. In their models, where electrons are precipitating into the ionosphere to carry an upward current, the j_z term serves as a source of electrons in the E region; in ours, it is a loss term.

5.2.2 Magnetosphere-Ionosphere boundary condition

In our model, the field-aligned current j_z in equation (5.8) is driven by a shear flow in the magnetosphere, as shown in Figure 5.3. The incident Alfvén wave is reflected from the ionosphere, and the incident and reflected waves add to give a total perpendicular magnetic field component ($b_x^T\hat{\mathbf{x}}$). The shear in incident Alfvén velocity ($-u_i\hat{\mathbf{x}}$) shown in Figure 5.3 gives rise to a shear in b_x^T, which generates a parallel current density via Maxwell's equation (1.12).

In the magnetosphere, the plasma is ideal, i.e. has no resistivity, such that

$$\mathbf{E} = -\mathbf{v} \times \mathbf{B} \tag{5.9}$$

where $\mathbf{E}$ is electric field, $\mathbf{v}$ is velocity and $\mathbf{B}$ is magnetic field strength. Thus, when $\mathbf{B_0} = -B_0\hat{\mathbf{z}}$ and $\mathbf{v} = -u_x^T\hat{\mathbf{x}}$ (where u_x^T is the total speed of the combined incident and reflected Alfvén waves) the magnetospheric electric field, $\mathbf{E_m}$, is given by

$$\mathbf{E_m} = u_x^T B_0\hat{\mathbf{y}} \tag{5.10}$$

The ionosphere is non-ideal and at rest ($\mathbf{v} = 0$), so the ionospheric electric field, $\mathbf{E_i}$, can be expressed as

$$\mathbf{E_i} = \frac{1}{\sigma_p}\mathbf{j} \tag{5.11}$$

where σ_p is Pedersen conductivity and $\mathbf{j}$ is current density. Across the discontinuity between the mag-

netosphere and the ionosphere, the tangential component of the electric field (in the y direction) and the normal component of the magnetic field (in the z direction) are both continuous. We can now integrate equation (5.11) over the ionospheric height using Maxwell's equation (1.12), to give

$$E_i \int_0^h \sigma_p \, \mathrm{d}z = \frac{1}{\mu_0} \int_0^h \frac{\partial b_x^T}{\partial z} \, \mathrm{d}z \tag{5.12}$$

We let $\Sigma_p = \int_0^h \sigma_p \, \mathrm{d}z$ be the height-integrated Pedersen conductivity, and note that, as in Figure 5.2, $b_x^T = 0$ at the base of the ionosphere. We can then substitute equation (5.10) into the expression above to see that

$$b_x^T = \mu_0 \Sigma_p u_x^T B_0 \tag{5.13}$$

This is an ionospheric boundary condition at $z = h$ relating the total x component of the magnetic field perturbation (b_x^T) and velocity ($-u_x^T$). We can decompose these into an incident Alfvén wave with velocity $\mathbf{v} = -u_i \hat{\mathbf{x}}$ and magnetic field perturbation $\mathbf{b} = b_i \hat{\mathbf{x}}$, and a reflected Alfvén wave with $\mathbf{v} = -u_r \hat{\mathbf{x}}$ and $\mathbf{b} = b_r \hat{\mathbf{x}}$, such that

$$b_x^T = b_i + b_r \tag{5.14}$$

and

$$u_x^T = u_i + u_r \tag{5.15}$$

If a general Alfvén wave propagates parallel to the background magnetic field, its magnetic field perturbation, b_x, and velocity, v_x, are related via $b_x = -v_x \sqrt{\mu_0 \rho_0}$, where $\rho_0 = n_0 m_i$ is the magnetospheric mass density, n_0 being magnetospheric ion number density and m_i being ion mass. For our incident Alfvén wave travelling in the direction of $\mathbf{B_0}$, this corresponds to

$$b_i = u_i \sqrt{\mu_0 \rho_0} \tag{5.16}$$

For a general Alfvén wave propagating anti-parallel to the background magnetic field, the corresponding relation is $b_x = v_x \sqrt{\mu_0 \rho_0}$. For our reflected Alfvén wave, this gives

$$b_r = -u_r \sqrt{\mu_0 \rho_0} \tag{5.17}$$

We now introduce the reflection coefficient, a, where

$$u_r = a u_i \tag{5.18}$$

This form can be substituted into equation (5.15) to give

$$u_x^T = u_i \left(1 + a\right) \tag{5.19}$$

Substituting equation (5.18) into (5.17) and using equation (5.16), we deduce that

$$b_r = -a b_i \tag{5.20}$$

which can be substituted into equation (5.14) to yield

$$b_x^T = b_i \left(1 - a\right) \tag{5.21}$$

Substituting equations (5.19) and (5.21) into the boundary condition in (5.13) gives us an expression for the reflection coefficient

$$a = \frac{1 - \mu_0 \Sigma_p V_A}{1 + \mu_0 \Sigma_p V_A} \tag{5.22}$$

where

$$V_A = \frac{B_0}{\sqrt{\mu_o \rho_0}} \tag{5.23}$$

is the Alfvén speed. Now we are in a position to find an expression for the combined wave speed, u_x^T, by substituting equation (5.22) into (5.19):

$$u_x^T = \frac{2 u_i}{1 + \mu_0 \Sigma_p V_A} \tag{5.24}$$

We can also find an expression for the combined magnetic field perturbation, b_x^T, using equations (5.21) and (5.22) to obtain

$$b_x^T = \frac{2 b_i \mu_0 \Sigma_p V_A}{1 + \mu_0 \Sigma_p V_A} \tag{5.25}$$

This expression can be recast in terms of height-integrated number densities, since the Pedersen conductivity can be expressed as

$$\sigma_p = ne^2 \sum_s \frac{v_s/m_s}{v_s^2 + \Omega_s^2} \tag{5.26}$$

where v_s is the collision frequency of plasma species s with neutrals and Ω_s is its gyrofrequency *(Lysak (1990))*. In the ionosphere, the electron collision frequency is much smaller than its gyrofrequency, so the main contribution to the Pedersen conductivity is given by the ions, such that equation (5.26) simplifies to

$$\sigma_p = \frac{ne}{B} \frac{v_i/\Omega_i}{1 + \left(\frac{v_i}{\Omega_i}\right)^2} \tag{5.27}$$

where the subscript i denotes that the quantity refers to ions. Thus, we can see that when the ion-neutral collision frequency is constant, then $\sigma_p \propto n$. Thus, we can express the height-integrated Pedersen conductivity as

$$\Sigma_p = \Sigma_{P0} \frac{N}{N_e} \tag{5.28}$$

where Σ_{P0} represents the equilibrium height-integrated Pedersen conductivity when $N = N_e$. Using this expression and equations (5.23) and (5.16), we can rewrite equation (5.25) as

$$b_x^T = \frac{2\mu_0 B_0 u_i \Sigma_{P0} N}{N_e \left(1 + \sqrt{\frac{\mu_o}{\rho_0}} \Sigma_{P0} B_0 \frac{N}{N_e}\right)} \tag{5.29}$$

Differentiating this expression with respect to y and using Maxwell's equation (1.12), we see that

$$\frac{j_z(y,h)}{e} = -N_e \frac{\partial}{\partial y} \left(\frac{\eta u_i \bar{N}}{1 + \beta \bar{N}} \right) \tag{5.30}$$

where

$$\eta = \frac{2\Sigma_{P0} B_0}{N_e c}, \tag{5.31}$$

$$\beta = \sqrt{\frac{\mu_0}{\rho_0}} \Sigma_{P0} B_0 \tag{5.32}$$

and

$$\bar{N} = \frac{N}{N_e} \tag{5.33}$$

Substituting equation (5.30) into (5.8), we have a partial differential equation such that

$$\frac{\partial N}{\partial t} + N_e \frac{\partial}{\partial y}\left(\frac{\eta u_i \bar{N}}{1+\beta\bar{N}}\right) = \frac{\alpha}{h}\left(N_e^2 - N^2\right) \tag{5.34}$$

We can normalise this equation completely by using

$$\bar{y} = \frac{y}{y_0}, \tag{5.35}$$

$$\bar{u}_i = \frac{u_i}{u_{i0}} \tag{5.36}$$

and

$$\bar{t} = \frac{t}{\tau} = \frac{u_{i0}t}{y_0} \tag{5.37}$$

where y_0 is a characteristic length-scale, u_{i0} is the equilibrium incoming Alfvén wave amplitude and $\tau = y_0/u_{i0}$ is a characteristic timescale. Using these normalised variables, our partial differential equation in (5.34) transforms to

$$\frac{\partial \bar{N}}{\partial \bar{t}} + \frac{\partial}{\partial \bar{y}}\left(\frac{\eta \bar{u}_i \bar{N}}{1+\beta\bar{N}}\right) = \bar{\alpha}\left(1 - \bar{N}^2\right) \tag{5.38}$$

where

$$\bar{\alpha} = \frac{\alpha y_0 N_e}{u_{i0} h} \tag{5.39}$$

is a normalised recombination coefficient. Taking typical nightside parameters of $\Sigma_{P0} = 1$ mho, $B_0 = 5 \times 10^4$ nT, $n_e = 10^{10}$ m^{-3} and $h = 20$ km yields $N_e = 2 \times 10^{14}$ m^{-2}, and $n_0 = 10^6$ m^{-3} giving $\rho_0 = 1.67 \times 10^{-21}$ kg m^{-3} in the magnetosphere. These values give $\beta = 1370$ and $\eta = 3.12$, which we will use in the rest of this Chapter, unless stated otherwise.

5.3 Method of characteristics

Firstly, we will consider some simple limits of equation (5.38) in order to illustrate its general behaviour and gain understanding of the system. In equation (5.38), the downward current may initially be generated by a gradient in either $\bar{N}$ or $\bar{u}_i$. If we firstly let $\bar{u}_i = 1$ everywhere and set $\bar{\alpha} = 0$, then equation (5.38) simplifies to

$$\frac{\partial \bar{N}}{\partial \bar{t}} + \frac{\eta}{\left(1+\beta \bar{N}\right)^2} \frac{\partial \bar{N}}{\partial \bar{y}} = 0 \tag{5.40}$$

which corresponds to the depletion of the E region in the absence of photoionisation and recombination, but retaining depletion due to downward current. We can use the method of characteristics to solve this partial differential equation, such that

$$\frac{\mathrm{d}\bar{N}}{\mathrm{d}r} = \frac{\partial \bar{N}}{\partial \bar{t}} \frac{\mathrm{d}\bar{t}}{\mathrm{d}r} + \frac{\partial \bar{N}}{\partial \bar{y}} \frac{\mathrm{d}\bar{y}}{\mathrm{d}r} \tag{5.41}$$

where r is a coordinate along characteristics. Comparing equation (5.41) with (5.40), we see that

$$\frac{\mathrm{d}\bar{N}}{\mathrm{d}r} = 0 \tag{5.42}$$

that is, $\bar{N}$ is constant on a characteristic. Secondly,

$$\frac{\mathrm{d}\bar{t}}{\mathrm{d}r} = 1 \Rightarrow \bar{t} = r + \text{ constant} \tag{5.43}$$

From this result, we can also see that

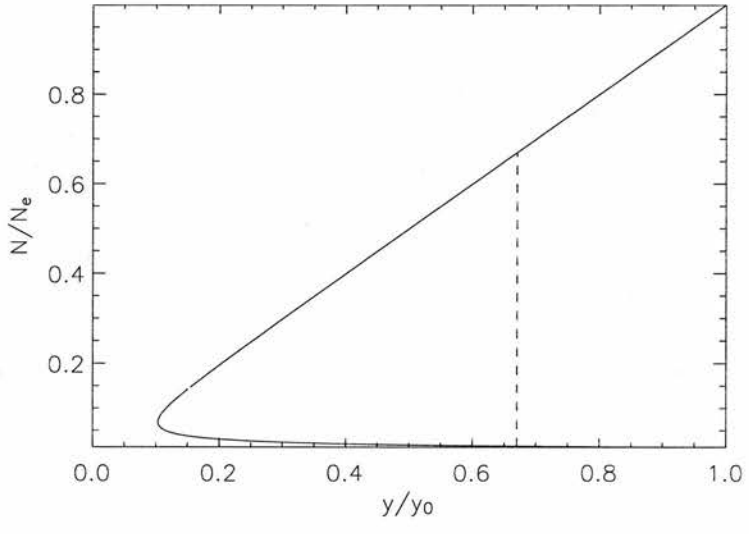

Figure 5.4: Plot of $\bar{N}(\bar{y}, \bar{t} = 100)$ from equation (5.48) using the method of characteristics. The multiple solutions in the range $0.1 < \bar{y} < 1.0$ indicate the existence of a shock in this region (dashed line).

$$\frac{\mathrm{d}\bar{y}}{\mathrm{d}r} \equiv \frac{\mathrm{d}\bar{y}}{\mathrm{d}\bar{t}} = \frac{\eta}{\left(1+\beta\bar{N}\right)^2} \tag{5.44}$$

which can easily be integrated, since $\bar{N}$ has been shown to be constant on a characteristic. Thus,

$$\bar{y} = Y_0 + \frac{\eta\bar{t}}{\left(1+\beta\bar{N}\right)^2} \tag{5.45}$$

So, when no time has elapsed, $\bar{y} = Y_0$. If we take an initial number density profile of

$$\bar{N}\left(\bar{y}, \bar{t}=0\right) = \bar{N}\left(Y_0\right) = \begin{cases} 0, & Y_0 < 0 \\ Y_0, & 0 < Y_0 < 1 \\ 1, & Y_0 > 1 \end{cases} \tag{5.46}$$

then a downward current flows in the region $0 < Y_0 = \bar{y} < 1$ due to the non-zero gradient of $\bar{N}$ in this region, as seen in equation (5.30). Then, we know that

$$\bar{N}\left(\bar{y}, \bar{t}\right) = \bar{N}\left(Y_0\right) = \bar{N}\left(\bar{y} - \frac{\eta\bar{t}}{\left(1+\beta\bar{N}\right)^2}\right) \tag{5.47}$$

So, in the section where $\bar{N}$ is not constant, the solution becomes

$$\bar{N}\left(\bar{y}, \bar{t}\right) = \bar{y} - \frac{\eta\bar{t}}{\left(1+\beta\bar{N}\right)^2}, \quad 0 < \bar{y} - \frac{\eta\bar{t}}{\left(1+\beta\bar{N}\right)^2} < 1 \tag{5.48}$$

This can be expressed as

$$\bar{N}\left(\bar{y}, \bar{t}\right) = Y_0, \quad \frac{\eta\bar{t}}{\left(1+\beta\bar{N}\right)^2} < \bar{y} < 1 + \frac{\eta\bar{t}}{\left(1+\beta\bar{N}\right)^2} \tag{5.49}$$

It is not entirely clear from this what the region of validity of this expression (given by the inequality) will be, since we do not know the values of $\bar{N}$ to substitute into the limits above. Thus, we plot $\bar{N}(\bar{y}, \bar{t} = 100)$ in Figure 5.4: this is achieved by choosing a range of Y_0, substituting these values and $\bar{t} = 100$ into equation (5.45) with $\bar{N} = Y_0$ as our chosen form, and plotting $Y_0 = \bar{N}$ against $\bar{y}$. It can clearly be seen that the solution is multivalued in the range $0.1 < \bar{y} < 1.0$, which indicates the presence of a shock in this region (shown by a dashed line in Figure 5.4), the exact position of which is as yet unknown. We can estimate the first time at which a shock appears by differentiating equation (5.48) with respect to $\bar{y}$:

$$\frac{\partial\bar{N}}{\partial\bar{y}} = \left(1 - \frac{2\eta\beta\bar{t}}{\left(1+\beta\bar{N}\right)^3}\right)^{-1} \tag{5.50}$$

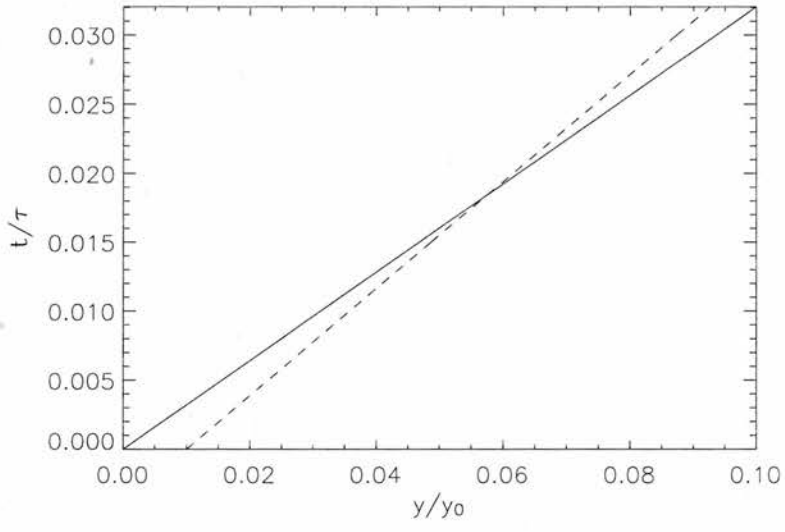

Figure 5.5: Variation of $\bar{t}$ with $\bar{y}$ for $Y_0 = 0$ (solid line) and $Y_0 = 0.01$ (dashed line). These lines cross at $\bar{t} = 0.0185$, indicating that a shock first develops between $Y_0 = \bar{N} = 0$ and 0.01 at this time.

Thus, $\partial\bar{N}/\partial\bar{y} \to \infty$, indicating a shock, when the expression in brackets on the RHS is equal to zero, giving

$$\bar{t} = \frac{\left(1 + \beta\bar{N}\right)^3}{2\eta\beta} \tag{5.51}$$

This takes its smallest value when $\bar{N} = 0$, indicating that a shock first forms at the lower end of the $\bar{N}$ curve at a time

$$\bar{t}_{\text{shock}} = \frac{1}{2\eta\beta} \tag{5.52}$$

In order to substantiate this, we can substitute $\bar{N} = Y_0$ into equation (5.45) (since $\bar{N}$ is constant on a characteristic and this is the form of $\bar{N}$ chosen in equation (5.46)) and plot $\bar{t}(\bar{y})$ for different values of Y_0. This has been done in Figure 5.5 for $\eta = 3.12$ and $\beta = 10.0$, with $Y_0 = 0$ (solid line) and $Y_0 = 0.01$ (dashed line). These curves cross at $\bar{t} = 0.0185$: this indicates that a shock has formed between $Y_0 = \bar{N} = 0$ and 0.01 at this point. If we take $Y_0 = 0$ and $Y_0 = 10^{-4}$, the curves cross at $\bar{t} = 0.0160$, indicating a shock at this earlier time between $\bar{N} = 0$ and 10^{-4}. This value of $\bar{t}$ agrees with that obtained by substituting $\beta = 10$ and $\eta = 3.12$ into equation (5.52) to 3 decimal places. Thus, the shock forms almost straight away, especially for large β. With our standard values of $\eta = 3.12$ and $\beta = 1370$, $\bar{t}_{\text{shock}} = 1.2 \times 10^{-4}$. Since typically, $u_{i0} \sim 10^5$ m/s and $y_0 \sim 10^4$ m, equation (5.37) tells us that $t_{\text{shock}} = 1.2 \times 10^{-5}$ s.

Since we now know that the shock forms almost immediately, we can estimate the position of the shock, $\bar{y}_s$, at a time $\bar{t}$ using continuity of electrons. Recalling that $\bar{u}_i = 1$ in this subsection, equation (5.30) can

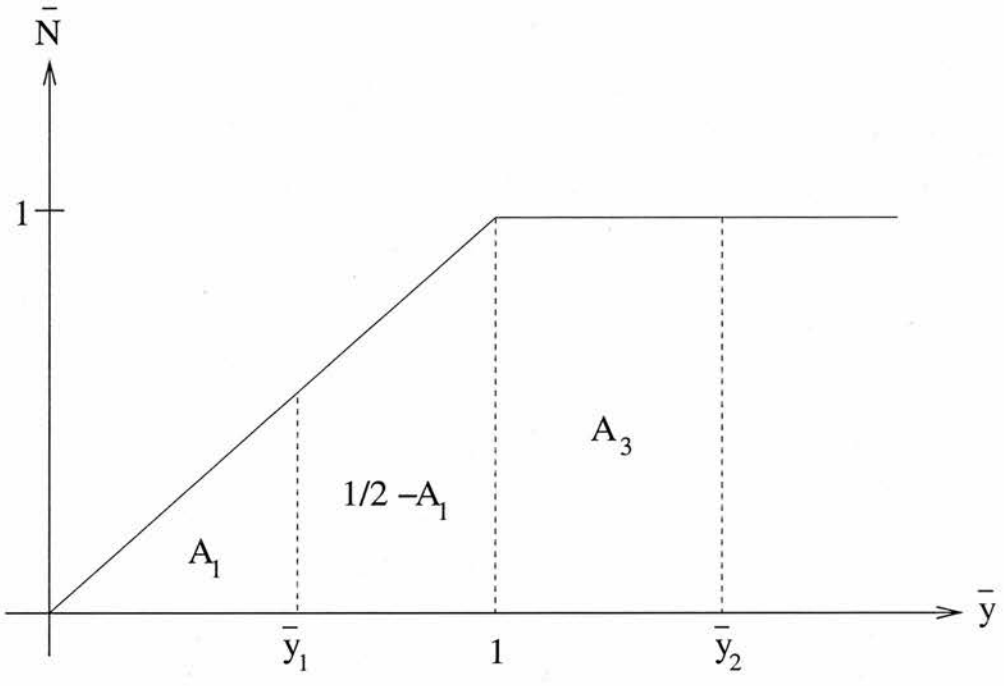

Figure 5.6: A schematic of the number density profile evolution in time. The initial profile is indicated by a solid line. When the shock (dotted line) has moved to $\bar{y}_s = \bar{y}_1 < 1$, a triangular region ($A_1$) has been depleted; when $\bar{y}_s = 1$, a triangular region of area 1/2 has been depleted; and when $\bar{y}_s = \bar{y}_2 > 1$, an additional rectangular region has been depleted, giving an area of $1/2 + A_3$.

be integrated in the y direction to find the magnitude of the normalised total current, $\bar{I}$

$$\begin{aligned} \bar{I} &= \int_0^\infty \frac{\partial}{\partial \bar{y}} \left(\frac{\eta \bar{N}}{1 + \beta \bar{N}} \right) \, \mathrm{d}\bar{y} \\ &= \frac{\eta}{1+\beta} \end{aligned} \tag{5.53}$$

since $\bar{N}(\infty) = 1$ and $\bar{N}(0) = 0$. This current remains constant in time, so $\bar{I}\bar{t} = \eta\bar{t}/(1+\beta)$ represents the normalised loss of electrons due to the flow of current up to a time $\bar{t}$. This loss will equate to the depleted area under the original curve $\bar{N}(Y_0)$ and above $\bar{N}(\bar{y}, \bar{t})$, which is illustrated in Figure 5.6. The dashed lines represent the position of the shock at three different times. The solutions fall into two regimes: one where the shock has moved to a general point $\bar{y}_1 < 1$, where a triangular region of area $A_1 < 1/2$ has been depleted, and another where the shock has moved beyond the triangular region to a point $\bar{y}_2 > 1$, leaving a depleted area of $A_3 + 1/2$. The limit between these two regimes occurs when the shock has reached $\bar{y} = 1$ and the triangular region is just depleted, giving a depleted area of $1/2$ in Figure 5.6. Equating this to $\bar{I}\bar{t}_L$, where $\bar{t}_L$ is the limiting time when the shock reaches $\bar{y} = 1$, we find that

$$\bar{t}_L = \frac{1+\beta}{2\eta} \tag{5.54}$$

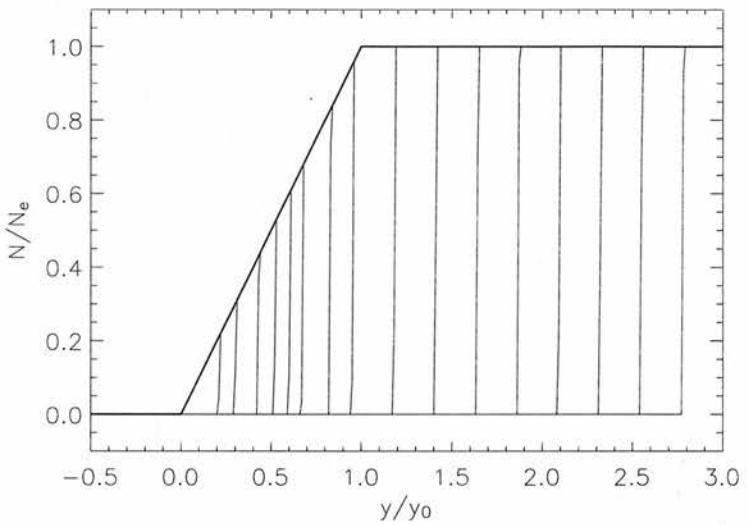

Figure 5.7: Numerically-derived number density profiles for $\beta = 1370$, $\eta = 3.12$, and the initial number density profile in equation (5.46). The profiles given are at $\bar{t} = 0$, 10, 20, 40, 60, 80, 100, 150, 200, 300, 400, 500, 600, 700, 800, 900, and 1000. This shows the predicted shock propagating to the right as electrons are drawn up out of the E region to carry a downward field-aligned current.

When $\bar{t} < \bar{t}_L$, the depleted area is triangular (A_1 in Figure 5.6), and is equal to $\bar{y}_s^2/2$. Thus, equating this to $\bar{I}\bar{t}$ and substituting in equation (5.53), we see that in this regime

$$\bar{y}_s = \sqrt{\frac{2\eta\bar{t}}{1+\beta}} \tag{5.55}$$

In the other regime, when $\bar{t} > \bar{t}_L$, the depleted area is a triangle and a rectangle ($1/2 + A_3$ in Figure 5.6), and is given by $1/2 + (\bar{y}_s - 1) = \bar{y}_s - 1/2$. Again, equating this to $\bar{I}\bar{t}$ and using equation (5.53), we see that

$$\bar{y}_s = \frac{1}{2} + \frac{\eta\bar{t}}{1+\beta} \tag{5.56}$$

Thus, the position of the shock, $\bar{y}_s$, can be expressed as

$$\bar{y}_s = \begin{cases} \sqrt{\frac{2\eta\bar{t}}{1+\beta}}, & \bar{t} \le \frac{1+\beta}{2\eta} \\ \frac{1}{2} + \frac{\eta\bar{t}}{1+\beta}, & \bar{t} > \frac{1+\beta}{2\eta} \end{cases} \tag{5.57}$$

We now compare these results to a numerical simulation. We use first-order backward differencing in time and space: although not as accurate as other higher-order methods, this method has the advantage of being able to capture the shock when it arises. The results of the simulation are shown in Figure 5.7. The

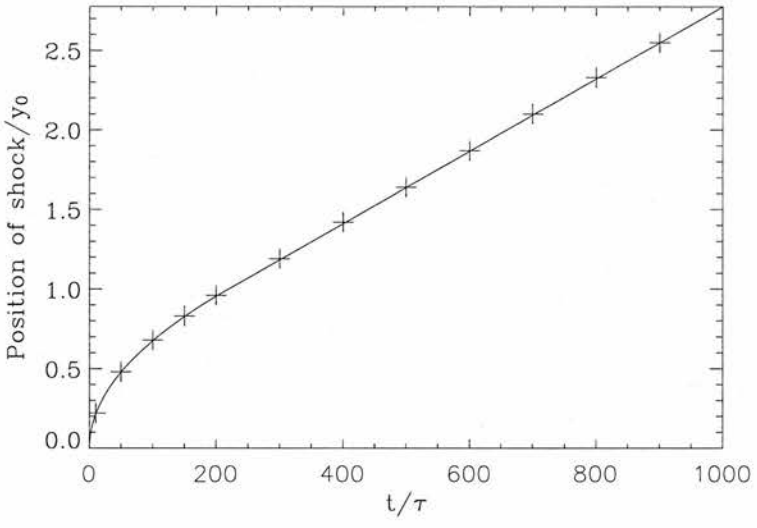

Figure 5.8: Variation of shock position, $\bar{y}_s$, with time derived from the analytical expression in equation (5.57) (solid line) and from the numerical simulation (crosses). The results show good agreement.

number density profiles do indeed exhibit the predicted shock, which propagates to the right as electrons are drawn out of the E region to carry the downward field-aligned current. Figure 5.8 compares the predicted position of the shock in time (solid line) given in equation (5.57) to the numerically-derived position of the shock (crosses): the two methods agree to the order of the spacial gridspacing in our numerical simulation, which is in this case 3dp. This lends confidence to the results of our numerical simulation.

5.4 Numerical solution

We now wish to solve the partial differential equation in (5.38) numerically, including the photoionisation source term and the recombination loss term. We have an initially undepleted ionosphere with $N = N_e$ everywhere, and $\bar{u}_i = \tanh(\bar{y})$ giving an initial current density magnitude, $j_\parallel$, which can be determined from equation (5.30) to be

$$\begin{aligned} j_\parallel &= \frac{N_e e u_{i0}}{y_0}\left(\frac{\eta}{1+\beta}\right)\frac{\mathrm{d}\bar{u}_i}{\mathrm{d}\bar{y}} \\ &= \frac{N_e e u_{i0}}{y_0}\left(\frac{\eta}{1+\beta}\right)\mathrm{sech}^2\bar{y} \end{aligned} \tag{5.58}$$

The maximum initial current density, $j_{\parallel 0}$, occurs at $\bar{y} = 0$ and is given by

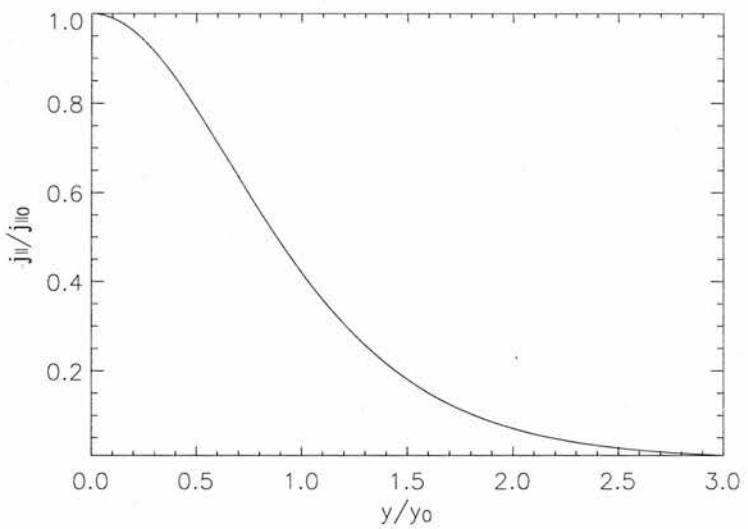

Figure 5.9: Initial current density profile caused by a shear flow in the magnetosphere.

$$\begin{aligned} j_{\parallel 0} &= \frac{N_e e u_{i0}}{y_0} \frac{\eta}{1+\beta} \\ &\approx \frac{2u_{i0}}{y_0}\sqrt{\frac{\rho_0}{\mu_0}}, \text{ for } \beta \gg 1 \end{aligned} \tag{5.59}$$

This initial current density profile is shown in Figure 5.9. In all of the following work, the solution is taken to be symmetrical around the y axis, and only the region $y > 0$ is shown. Although the analysis of the previous section ignored the photoionisation and recombination terms on the right hand side of equation (5.38), it demonstrated that the system is liable to produce a shock, so we use the same first-order backward differencing method as that used in the previous section to solve this system.

Taking the same parameters as in the previous section, which are a good description of the nightside E region, Figure 5.10 shows the evolution of the number density in time for four different initial current densities. All of these cases reach a steady state when the ionisation rate matches the combined loss rate due to recombination and downward current being drawn. The smallest current density in Figure 5.10(d) only requires a partial depletion of the initial shear width $\sim y_0$ before a steady state is reached. In Figure 5.10(c), we can see that the number density depletes down to zero at $\bar{y} = 0$, when the system then develops a shock as it requires a slight broadening of the depletion region in order to carry the current. The larger current densities in Figure 5.10(a) and (b) require even more broadening, and exhibit the shock feature that was predicted by the method of characteristics in the previous section.

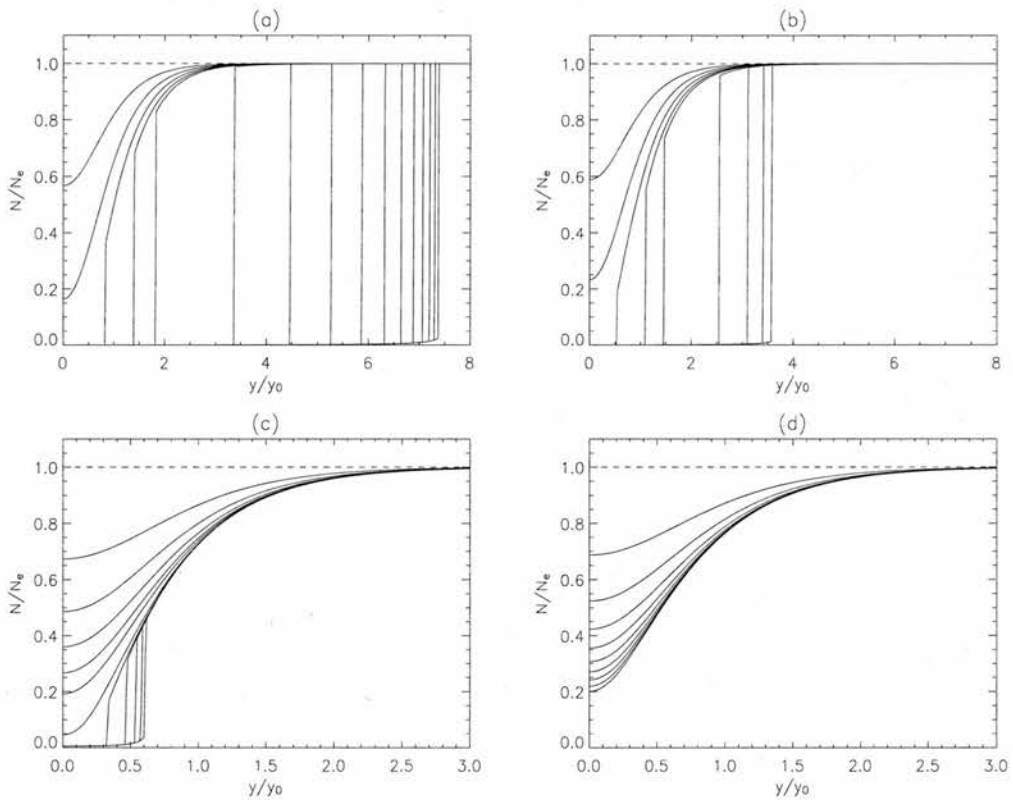

Figure 5.10: Number density evolution in time for $j_{\|0}$ (u_{i0}) values of (a) 0.73 μAm^{-2} (1×10^5 ms^{-1}); (b) 0.36 μAm^{-2} (5×10^4 ms^{-1}); (c) 0.11 μAm^{-2} (1.5×10^4 ms^{-1}); and (d) 0.096 μAm^{-2} (1.3×10^4 ms^{-1}). The number density profiles shown are for $t =$ (a) 0, 20, 40, 60, 80, 100, 200, 300, 400, 500, 600, 700, 800, 900, 1000, 1100 and 1200 s; (b) 0, 40, 80, 120, 160, 200, 400, 600, 800 and 1000 s; (c) 0, 133, 267, 400, 533, 667, 1000, 1333, 1667, 2000, 2333 and 2667 s; and (d) 0, 146, 292, 438, 583, 729, 875, 1021, 1167 and 1313 s. Smaller current densities only cause a partial depletion of the E region, whereas for larger current densities, the region of depletion must spread out in order to access sufficient current-carriers.

5.5 Depletion width

In this Section, we wish to obtain analytical approximations for the width to which the depleted region spreads. Our numerical simulations show that there are two regimes. For large initial current densities, the region of depleted density broadens to a depletion width that is larger than the original shear width (as in Figure 5.10(a) and (b)). For smaller initial current densities, only partial depletion occurs, and the depletion width is approximately equal to the shear width (as illustrated by Figure 5.10(d)). We begin by considering the first of these two cases. As can be seen from Figure 5.10(a) and (b), when significant depletion takes place, the recombination term can safely be ignored within the depleted region, since $\bar{N} \approx 0$ there. Thus, taking the steady state of equation (5.38) and neglecting the recombination term, we obtain

$$\frac{\partial}{\partial \bar{y}} \left(\frac{\eta \bar{u}_i \bar{N}}{1 + \beta \bar{N}} \right) = \bar{\alpha} \tag{5.60}$$

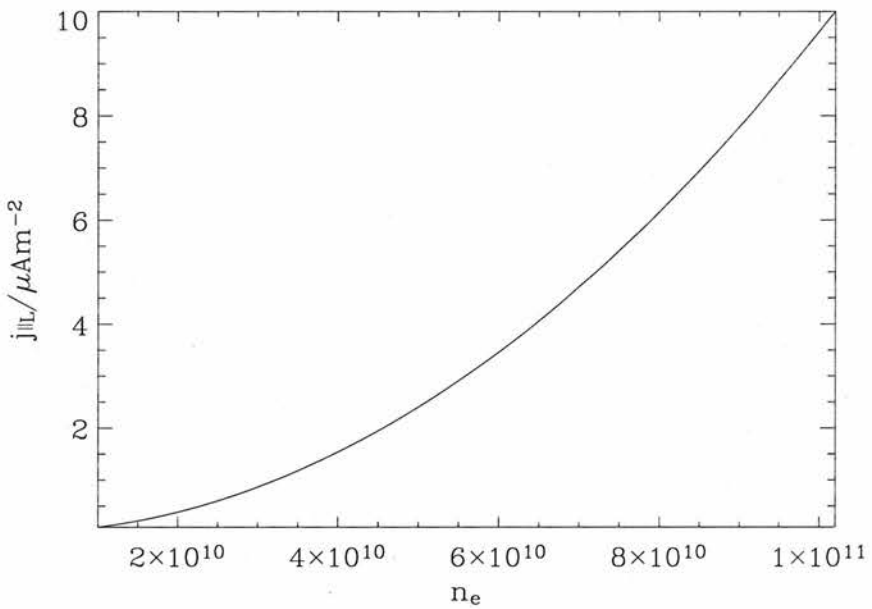

Figure 5.11: Variation of $j_{\parallel L}$ with E region number density for typical parameters $h = 2 \times 10^4$ m and $\alpha = 3 \times 10^{-13}$ m^3 s^{-1}. This shows that significant E region depletion should be far more common on the nightside (with lower ionospheric number densities) than on the dayside.

Integrating this over the estimated depletion width $\bar{W} = W/y_0$ gives us

$$\int_0^{\bar{W}} \frac{\partial}{\partial \bar{y}} \left(\frac{\eta \bar{u}_i \bar{N}}{1 + \beta \bar{N}} \right) \, \mathrm{d}\bar{y} = \left[\frac{\eta \bar{u}_i \bar{N}}{1 + \beta \bar{N}} \right]_0^{\bar{W}} = \bar{\alpha} \bar{W} \tag{5.61}$$

We can evaluate this integral by noting that $\bar{N} \approx 0$ at $\bar{y} = 0$, and $\bar{N} = 1$ and $\bar{u}_i = 1$ at $\bar{y} = \bar{W}$. Thus, an estimate of the depletion width is given by

$$W = y_0 \frac{\eta}{\bar{\alpha}\,(1 + \beta)} \tag{5.62}$$

Substituting equations (5.39) and (5.59) into this expression, we can see that

$$W = \frac{y_0 h j_{\parallel 0}}{\alpha e N_e^2} = \frac{y_0 j_{\parallel 0}}{\alpha e n_e^2 h} \tag{5.63}$$

Thus, the width can be seen to increase linearly with current density: a larger current density requires more current-carriers and thus a wider depletion width. The width is inversely proportional to α and h; a smaller photoionisation rate produces fewer electrons per unit area, and so the depletion region will broaden more before a steady state is reached; and a decreased ionospheric height also provides fewer electrons,

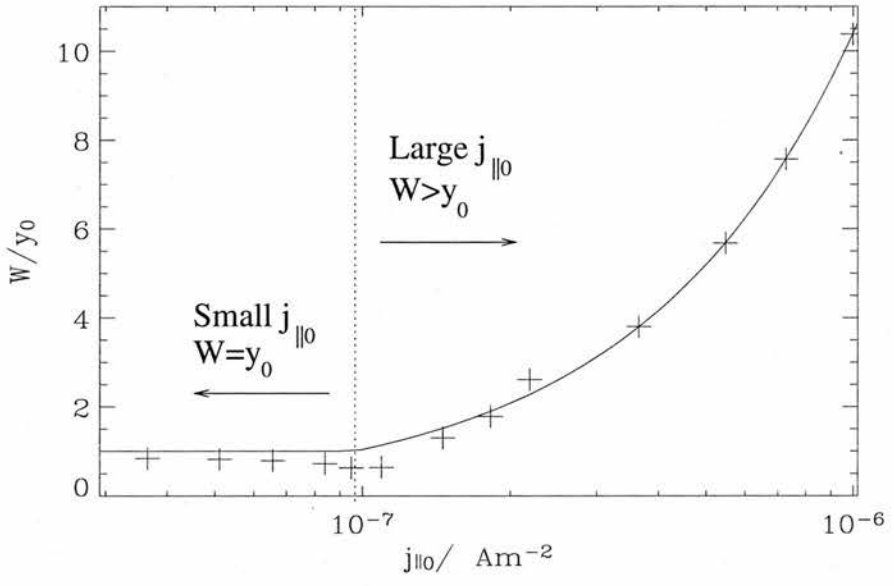

Figure 5.12: Simulation depletion widths (crosses) and estimate (solid line) from equation (5.65) for varying initial current densities, using $n_e = 10^{10}$ m^{-3} and $h = 20$ km. The estimate is seen to be very accurate for large depletion widths.

resulting in a higher depletion width. The depletion width also increases as the ionospheric number density decreases, since this implies fewer current-carriers per unit volume.

The depletion width in equation (5.63) can be used to determine whether broadening occurs for a given system: significant broadening occurs when $W > y_0$, and no broadening occurs when $W < y_0$. We can estimate the critical lowest current density, $j_{\parallel L}$, for which broadening begins to occur by substituting $W = y_0$ into equation (5.63) to obtain

$$j_{\parallel L} = \frac{N_e^2 e\alpha}{h} = n_e^2 he\alpha \tag{5.64}$$

As the number density of the E region increases, so does the minimum current density necessary to require a broadening of the depletion region, since more current-carriers are available. The variation of $j_{\parallel L}$ with n_e is illustrated in Figure 5.11. For a typical nightside E region number density of 10^{10} m^{-3}, $j_{\parallel L} \sim 0.1$ μAm^{-2}, so significant depletion will occur for even very small downward current densities. On the dayside, however, typical E region number densities are generally an order of magnitude higher: in this regime, significant depletion only begins to occur for downward currents of $\sim$10 μAm^{-2}, so only very strong events will cause significant density holes in the dayside E region. Density cavities should therefore be far rarer on the dayside.

When equation (5.63) yields a width less than y_0, we are in the regime where no significant broadening occurs, and we can instead give the estimate $W = y_0$, since this is the initial shear width. Thus, our estimate for the depletion width can be written as

$$W = \begin{cases} \frac{y_0 j_{\parallel 0}}{j_{\parallel L}}, & j_{\parallel 0} > j_{\parallel L} \\ y_0, & j_{\parallel 0} \leq j_{\parallel L} \end{cases} \tag{5.65}$$

This estimate is plotted in Figure 5.12 for $n_e = 10^{10}$ m^{-3}, along with depletion widths taken from numerical simulations for comparison. The width was estimated from simulations by the following method: If the minimum number density at steady state at the origin is $N_{\min}$, then the depletion width is defined to be the distance from the origin to the steady state number density curve at $N = (N_e + N_{\min})/2$ (see Figure 5.13). Figure 5.12 shows that the estimate in equation (5.65) is very accurate for depletion widths greater than the shear width (y_0), and is good at predicting the current density for which broadening begins to be important. Figure 5.14 shows the variation of the depletion width estimate in equation (5.65) with E region number density for various initial current densities: as n_e increases, the depletion width required for a given current density decreases, as more current-carriers are available. Depletion widths of $\sim 10\ y_0$ are required for lower E region number densities to carry these currents.

5.6 Depletion time

We can also obtain analytical estimates of the timescale on which the E region depletes, both for small currents ($j_{\parallel 0} < j_{\parallel L}$) and for larger ones ($j_{\parallel 0} > j_{\parallel L}$). We do this by ignoring the photoionisation and recombination terms in equation (5.38) and estimating the total number of electrons removed by the time

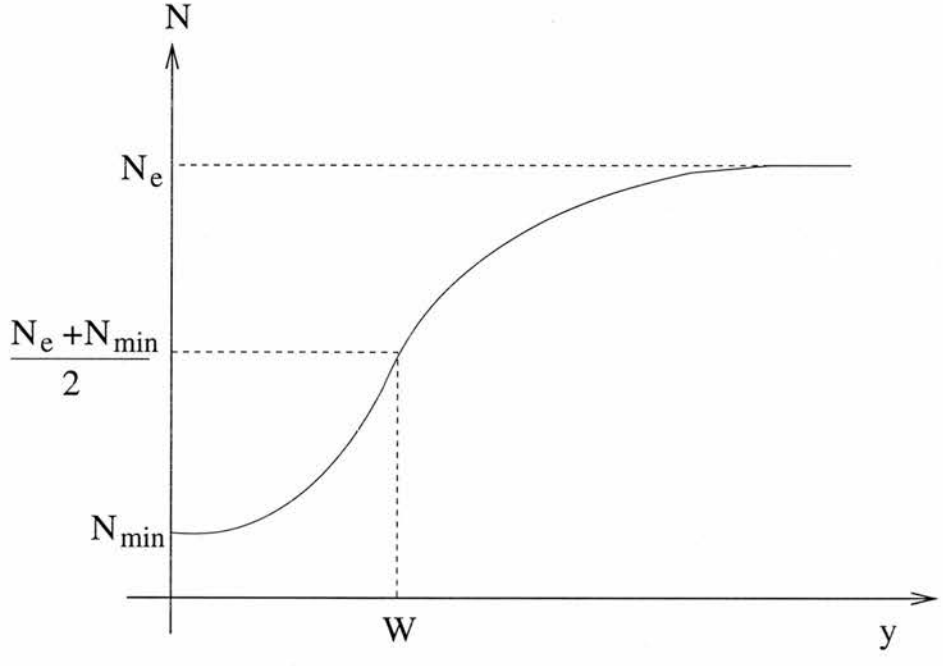

Figure 5.13: Schematic of the method used to find the depletion width from our numerical simulation. If the minimum number density at steady state at the origin is $N_{\min}$, then the depletion width is defined to be the distance from the origin to the steady state number density curve at $N = (N_e + N_{\min})/2$.

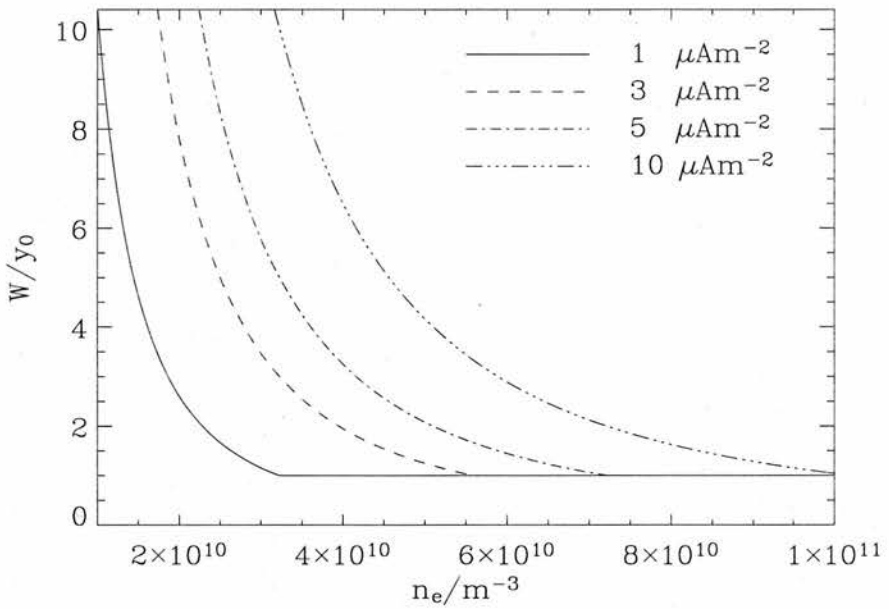

Figure 5.14: Variation of depletion width in equation (5.65) with E region number density for different initial current densities ($j_{\parallel 0}$) and $h = 20$ km.

the system reaches steady state. This is represented by the area bounded by the steady state number density profile and $\bar{N} = 1$ in Figure 5.10. Since the total current is constant in time, we can calculate how long it takes for the current to remove the required number of electrons, giving an estimate of the characteristic depletion time. Note that this will yield a lower limit, as we are ignoring the production of electrons due to photoionisation, which always outweighs the loss due to recombination in depleted regions.

5.6.1 $j_{\parallel 0} > j_{\parallel L}$ case

Firstly, we consider the regime where a large current density ($j_{\parallel 0} > j_{\parallel L}$) causes significant broadening ($W > y_0$) of the depletion region. The magnitude of the total current, I, is found by integrating equation (5.30) in the y direction,

$$\begin{aligned} I &= N_e e u_{i0} \int_0^\infty \frac{\partial}{\partial \bar{y}} \left(\frac{\eta \tanh(\bar{y}) \bar{N}}{1 + \beta \bar{N}} \right) \, \mathrm{d}\bar{y} \\ &= N_e e u_{i0} \left(\frac{\eta}{1+\beta} \right) \end{aligned} \tag{5.66}$$

and remains constant in time. In this regime, significant depletion to $\bar{N} = 0$ occurs within the depletion width W, and so an estimate of the total number of electrons which have been removed when the steady

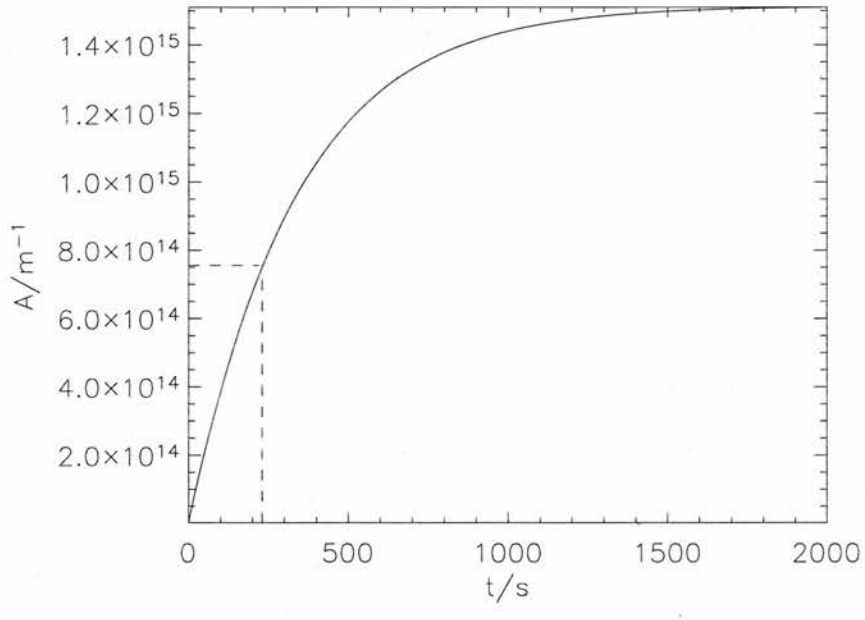

Figure 5.15: An illustration of the method used to find a characteristic depletion time from the simulation. This plot shows the variation of the depleted number of electrons, $A(t)$, with time for $j_{\parallel 0} = 0.73\ \mu\text{Am}^{-2}$ and $n_e = 10^{10}\ \text{m}^{-3}$. $A(t)$ asymptotes to a constant value as time increases and the steady state is reached: the depletion time is taken to be the time it takes to deplete half that constant value (illustrated with dashed lines).

state is reached is $N_e W$. Thus, if t_s is the estimate of the time it takes for the system to reach a steady state, then

$$\frac{It_s}{e} = N_e W \tag{5.67}$$

Using equations (5.62) and (5.66) and the definition of $\bar{\alpha}$ in equation (5.39), we see that

$$t_s = \frac{h}{\alpha N_e} = \frac{1}{\alpha n_e} \tag{5.68}$$

This depletion time is seen to be independent of initial current density; this is due to the fact that the depletion width estimate W and the total current I are both proportional to $j_{\parallel 0}$, so it cancels in equation (5.67). The depletion time is also inversely proportional to the E region number density. It will always give an underestimate of the actual depletion time, since in our model, the photoionisation rate is always greater than the recombination rate in the depletion region, that is $N < N_e$.

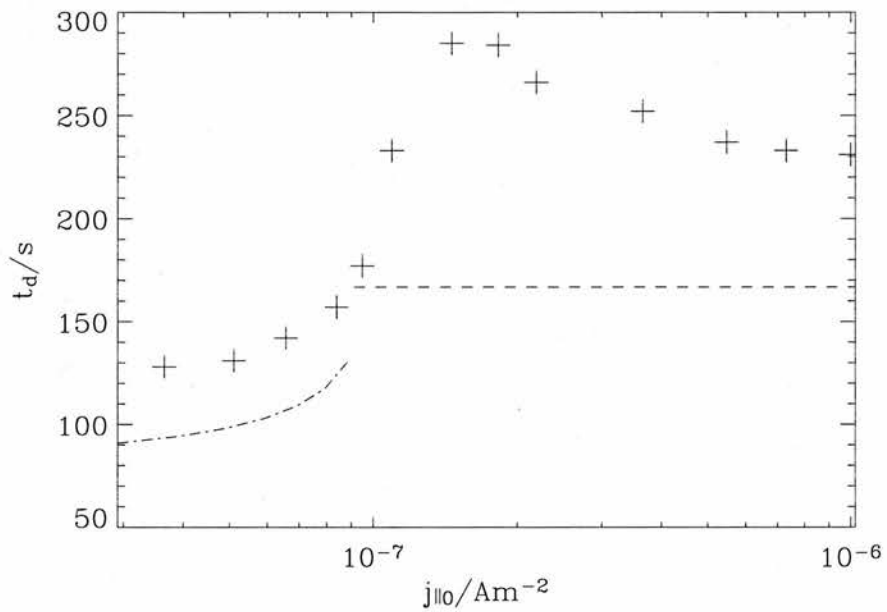

Figure 5.16: Simulation depletion times (crosses) and estimate (dashed line for $j_{\|0} > j_{\|L}$ estimate, and dot-dashed line for $j_{\|0} < j_{\|L}$ estimate) from equation (5.74) for varying initial current densities. The estimate is seen to provide a good lower bound for the depletion time.

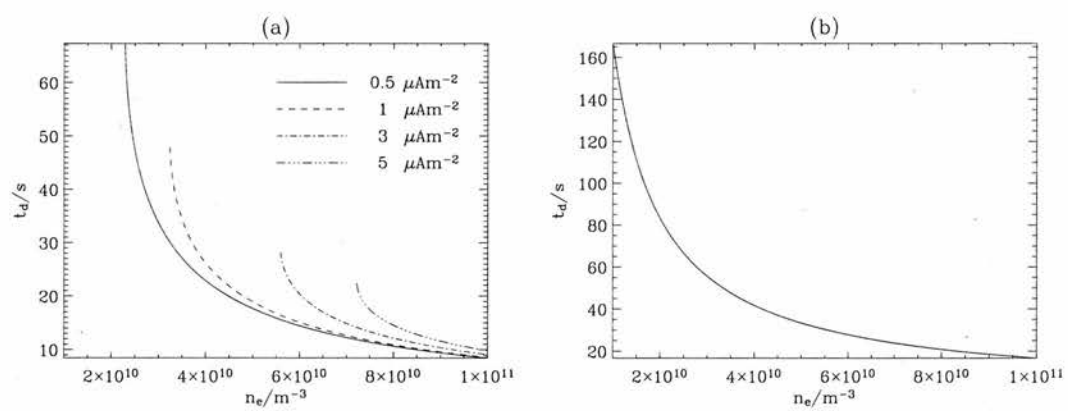

Figure 5.17: Variation of depletion time estimate with E region number density for various initial current densities under the two regimes of (a) no broadening ($j_{\|0} < j_{\|L}$) and (b) significant broadening ($j_{\|0} > j_{\|L}$).

5.6.2 $j_{\|0} < j_{\|L}$ case

Secondly, we consider the regime where a small current density ($j_{\|0} < j_{\|L}$) results in no significant broadening beyond y_0, as in Figure 5.10(d), and we can approximate $W = y_0$. At steady state, we can assume an average number density $\bar{N}_{\text{av}}$ in the shear width y_0, since depletion is only partial in this regime, i.e.

$$\bar{N} = \begin{cases} \bar{N}_{\text{av}}, & \bar{y} < 1 \\ 1, & \bar{y} > 1 \end{cases} \tag{5.69}$$

We then integrate the steady state version of equation (5.38) from 0 to ∞ in the y direction, assuming this profile, to obtain

$$\frac{\eta}{1+\beta} = \bar{\alpha}\left(1 - \bar{N}_{\text{av}}^2\right) \tag{5.70}$$

from which we can get an estimate of the average number density at equilibrium:

$$\bar{N}_{\text{av}} = \sqrt{1 - \frac{\eta}{\bar{\alpha}\left(1+\beta\right)}} = \sqrt{1 - \frac{j_{\parallel 0} h}{\alpha e N_e^2}} \tag{5.71}$$

using equation (5.59). Again ignoring the effects of recombination and photoionisation, a lower bound of the number of electrons removed at equilibrium can be approximated by $\left(1 - \bar{N}_{\text{av}}\right) N_e y_0$. Thus, as before, we use the expression for total current I in equation (5.66) and equation (5.59) to obtain

$$\begin{aligned} \frac{I t_s}{e} &= \left(1 - \bar{N}_{\text{av}}\right) N_e y_0 \\ \Rightarrow t_s &= \frac{N_e e}{j_{\parallel 0}}\left(1 - \bar{N}_{\text{av}}\right) \end{aligned} \tag{5.72}$$

To quantify the approach to a steady state in the simulations, we calculate the number of electrons, $A(t)$, that have been removed per metre at a time t via the following:

$$A(t) = \int_0^\infty N_e - N(y,t)\ \mathrm{d}y \tag{5.73}$$

This corresponds to the area above the curves in Figure 5.10 and below $\bar{N} = 1$. $A(t)$ will asymptote to a limiting value, A_s, as the steady state is reached. Thus, the depletion time, t_d, is taken to be the time at which $A(t) = A_s/2$. This method is illustrated in Figure 5.15. Our estimates of the depletion time in equations (5.68) and (5.72) are for total depletion. Thus, in order to compare similar quantities, we divide these estimates by two. The estimates can be summarised as

$$t_d = \begin{cases} 1/2\alpha n_e, & j_{\parallel 0} > j_{\parallel L} \\ \frac{N_e e}{2 j_{\parallel 0}}\left(1 - \bar{N}_{\text{av}}\right), & j_{\parallel 0} \leq j_{\parallel L} \end{cases} \tag{5.74}$$

This estimate is shown in Figure 5.16, along with simulation depletion times calculated using the

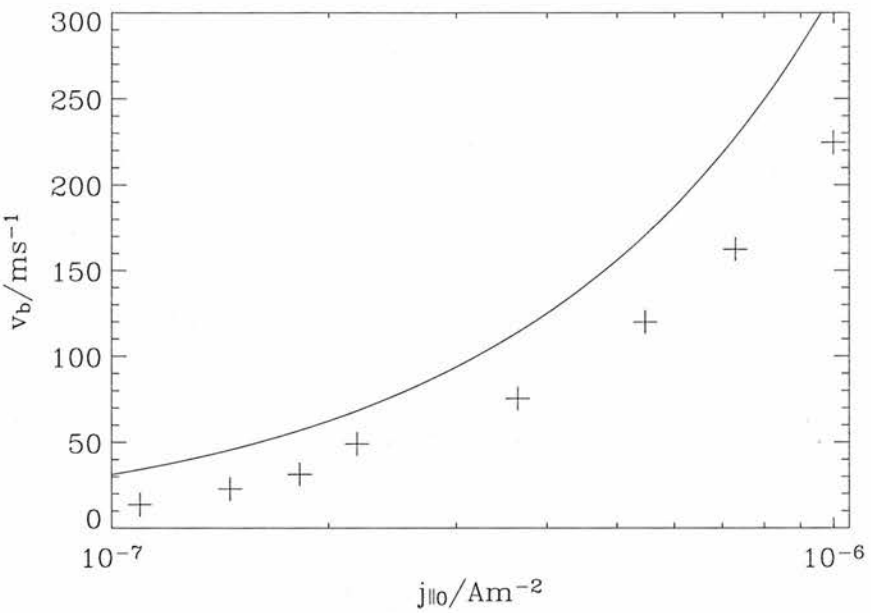

Figure 5.18: Simulation broadening speeds (crosses) and estimate (solid line) from equation (5.75) for varying initial current densities and $n_e = 10^{10}$ m^{-3}. The estimate is seen to follow the general trend well: it is an over-estimate, since the depletion time estimate is a lower bound which neglects photoionisation.

method described above. The estimate is seen to provide a good lower bound for the depletion time, especially when there is no significant broadening. The depletion is seen to take place over ~100 - 300 s, which agrees well with similar broadening observed by *Aikio et al. (2004)* (70 s) and *Marklund et al. (2001)* (280 s). Figure 5.17 shows the variation of the depletion time estimate in equation (5.74) with n_e for various initial current densities. Figure 5.17(a) is valid when no significant widening beyond y_0 occurs ($j_{\|0} < j_{\|L}$): the characteristic depletion time is ~30 s, and as n_e increases, the depletion time for a given current density decreases. There is a lower cutoff value of n_e for each current density: for smaller values of n_e, broadening will be required to carry the required current. Figure 5.17(b) shows the depletion time estimate when such broadening occurs ($j_{\|0} > j_{\|L}$). It is of the order of ~10 - 100 s, and decreases as n_e increases, since it takes less time to reach a steady state as less broadening is required.

5.7 Speed of broadening

In the regime where broadening of the depletion region occurs, i.e. where $j_{\|0} > j_{\|L}$ and $W > y_0$, it is useful to obtain an expression for the average speed of broadening, v_b. This can be written as follows, using the expressions for W and t_d in equations (5.65) and (5.74) respectively:

$$v_b = \frac{W}{2t_d} = \frac{y_0 j_{\|0}}{n_e e h} \tag{5.75}$$

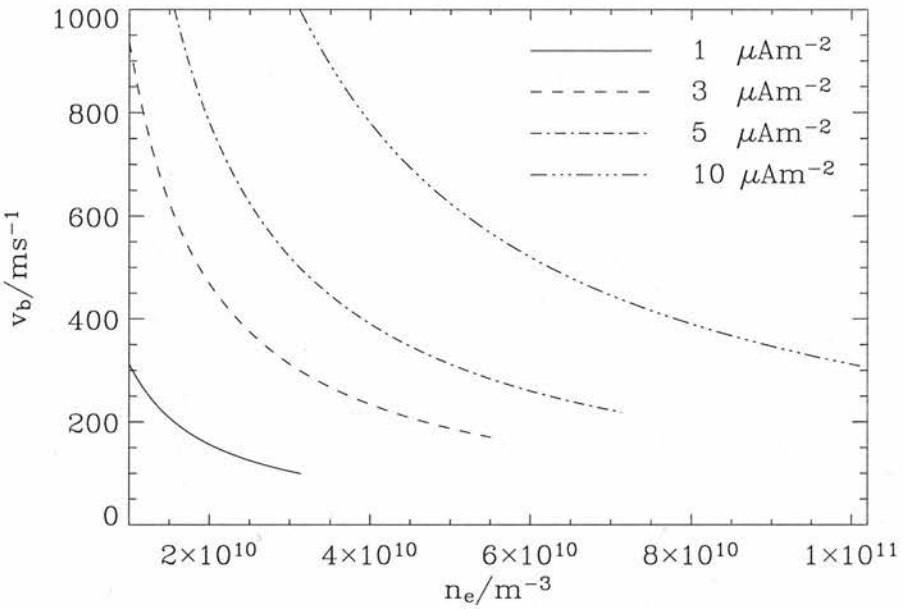

Figure 5.19: Variation of speed of broadening with E region number density for varying initial current densities. The cutoff point of each curve occurs where the ionospheric number density is large enough that no broadening is required for a given current density.

Figure 5.18 shows this estimate along with broadening speeds calculated from the simulation: the broadening speed is taken to be half the depletion width divided by the depletion time, t_d (the time taken to deplete half the electrons). The estimate follows the general trend well: the broadening speed is seen to increase as the initial current density increases, as more current-carriers are required per second. Figure 5.19 shows the variation of broadening speed with E region number density for various initial current densities The broadening speed is generally $\sim$100 m/s to 1 km/s. For a given current density, the broadening speed decreases for increasing n_e, since more current-carriers are available per unit area. The cutoff points on the graph occur when the n_e value is reached where no broadening is required for a given current density i.e. when $j_{\|0} = j_{\|L}$. Using equation (5.64), we see that this cutoff value is given by

$$n_e = \sqrt{\frac{j_{\|0}}{he\alpha}} \tag{5.76}$$

5.8 Comparison with data

We now compare our simulation with the data from *Marklund et al. (2001)* shown in Figure 5.1(b). This Figure shows that the region of downward current expands from 15 km *(Marklund et al. (2001))* to 51 km at ionospheric level in 280 s, assuming that the first and last spacecrafts travel at the same speed through the structure. Thus, since our model is symmetric about the y axis, we take $y_0 = 7.5 \times 10^3$ m, and we want to model broadening of $\bar{W} = 51/15 = 3.4$. The initial current density at Cluster's altitude of 21,000 km

($r = 4.3\ R_E$) is 0.16 μAm^{-2}; we need to know how this maps to ionospheric level, where $r = R_E$. The flux tube area scale factor is given by

$$F_A = \frac{r^3}{\sqrt{1 + 3\sin^2\theta}} \tag{5.77}$$

where r and θ are polar co-ordinates, and on a flux tube

$$\frac{r}{R_E} = L\cos^2\theta \tag{5.78}$$

where L is L-shell. The event occurred at a magnetic latitude of 69.8°, which corresponds to the invariant latitude, θ_I, at ionospheric level where $r = R_E$. Substituting these values into equation (5.78), we find that $L = 8.39$. From this, we can work out that the polar angle at the Cluster altitude of $r = 4.3R_E$ is $\theta_c = 44.3°$. Using these values, we can find the ratio of F_A in equation (5.77) at ionospheric level and Cluster altitude to be

$$\frac{F_A^{\text{iono}}}{F_A^{\text{cluster}}} = 96.7 \tag{5.79}$$

which tells us that the initial current density for this event at ionospheric level is given by $j_{\|0} = 15.5$ μAm^{-2}. This shows that we are examining a strong downward current event, where ionospheric electron depletion and broadening should both be important factors. Since we do not know from the data what the ionospheric number density is, we use equation (5.63) with $\alpha = 3 \times 10^{-13}$ m^{3}s^{-1} and $h = 20$ km to infer that $n_e = 6.88 \times 10^{10}$ m^{-3}. This event occurred at 0336 MLT, so this number density is relatively large but reasonable for the nightside E region.

With these parameter values, we can calculate the normalised quantities necessary for the numerical simulation using equations (5.31), (5.32) and (5.39): $\beta = 1370$, $\eta = 0.454$ and $\bar{\alpha} = 9.73 \times 10^{-5}$. Equation (5.59) tells us that the shear flow is $u_{i0} = 1.59 \times 10^6$ m/s, yielding $\tau = 4.71 \times 10^{-3}$ (equation (5.37)). Running our simulation with these parameters gave results shown in Figure 5.20: part (a) shows the number density contours, giving depletion to $y = 3.4y_0$ (51 km), whilst part (b) shows the number of depleted electrons, $A(t)$, defined in equation (5.73). This asymptotes to a constant value as the steady state is reached, and Figure 5.20 shows that full broadening has occurred after ~200 - 300 s, agreeing very well with the time between the first and fourth Cluster spacecraft crossings (280 s). This good comparison with data lends confidence to the results of our model and simulations.

5.9 Accuracy of code

In order to test the accuracy of the code used to solve the partial differential equation in (5.38), we ran a simulation with timestep $\bar{t} = 0.001$ and $\bar{y} = 0.01$ to obtain $\bar{N}_1(\bar{y}, \bar{t})$, and compared this with the result

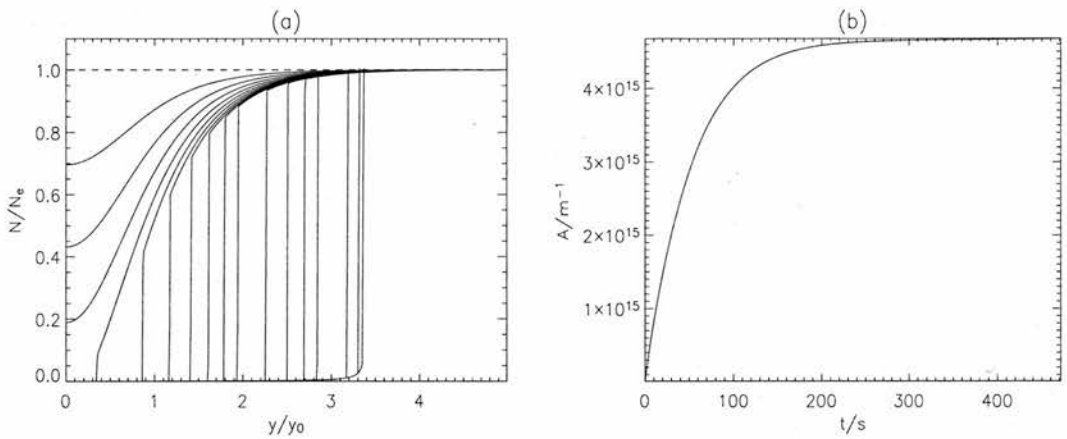

Figure 5.20: Comparison with *Marklund et al. (2001)* Figure 3: (a) Snapshots of number density profile show depletion to $y = 3.4y_0$, corresponding to 51 km. Number density profiles are shown for $t = 0.0$, 4.7, 9.4, 14.1, 18.9, 23.6, 28.3, 33.0, 37.7, 42.4, 47.1, 58.9, 70.7, 82.5, 94.3, 141.4, 188.6, and 235.7 s. (b) The number of depleted electrons, A, shows that the time for total depletion to occur is ~200 - 300 s, agreeing well with the satellite data.

obtained with a halved timestep and gridspacing, $\bar{N}_2(\bar{y}, \bar{t})$. An estimate of the error over n points at a time $\bar{t}$ was given by

$$E_A(\bar{t}) = \frac{1}{n}\sqrt{\sum_i \left(\bar{N}_2(\bar{y}_i, \bar{t}) - \bar{N}_1(\bar{y}_i, \bar{t})\right)^2} \tag{5.80}$$

Summing from $i = 0$ to the $\bar{y}$ value where $\bar{N} = 1$, E_A was found to be less than 2×10^{-4} for $\bar{t} = 0$ to 20,000. We can also test the accuracy of the code by setting $\bar{\alpha} = 0$ in equation (5.38). Integrating in the $\bar{y}$ direction yields

$$\begin{aligned} \frac{\partial}{\partial \bar{t}} \int_0^\infty \bar{N}\ \mathrm{d}\bar{y} + \left[\frac{\eta \bar{u}_i \bar{N}}{1+\beta\bar{N}}\right]_0^\infty &= 0 \\ \Rightarrow \frac{\partial}{\partial \bar{t}} \int_0^\infty \bar{N}\ \mathrm{d}\bar{y} + \frac{\eta}{1+\beta} &= 0 \end{aligned} \tag{5.81}$$

We can now integrate this in time to obtain

$$\left[\int_0^\infty \bar{N}\ \mathrm{d}\bar{y}\right]_0^{\bar{t}} + \frac{\eta \bar{t}}{1+\beta} = \text{constant} \tag{5.82}$$

Since $\bar{N} = 1$ everywhere at $\bar{t} = 0$, this simplifies to

$$\int_0^\infty 1 - \bar{N}(\bar{y}, \bar{t}) \ \mathrm{d}\bar{y} = \frac{\eta \bar{t}}{1+\beta} \tag{5.83}$$

where the constant is equal to zero due to initial conditions. This expresses conservation of electrons: the right hand side represents the number of electrons removed by the current, and the left hand side represents the number of electrons depleted. We can evaluate the left hand side at different values of $\bar{t}$ using the trapezium rule in our numerical simulation, and compare the answer with the right hand side to get an idea of the errors accumulated by the code. It was found that for $\eta = 3.12$ and $\beta = 1370$, the relative error was never greater than $\sim$0.5 % (the simulation was run until $\bar{t} = 650$).

5.10 Discussion and conclusions

In this Chapter, we have used an Alfvén wave model of magnetosphere-ionosphere interaction to describe the ionospheric E region number density evolution under the influence of downward field-aligned current, photoionisation and recombination. The flow of a downward field-aligned current, set up via a shear flow in the magnetosphere, leads to the evacuation of electrons from the E region up into the magnetosphere. The system reaches a steady state when the electron loss and production rates balance. The behaviour of the E region falls into two regimes: if the current density is small enough ($j_{\parallel 0} < \alpha e n_e^2 h$), then the E region is partially depleted within the original shear flow width ($y < y_0$), and reaches steady state before total depletion has occurred; when the current density is larger ($j_{\parallel 0} > \alpha e n_e^2 h$), the E region becomes totally depleted within the original shear width and the current region is forced to broaden. On the dayside, where E region number densities are typically $\sim 10^{11}$ m^{-3} or more, broadening only occurs for strong current densities above 10 μAm^{-2}, whereas on the nightside, where E region number densities can fall by a factor of 10 due to reduced production processes, broadening occurs for any downward current greater than $\sim$0.1 μAm^{-2}. Thus, our model predicts that significant E region depletion and current region broadening should be much more common on the nightside than on the dayside. The observations of current region broadening and depleted ionospheric number densities by *Marklund et al. (2001)* and *Aikio et al. (2004)* were all in the post-midnight sector, offering some support for our conclusions.

We have derived expressions estimating the depletion width (generally $\sim$1 - 10 y_0) and characteristic timescale of depletion ($\sim$10-100 s). The timescales agree well with simulations by *Karlsson and Marklund (1998)*, who find that depletions are noticeable on the order of seconds. Typical average speeds of broadening are found to be $\sim$100 m/s to 1 km/s, and decrease for a given current density as the ionospheric number density increases. We have directly compared our model with Cluster data from *Marklund et al. (2001)*, and were able to estimate the depletion time with accuracy, given the observed broadening width and other parameters.

The source of electrons for the upward current is the magnetosphere, which can give an almost limitless supply: *Wright et al. (2002)* estimate that less than 5 % of magnetospheric electrons would be removed from a flux tube during the upward current phase of a (μAm^{-2}) ULF field line resonance ($\sim$minutes). In contrast, the electrons which carry the downward current are supplied by the E region, a finite resource. This

Chapter has demonstrated how important the magnetosphere-ionosphere boundary is to the evolution of the downward field-aligned current, and how the E region cannot simply be regarded as a limitless source of current-carriers, since total depletion can occur in ~30 s. This illustrates that our one-dimensional downward current model in Chapters 2 and 3 could be extended into two dimensions, including the E region, to provide a more dynamic picture of downward current flow. Another modification to this model could be the inclusion of the dense, thick (150-500 km altitude) F region: this would have the effect of reflecting some of the incoming Alfvén wave at the magnetosphere-F region boundary, so that the Alfvén wave which reaches the E region has already been modified. These extra features would give a better picture of the evolution of a downward current region and the associated accelerating potentials.

Chapter 6

Conclusions and Further Work

In this Thesis, Vlasov models of the upward and downward field-aligned current regions have been presented. In these models, the ion distribution is fixed along an auroral flux tube, and the electrons are described via distribution functions. This formulation enables us to isolate the different electron populations involved. In the downward current region, most of the ionospheric electrons are trapped close to the Earth by a small ambipolar electric field; the most energetic ionospheric electrons escape the ionosphere and penetrate into the magnetosphere to carry the current; and the magnetosphere is populated by a Maxwellian electron population. In the upward current region, all of the ionospheric electrons are trapped in the ionosphere. A Maxwellian electron population again populates the magnetosphere, and the most energetic of those electrons that have a small pitch angle precipitate into the ionosphere to carry current.

There are both similarities and important differences between the findings from the two models. Both exhibit an ambipolar electric field close to the Earth: for downward currents, this extends to an altitude of $\sim$500 - 600 km, whilst for upward currents, it extends to the B/n peak at $\sim$1700 km altitude. In both current regions, a potential difference of $\sim$100 V - 1 kV accelerates electrons to carry current; the parallel electric field is $\sim$mV/m. We assume that the ion density is constant on the electron transit time in our models. For downward currents, continuous potential solutions can be found for any current density; however, it is only possible to obtain continuous solutions in the upward current region for a smaller range of current densities $\sim$1 μAm^{-2}. Acceleration in the downward current region begins Earthward of the B/n peak and extends for $\sim$1000 - 3000 km: the maximum parallel electric field occurs a few density scale heights Earthward of the B/n peak. In the upward current region, acceleration takes place at the B/n peak. For smaller current densities in our continuous range, acceleration extends for $\sim$1 R_E beyond the peak; as the current density increases, the potential is increasingly concentrated at the B/n peak until much of the acceleration occurs over a small distance $\sim$100 km. The largest current density for which we are able to find a continuous solution gives 42% of the potential increase at the B/n peak.

Our upward current model satisfies the linear *Knight (1973)* current-voltage relation which is independent of the ion density profile along the field line. However, we have demonstrated that this profile will determine the location and magnitude of the associated parallel electric field. We have found that, for the

largest potentials in our continuous range, the parallel pressure gradient of the mirroring magnetospheric population supports most of the parallel electric field concentrated around the B/n peak. The plasma anisotropy and magnetic field gradient term is dominant at higher altitudes, indicating that most of the potential here is necessary for electrons to overcome the magnetic mirror force. We also found that although the precipitating electrons actually carry the current, the presence of the mirroring electrons is vital to their acceleration: the mirroring electrons play the major role in satisfying quasi-neutrality along the field line, and also support most of the accelerating parallel electric field.

In the downward current region, we found that the equilibrium properties immediately around the B/n peak solely determine the altitude and magnitude of the accelerating potential. We have used our model to derive a near-exact expression for the total potential drop along the field line, which is independent of ionospheric quantities. Carrying out Taylor series expansions on this expression yields two simpler non-linear current-voltage relations: one is valid for lower current densities and medium to high magnetospheric temperatures $\sim$1 keV, and the other is valid for higher current densities and lower magnetospheric temperatures. These expansions are found to be accurate to within 6.4% of the potential increase found from the numerical solution.

In both current regions, the potential distribution and accompanying parallel electric field variation are heavily dependent on the ion density profile along the field line, since this will determine the altitude of the B/n peak. Observations by *Marklund (1993)* suggest that acceleration occurs at lower altitudes in the downward current region ($<$ 4000 km) than in the upward current region ($>$ 4000 km). Ion outflow occurs in both regions, but is stronger and extends to lower altitudes in the downward current region. When we allow for this difference, we find that acceleration occurs at $\sim$2000 km altitude in the downward current region, and at $\sim$4000 km altitude in the upward current region, consistent with the observations.

It is apparent from observations of the upward *(Ergun et al. (2004))* and downward *(Ergun et al. (2003a))* current regions that electron acceleration can occur over a very small distance (a double layer). Thus, the change in potential occurs over a very small region, which could be viewed as an extreme version of our upward and downward current models with a compacted acceleration width. In our models, this can be achieved by choosing an ion number density profile with a sharp gradient at the required altitude. Such a density profile could evolve from a model which incorporated ion motion. Ions will respond much more slowly to a parallel electric field than electrons, due to their much higher mass, but on longer timescales, this ion motion will affect the ion density profile and the resulting potential variation. In such a model, it is possible that an initially exponentially-decaying ionospheric ion density profile could steepen up into a step function, which would have the effect of concentrating the potential into a double layer.

Finally, we presented an Alfvén wave model of magnetosphere-ionosphere interaction to describe the evolution of number density in the ionospheric E region during a flow of downward field-aligned current. This downward current is set up via a shear flow gradient in the magnetosphere, and the ionospheric electron number density is subject to gain via photoionisation and to loss via recombination and electron evacuation. For smaller current densities, the E region is partially depleted within the original shear flow width, and reaches steady state before total depletion has occurred. For larger current densities, the E region becomes totally depleted within the original shear flow width and the current region must broaden in order to carry the current. Our model predicts that broadening will be a common feature of the nightside, since low number

densities $\sim 10^{10}$ m^{-3} here mean that broadening occurs for any current density greater than ~ 0.1 μAm^{-2}. On the dayside, however, where number densities are at least an order of magnitude bigger, broadening only occurs for current densities larger than ~ 10 μAm^{-2}. On the nightside, we have found that the depletion width is generally ~ 1 - 10 times the original shear flow width and is proportional to the initial downward current density. Depletion occurs on a timescale of ~ 10 - 100 s.

A modification to this model would be the inclusion of the ionospheric F region at 150-500 km altitude, which would act as a dense, thick region between the magnetosphere and the E region. In this case, some of the incoming Alfvén wave would be reflected at the magnetosphere-F region boundary, so that the Alfvén wave which reached the E region would already be modified. This extra feature would give an even better picture of the evolution of a downward current region.

The final aim of this work is to model the entire field-aligned current region in two dimensions, including horizontal Pedersen currents which flow mainly in the E region, between upward and downward field-aligned currents. The regions are very much inter-connected, so a complete model would reveal the dynamics and interplay between the different current regions. It would include ion motion and E region depletion (in the downward current region) and enhancement (in the upward current region). Such a model would bring elements of our previous research together, and from it, we would be able to predict the two-dimensional potential structures across the region and their evolution in time. This study would be a next step in the direction of understanding the Earth's current circuit as a whole, which is of considerable interest to "global" modelling of the magnetosphere.

Appendix A

Evaluation of moment integrals

A.1 Field-aligned current density

Equation (4.91) is derived in the following manner:

$$
\begin{aligned}
i_{\parallel I} &= \frac{\zeta_M}{\sqrt{2\pi}} \int\limits_{\text{source cone}} \int e^{-W_{\parallel M}} e^{-W_{\perp M}} \, \mathrm{d}W_{\perp M} \mathrm{d}W_{\parallel M} \\
&= \frac{\zeta_M}{\sqrt{2\pi}} \int\limits_{W_{\parallel M}=0}^{\infty} \int\limits_{W_{\perp M}=0}^{\frac{W_{\parallel M}-U_M}{\zeta_M-1}} e^{-W_{\parallel M}} e^{-W_{\perp M}} \, \mathrm{d}W_{\perp M} \mathrm{d}W_{\parallel M} \\
&= \frac{\zeta_M}{\sqrt{2\pi}} \int\limits_{W_{\parallel M}=0}^{\infty} e^{-W_{\parallel M}} \left(1 - \exp\left(-\frac{W_{\parallel M}}{\zeta_M - 1}\right) \exp\left(\frac{U_M}{\zeta_M - 1}\right)\right) \, \mathrm{d}W_{\parallel M} \\
&= \frac{\zeta_M}{\sqrt{2\pi}} \int\limits_{W_{\parallel M}=0}^{\infty} e^{-W_{\parallel M}} - \exp\left(-\frac{\zeta_M W_{\parallel M}}{\zeta_M - 1}\right) \exp\left(\frac{U_M}{\zeta_M - 1}\right) \, \mathrm{d}W_{\parallel M} \\
&= \frac{\zeta_M}{\sqrt{2\pi}} \left[-e^{-W_{\parallel M}} + \frac{\zeta_M - 1}{\zeta_M} \exp\left(-\frac{\zeta_M W_{\parallel M}}{\zeta_M - 1}\right) \exp\left(\frac{U_M}{\zeta_M - 1}\right)\right]_0^{\infty} \\
&= \frac{\zeta_M}{\sqrt{2\pi}} \left(1 - \frac{\zeta_M - 1}{\zeta_M} e^{\frac{U_M}{\zeta_M - 1}}\right) \\
&= \frac{\zeta_M - (\zeta_M - 1)\, e^{\frac{U_M}{\zeta_M - 1}}}{\sqrt{2\pi}}
\end{aligned}
\tag{A.1}
$$

A.2 Evaluation of magnetospheric parallel integrals

Equation (4.160) is found as follows:

$$\begin{aligned}
\eta_1 &= \int_{A_1+A_2} u_\parallel^2 \bar{f}_M \ \mathrm{d}\mathbf{u} \\
&= \int_{W_\parallel=0}^{\infty}\int_{W_\perp=0}^{\infty} u_\parallel^2 \bar{f}_M \ \mathrm{d}\mathbf{u} - \int_{W_\parallel=0}^{U-U_M}\int_{W_\perp=0}^{\frac{W_\parallel-U+U_M}{\zeta/\zeta_M-1}} u_\parallel^2 \bar{f}_M \ \mathrm{d}\mathbf{u} \\
&= \eta_{11} - \eta_{12}
\end{aligned} \tag{A.2}$$

So, we will examine each of these in turn. Firstly,

$$\begin{aligned}
\sqrt{\pi}\ \eta_{11} &= \int_{W_\parallel=0}^{\infty}\int_{W_\perp=0}^{\infty} \sqrt{W_\parallel}\ e^{-W_\parallel}\ e^{-W_\perp}\ e^{U-U_M}\ \mathrm{d}W_\parallel\ \mathrm{d}W_\perp \\
&= e^{U-U_M} \int_{W_\parallel=0}^{\infty} \sqrt{W_\parallel}\ e^{-W_\parallel}\ \left[-e^{-W_\perp}\right]_0^\infty\ \mathrm{d}W_\parallel \\
&= e^{U-U_M} \int_{W_\parallel=0}^{\infty} \sqrt{W_\parallel}\ e^{-W_\parallel}\ \mathrm{d}W_\parallel \\
&= e^{U-U_M} \int_{x=0}^{\infty} 2x^2\ e^{-x^2}\ \mathrm{d}x, \text{where } x^2 = W_\parallel \\
&= e^{U-U_M} \left(\left[-xe^{-x^2}\right]_0^\infty + \int_{x=0}^{\infty} e^{-x^2}\ \mathrm{d}x \right) \\
&= \frac{e^{U-U_M}}{2}
\end{aligned} \tag{A.3}$$

Now, we compute η_{12}:

$$\begin{aligned}
\sqrt{\pi}\ \eta_{12} &= \int_{W_\parallel=0}^{U-U_M}\int_{W_\perp=0}^{\frac{W_\parallel-U+U_M}{\zeta/\zeta_M-1}} \sqrt{W_\parallel}\ e^{-W_\parallel}\ e^{-W_\perp}\ e^{U-U_M}\ \mathrm{d}W_\parallel\ \mathrm{d}W_\perp \\
&= e^{U-U_M} \int_{W_\parallel=0}^{U-U_M} \sqrt{W_\parallel}\ e^{-W_\parallel} \left[-e^{-W_\perp}\right]_0^{\frac{W_\parallel-U+U_M}{\zeta/\zeta_M-1}}\ \mathrm{d}W_\parallel
\end{aligned}$$

$$
\begin{aligned}
&= e^{U-U_M} \int_{W_\parallel=0}^{U-U_M} \sqrt{W_\parallel}\ e^{-W_\parallel} \left(1-\exp\left(-\frac{W_\parallel}{\frac{\zeta}{\zeta_M}-1}\right)\ \exp\left(\frac{U-U_M}{\frac{\zeta}{\zeta_M}-1}\right)\right)\ \mathrm{d}W_\parallel \\
&= e^{U-U_M} \int_{W_\parallel=0}^{U-U_M} \sqrt{W_\parallel}\ e^{-W_\parallel}\ \mathrm{d}W_\parallel \\
&\quad -e^{-s(U-U_M)} \int_{W_\parallel=0}^{U-U_M} \sqrt{W_\parallel}\ e^{sW_\parallel}\ \mathrm{d}W_\parallel, \text{ using equation (4.66)} \\
&= e^{U-U_M} \int_{x=0}^{\sqrt{U-U_M}} 2x^2\ e^{-x^2}\ \mathrm{d}x \\
&\quad -s^{-3/2}e^{-s(U-U_M)} \int_{y=0}^{\sqrt{s(U-U_M)}} 2y^2\ e^{y^2}\ \mathrm{d}y, \text{ where } y^2 = sW_\parallel \\
&= e^{U-U_M} \left(\left[-xe^{-x^2}\right]_0^{\sqrt{U-U_M}} + \int_{x=0}^{\sqrt{U-U_M}} e^{-x^2}\ \mathrm{d}x\right) \\
&\quad -s^{-3/2}e^{-s(U-U_M)} \left(\left[ye^{y^2}\right]_0^{\sqrt{s(U-U_M)}} - \int_{y=0}^{\sqrt{s(U-U_M)}} e^{y^2}\ \mathrm{d}y\right) \\
\Rightarrow \eta_{12} &= -\frac{1}{\sqrt{\pi}}\left(\sqrt{U-U_M}+\frac{\sqrt{U-U_M}}{s}\right)+\frac{e^{U-U_M}}{2}\mathrm{erf}\left(\sqrt{U-U_M}\right) \\
&\quad +\frac{s^{-3/2}}{\sqrt{\pi}}\mathrm{D}\left(\sqrt{s(U-U_M)}\right)
\end{aligned}
\tag{A.4}
$$

In a final simplification,

$$1+\frac{1}{s}=\frac{\zeta_M}{\zeta} \tag{A.5}$$

So,

$$\eta_{12} = -\frac{\zeta_M}{\zeta}\sqrt{\frac{U-U_M}{\pi}}+\frac{e^{U-U_M}}{2}\mathrm{erf}\left(\sqrt{U-U_M}\right)+\frac{s^{-3/2}}{\sqrt{\pi}}\mathrm{D}\left(\sqrt{s(U-U_M)}\right) \tag{A.6}$$

Thus, using the contributions from equations (A.3) and (A.6), we can see that

$$\eta_1 = \frac{e^{U-U_M}}{2}\mathrm{erfc}\left(\sqrt{U-U_M}\right)-\frac{s^{-3/2}}{\sqrt{\pi}}\mathrm{D}\left(\sqrt{s(U-U_M)}\right)+\frac{\zeta_M}{\zeta}\sqrt{\frac{U-U_M}{\pi}} \tag{A.7}$$

Now, we need to move on to area A_2 to derive equation (4.161):

$$\begin{aligned}
\eta_2 &= \int_{A_2} u_\parallel^2 \bar{f}_M \, \mathrm{d}\mathbf{u} \\
&= \int_{W_\parallel=0}^{U-U_D} \int_{W_\perp=\frac{W_\parallel - U + U_M}{\zeta/\zeta_M - 1}}^{\infty} u_\parallel^2 \bar{f}_M \, \mathrm{d}\mathbf{u} + \int_{W_\parallel=U-U_D}^{\infty} \int_{W_\perp=\frac{W_\parallel - U}{\zeta - 1}}^{\infty} u_\parallel^2 \bar{f}_M \, \mathrm{d}\mathbf{u} \\
&= \eta_{21} + \eta_{22}
\end{aligned} \tag{A.8}$$

Examining the first of these:

$$\begin{aligned}
\sqrt{\pi}\ \eta_{21} &= e^{U-U_M} \int_{W_\parallel=0}^{U-U_D} \int_{W_\perp=\frac{W_\parallel - U + U_M}{\zeta/\zeta_M - 1}}^{\infty} \sqrt{W_\parallel}\ e^{-W_\parallel}\ e^{-W_\perp}\ \mathrm{d}W_\perp\ \mathrm{d}W_\parallel \\
&= e^{U-U_M} \int_{W_\parallel=0}^{U-U_D} \sqrt{W_\parallel}\ e^{-W_\parallel} \left[-e^{-W_\perp}\right]_{\frac{W_\parallel - U + U_M}{\zeta/\zeta_M - 1}}^{\infty} \mathrm{d}W_\parallel \\
&= e^{U-U_M} \int_{W_\parallel=0}^{U-U_D} \sqrt{W_\parallel}\ e^{-W_\parallel}\ \exp\left(-\frac{W_\parallel}{\frac{\zeta}{\zeta_M} - 1}\right)\ \exp\left(\frac{U - U_M}{\frac{\zeta}{\zeta_M} - 1}\right)\ \mathrm{d}W_\parallel \\
&= e^{-s(U-U_M)} \int_{W_\parallel=0}^{U-U_D} \sqrt{W_\parallel}\ e^{sW_\parallel}\ \mathrm{d}W_\parallel, \text{ using equation (4.66)} \\
&= s^{-3/2} e^{-s(U-U_M)} \int_{y=0}^{\sqrt{s(U-U_D)}} 2y^2\ e^{y^2}\ \mathrm{d}y \\
&= s^{-3/2} e^{-s(U-U_M)} \left(\left[y e^{y^2} \right]_0^{\sqrt{s(U-U_D)}} - \int_{y=0}^{\sqrt{s(U-U_D)}} e^{y^2}\ \mathrm{d}y \right) \\
&= s^{-3/2} e^{-s(U-U_M)} \left(\sqrt{s(U-U_D)}\, e^{s(U-U_D)} - \int_{y=0}^{\sqrt{s(U-U_D)}} e^{y^2}\ \mathrm{d}y \right)
\end{aligned} \tag{A.9}$$

Now, we can use the relation in equation (4.73) to simplify η_{21} to

$$\eta_{21} = e^{-k} \left(\frac{1}{s} \sqrt{\frac{U-U_D}{\pi}} - \frac{s^{-3/2}}{\sqrt{\pi}} D\left(\sqrt{s(U-U_D)}\right) \right) \tag{A.10}$$

Finally,

$$
\begin{aligned}
\sqrt{\pi}\ \eta_{22} &= e^{U-U_M} \int_{W_\parallel=U-U_D}^{\infty} \int_{W_\perp=\frac{W_\parallel-U}{\zeta-1}}^{\infty} \sqrt{W_\parallel}\ e^{-W_\parallel}\ e^{-W_\perp}\ \mathrm{d}W_\perp\ \mathrm{d}W_\parallel \\
&= e^{U-U_M} \int_{W_\parallel=U-U_D}^{\infty} \sqrt{W_\parallel}\ e^{-W_\parallel} \left[-e^{-W_\perp}\right]_{\frac{W_\parallel-U}{\zeta-1}}^{\infty}\ \mathrm{d}W_\parallel \\
&= e^{U-U_M} \int_{W_\parallel=U-U_D}^{\infty} \sqrt{W_\parallel}\ e^{-W_\parallel}\ e^{-\frac{W_\parallel}{\zeta-1}}\ e^{\frac{U}{\zeta-1}}\ \mathrm{d}W_\parallel \\
&= e^{tU-U_M} \int_{W_\parallel=U-U_D}^{\infty} \sqrt{W_\parallel}\ e^{-tW_\parallel}\ \mathrm{d}W_\parallel, \text{ using equation (4.76)} \\
&= t^{-3/2}\ e^{tU-U_M} \int_{z=\sqrt{t(U-U_D)}}^{\infty} 2z^2\ e^{-z^2}\ \mathrm{d}z, \text{ where } z^2 = tW_\parallel \\
&= t^{-3/2}\ e^{tU-U_M} \left(\left[-ze^{-z^2}\right]_{\sqrt{t(U-U_D)}}^{\infty} + \int_{z=\sqrt{t(U-U_D)}}^{\infty} e^{-z^2}\ \mathrm{d}z \right) \\
&= t^{-3/2}\ e^{tU-U_M} \left(\sqrt{t(U-U_D)}e^{-t(U-U_D)} + \frac{\sqrt{\pi}}{2}\mathrm{erfc}\left(\sqrt{t(U-U_D)}\right)\right) \qquad \text{(A.11)}
\end{aligned}
$$

Now, using the relation in equation (4.78), η_{22} simplifies as follows:

$$
\eta_{22} = e^{-k}\left[\frac{1}{t}\sqrt{\frac{U-U_D}{\pi}} + \frac{e^{t(U-U_D)}}{2t^{3/2}}\mathrm{erfc}\left(\sqrt{t(U-U_D)}\right)\right] \qquad \text{(A.12)}
$$

So, adding the contributions from equations (A.10) and (A.12), and using the definitions for s and t in equations (4.66) and (4.76), we obtain

$$
\begin{aligned}
\eta_2 &= e^{-k}\left[\left(\frac{\zeta_M-1}{\zeta}\right)\sqrt{\frac{U-U_D}{\pi}} + \frac{t}{2}^{-3/2} e^{t(U-U_D)}\mathrm{erfc}\left(\sqrt{t(U-U_D)}\right)\right. \\
&\quad \left. -\frac{s^{-3/2}}{\sqrt{\pi}}D\left(\sqrt{s(U-U_D)}\right)\right] \qquad \text{(A.13)}
\end{aligned}
$$

A.3 Evaluation of magnetospheric perpendicular integrals

We now derive equation (4.165):

$$\begin{aligned}
\mu_1 &= \int_{A_1+A_2} u_\perp^2 \bar{f}_M \ \mathrm{d}\mathbf{u} \\
&= \int_{W_\parallel=0}^{\infty}\int_{W_\perp=0}^{\infty} u_\perp^2 \bar{f}_M \ \mathrm{d}\mathbf{u} - \int_{W_\parallel=0}^{U-U_M}\int_{W_\perp=0}^{\frac{W_\parallel-U+U_M}{\zeta/\zeta_M-1}} u_\perp^2 \bar{f}_M \ \mathrm{d}\mathbf{u} \\
&= \mu_{11} - \mu_{12}
\end{aligned} \tag{A.14}$$

So, firstly,

$$\begin{aligned}
\sqrt{\pi}\ \mu_{11} &= e^{U-U_M} \int_{W_\parallel=0}^{\infty}\int_{W_\perp=0}^{\infty} \frac{W_\perp}{\sqrt{W_\parallel}}\ e^{-W_\parallel}\ e^{-W_\perp}\ \mathrm{d}W_\perp\ \mathrm{d}W_\parallel \\
&= e^{U-U_M} \int_{W_\parallel=0}^{\infty} \frac{e^{-W_\parallel}}{\sqrt{W_\parallel}} \left(\left[-W_\perp\ e^{-W_\perp}\right]_0^\infty + \int_{W_\perp=0}^{\infty} e^{-W_\perp}\ \mathrm{d}W_\perp \right) \mathrm{d}W_\parallel \\
&= e^{U-U_M} \int_{W_\parallel=0}^{\infty} \frac{e^{-W_\parallel}}{\sqrt{W_\parallel}} \left[-e^{-W_\perp}\right]_0^\infty \ \mathrm{d}W_\parallel \\
&= e^{U-U_M} \int_{W_\parallel=0}^{\infty} \frac{e^{-W_\parallel}}{\sqrt{W_\parallel}}\ \mathrm{d}W_\parallel \\
&= e^{U-U_M} \int_{x=0}^{\infty} 2e^{-x^2}\ \mathrm{d}x \\
&= e^{U-U_M} \frac{2}{\sqrt{\pi}} \mathrm{erf}\,(\infty) \\
&= e^{U-U_M}
\end{aligned} \tag{A.15}$$

Next,

$$\begin{aligned}
\sqrt{\pi}\ \mu_{12} &= e^{U-U_M} \int_{W_\parallel=0}^{U-U_M}\int_{W_\perp=0}^{\frac{W_\parallel-U+U_M}{\zeta/\zeta_M-1}} \frac{W_\perp}{\sqrt{W_\parallel}}\ e^{-W_\parallel}\ e^{-W_\perp}\ \mathrm{d}W_\perp\ \mathrm{d}W_\parallel \\
&= e^{U-U_M} \int_{W_\parallel=0}^{U-U_M} \frac{e^{-W_\parallel}}{\sqrt{W_\parallel}} \left(\left[-W_\perp e^{-W_\perp}\right]_0^{\frac{W_\parallel-U+U_M}{\zeta/\zeta_M-1}} + \int_{W_\perp=0}^{\frac{W_\parallel-U+U_M}{\zeta/\zeta_M-1}} e^{-W_\perp}\ \mathrm{d}W_\perp \right) \mathrm{d}W_\parallel
\end{aligned}$$

$$
\begin{aligned}
&= e^{U-U_M} \int_{W_\parallel=0}^{U-U_M} \frac{e^{-W_\parallel}}{\sqrt{W_\parallel}} \left(\left(\frac{U-U_M-W_\parallel}{\frac{\zeta}{\zeta_M}-1} - 1 \right) \exp\left(-\frac{W_\parallel}{\frac{\zeta}{\zeta_M}-1} \right) \exp\left(\frac{U-U_M}{\frac{\zeta}{\zeta_M}-1} \right) + 1 \right) \, \mathrm{d}W_\parallel \\
&= e^{U-U_M} \int_{W_\parallel=0}^{U-U_M} \frac{e^{-W_\parallel}}{\sqrt{W_\parallel}} \, \mathrm{d}W_\parallel \; + \; e^{-s(U-U_M)} \int_{W_\parallel=0}^{U-U_M} \frac{e^{sW_\parallel}}{\sqrt{W_\parallel}} \left(\frac{U-U_M}{\frac{\zeta}{\zeta_M}-1} - 1 \right) \, \mathrm{d}W_\parallel \\
&\quad -e^{-s(U-U_M)} \int_{W_\parallel=0}^{U-U_M} \frac{\sqrt{W_\parallel}}{\frac{\zeta}{\zeta_M}-1} \, e^{sW_\parallel} \, \mathrm{d}W_\parallel, \text{ using equation (4.66)} \\
&= e^{U-U_M} \int_{x=0}^{\sqrt{U-U_M}} 2e^{-x^2} \, \mathrm{d}x \; + \; \frac{e^{-s(U-U_M)}}{\sqrt{s}} \int_{y=0}^{\sqrt{s(U-U_M)}} 2e^{y^2} \left(\frac{U-U_M}{\frac{\zeta}{\zeta_M}-1} - 1 \right) \, \mathrm{d}y \\
&\quad -\frac{e^{-s(U-U_M)}}{s^{3/2}} \int_{y=0}^{\sqrt{s(U-U_M)}} \frac{2y^2}{\frac{\zeta}{\zeta_M}-1} \, e^{y^2} \, \mathrm{d}y \\
&= \sqrt{\pi} e^{U-U_M} \operatorname{erf}\left(\sqrt{U-U_M} \right) + \frac{2}{\sqrt{s}} \left(\frac{U-U_M}{\frac{\zeta}{\zeta_M}-1} - 1 \right) D\left(\sqrt{s(U-U_M)} \right) \\
&\quad -\frac{e^{-s(U-U_M)}}{s^{3/2}\left(\frac{\zeta}{\zeta_M}-1\right)} \left(\left[y e^{y^2} \right]_0^{\sqrt{s(U-U_M)}} - \int_{y=0}^{\sqrt{s(U-U_M)}} e^{y^2} \, \mathrm{d}y \right) \\
&= \sqrt{\pi} e^{U-U_M} \operatorname{erf}\left(\sqrt{U-U_M} \right) + \frac{2}{\sqrt{s}} \left(\frac{U-U_M}{\frac{\zeta}{\zeta_M}-1} - 1 \right) D\left(\sqrt{s(U-U_M)} \right) \\
&\quad -\frac{s^{-3/2}}{\frac{\zeta}{\zeta_M}-1} \left(\sqrt{s(U-U_M)} - D\left(\sqrt{s(U-U_M)} \right) \right)
\end{aligned}
\tag{A.16}
$$

To simplify, we note that

$$
\begin{aligned}
s\left(\frac{\zeta}{\zeta_M} - 1 \right) &= \left(\frac{\zeta}{\zeta_M - \zeta} \right) \left(\frac{\zeta - \zeta_M}{\zeta_M} \right) \\
&= -\frac{\zeta}{\zeta_M}
\end{aligned}
\tag{A.17}
$$

Thus,

$$
\begin{aligned}
\mu_{12} &= e^{U-U_M} \operatorname{erf}\left(\sqrt{U-U_M} \right) + \frac{\zeta_M}{\zeta} \sqrt{\frac{U-U_M}{\pi}} \\
&\quad + \frac{2}{\sqrt{s\pi}} \left(\frac{U-U_M}{\frac{\zeta}{\zeta_M}-1} - 1 - \frac{\zeta_M}{2\zeta} \right) D\left(\sqrt{s(U-U_M)} \right)
\end{aligned}
\tag{A.18}
$$

Using the contributions from equations (A.15) and (A.18),

$$\begin{aligned}\mu_1 &= e^{U-U_M}\operatorname{erfc}\left(\sqrt{U-U_M}\right) - \frac{\zeta_M}{\zeta}\sqrt{\frac{U-U_M}{\pi}} \\ &\quad + \frac{2}{\sqrt{s\pi}}\left(1+\frac{\zeta_M}{2\zeta}-\frac{U-U_M}{\frac{\zeta}{\zeta_M}-1}\right) D\left(\sqrt{s(U-U_M)}\right) \end{aligned} \tag{A.19}$$

Now, we work out the contribution to the second-order perpendicular velocity moment from area A_2 to derive equation (4.166):

$$\begin{aligned}\mu_2 &= \int\int_{A_2} u_\perp^2 \bar{f}_M \ \mathrm{d}\mathbf{u} \\ &= \int_{W_\parallel=0}^{U-U_D} \int_{W_\perp=\frac{W_\parallel-U+U_M}{\zeta/\zeta_M-1}}^{\infty} u_\perp^2 \bar{f}_M \ \mathrm{d}\mathbf{u} + \int_{W_\parallel=U-U_D}^{\infty} \int_{W_\perp=\frac{W_\parallel-U}{\zeta-1}}^{\infty} u_\perp^2 \bar{f}_M \ \mathrm{d}\mathbf{u} \\ &= \mu_{21} + \mu_{22} \end{aligned} \tag{A.20}$$

Firstly,

$$\begin{aligned}\sqrt{\pi}\ \mu_{21} &= e^{U-U_M} \int_{W_\parallel=0}^{U-U_D} \int_{W_\perp=\frac{W_\parallel-U+U_M}{\zeta/\zeta_M-1}}^{\infty} \frac{W_\perp}{\sqrt{W_\parallel}}\ e^{-W_\parallel}\ e^{-W_\perp}\ \mathrm{d}W_\perp\ \mathrm{d}W_\parallel \\ &= e^{U-U_M} \int_{W_\parallel=0}^{U-U_D} \frac{e^{-W_\parallel}}{\sqrt{W_\parallel}} \left(\left[-W_\perp\, e^{-W_\perp}\right]_{\frac{W_\parallel-U+U_M}{\zeta/\zeta_M-1}}^{\infty} + \int_{W_\perp=\frac{W_\parallel-U+U_M}{\zeta/\zeta_M-1}}^{\infty} e^{-W_\perp}\ \mathrm{d}W_\perp \right) \mathrm{d}W_\parallel \\ &= e^{U-U_M} \int_{W_\parallel=0}^{U-U_D} \frac{e^{-W_\parallel}}{\sqrt{W_\parallel}} \left(\frac{W_\parallel-U+U_M}{\frac{\zeta}{\zeta_M}-1}+1\right) \exp\left(-\frac{W_\parallel}{\frac{\zeta}{\zeta_M}-1}\right) \exp\left(\frac{U-U_M}{\frac{\zeta}{\zeta_M}-1}\right)\ \mathrm{d}W_\parallel \\ &= e^{-s(U-U_M)} \int_{W_\parallel=0}^{U-U_D} \frac{e^{sW_\parallel}}{\sqrt{W_\parallel}} \left(1+\frac{U_M-U}{\frac{\zeta}{\zeta_M}-1}\right) + \frac{\sqrt{W_\parallel}}{\frac{\zeta}{\zeta_M}-1} e^{sW_\parallel}\ \mathrm{d}W_\parallel, \text{ using equation (4.66)} \\ &= \frac{e^{-s(U-U_M)}}{\sqrt{s}} \int_{y=0}^{\sqrt{s(U-U_D)}} 2e^{y^2}\left(1+\frac{U_M-U}{\frac{\zeta}{\zeta_M}-1}\right)\ \mathrm{d}y \end{aligned}$$

$$+\frac{e^{-s(U-U_M)}}{s^{3/2}\left(\frac{\zeta}{\zeta_M}-1\right)}\int_{y=0}^{\sqrt{s(U-U_D)}} 2y^2e^{y^2}\ \mathrm{d}y \tag{A.21}$$

Using equation (4.73) and integration by parts, we can simplify this to

$$\begin{aligned}
\sqrt{\pi}\ \mu_{21} &= \frac{2}{\sqrt{s}}e^{-k}\left(1+\frac{U_M-U}{\frac{\zeta}{\zeta_M}-1}\right)D\left(\sqrt{s(U-U_D)}\right) \\
&\quad +\frac{e^{-s(U-U_M)}}{s^{3/2}\left(\frac{\zeta}{\zeta_M}-1\right)}\left(\left[ye^{y^2}\right]_0^{\sqrt{s(U-U_D)}}-\int_{y=0}^{\sqrt{s(U-U_D)}} e^{y^2}\ \mathrm{d}y\right) \\
&= \frac{2}{\sqrt{s}}e^{-k}\left(1+\frac{U_M-U}{\frac{\zeta}{\zeta_M}-1}\right)D\left(\sqrt{s(U-U_D)}\right) \\
&\quad +\frac{e^{-s(U-U_M)}}{s^{3/2}\left(\frac{\zeta}{\zeta_M}-1\right)}\left(\sqrt{s(U-U_D)}e^{s(U-U_D)}-\int_{y=0}^{\sqrt{s(U-U_D)}} e^{y^2}\ \mathrm{d}y\right),
\end{aligned} \tag{A.22}$$

giving a final answer of

$$\begin{aligned}
\mu_{21} &= \frac{2e^{-k}}{\sqrt{s\pi}}\left(1-\frac{U-U_M}{\frac{\zeta}{\zeta_M}-1}+\frac{\zeta_M}{2\zeta}\right)D\left(\sqrt{s(U-U_D)}\right) \\
&\quad -\frac{\zeta_M}{\zeta}e^{-k}\sqrt{\frac{U-U_D}{\pi}}
\end{aligned} \tag{A.23}$$

Finally,

$$\begin{aligned}
\sqrt{\pi}\ \mu_{22} &= e^{U-U_M}\int_{W_\parallel=U-U_D}^{\infty}\int_{W_\perp=\frac{W_\parallel-U}{\zeta-1}}^{\infty}\frac{W_\perp}{\sqrt{W_\parallel}}\ e^{-W_\parallel}\ e^{-W_\perp}\ \mathrm{d}W_\perp\ \mathrm{d}W_\parallel \\
&= e^{U-U_M}\int_{W_\parallel=U-U_D}^{\infty}\frac{e^{-W_\parallel}}{\sqrt{W_\parallel}}\left(\left[-W_\perp e^{-W_\perp}\right]_{\frac{W_\parallel-U}{\zeta-1}}^{\infty}+\int_{W_\perp=\frac{W_\parallel-U}{\zeta-1}}^{\infty}e^{-W_\perp}\ \mathrm{d}W_\perp\right)\ \mathrm{d}W_\parallel \\
&= e^{U-U_M}\int_{W_\parallel=U-U_D}^{\infty}\frac{e^{-W_\parallel}}{\sqrt{W_\parallel}}\left(\frac{W_\parallel-U}{\zeta-1}+1\right)\ e^{-\frac{W_\parallel}{\zeta-1}}\ e^{\frac{U}{\zeta-1}}\ \mathrm{d}W_\parallel
\end{aligned}$$

$$
\begin{aligned}
&= e^{tU-U_M}\left(\int_{W_\parallel=U-U_D}^{\infty}\frac{e^{-tW_\parallel}}{\sqrt{W_\parallel}}\left(1-\frac{U}{\zeta-1}\right)\,\mathrm{d}W_\parallel\right.\\
&\quad\left.+\int_{W_\parallel=U-U_D}^{\infty}\frac{\sqrt{W_\parallel}}{\zeta-1}\,e^{-tW_\parallel}\,\mathrm{d}W_\parallel\right),\ \text{using equation (4.76)}\\
&= \frac{e^{tU-U_M}}{\sqrt{t}}\int_{z=\sqrt{t(U-U_D)}}^{\infty}2e^{-z^2}\left(1-\frac{U}{\zeta-1}\right)\,\mathrm{d}z\\
&\quad+\frac{e^{tU-U_M}}{t^{3/2}\,(\zeta-1)}\int_{z=\sqrt{t(U-U_D)}}^{\infty}2z^2\,e^{-z^2}\,\mathrm{d}z
\end{aligned}
\tag{A.24}
$$

Now, using equation (4.78) and performing integration by parts,

$$
\begin{aligned}
\mu_{22} &= \frac{e^{tU-U_M}}{\sqrt{t}}\left(1-\frac{U}{\zeta-1}\right)\operatorname{erfc}\left(\sqrt{t(U-U_D)}\right)\\
&\quad+\frac{e^{tU-U_M}}{\zeta\sqrt{t\pi}}\left(\left[-ze^{-z^2}\right]_{\sqrt{t(U-U_D)}}^{\infty}+\int_{z=\sqrt{t(U-U_D)}}^{\infty}e^{-z^2}\,\mathrm{d}z\right)\\
&= \frac{e^{-k}\,e^{t(U-U_D)}}{\sqrt{t}}\left(1-\frac{U}{\zeta-1}+\frac{1}{2\zeta}\right)\operatorname{erfc}\left(\sqrt{t(U-U_D)}\right)\\
&\quad+\frac{e^{-k}}{\zeta}\sqrt{\frac{U-U_D}{\pi}}
\end{aligned}
\tag{A.25}
$$

Thus, we can add the contributions from equations (A.23) and (A.25) to obtain the value of the integral over area A_2:

$$
\begin{aligned}
\mu_2 &= e^{-k}\left[\left(\frac{1-\zeta_M}{\zeta}\right)\sqrt{\frac{U-U_D}{\pi}}+\frac{e^{t(U-U_D)}}{\sqrt{t}}\left(1-\frac{U}{\zeta-1}+\frac{1}{2\zeta}\right)\operatorname{erfc}\left(\sqrt{t(U-U_D)}\right)\right.\\
&\quad\left.+\frac{2}{\sqrt{s\pi}}\left(1-\frac{U-U_M}{\frac{\zeta}{\zeta_M}-1}+\frac{\zeta_M}{2\zeta}\right)D\left(\sqrt{s(U-U_D)}\right)\right]
\end{aligned}
\tag{A.26}
$$

A.4 Evaluation of ionospheric pressure integrals

Firstly, we evaluate the parallel pressure integral over area $A_5 + A_6$ to derive equation (4.172)

$$\begin{aligned}
\frac{\sqrt{\pi}}{\nu}\,\gamma_1 &= e^{\frac{U}{\tau}} \int_{\tilde{W}_\parallel=0}^{\infty} \int_{\tilde{W}_\perp=0}^{\frac{\tilde{W}_\parallel - U/\tau}{\zeta-1}} \sqrt{\tilde{W}_\parallel} e^{-\tilde{W}_\parallel} e^{-\tilde{W}_\perp}\, \mathrm{d}\tilde{W}_\perp \mathrm{d}\tilde{W}_\parallel \\
&= e^{\frac{U}{\tau}} \int_{\tilde{W}_\parallel=0}^{\infty} \sqrt{\tilde{W}_\parallel} e^{-\tilde{W}_\parallel} \left(1 - \exp\left(-\frac{\tilde{W}_\parallel}{\zeta-1}\right) \exp\left(\frac{U}{\tau(\zeta-1)}\right)\right)\, \mathrm{d}\tilde{W}_\parallel \\
&= e^{\frac{U}{\tau}} \int_{\tilde{W}_\parallel=0}^{\infty} \sqrt{\tilde{W}_\parallel} e^{-\tilde{W}_\parallel}\, \mathrm{d}\tilde{W}_\parallel - e^{\frac{tU}{\tau}} \int_{\tilde{W}_\parallel=0}^{\infty} \sqrt{\tilde{W}_\parallel} e^{-t\tilde{W}_\parallel}\, \mathrm{d}\tilde{W}_\parallel, \text{ using equation (4.76)} \\
&= e^{\frac{U}{\tau}} \int_{x=0}^{\infty} 2x^2 e^{-x^2}\, \mathrm{d}x - \frac{e^{\frac{tU}{\tau}}}{t^{3/2}} \int_{z=0}^{\infty} 2z^2 e^{-z^2}\, \mathrm{d}z
\end{aligned} \tag{A.27}$$

where $x^2 = \tilde{W}_\parallel$ and $z^2 = t\tilde{W}_\parallel$. Performing integration by parts yields the result

$$\gamma_1 = \frac{\nu e^{\frac{U}{\tau}}}{2} - \frac{\nu e^{\frac{tU}{\tau}}}{2t^{3/2}} \tag{A.28}$$

Secondly, we integrate the perpendicular term over area $A_5 + A_6$ to derive equation (4.175):

$$\begin{aligned}
\frac{\sqrt{\pi}}{\nu}\,\delta_1 &= e^{\frac{U}{\tau}} \int_{\tilde{W}_\parallel=0}^{\infty} \int_{\tilde{W}_\perp=0}^{\frac{\tilde{W}_\parallel - U/\tau}{\zeta-1}} \frac{\tilde{W}_\perp}{\sqrt{\tilde{W}_\parallel}} e^{-\tilde{W}_\parallel} e^{-\tilde{W}_\perp}\, \mathrm{d}\tilde{W}_\perp \mathrm{d}\tilde{W}_\parallel \\
&= e^{\frac{U}{\tau}} \int_{\tilde{W}_\parallel=0}^{\infty} \frac{e^{-\tilde{W}_\parallel}}{\sqrt{\tilde{W}_\parallel}} \left(\left[-\tilde{W}_\perp e^{-\tilde{W}_\perp}\right]_0^{\frac{\tilde{W}_\parallel - U/\tau}{\zeta-1}} + \int_{\tilde{W}_\perp=0}^{\frac{\tilde{W}_\parallel - U/\tau}{\zeta-1}} e^{-\tilde{W}_\perp}\, \mathrm{d}\tilde{W}_\perp \right) \mathrm{d}\tilde{W}_\parallel \\
&= e^{\frac{U}{\tau}} \int_{\tilde{W}_\parallel=0}^{\infty} \frac{e^{-\tilde{W}_\parallel}}{\sqrt{\tilde{W}_\parallel}}\, \mathrm{d}\tilde{W}_\parallel + e^{\frac{tU}{\tau}} \left(\frac{U/\tau}{\zeta-1} - 1\right) \int_{\tilde{W}_\parallel=0}^{\infty} \frac{e^{-t\tilde{W}_\parallel}}{\sqrt{\tilde{W}_\parallel}}\, \mathrm{d}\tilde{W}_\parallel \\
&\quad - e^{\frac{tU}{\tau}} \int_{\tilde{W}_\parallel=0}^{\infty} \frac{\sqrt{\tilde{W}_\parallel}}{\zeta-1} e^{-t\tilde{W}_\parallel}\, \mathrm{d}\tilde{W}_\parallel, \text{ using equation (4.76)} \\
&= e^{\frac{U}{\tau}} \int_{x=0}^{\infty} 2e^{-x^2}\, \mathrm{d}x + \frac{e^{\frac{tU}{\tau}}}{\sqrt{t}} \left(\frac{U/\tau}{\zeta-1} - 1\right) \int_{z=0}^{\infty} 2e^{-z^2}\, \mathrm{d}z \\
&\quad - \frac{e^{\frac{tU}{\tau}}}{t^{3/2}(\zeta-1)} \int_{z=0}^{\infty} 2z^2 e^{-z^2}\, \mathrm{d}z
\end{aligned} \tag{A.29}$$

Using integration by parts on the last term, we obtain

$$\frac{\delta_1}{\nu} = e^{\frac{U}{\tau}} + \frac{e^{\frac{\iota U}{\tau}}}{\sqrt{t}} \left(\frac{U}{\tau (\zeta - 1)} - 1 - \frac{1}{2\zeta} \right) \tag{A.30}$$

List of Publications

A. P. Cran-McGreehin and A. N. Wright, Electron acceleration in downward auroral field-aligned currents, *J. Geophys. Res.*, Vol. 110, A10S15, doi:10.1029/2004JA010898, 2005

A. P. Cran-McGreehin and A. N. Wright, Current-voltage relationship in downward field-aligned current region, *J. Geophys. Res.*, Vol. 110, A10S10, doi:10.1029/2004JA010870, 2005

Web Page Bibliography

1 http://www.geocities.com/Athens/Aegean/7023

2 http://en.wikipedia.org/wiki/Kristian_Birkeland

3 http://www-ssg.sr.unh.edu/tof/Smart/Students/lees/Pictures/mag_sun.jpg

4 http://observe.arc.nasa.gov/nasa/ootw/1996/ootw_960417/ob960417.html

5 http://www-istp.gsfc.nasa.gov/Education

6 http://www.gae.ucm.es/m̃arcos

7 http://ion.le.ac.uk/ionosphere

8 http://sprg.ssl.berkeley.edu/fast

9 http://sci.esa.int

Bibliography

A. T. Aikio, T. Lakkala, A. Kozlovsky, and P. J. S. Williams. Electric fields and currents of stable drifting auroral arcs in the evening sector. *J. Geophys. Res.*, 107(A12), 2002. doi:10.1029/2001JA009172.

A. T. Aikio, K. Mursula, S. Buchert, F. Forme, O. Amm, G. Marklund, M. Dunlop, D. Fontaine, A. Vaivads, and A. Fazakerley. Temporal evolution of two auroral arcs as measured by the Cluster satellite and coordinated ground-based instruments. *Ann. Geophys.*, 22:4089, 2004.

L. Andersson, R. E. Ergun, D. L. Newman, J. P. McFadden, C. W. Carlson, and Y.-J. Su. Characteristics of parallel electric fields in the downward current region of the aurora. *Phys. Plasmas*, 9:3600, 2002.

C. A. Barth and D. N. Baker. Seasonal variation of auroral electron precipitation. *Geophys. Res. Lett.*, 31 (L04809), 2004. doi: 10.1029/2003GL018892.

W. Baumjohann and R. A. Treumann. *Basic space plasma physics*. Imperial College Press, London, 1997.

L. P. Block and C. G. Fälthammar. The role of magnetic-field-aligned electric fields in auroral acceleration. *J. Geophys. Res.*, 95(A5):5877, 1990.

M. H. Boehm, J. Clemmons, J.-E. Wahlund, A. Eriksson, L. Eliasson, L. Blomberg, P. Kintner, and H. Höfner. Observations of an upward-directed electron beam with the perpendicular temperature of the cold ionosphere. *Geophys. Res. Lett.*, 22:2103, 1995.

R. Boström. Kinetic and space charge control of current flow and voltage drops along magnetic flux tubes: Kinetic effects. *J. Geophys. Res.*, 108(A4):8004, 2003. doi:10.1029/2002JA009295.

R. Boström. Kinetic and space charge control of current flow and voltage drops along magnetic flux tubes: 2. Space charge effects. *J. Geophys. Res.*, 109(A01208), 2004. doi:10.1029/2003JA010078.

R. Boström, G. Gustafsson, B. Holback, B. Holmgren, H. Koskinen, and P. Kintner. Characteristics of solitary waves and weak double layers in the magnetospheric plasma. *Phys. Rev. Lett.*, 61:82, 1988.

T. J. M. Boyd and J. J. Sanderson. *Plasma Dynamics*. Thomas Nelson and Sons Ltd, 1969.

T. J. M. Boyd and J. J. Sanderson. *The Physics of Plasmas*. Cambridge University Press, 2003.

A. Brekke and A. Egeland. *The northern light from mythology to space research*. Springer-Verlag Berlin Heidelberg, 1983.

D. A. Bryant. *Electron acceleration in the aurora and beyond*. Institute of Physics, Bristol, 1999.

D. A. Bryant. The roles of static and dynamic electric fields in the auroral acceleration region. *J. Geophys. Res.*, 107(A6), 2002. doi: 10.1029/2001JA900162.

D. A. Bryant and C. H. Perry. Velocity-space distributions of wave-accelerated auroral electrons. *J. Geophys. Res.*, 100(A12):23,711, 1995.

C. W. Carlson, J. P. McFadden, R. E. Ergun, M. Temerin, W. Peria, F. S. Mozer, D. M. Klumpar, E. G. Shelley, W. K. Peterson, E. Moebius, R. Elphic, R. Stangeway, C. Cattell, and R. Pfaff. FAST observations

in the downward auroral current region: Energetic up-going electron beams, parallel electric fields, and ion heating. *Geophys. Res. Lett.*, 25:2017, 1998a.

C. W. Carlson, R. F. Pfaff, and J. G. Watzin. The Fast Auroral SnapshoT mission. *Geophys. Res. Lett.*, 25 (12):2013, 1998b.

C. Cattell, R. Bergmann, K. Sigsbee, C. Carlson, C. Chaston, R. Ergun, J. McFadden, F. S. Mozer, M. Temerin, R. Strangeway, R. Elphic, L. Kistler, E. Moebius, L. Tang, D. Klumpar, and R. Pfaff. The association of electrostatic ion cyclotron waves, ion and electron beams and field-aligned currents: FAST observations of an auroral zone crossing near midnight. *Geophys. Res. Lett.*, 25(12):2053, 1998.

C. Cattell, J. Dombeck, C. Carlson, and J. McFadden. FAST observations of the solar illumination dependence of downgoing auroral electron beams: Relationship to electron energy flux. *J. Geophys. Res.*, 111, 2006. doi:10.1029/2005JA011337.

C. C. Chaston, J. W. Bonnell, L. M. Peticolas, C. W. Carlson, J. P. McFadden, and R. E. Ergun. Driven Alfvén waves and electron acceleration: A FAST case study. *Geophys. Res. Lett.*, 29(11), 2002. doi: 10.1029/2001GL013842.

Y. T. Chiu and M. Schultz. Self-consistent particle and parallel electrostatic field distributions in the magnetospheric-ionospheric auroral region. *J. Geophys. Res.*, 83:629, 1978.

J. T. Clarke, J. Ajello, G. Ballester, L. Ben Jaffel, J. Connerney, , J. C. Gérard, G. R. Gladstone, D. Grodent, W. Pryor, J. Trauger, and J. H. White Jr. Ultraviolet emissions from the magnetic footprints of Io, Ganymede and Europa on Jupiter. *Nature*, 415:997, 2002. doi: 10.1038/415997a.

H. L. Collin, W. K. Peterson, O.W. Lennartsson, and J. F. Drake. The seasonal variation of auroral ion beams. *Geophys. Res. Lett.*, 25(21):4071, 1998.

R. H. Comfort. *Modeling Magnetospheric Plasma*, chapter The magnetic mirror force in plasma fluid models, pages 51–53. American Geophysical Union, 1988.

J. E. P. Connerney, R. Baron, T. Satoh, and T. Owen. Images of excited H_3^+ at the foot of the Io flux tube in Jupiter's atmosphere. *Science*, 262(5136), 1993.

S. Cowley. *Magnetospheric Current Systems*, volume 118 of *Geophys. Monogr. Ser.*, chapter Magnetosphere-ionosphere interactions: A tutorial review, page 91. AGU, Washington D.C., 2000.

S. W. H. Cowley. A beginner's guide to the Earth's magnetosphere. *Earth in Space*, 8(7), 1996.

C. Davisson. A note on Schottky's method of determining the distribution of velocities among thermionic electrons. *Phys. Rev.*, 25:808–811, 1925.

C. S. Deehr, M. H. Rees, A. E. H. Belon, G. J. Romick, and D. Lummerzheim. Influence of the ionosphere on the altitude of discrete auroral arcs. *Ann. Geophys.*, 23:759, 2005.

R. A. Doe, J. F. Vickrey, and M. Mendillo. Electrodynamic model for the formation of auroral ionospheric cavities. *J. Geophys. Res.*, 100(A6):9683, 1995.

J. Dombeck, C. Cattell, J. R. Wygant, A. Keiling, and J. Scudder. Alfvén waves and Poynting flux observed simultaneously by Polar and FAST in the plasma sheet boundary layer. *J. Geophys. Res.*, 110(A12S90), 2005. doi:10.1029/2005JA011269.

R. Elphic, J. Bonnell, R. J. Strangeway, C. W. Carlson, M. Temerin, J. P. McFadden, R. E. Ergun, and W. Peria. *Magnetospheric Current Systems*, volume 118 of *Geophys. Monogr. Ser.*, chapter FAST observations of upward accelerated electron beams and the downward field-aligned current region, page 173. AGU, Washington D.C., 2000.

R. C. Elphic, J. W. Bonnell, R. J. Strangeway, L. Kepko, R. E. Ergun, J. P. McFadden, C. W. Carlson, W. Peria, C. A. Cattell, D. Klumpar, E. Shelley, W. Peterson, E. Moebius, L. Kistler, and R. Pfaff. The

auroral current circuit and field-aligned currents observed by FAST. *Geophys. Res. Lett*, 25(12):2033, 1998.

R. E. Ergun, L. Andersson, C. W. Carlson, D. L. Newman, and M. V. Goldman. Double layers in the downward current region of the aurora. *Nonlinear Processes in Geophysics*, 10:45–52, 2003a.

R. E. Ergun, L. Andersson, D. Main, Y.-J. Su, D. L. Newman, M. V. Goldman, C. W. Carlson, A. J. Hull, J. P. McFadden, and F. S. Mozer. Auroral particle acceleration by strong double layers: The upward current region. *J. Geophys. Res.*, 109(A12220), 2004. doi:10.1029/2004JA010545.

R. E. Ergun, C. W. Carlson, J. P. McFadden, F. S. Mozer, G. T. Delory, W. Peria, C. C. Chaston, M. Temerin, R. Elphic, R. Strangeway, R. Pfaff, C. A. Cattell, D. Klumpar, E. Shelley, W. Peterson, E. Moebius, and L. Kistler. FAST satellite observations of electric field structures in the auroral zone. *Geophys. Res. Lett.*, 25(12):2025, 1998a.

R. E. Ergun, C. W. Carlson, J. P. McFadden, F. S. Mozer, G. T. Delory, W. Peria, C. C. Chaston, M. Temerin, R. Elphic, R. Strangeway, R. Pfaff, C. A. Cattell, D. Klumpar, E. Shelley, W. Peterson, E. Moebius, and L. Kistler. FAST satellite wave observations in the AKR source region. *Geophys. Res. Lett.*, 25(12): 2061, 1998b.

R. E. Ergun, C. W. Carlson, J. P. McFadden, F. S. Mozer, G. T. Delory, W. Peria, C. C. Chaston, M. Temerin, I. Roth, L. Muschietti, R. Elphic, R. Strangeway, R. Pfaff, C. A. Cattell, D. Klumpar, E. Shelley, W. Peterson, E. Moebius, and L. Kistler. FAST satellite observations of large-amplitude solitary structures. *Geophys. Res. Lett.*, 25(12):2041, 1998c.

R. E. Ergun, C. W. Carlson, J. P. McFadden, F. S. Mozer, and R. J. Strangeway. Parallel electric fields in discrete arcs. *Geophys. Res. Lett.*, 27(24):4053, 2000.

R. E. Ergun, C. W. Carlson, J. P. McFadden, R. J. Strangeway, M. V. Goldman, and D. L. Newman. Fast auroral snapshot satellite observations of very low frequency saucers. *Phys. Plasma*, 10(2):454, 2003b.

R. E. Ergun, Y.-J. Su., L. Andersson, C. W. Carlson, J. P. McFadden, F. S. Mozer, D. L. Newman, and M. V. Goldman. Direct observation of localized parallel electric fields in a space plasma. *Phys. Rev. Lett.*, 87 (4), 2001. 045003.

D. H. Fairfield and L. J. Cahill. Transition region magnetic field and polar magnetic disturbances. *J. Geophys. Res.*, 71:155, 1966.

L. A. Frank and W. R. Paterson. Galileo observations of electron beams and thermal ions in Jupiter's magnetosphere and their relationship to the auroras. *J. Geophys. Res.*, 107(A12):1478, 2002. doi: 10.1029/2001JA009150.

H. U. Frey, G. Haerendel, J. H. Clemmons, M. H. Boehm, J. Vogt, O. H. Bauer, D. D. Wallis, L. Blomberg, and H. Lühr. Freja and ground-based analysis of inverted-V events. *J. Geophys. Res.*, 103(A3):4303, 1998.

D. Grodent, J.-C. Gérard, J. Gustin, B. H. Mauk, J. E. P. Connerney, and J. T. Clarke. Europa's FUV auroral tail on Jupiter. *Geophys. Res. Lett.*, 33(L06201), 2006. doi:10.1029/2005GL025487.

D. A. Gurnett, W. S. Kurth, G. B. Hospodarsky, A. M. Persoon, P. Zarka, A. Lecacheux, S. J. Bolton, M. D. Desch, W. M. Farrell, M. L. Kaiser, H. P. Ladreiter, H. O. Rucker, P. Galopeau, P. Louarn, D. T. Young, W. R. Pryor, and M. K. Dougherty. Control of Jupiter's radio emission and aurorae by the solar wind. *Nature*, 415:985, 2002. doi: 10.1038/415985a.

G. Haerendel, H. U. Frey, O. H. Bauer, E. Rieger, J. Clemmons, M. H. Boehm, D. D. Wallis, and H. Lühr. Inverted-V events simultaneously observed with the Freja satellite and from the ground. *Geophys. Res. Lett.*, 21(17):1891, 1994.

M. Hamrin, M. André, P. Norqvist, and K. Rönnmark. The importance of a dark ionosphere for ion heating and auroral arc formation. *Geophys. Res. Lett.*, 27(11):1635, 2000.

T. W. Hill. Auroral structures at Jupiter and Earth. *Adv. Space Res.*, 33:2021, 2004. doi: 10.1016/j.asr.2003.05.037.

A. J. Hull, J. W. Bonnell, F. S. Mozer, and J. D. Scudder. A statistical study of large-amplitude parallel electric fields in the upward current region of the auroral acceleration region. *J. Geophys. Res.*, 108(A1), 2003a. doi:10.1029/2001JA007540.

A. J. Hull, J. W. Bonnell, F. S. Mozer, J. D. Scudder, and C. C. Chaston. Large parallel electric fields in the upward current region of the aurora: Evidence for ambipolar effects. *J. Geophys. Res.*, 108(A6):1265, 2003b. doi:10.1029/2002JA009682.

B. Hultqvist, R. Lundin, K. Stasiewicz, L. Block, P. A. Lindqvist, G. Gustafsson, H. Koskinen, A. Bahnsen, T. A. Potemra, and L. J. Zanetti. Simultaneous observation of upward moving field-aligned energetic electrons and ions on auroral zone field lines. *J. Geophys. Res.*, 93(A9):9765, 1988.

B. Hultqvist, H. Vo, R. Lundin, B. Aparicio, P. A. Lindqvist, G. Gustafsson, and B. Holback. On the upward acceleration of electron and ions by low-frequency electric field fluctuations observed by Viking. *J. Geophys. Res.*, 96(A7):11,609, 1991.

T. Iijima and T. A. Potemra. The amplitude distribution of field-aligned currents at northern high latitudes observed by TRIAD. *J. Geophys. Res.*, 81:2165, 1976.

L. Jago. *The Northern Lights*. Penguin Books, 2002.

P. Janhunen and A. Olsson. The current-voltage relationship revisited: exact and approximate formulas with almost general validity for hot magnetospheric electrons for bi-Maxwellian and kappa distributions. *Ann. Geophys.*, 16:292, 1998.

P. Janhunen and A. Olsson. New model for auroral acceleration: O-shaped structure cooperating with waves. *Ann. Geophys.*, 18:596, 2000.

P. Janhunen, A. Olsson, F. S. Mozer, and H. Laakso. How does the U-shaped potential close above the acceleration region? A study using Polar data. *Ann. Geophys.*, 17:1276, 1999.

J. Jasperse. Ion heating, electron acceleration, and the self-consistent parallel electric field in downward current regions. *Geophys. Res. Lett.*, 25:3485, 1998.

T. Johansson, S. Figueiredo, G. Marklund, A. Fazakerley, S. Buchert, P. A. Lindqvist, and H. Nilsson. Intense high-altitude auroral electric fields - temporal and spacial characteristics. *Ann. Geophys.*, 22: 2485, 2004.

M. T. Johnson, J. R. Wygant, C. A. Cattell, and F. S. Mozer. Seasonal variations along auroral field lines: Measurements from the Polar spacecraft. *Geophys. Res. Lett.*, 30(6):1344, 2003. doi: 10.1029/2002GL015866.

T. Karlsson and G. Marklund. Simulations of effects of small-scale auroral current closure in the return current region. *Phys. Space Plasmas*, (15), 1998.

T. Karlsson and G. T. Marklund. A statistical study of intense low-altitude electric fields observed by Freja. *Geophys. Res. Lett.*, 23(9):1005, 1996.

A. Keiling, J. R. Wygant, C. Cattell, W. Peria, G. Parks, M. Temerin, F. S. Mozer, C. T. Russell, and C. A. Kletzing. Correlation of Alfén wave Poynting flux in the plasma sheet at 4-7 R_E with ionospheric electron energy flux. *J. Geophys. Res.*, 107(A7), 2002. doi:10.1029/2001JA900140.

A. Keiling, J. R. Wygant, C. A. Cattell, F. S. Mozer, and C. T. Russell. The global morphology of wave Poynting flux: powering the aurora. *Science*, 299:383, 2003.

M. C. Kelley. *The Earth's Ionosphere: Plasma physics and electrodynamics*, chapter 1. Academic Press Limited, 1989.

M. G. Kivelson, K. K. Khurana, and R. J. Walker. Sheared magnetic field structure in Jupiter's dusk magnetosphere: Implications for return currents. *J. Geophys. Res.*, 107(A7):1116, 2002. doi: 1029/2001JA000251.

M. G. Kivelson and C. T. Russell, editors. *Introduction to space physics*. Cambridge University Press, 1995.

D. M. Klumpar and W. J. Heikkila. Electrons in the ionospheric source cone: Evidence for runaway electrons as carriers of downward Birkeland currents. *Geophys. Res. Lett.*, 9:873, 1982.

S. Knight. Parallel electric fields. *Planet. Space Sci.*, 21:741, 1973.

H. E. J. Koskinen, R. Lundin, and B. Holback. On the plasma environment of solitary waves and weak double layers. *J. Geophys. Res.*, 95(A5):5921, 1990.

W. S. Kurth, D. A. Gurnett, J. T. Clarke, P. Zarka, M. D. Desch, M. L. Kaiser, B. Cecconi, A. Lecacheux, W. M. Farrell, P. Galopeau, J. C. Gérard, D. Grodent, R. Prangé, M. K. Dougherty, and F. J. Crary. An Earth-like correspondence between Saturn's auroral features and radio emission. *Nature*, 433:722, 2005.

K. Liou, P. T. Newell, and C. I. Meng. Seasonal effects on auroral particle acceleration and precipitation. *J. Geophys. Res.*, 106(A4):5531, 2001.

K. Liou, P. Y. Newell, C. I. Meng, M. Brittnacher, and G. Parks. Synoptic auroral distribution: A survey using Polar ultraviolet imagery. *J. Geophys. Res.*, 102(A12):27,197, 1997.

W. W. Liu, B.-L. Zhu, J. C. Samson, and G. Rostoker. Theory and observation of auroral substorms: A magnetohydrodynamic approach. *J. Geophys. Res.*, 100(A1):79, 1995.

P. Louarn, J. E. Wahlund, T. Chust, H. de Feraudy, and A. Roux. Observation of kinetic Alfvén waves by the Freja spacecraft. *Geophys. Res. Lett.*, 21(17):1847, 1994.

G. Lu, P. H. Reiff, J. L. Burch, and J. D. Winningham. On the auroral current-voltage relationship. *J. Geophys. Res.*, 96(A3):3523, 1991.

R. Lundin, L. Eliasson, G. Haerendel, M. Boehm, and B. Holback. Large-scale auroral plasma density cavities observed by Freja. *Geophys. Res. Lett.*, 21(17):1903, 1994.

K. A. Lynch, J. W. Bonnell, C. W. Carlson, and W. J. Peria. Return current region aurora: $E_{\|}$, j_z, particle energization, and broadband ELF wave activity. *J. Geophys. Res.*, 107(A7):1115, 2002.

R. L. Lysak. Electrodynamic coupling of the magnetosphere and ionosphere. *Space Science Reviews*, 52: 33, 1990.

R. L. Lysak. The relationship between electrostatic shocks and kinetic Alfvén waves. *Geophys. Res. Lett.*, 25(12):2089, 1998.

R. L. Lysak and Y. Song. Energetics of the ionospheric feedback interaction. *J. Geophys. Res.*, 107(A8): 1160, 2002. doi:10.1029/2001JA000308.

G. Marklund. Viking investigations of auroral electrodynamical processes. *J. Geophys. Res.*, 98(A2):1691, 1993.

G. Marklund, L. Blomberg, C.-G. Falthammar, and P. A. Lindqvist. On intense diverging electric fields associated with black aurora. *Geophys. Res. Lett.*, 21:1859, 1994.

G. Marklund, T. Karlsson, and J. Clemmons. On low-altitude particle acceleration and intense electric fields and their relationship to black aurora. *J. Geophys. Res.*, 102(A8):17,509, 1997.

G. T. Marklund, N. Ivchenko, T. Karlsson, A. Fazakerley, M. Dunlop, P.-A. Lindqvist, S. Buchert, C. Owen, M. Taylor, A. Vaivads, P. Carter, M. André, and A. Balogh. Temporal evolution of the electric field

accelerating electrons away from the auroral ionosphere. *Nature*, 414:724, 2001. doi: 10.1038/414724a.

G. T. Marklund and T. Karlsson. Characteristics of the auroral particle acceleration in the upward and downward current regions. *Phys. Chem. Earth (C)*, 26(1-3):81, 2001.

G. T. Marklund, T. Karlsson, S. Figueiredo, T. Johansson, P. A. Lindqvist, M. André, S. Buchert, and L. M. Kistler. Dynamics and characteristics of electric-field structures in the auroral return current region observed by Cluster. *Phys. Scr.*, T122:34, 2006. doi: 10.1088/0031-8949/2006/T122/008.

J. P. McFadden, C. W. Carlson, and M. H. Boehm. Structure of an energetic narrow discrete arc. *J. Geophys. Res.*, 95(A5):6533, 1990.

J. P. McFadden, C. W. Carlson, and R. E. Ergun. Microstructure of the auroral acceleration region as observed by FAST. *J. Geophys. Res.*, 104(14):453, 1999.

J. P. McFadden, C. W. Carlson, R. E. Ergun, F. S. Mozer, M. Temerin, W. Peria, D. M. Klumpar, E. G. Shelley, W. K. Peterson, E. Moebius, L. Kistler, R. Elphic, R. Strangeway, C. Cattell, and R. Pfaff. Spacial structure and gradients of ion beams observed by FAST. *Geophys. Res. Lett.*, 25(12):2021, 1998.

T. E. Moore, R. Lundin, D. Alcayde, M. André, S. B. Ganguli, M. Temerin, and A. Yau. Source processes in the high-latitude ionosphere. *Space Science Reviews*, 88:7, 1999.

M. Morooka and T. Mukai. Density as a controlling factor for seasonal and altitudinal variations of the auroral particle acceleration region. *J. Geophys. Res.*, 108(A7):1306, 2003. doi: 10.1029/200JA009786.

M. Morooka, T. Mukai, and H. Fukunishi. Current-voltage relationship in the auroral particle acceleration region. *Ann. Geophys.*, 22:3641, 2004.

F. S. Mozer, C. W. Carlson, M. K. Hudson, R. B. Torbert, B. Parady, J. Yatteau, and M. C. Kelley. Observations of paired electrostatic shocks in the polar magnetosphere. *Phys. Rev. Lett.*, 38:292, 1977.

F. S. Mozer, R. Ergun, M. Temerin, C. Cattell, J. Dombeck, and J. Wygant. New features of time domain electric-field structures in the auroral acceleration region. *Phys. Rev. Lett.*, 79(7):1281, 1997.

F. S. Mozer and A. Hull. Origin and geometry of upward parallel electric fields in the auroral acceleration region. *J. Geophys. Res.*, 106(A4):5763, 2001.

F. S. Mozer and C. A. Kletzing. Direct observation of large, quasi-static, parallel electric fields in the auroral acceleration region. *Geophys. Res. Lett.*, 25(10):1629, 1998.

P. T. Newell, C. I. Meng, and K. M. Lyons. Suppression of discrete aurorae by sunlight. *Nature*, 381:766, 1996.

D. L. Newman, M. V. Goldman, R .E. Ergun, and A. Mangeney. Formation of double layers and electron holes in a current-driven space plasma. *Phys. Rev. Lett.*, 87(25), 2001.

A. Olsson, L. Andersson, A. I. Eriksson, J. Clemmons, R. E. Erlandsson, G. Reeves, and T. Hughes amd J. S. Murphee. Freja studies of the current voltage relation in substorm-related events. *J. Geophys. Res.*, 103(A3):4285, 1998.

M. Oppenheim, D.L. Newman, and M.V. Goldman. Evolution of electron phase-space holes in a 2D magnetized plasma. *Phys. Rev. Lett.*, 83(12), 1999.

R. J. Pellinen, T. I. Pulkkinen, A. Huuskonen, and K. H. Glassmeier. On the dynamical development of the downward field-aligned current in the substorm current wedge. *J. Geophys. Res.*, 100(A8):14,863, 1995.

D. Pokhotelov, W. Lotko, and A. V. Streltsov. Harmonic structure of field line eigenmodes generated by ionospheric feedback instability. *J. Geophys. Res.*, 107(A11), 2002. doi:10.1029/2001JA000134.

R. Pottelette and R. A. Treumann. Electron holes in the auroral upward current region. *Geophys. Res. Lett.*, 32(L12104), 2005. doi:10.1029/2005GL022547.

P. H. Reiff, H. L. Collin, J. D. Craven, J. L. Burch, J. D. Winningham, E. G. Shelley, L. A. Frank, and

M. A. Friedman. Determination of auroral electrostatic potentials using high- and low-altitude particle distributions. *J. Geophys. Res.*, 93(A7):7441, 1988.

K. Rönnmark. The auroral current-voltage relation. *J. Geophys. Res.*, 107(A12):1430, 2002. doi:10.1029/2002JA009294.

R. Rönnmark and M. Hamrin. Auroral electron acceleration by Alfvén waves and electrostatic fields. *J. Geophys. Res.*, 105(A11):25,333, 2000.

T. Sakanoi, H. Fukunishi, and T. Mukai. Relationship between field-aligned currents and inverted-V parallel potential drops observed at midlatitudes. *J. Geophys. Res.*, 100(A10):19,343, 1995.

S. Salas, E. Hille, and G. Etgen. *Calculus*, chapter 15. John Wiley & Sons, Inc., 9th edition, 2003.

J. C. Samson, L. L. Cogger, and Q. Pao. Observations of field line resonances, auroral arcs, and auroral vortex structures. *J. Geophys. Res.*, 101(A8):17,373, 1996.

J. Saur, B. H. Mauk, D. G. Mitchell, N. Krupp, K. K. Khurana, S. Livi, S. M. Krimigis, P. T. Newell, D. J. Williams, P. C. Brandt, A. Lagg, E. Roussos, and M. K. Dougherty. Anti-planetward auroral electron beams at Saturn. *Nature*, 439:699, 2006. doi: 10.1038/nature04401.

D. Schriver. Particle simulation of the auroral zone showing parallel electric fields, waves, and plasma acceleration. *J. Geophys. Res.*, 104(A7):14,655, 1999.

D. Schriver, M. Ashour-Abdalla, R. J. Strangeway, R. L. Richard, C. Klezting, Y. Dotan, and J. Wygant. FAST/Polar conjuction study of field-aligned auroral acceleration and corresponding magnetotail drivers. *J. Geophys. Res.*, 108(A9):8020, 2003.

H. C. Scoffield, T. K. Yeoman, D. M. Wright, S. E. Milan, A. N. Wright, and R. J. Strangeway. An investigation of the field-aligned currents associated with a large-scale ULF wave using data from CUTLASS and FAST. *Ann. Geophys.*, 23:487, 2005.

K. Shiokawa, H. Fukunishi andH. Yamagishi, H. Miyaoka, R. Fujii, and F. Tohyama. Rocket observation of the magnetosphere-ionosphere coupling process in quiet and active arcs. *J. Geophys. Res.*, 95(A7): 10,679, 1990.

J. H. Shue, P. T. Newell, K. Liou, and C. I. Meng. The quantitative relationship between auroral brightness and solar EUV Petersen conductance. *J. Geophys. Res.*, 106(A4):5883, 2001.

N. Singh, C. Deverapalli, I. Khazanov, N. Puthumbakum, and A. Rajagiri. Parallel electric fields in a diverging flux tube with upward current: Nature of quasi-static fields. *J. Geophys. Res.*, 110(A05205), 2005. doi:10.1029/2004JA010695.

D. P. Stern. One-dimensional models of quasi-neutral parallel electric fields. *J. Geophys. Res.*, 86:5839, 1981.

A. V. Streltsov and W. Lotko. Ultra-low-frequency electrodynamics of the magnetosphere-ionosphere interaction. *J. Geophys. Res.*, 110(A08203), 2005. doi:10.1029/2004JA010764.

D. W. Swift. On the formation of auroral arcs and acceleration of auroral electrons. *J. Geophys. Res.*, 86: 5839, 1975.

H. Tanaka, Y. Saito, S. Ishii, K. Asamura, and T. Mukai. Simultaneous observation of the electron acceleration and ion deceleration in the dayside high-latitude auroral region. *Geophys. Res. Lett.*, 30(12):1615, 2003. doi:10.1029/2003GL017071.

M. Temerin and C.W. Carlson. Current-voltage relationship in the downward auroral current region. *Geophysical Research Letters*, 25(13):2365–2368, 1998.

M. Temerin, K. Cerny, W. Lotko, and F. S. Mozer. Observations of double layers and solitary waves on auroral zone field lines. *Phys. Rev. Lett.*, 48:1175, 1982.

T. Ulich, E. Turunen, and T. Nygrén. Effective recombination coefficient in the lower ionosphere duing bursts of auroral electrons. *Adv. Space Res.*, 25(1):47, 2000.

A. Vaivads, M. André, S. Buchert, A. I. Eriksson, A. Olsson, J. E. Wahlund, P. Janhumen, G. Marklund, L. M. Kistler, C. Mouikis, D. Winnigham, A. Fazakerley, and P. Newell. What high altitude observations tell us about the auroral acceleration: A Cluster/DMSP conjunction. *Geophys. Res. Lett.*, 30(3):1106, 2003.

J. Vedin and K. Rönnmark. A linear auroral current-voltage relation in fluid theory. *Ann. Geophys*, 22: 1719, 2004.

J. Vedin and K. Rönnmark. Electron pressure effects on driven auroral Alfvén waves. *J. Geophys. Res.*, 110(A01214), 2005. doi:10.1029/2004JA010610.

D. R. Weimer, D. A. Gurnett, C. K. Goertz, J. D. Menietti, J. L. Burch, and M. Sugiura. The current-voltage relationship in auroral current sheets. *J. Geophys. Res.*, 92:187, 1987.

A. N. Wright. Transfer of magnetosheath momentum and energy to the ionosphere along open field lines. *J. Geophys. Res.*, 101(A6):13169, 1996.

A. N. Wright. Energy sources of field-aligned currents: Auroral electron energization. *J. Geophys. Res.*, 110(A10S08), 2005. doi:10.1029/2004JA010609.

A. N. Wright and W. Allan. Structure, phase motion, and heating within Alfvén resonances. *J. Geophys. Res.*, 101:17399, 1996.

A. N. Wright, W. Allan, and P. A. Damiano. Alfvén wave dissipation via electron energization. *Geophys. Res. Lett.*, 30(16):1847, 2003. doi: 10.1029/GL017605.

A. N. Wright, W. Allan, M. S. Ruderman, and R. C. Elphic. The dynamics of current carriers in standing Alfvén waves: Parallel electric fields in the auroral acceleration region. *J. Geophys. Res.*, 107(A7), 2002. doi:10.1029/2001JA900168.

A. N. Wright and A. W. Hood. Field-aligned electron acceleration in Alfvén waves. *J. Geophys. Res.*, 107 (A3):1135, 2003. doi:10.1029/2002JA009551.

J. R. Wygant, A. Keiling, C. A. Cattell, R. L. Lysak, M. Temerin, F. S. Mozer, C. A. Kletzing, J. D. Scudder, V. Streltsov, W. Lotko, and C. T. Russell. Evidence for kinetic Alfvén waves and parallel electron energization at 4-6 R_E altitudes in the plasma sheet boundary layer. *J. Geophys. Res.*, 107(A8): 1201, 2002. doi: 10.1029/2001JA900113.